Development of Finite Element Modeling and Bayesian Parameter Estimation Strategies for Corroded RC Bridges towards Probabilistic Seismic Performance Assessment

by

Shaghayegh Abtahi

A thesis submitted in partial fulfillment of the requirements for the degree of

Doctor of Philosophy

in

Structural Engineering

Department of Civil and Environmental Engineering

University of Alberta

ABSTRACT

Reinforced concrete (RC) structures, such as RC bridges, are designed to remain safe and functional for their lifetime, during which the impacts of aging may result in performance degradation. Steel bar corrosion is one of the most common causes of structural performance degradation in RC structures subjected to service loads or natural hazards, e.g., earthquakes in seismic-prone areas. Therefore, to ensure the adequate seismic performance of RC structures over the course of their life, it is necessary to investigate the effect of corrosion on seismic performance prediction.

To this end, this research work develops required tools for seismic performance assessment, including advanced finite element (FE) modeling and Bayesian parameter estimation strategies for corroded RC structures. The newly developed advanced FE modeling strategy in this thesis can capture the corrosion impact on bonding between steel bars and surrounding concrete, as well as the vulnerability of steel bars to buckling in addition to other effects on the steel bar cross-sectional area, cover concrete spalling, and confinement level for core concrete. One of the main novelties of this FE modeling approach is that an enhanced fiber-based frame element with bond-slip is developed and probabilistic models for uncorroded and corroded bonding properties are established in order to account for the corrosion-affected bonding in the nonlinear behavior simulation of corroded RC structures. Additionally, a constitutive model for steel bar with buckling is developed that can simulate the steel bar buckling behavior restrained by flexible transverse reinforcement. This newly developed model is capable to simulate bridge structures under extreme health and loading conditions, specifically, considering the impact of corroded longitudinal steel bar and transverse reinforcement on the steel bar buckling behavior, which reflects the increased vulnerability of corroded RC bridges to steel bar buckling due to corrosion. To estimate the corrosion-related properties of RC bridges, this research work extends the application of the nonlinear FE model updating to corroded RC structures and provides a methodology to estimate the corrosion state from the seismic measurement of RC structures with high nonlinearity.

Using these newly developed strategies, the seismic performance of an RC bridge, impacted by corrosion over the course of its life, is examined in a probabilistic framework. In particular, it has been demonstrated that the conventional FE modeling approach, which neglects the corrosion-affected bond-slip and steel bar buckling, would lead to underestimated seismic risk for corroded RC bridges, specifically the seismic risk associated with the post-peak behavior. In addition, adopting the corrosion state estimation strategy results in more accurate estimations for the corrosion-affected properties, which can be used to update the FE model. The updated FE model of the corroded RC bridge can potentially be utilized for a more reliable seismic performance assessment, which assists in future decision-making for the repair or retrofit of the existing bridge.

PREFACE

This thesis includes original research conducted by Shaghayegh Abtahi. Six journal papers have been published/under review/in preparation for publication on the basis of this thesis. The details of the corresponding chapters are summarized below:

A version of Chapter 2 is under review as ***Abtahi S., and Li Y., "Efficient Modeling of Steel Bar Slippage Effect in Reinforced Concrete Structures using a Newly Implemented Nonlinear Element", Computers & Structures***. For the consistency and coherence of this thesis, contents have been modified, removed, or added to the submitted paper. Shaghayegh Abtahi was responsible for conceptualization, methodology development, numerical model development, analysis implementation, and paper composition. Yong Li was in charge of conceptualization, supervision, funding acquisition, and paper revision.

A version of Chapter 3 has been published as ***Abtahi S., and Li Y., "Bond-Slip Model Uncertainty Quantification and Effect on Nonlinear Behavior Simulations of Reinforced Concrete Columns", Engineering Structures, 266: 114525, 2022.*** For the consistency and coherence of this thesis, contents have been modified, removed, or added to the submitted paper. Shaghayegh Abtahi was responsible for conceptualization, methodology development, numerical model development, analysis implementation, and paper composition. Yong Li was in charge of conceptualization, supervision, funding acquisition, and paper revision.

A version of Chapter 4 is in press as ***Abtahi S., and Li Y., "Investigation of Corroded Bond-Slip Effects using a Newly Proposed Fiber-based FE Modeling Approach for Corroded RC Columns", ASCE Journal of Structural Engineering***. For the consistency and coherence of this thesis, contents have been modified, removed, or added to the submitted paper. Shaghayegh Abtahi was responsible for conceptualization, methodology development, numerical model development, analysis implementation, and paper composition. Yong Li was in charge of conceptualization, supervision, funding acquisition, and paper revision.

A version of Chapter 5 is in preparation as ***Abtahi S., and Li Y., "Material Model of Corroded Reinforcing Bars with Buckling Considering the Effects of Stirrups", ASCE Journal of Structural Engineering***. For the consistency and coherence of this thesis, contents have been modified, removed, or added to the submitted paper. Shaghayegh Abtahi was responsible for conceptualization, methodology development, numerical model development, analysis implementation, and paper composition. Yong Li was in charge of conceptualization, supervision, funding acquisition, and paper revision.

A version of Chapter 6 is under review as ***Abtahi S., Liu Z., and Li Y., "Corrosion State Estimation for RC Structures Based on Bayesian Nonlinear Finite Element Model Updating with Seismic Data", Mechanical Systems and Signal Processing***. For the consistency and coherence of this thesis, contents have been modified, removed, or added to the submitted paper. Shaghayegh Abtahi was responsible for conceptualization, methodology development, numerical model development, analysis implementation, and paper composition. Yong Li was in charge of conceptualization, supervision, funding acquisition, and paper revision.

A version of Chapter 7 is in preparation as ***Abtahi S., and Li Y., "Probabilistic Seismic Performance Assessment of RC Bridges under Corrosion", Structural Safety***. For the consistency and coherence of this thesis, contents have been modified, removed, or added to the submitted paper. Shaghayegh Abtahi was responsible for conceptualization, methodology development, numerical model development, analysis implementation, and paper composition. Yong Li was in charge of conceptualization, supervision, funding acquisition, and paper revision.

DEDICATION

To my husband, Nima,

and

my parents

ACKNOWLEDGMENTS

Foremost, I would like to express my deepest gratitude to my supervisor, Dr. Yong Li, for his invaluable guidance and encouragement over the course of my Ph.D. studies, from inception to completion. His brilliant insights guided me through my research and trained me to be an independent researcher. This dissertation would not have been possible without his overwhelming support and mentorship.

Besides my supervisor, I would like to thank my supervisory committee members, Dr. Carlos A. “Lobo” Cruz-Noguez and Dr. Lijun Deng, for their constructive feedback on my research. I would also like to thank my Ph.D. defense examiners, Dr. Mustafa Gul and Dr. Tracy Becker.

I thank my fellow Structural Modeling and Reliability Analysis (SM&RA) research group members, and my collaborator, Dr. Rodrigo Astroza and Zhenning Liu, for their valuable feedback and assistance throughout my Ph.D. research. Also, I would like to thank my friends, Mahyar, Massoud, Elnaz, Mozhgan, Marjan, Arman, Reihaneh, and Ali, for their love, support, and inspiration.

Primary funding support from the Natural Sciences and Engineering Research Council of Canada (NSERC) and additional funding obtained through scholarships from the University of Alberta and Alberta Innovates are gratefully acknowledged.

And last but not the least, I want to thank my family members, my parents, my brother, my sister-in-law, and especially my husband, for all their unwavering love, support, and patience in the most difficult times during this chapter of my life.

TABLE OF CONTENTS

LIST OF TABLES

LIST OF FIGURES

Chapter 1. INTRODUCTION

1.1. BACKGROUND

Sustainable infrastructure development, which aims to meet the needs of the present and future generations, has become an international priority [1]. Reinforced concrete (RC) structures, widely used for infrastructural systems, play a significant role in socio-economic development, and notable efforts have been devoted to the sustainable design of new RC structures [2,3]. For example, the development of performance-based design and evaluation has taken a central role in modern structural engineering, where damage-control design targets have been pursued particularly for extreme loadings (e.g., strong earthquakes).

On the other hand, a concerning number of existing infrastructural systems are structurally deficient and in need of sustainable maintenance and management. Specifically for RC bridges, as integral parts of the transportation infrastructure system, about 38.7% of bridges in Canada are in fair, poor, or very poor conditions, which are under the risk of further deterioration, according to Canadian Infrastructural Report Card 2019 [4]. As global climate change has emerged during recent decades, many studies have focused on how climate change impacts the performance of structures [5]. In particular, it has been shown that growing CO_2 emission with global warming has led to an increase in the probability of carbonation-induced corrosion, and additionally, temperature rises increase corrosion rates [6,7]. Furthermore, severe weather conditions have led to increasing use of de-icing salts, which causes chloride penetration resulting from traffic spray scenario, i.e., de-icing salt chlorides becoming air-borne as a result of the vehicle passing through chloride-laden water [8]. Corrosion weakens structural components in the long term and increases their vulnerability to extreme loads (e.g., earthquakes).

In seismic-prone areas, earthquakes can be possibly the most hazardous natural disaster among the others, which lead to millions of dollars of financial and human losses. Many strong earthquakes have occurred in the 20th century in Canada, such as Cornwall, Ontario in 1940, southern Vancouver Island, British Columbia in 1946, and Saguenay region of Quebec in 1988 [9]. Specifically, in Alberta, human-induced earthquakes due to hydraulic fracturing and others have become more frequent and stronger than in past decades [10]. The seismic demand can be aggravated by the corrosion-damage in structures, which in turn causes larger losses in future earthquakes and raises the need for constructing new structures. However, many studies have investigated the effect of building new structures on the environment [11,12], and have shown it exacerbates global climate change by producing more CO_2. Hence, as shown in Figure 1-1, a vicious cycle forms since global climate change is intensifying the corrosion effect and deteriorating existing structures rapidly, and simultaneously, constructing new structures is accelerating the corrosion process through environmental effects during global climate change. In order to break this cycle, sustainable design and maintenance are required to extend the lifetime of existing structures under severe environmental conditions [13], which will delay the need for new constructions. To achieve this ultimate goal, emerging performance-based engineering is revolutionizing the current structural engineering, particularly in designing structures against strong earthquakes [14], hurricanes [15], blasts [16], fire [17], and tsunamis [18].

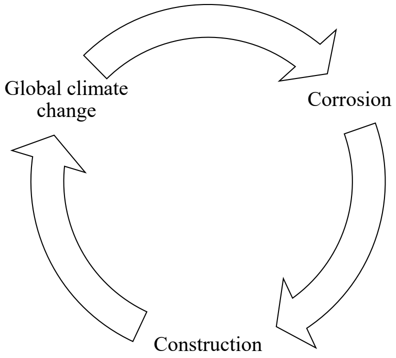

Figure 1-1: Global climate change and construction relationship

1.2. PROBLEM STATEMENT

Corrosion-induced deterioration can lead to pre-mature decommissioning or failures of structures. Accordingly, significant resources have been spent to prevent or mitigate deterioration effects through design details, maintenance, and monitoring. To optimally plan the mitigation measures of deterioration, a proper assessment of the reliability of deteriorating structures in the face of uncertainty is required.

In the current practice, structures have been assessed without explicitly considering deterioration due to aging (e.g., corrosion) [19]. Nevertheless, as illustrated in Figure 1-2, the structure can experience recurring hazards during its lifetime as well as aging. Specifically, the concrete may undergo different deteriorations such as freeze-thaw, erosion, temperature gradients, etc. [20,21]. For RC structures, corrosion of reinforcements is the most prominent aging effect, which is caused by using de-icing salts [22], coastal zone effect [23], or exposure to atmospheric CO_2 [24]. In this study, particular attention is devoted to the corroded RC structures.

Corrosion can alter the seismic performance of RC structures through degrading structural properties [25–27], such as the reduction in the steel bar areas, confinement provided for concrete, concrete material strength, bonding between steel bar and the surrounding concrete, and more vulnerability to steel bar buckling. Due to such deteriorations, estimation of the current state and seismic resistance or performance of a structure (with or without measurements) is essential to protect the structure against future seismic hazards with more transparency. The relevant information gained on the seismic performance of corroded RC structures, especially when prevailing uncertainties are considered explicitly, can be used to assist decision making for the repair or retrofitting of existing structures.

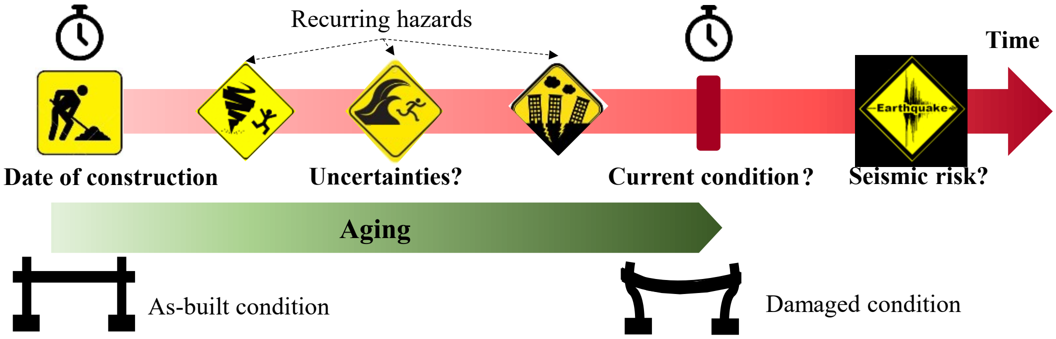

Figure 1-2: Profile of a structure lifetime

1.3. LITERATURE REVIEW AND RESEARCH MOTIVATION

RC structures, such as RC bridges, are designed to remain safe and functional for an extended period of time, during which the impacts of aging may cause performance degradation [26,28–30]. Corrosion of reinforcing steel, as one of the main environmental stressors that contributes to aging, is more likely to occur in RC bridges [31]. The corrosion-induced deterioration may affect the performance of RC bridges subjected to service loads or natural hazards, e.g., earthquakes in seismic-prone areas [32]. Specifically, numerous studies in the literature demonstrated that the impact of corrosion becomes more crucial when the bridges are subjected to seismic loading since the corrosion of reinforcing steel can significantly reduce the lateral strength capacity [26,32–35]. Therefore, it is necessary to reliably estimate the safety and functionality of corroded RC bridges subjected to seismic loading by assessing their seismic performance during the course of their service life.

To assess the seismic performance of the corroded RC bridges, an adequate finite element (FE) model considering different aspects of corrosion is required. The corrosion-affected parameters can be estimated through numerical/empirical models or identified by FE model updating techniques, depending on the availability of field measurements (e.g., during previous seismic events). Accordingly, the literature review is divided into three key sub-sections as follows. Note that a more detailed literature view over specific aspects will be provided in the following chapters.

1.3.1. Nonlinear FE modeling

To model frame-type RC structures, such as RC bridges, particularly when corrosion effect is considered, there mainly exist two different FE modeling approaches: one using fiber-based beam-column elements with distributed nonlinearities, i.e., fiber-based FE approach [26,36], and the other using continuum elements, i.e., continuum-based FE approach [37,38]. In the fiber-based FE approach, as shown in Figure 1-3, the cross sections are discretized into fibers and the section constitutive behavior is explicitly derived through the uniaxial stress-strain behavior of fibers [39]. Comparing these two techniques, despite higher accuracy, the continuum-based FE modeling approach is less advantageous compared with the fiber-based FE modeling approach for frame-type structures (e.g., bridges), which is computationally efficient and has been widely used in the field of structural earthquake engineering.

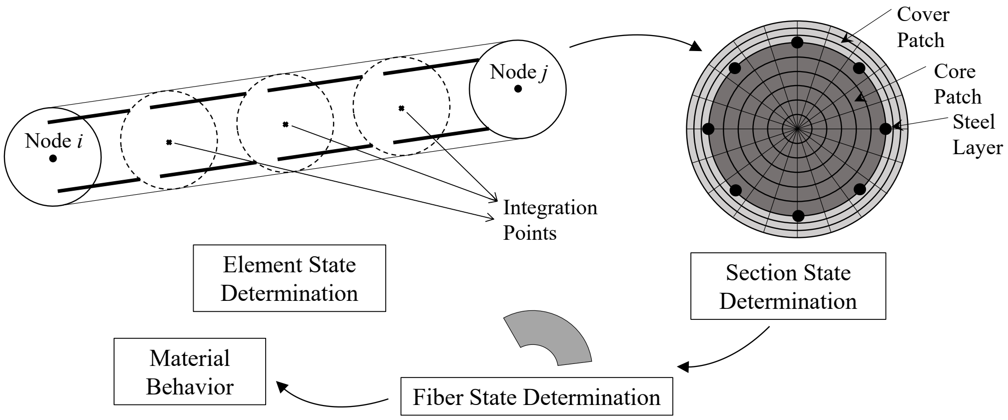

Figure 1-3: Fiber frame element used for modeling RC structures

For modeling corroded RC structures, it is required to incorporate different aspects of the corrosion effect, including:

(1) Reduction in steel bar area [25,40], which can be included through modifying the geometrical properties of the steel bar section;
(2) Cover concrete deterioration [41,42], where the splitting stresses caused by volumetric expansion due to transforming steel to rust would reduce the strength of concrete [43,44], which can be represented by modifying the uniaxial stress-strain behavior;
(3) Reduction of confinement [41,42], which can be applied through updating the confinement properties based on the corroded transverse reinforcement [45];
(4) Vulnerability to steel bar buckling [46], which is caused by the reduction of lateral confinement and longitudinal bar cross-sectional area. It is required to use the proper steel material behavior with the effect of buckling under corrosion;
(5) Degradation of bonding [47], which requires an FE modeling tool capable of considering the corroded bond-slip.

Among all of these five aspects, the first three aspects can be applied through modifying the geometrical properties and using existing models, while the last two aspects need further investigation and development due to the gap in the literature.

1.3.2. Corrosion-state identification

To develop a nonlinear FE model, which can predict accurately the measured structural response, the parameter estimation or identification of the corrosion-affected mechanical properties is essential. This can be achieved by nonlinear FE model updating (FEMU) when measurements are available for a structural system (e.g., seismic measurements of an instrumented bridge during an earthquake). Several studies have proposed different techniques for nonlinear FEMU, including Bayesian inference or stochastic filtering methods, such as extended Kalman filter (EKF) and unscented Kalman filter (UKF) [48–50]. In general, Kalman filtering is an algorithm employing a set of measurements as observations to evaluate the unknown variables through estimating a joint probability distribution over the variables. Some recent studies have applied EKF to nonlinear FEMU problems using simulated seismic response data (e.g., [51]); however, this approach has limited capability when applied to highly nonlinear problems because it is based on Taylor series expansion for linearization in the first-order approximation of statistics. By contrast, the UKF, another stochastic filtering method based on the Kalman filter, uses the unscented transform for a more accurate estimation of the first-order and second-order statistics (i.e., mean, covariance) [52]. The broad use of this method in the literature (e.g., [53–55]) indicates its robustness to solve nonlinear FEMU problems. However, to the best knowledge of the authors, the aforementioned stochastic filtering methods have not been utilized for system identification of corroded structures (e.g., health condition assessment of corroded structures).

1.3.3. Seismic performance assessment

Different aspects of deterministic and probabilistic seismic performance of new structures have been extensively studied in the literature, such as the effect of aftershocks on the structural performance [56], the effect of soil flexibility (i.e., soil-structure interaction) on the seismic performance [57,58], fragility curve development (i.e., probability of occurrence of some specific outcome versus a measure of demand) [59,60], etc. On the other hand, several studies have focused on the deterministic and probabilistic seismic performance of aged structures [32,61]. However, the FE models used in these studies are not considering different aspects of corrosion effects as discussed previously. By concentrating solely on the steel bar cross-sectional area reduction, which is relatively easier to account for in the modeling process, several studies investigated the impact of corrosion-induced deterioration on the structural reliability of the RC bridges [25,40]. The seismic performance of corroded RC bridges was later studied by accounting for the effect of corrosion on both the concrete and reinforcing steel [41,42]. These studies revealed that both strength and ductility of the structural members deteriorate over time by corrosion, affecting the seismic capacity of the bridge and eventually resulting in a shift to an undesirable mechanism of collapse. It is worth noting that other aspects of corrosion, particularly corrosion-damaged bonding and steel bar buckling that are relatively challenging to consider, were neglected in these studies. The impact of corrosion on the seismic performance of RC bridges was further explored in [62,63] by capturing the strain penetration in the FE model of RC bridges using an oversimplified method, which lumps the bond-slip effect at the bottom of the bridge column [64]. These studies showed that the deterioration in strain penetration increases the seismic fragility of corroded RC bridges, highlighting the importance of considering different aspects of corrosion.

Additionally, there is no study considering seismic measurements to estimate the corroded properties with more accuracy, which can be used to reduce the uncertainty in structural and corrosion properties for the informed seismic performance of bridges. Hence, the seismic performance of aged RC structures needs further investigation. These limitations and gaps in the literature are the principal motivations for this study.

1.4. RESEARCH OBJECTIVES AND SCOPE

In light of the aforementioned needs, the overall objective of this research is to develop finite element modeling and Bayesian parameter estimation strategies for corroded RC structures for seismic performance assessment, and their corresponding seismic reliability, which can be potentially used in the future to assist decision making for repair or retrofitting of existing structures. To this end, the research work is mainly coordinated with the following three sub-objectives:

(1) developing an efficient and comprehensive FE modeling tool for corroded RC structures, which is capable of considering different corrosion aspects, such as degraded bonding and steel bar behavior considering buckling;

(2) developing the corrosion condition identification tool to estimate the corroded properties indirectly based on the measured structural responses (e.g., accelerations, displacements) during an experience seismic event; and

(3) assessing the probabilistic seismic performance of corroded RC structures using the FE modeling tool, as well as the condition identification tool when seismic measurements are available to identify the corrosion states.

Note that significant uncertainties are associated with corroded RC structures, such as the corrosion-affected properties of the structure, as well as the seismic loading when it comes to their seismic performance assessment. Therefore, probabilistic analysis approaches are utilized to study the performance of corroded RC structures with pertinent uncertainties considered in this study.

Moving towards accomplishing the central objective of this research, an overall methodology is proposed here as shown in Figure 1-4, which incorporates nonlinear FE modeling of corroded RC structures, corrosion condition identification through nonlinear FE model updating, and probabilistic seismic performance assessment. Considering an existing RC structure, both the pre-event (i.e., before experiencing an earthquake) and post-event (i.e., after an earthquake) seismic performance is of concern. Thus, to predict its seismic performance, there are two scenarios as shown in Figure 1-4: (1) pre-event assessment, when there are no seismic measurements for the structure before experiencing an earthquake, so the current condition is determined based on the existing models and assumptions; and (2) post-event assessment, when the structure has experienced a small or moderate earthquake and the current condition can be determined based on the measured responses during this event. The future seismic risk of this structure can then be re-evaluated based on the identified current condition.

For both scenarios discussed above, a proper nonlinear FE model is required. Depending on the availability of seismic measurements, the corroded properties of this FE model are either predicted or estimated, and then, the FE model will be used for the probabilistic seismic performance assessment. Hence, this methodology has three main steps, which are self-contained and integrated within the proposed framework, as discussed in the following:

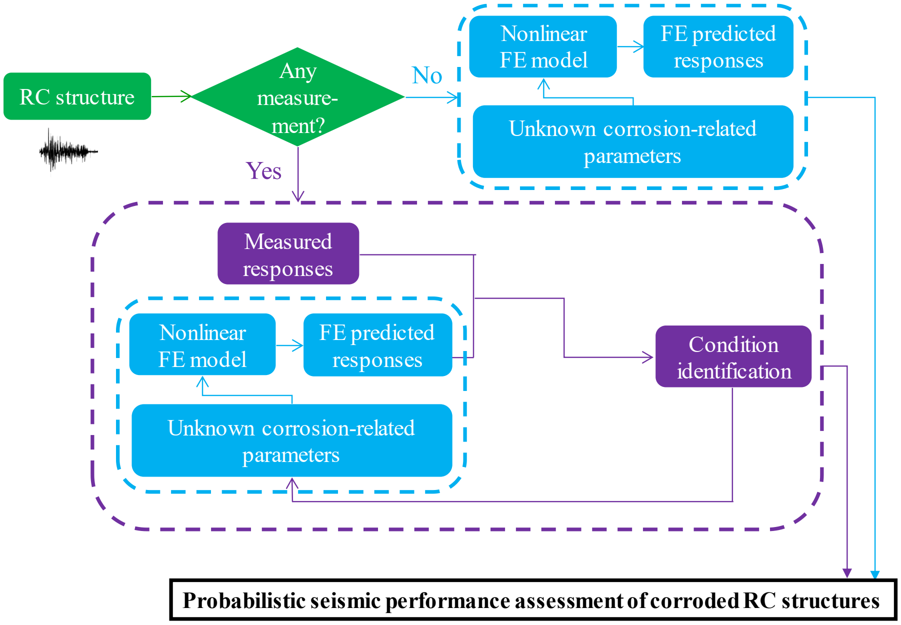

Figure 1-4: Proposed framework for probabilistic seismic performance assessment of corroded RC structures

(1) **Nonlinear FE model development for corroded RC structures:** This study contributes to the development and application of the fiber frame elements to model corroded RC structures. In particular, developing an FE modeling approach capable of capturing the effect of corroded bond-slip and steel bar buckling behavior is of primary goals of this step.

(2) **Corrosion-state estimation using nonlinear FE model updating:** Direct measurements of the corroded properties in RC structures are challenging even with advanced non-destructive techniques, and thus accurate modeling parameters are typically not readily available. Such

uncertainties in the FE modeling aspects can compromise the reliability of the model prediction and in turn, bias the residual performance evaluation of corroded RC structures. As such, to develop a nonlinear FE model, the nonlinear FEMU can be used when measurements are available for a structural system. Nonlinear FEMU is also known as inverse FE modeling shown in Figure 1-5, which is defined as the process of estimating the optimal model parameters by minimizing the discrepancy between the FE predictions and experimental observations. In particular, the responses recorded through sensors from the structure are compared with the responses resulting from the corresponding FE model. The initial comparison shows a significant difference between these two responses; however, by using the nonlinear FEMU approach, the properties of the FE model would be updated so that the results from the FE model matches well with the true responses. This step focuses on the identification of corroded properties of RC columns using simulated seismic data with various noise levels. Applying this methodology to some examples demonstrates the capability of Bayesian inference to estimate the corroded properties in aged RC structures.

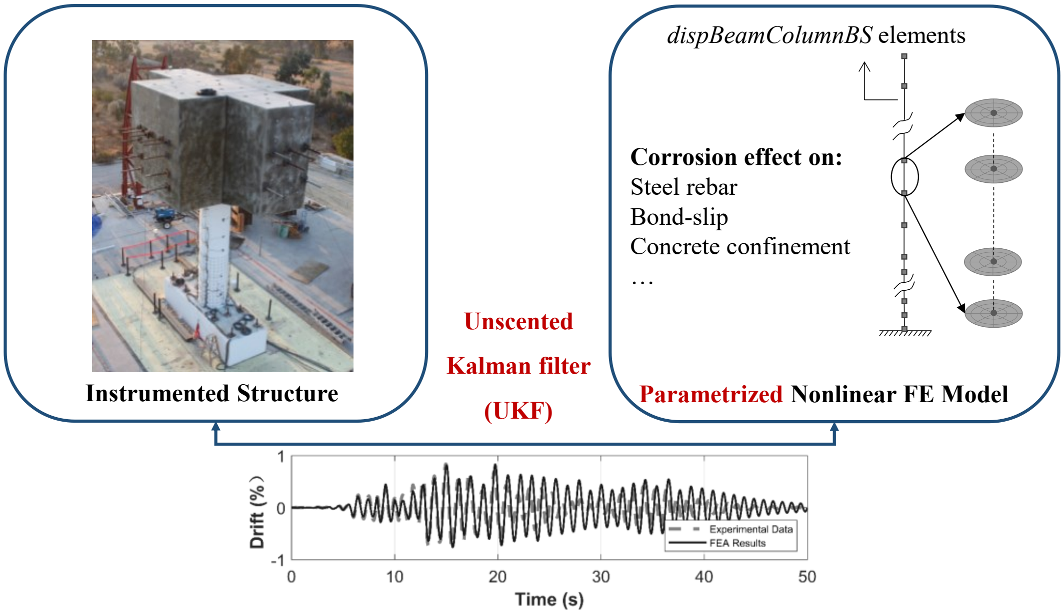

Figure 1-5: Conceptual view of nonlinear FEMU

(3) **Probabilistic seismic performance assessment of corroded RC bridges:** The last step of the proposed methodology assesses the seismic performance of corroded RC bridges in a probabilistic framework using the developed tools in the previous steps. In this regard, similar to other studies in the literature [26], a two-span bridge, located in Ripon, California, is considered here as an application example. This bridge is modeled in *OpenSees* [65], considering that the superstructure is modeled with linear elastic beam-column elements for the composite actions of steel girders and bridge deck since the superstructure is protected by a capacity design and expected to remain in the elastic range [66]. The introduced fiber-based frame element with bond-slip is used for modeling the circular RC column of the bridge. In addition, for the abutments and bearings of the bridge, existing analytical models are employed [67–69]. To incorporate the effect of corrosion on different structural aspects, the FE modeling approach discussed previously is applied to the pristine bridge model and used for the analysis. In addition to the uncertainties in the corrosion level of the bridge, the main source of uncertainty stems from earthquakes, for which a large suite of ground motions selected from [70] according to the probabilistic seismic hazard analysis. Therefore, the probabilistic seismic demand of this bridge is studied, demonstrating the pre-event and post-event analysis with the aid of corrosion-state identification tool using seismic measurements. The comparison between the findings of these two parts would give an insight into the performance of the corroded RC bridges and the importance of condition identification. Furthermore, the impact of corrosion on capacity analysis of this RC bridge is investigated, along with the relevance of incorporating corroded bonding and steel bar buckling. Finally, the probabilistic performance prediction can be used to assist decision making for repair or retrofit.

1.5. NOVELTY AND SIGNIFICANCE OF RESEARCH

Comparing to the state-of-the-art in the literature, this research work is innovative in modeling of corrosion at the macro level in the advanced mechanics-based FE model. In addition to the comprehensive and accurate FE modeling approach proposed in this work for corrosion-affected RC structures, the corrosion state estimation methodology is the first of its kind in this field of study to identify corroded properties that cannot be measured directly. Hence, the probabilistic analysis of capacity and seismic demand carried out in this research using the newly developed tools provides insights into the performance prediction of aged RC structures, which is commonly neglected or overestimated in the literature.

In addition to the novelties of this study, the primary significance of this research work is its contribution to risk-informed decision making for the life cycle performance of infrastructure with consideration of sustainability and resilience. In particular, breaking the cycle shown in Figure 1-1 will help to achieve sustainable infrastructure development that takes environmental impacts into account. Accurately anticipating the performance of the corroded structure and corresponding seismic risk results in a more sustainable design, which may limit the corrosion-related structural deterioration. The decision making process for required repair or retrofit can also be assisted by identifying the corrosion state of the existing structure and updating its seismic performance prediction in light of the current condition. This will reduce the need to demolish the deteriorated infrastructure and build a new one, which implies sustainable maintenance. In addition to sustainability, this research work contributes to the resiliency of infrastructures. Following a hazard event (e.g., earthquake), resilient indicators take strength, functionality, and recovery time into consideration. Through assessing the probabilistic seismic performance of corrosion-affected infrastructures, the effect of seismic hazard events on structural performance and recovery time while maintaining functionality and safety can be investigated, which contributes to maintaining the resilience of aged infrastructures.

1.6. ORGANIZATION OF THESIS

Details of this research work have been thoroughly documented in the form of this thesis, consisting of eight chapters as briefly outlined below:

- **Chapter 1** provides an introduction by highlighting the research gaps through an overall literature review and discussing the necessity of probabilistic seismic assessment of corroded RC structures. The research objectives and proposed methodology are also outlined in this chapter.
- **Chapter 2** introduces the geometrically nonlinear fiber-based frame element with bond-slip, which can be used for advanced FE modeling of RC structures, accompanied by the model validation and exploring the effect of imperfect bonding on the nonlinear behavior simulation of RC columns in different scenarios.
- To explore the impact of bond-slip model uncertainties used in the newly developed fiber-based frame element on the nonlinear behavior simulations of RC columns, **Chapter 3** proposes a novel probabilistic model for bonding properties. The effects of variations in bonding properties on the static and dynamic behavior simulations of RC columns are then examined using this new model.
- A new probabilistic model is proposed for corrosion-affected bonding properties in **Chapter 4** along with the FE modeling approach for corroded RC columns considering corroded bond-slip. This approach is then employed to demonstrate the importance of corroded bonding in the static and dynamic behavior simulations of corroded RC columns.

- Accounting for the steel bar buckling behavior is one of the key aspects of advanced modeling of corroded RC structures. To this end, **Chapter 5** presents the constitutive model development for steel bar with buckling considering lateral reinforcement flexibility, which can be applied to the seismic simulation of RC structures with and without corrosion.
- **Chapter 6** outlines the corrosion state estimation methodology for RC structures based on the nonlinear FE model updating with seismic data. In this chapter, the proposed corrosion state estimation methodology is examined in different scenarios to identify corrosion-affected properties of corroded RC columns.
- In **Chapter** 7, an RC bridge is considered as an application example to assess its probabilistic seismic performance at different ages using the newly developed advanced FE modeling and corrosion state estimation tools. This chapter presents the probabilistic seismic demand analysis of the corroded RC bridges for pre-event and post-event scenarios, as well as the relevance of incorporating corroded bonding and steel bar buckling in the probabilistic capacity analysis.
- Finally, **Chapter 8** summarizes the research work and provides the corresponding conclusions, highlights, and contributions. In addition, the limitations of the current work and recommendations for future work are presented in this chapter.

Chapter 2. NEWLY IMPLEMENTED NONLINEAR ELEMENT FOR EFFICIENT MODELING OF STEEL BAR SLIPPAGE EFFECT IN RC STRUCTURES

2.1. INTRODUCTION

As a typical engineered composite material, the interaction between concrete and steel allows reinforced concrete (RC) structures to take advantage of the strength of both materials, including concrete mainly for compression and ductile steel reinforcements for tension. In the past decades, considerable research efforts have been spent to further understand the mechanical behavior of RC structures experimentally and refine the analysis tools for performance evaluation numerically. As evidenced in historical failure events (e.g., [71–76]) and experimental tests (e.g., [77–80]), one of the important issues worth investigation is the composite action between steel and the surrounding concrete, which plays a significant role in the behavior of RC structures (e.g., at high loading levels or in scenarios with insufficient anchorage). Particularly, imperfect bonding or bond-slip can postpone the yielding of steel or lessen the contribution of steel, which in turn affects the hysteretic energy dissipation capability of RC columns. The objective of this study is two-fold: (1) developing an efficient tool to account for imperfect bonding, i.e., advanced fiber-based frame element, for better prediction accuracy, and (2) applying this new tool to explore the need and importance of considering imperfect bonding by investigating the effect of imperfect bonding on nonlinear behavior of RC columns under different scenarios.

As revealed from experimental research and post-earthquake reconnaissance, the slippage between steel bars and the surrounding concrete can alter the overall behavior or cause structural failure due to de-bonding (e.g., the anchorage failure of bridge columns in the footing). Specifically, experimental tests indicated the load-deformation behavior of RC structures is characterized by more pinched hysteresis with less energy dissipation than predicted when assuming perfect bonding [81,82]. Furthermore, steel-concrete bonding can deteriorate for existing RC structures due to corrosion [83]. These observations highlight the need to develop finite element (FE) modeling techniques for RC structures to incorporate realistic bond-slip behavior.

To account for imperfect bonding between steel and concrete, different modeling approaches have been developed and used in the literature. In continuum-based FE modeling of RC structures, the slippage or the relative movement between steel and concrete can be represented simply by interface elements or spring elements [84]. While the continuum-based FE modeling approach is more accurate compared to the fiber-based FE modeling approach [39] as it avoids discretization approximations, it is more suitable for the detailed study of structural components rather than frame-type structure systems (e.g., bridges, frame buildings). The fiber-based FE modeling approach has proved to be computationally efficient for frame-type structures, and it has been widely used in the field of structural earthquake engineering. As such, several studies have initiated further development to enhance the conventional fiber-based frame elements with advanced modeling capabilities, e.g., including bond-slip (e.g., [64,85–87]). Some of the strategies aimed to incorporate the steel bar slippage in the anchored region by either using a zero-length element [64], modifying the stress-strain behavior of steel [87], or altering the composite behavior of steel and concrete at the section level [85]. The first two approaches consider the effect of bonding implicitly (i.e., the effect of bond-slip is integrated into a part of structural model with no external control, such as modified steel material behavior or lumped flexibility), and their applicability for a wide range of bond-slip properties can be questionable. For example, they cannot be used for deteriorated structures (e.g., corroded RC structures), where degraded bond-slip behavior needs to be modeled. In such scenarios, where the bonding stress-slip relationship is required to be modified, considering the bond-slip effect implicitly cannot reflect the modification since there is no independent control on the bond-slip behavior. On the other hand, the third method allows explicit bond-slip behaviors (i.e., the bonding stress-slip relationship obtained from the pull-out tests can be used directly) but is limited to the anchorage slippage only (e.g., in the column footing). In contrast, the strategy proposed by [86] can consider an explicit bond-slip relationship between steel and concrete inside both the entire structural member and the adjacent members (e.g., footing), since the relative slip is considered by introducing additional degrees of freedom (DOFs) for steel bar movements. However, the original formulation of the element was limited to small deformation problems based on linear geometry transformation [86,88]. This study enhances the element through considering the geometric nonlinearity for both steel bars and concrete components. Subsequently, this newly developed element is implemented in the open-source finite element software framework, *OpenSees* [65].

To reveal the importance of bond-slip, this study employs the newly developed element to investigate the role of bond-slip in the behavior of RC columns under various scenarios. The experimental pullout tests (e.g., [89]) witnessed the role of bond-slip in the anchorage zone, where bond breaking with steel bar slip penetrated the anchorage zone until reaching the bar end. As such, the detailing of steel bar ends (i.e., hooked or unhooked) can be notably effective on the contribution of bond-slip. Moreover, as experimental studies [90,91] implied, the insufficient anchorage length in the anchorage area highly impacts the behavior of RC structures. Naturally, different anchorage scenarios (i.e., with various anchorage lengths, hooked/unhooked) need to be considered when examining the importance of bond-slip in RC columns. Additionally, the role of bond-slip in the behavior of RC columns depends on some other aspects, such as load levels and seismic loading characteristics (e.g., short-duration and long-duration). Thus, this study investigates the relative importance of bond-slip in RC columns under different anchorage and loading scenarios, using the newly implemented fiber-based frame element. This, in turn, can shed light on the reflection of the commonly used assumption of perfect bonding for accurate FE modeling of RC columns.

To this end, this paper is organized as follows: Section 2 first describes the formulation of the geometrically nonlinear fiber-based frame element considering bond-slip and its implementation in *OpenSees*. Then, in Section 3, the newly implemented fiber-based frame element considering bond-slip is employed to model four experimental RC columns tested in the literature to validate the FE modeling approach. In the end, Section 4 presents the study of the relative importance of incorporating bond-slip in FE modeling by evaluating the structural behavior of RC columns considering imperfect bonding against the perfect bonding assumption.

2.2. GEOMETRICALLY NONLINEAR FIBER-BASED FRAME ELEMENT WITH BOND-SLIP

This section presents the formulation of the geometrically nonlinear fiber-based frame element considering the slippage between steel bars and the surrounding concrete. This element extends the fiber-based frame element with bond-slip, initially presented by Spacone and Limkatanyu [86], by incorporating corotational formulation to consider the effect of nonlinear geometry, which is essential for frame-type structures subjected to extreme earthquake loading. In the following, the element formulation is first revisited with a summary of the element formulation, followed by the newly added coordinate transformation to consider the effect of nonlinear geometry for the fiber-based frame element.

2.2.1. Element Formulation

The two-dimensional (2D) RC fiber-based frame element contains two nodes, each node with three conventional DOFs for the concrete part and n axial DOFs for n steel bars. Figure 2-1 presents the two-node beam with the concrete part denoted by solid gray area and the steel reinforcement (e.g., the i^{th} steel bar) denoted by hatched area. In this element, it is assumed that plane sections remain plane and normal to the longitudinal axis (i.e., Euler-Bernoulli beam element). Considering different DOFs for the concrete and reinforcement in the axial direction would allow the steel bar to slip with respect to the surrounding concrete. The nodal displacement vector **U** is $\{u_1\ u_2\ u_3\ \bar{u}_1^1 \ldots \bar{u}_1^{\mathrm{i}} \ldots \bar{u}_1^n\ u_4\ u_5\ u_6\ \bar{u}_2^1 \ldots \bar{u}_2^{\mathrm{i}} \ldots \bar{u}_2^n\}^{\mathrm{T}}$, in which $\{u_1\ u_2\ u_3\}$ and $\{u_4\ u_5\ u_6\}$ indicate the axial, transverse, and rotational DOFs of the concrete part at Node 1 and 2, respectively; $\{\bar{u}_1^1 \ldots \bar{u}_1^{\mathrm{i}} \ldots \bar{u}_1^n\}$ and $\{\bar{u}_2^1 \ldots \bar{u}_2^{\mathrm{i}} \ldots \bar{u}_2^n\}$ indicate the axial DOFs of n steel bars at Node 1 and 2, respectively. As such, the section displacement at location x is characterized by the augmented vector $\mathbf{u}(x) = \{u_B(x)\ v_B(x)\ \bar{u}_1 \ldots \bar{u}_{\mathrm{i}} \ldots \bar{u}_n\}^{\mathrm{T}}$, including the axial displacement $u_B(x)$ and transverse displacement $v_B(x)$ of concrete part, and the axial displacement of n steel bars $\{\bar{u}_1 \ldots \bar{u}_{\mathrm{i}} \ldots \bar{u}_n\}$.

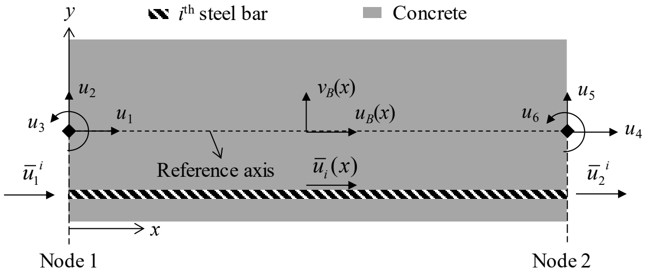

Figure 2-1: Schematic view for RC frame element considering bond-slip

Similar to the conventional displacement-based beam element formulation, classic linear and Hermitian cubic shape functions are used to interpolate the axial and transverse displacement fields of the concrete part, respectively. Linear shape functions are used to interpolate the axial displacement fields of steel bars. To summarize, the augmented displacement field $\mathbf{u}(x)$ can be defined as

$$\mathbf{u}(x) = \mathbf{N_u}(x)\mathbf{U} \tag{2-1}$$

in which the shape function matrix $\mathbf{N_u}(x)$ is defined in Appendix A.

Consequently, the corresponding augmented section deformation vector $\mathbf{d}(x) = \{\ \varepsilon_B(x)\ \kappa_B(x)\ \bar{\varepsilon}_1(x)\ \ldots\ \bar{\varepsilon}_i(x)\ \ldots\ \bar{\varepsilon}_n(x)\}^T$ is related to the augmented section displacement vector through compatibility equations. Namely, the section axial strain $\varepsilon_B(x) = \mathrm{d}u_B(x)/\mathrm{d}x$, the section curvature $\kappa_B(x) = \mathrm{d}^2v_B(x)/\mathrm{d}x^2$, and the axial strain of the i^{th} steel bar $\bar{\varepsilon}_i = \mathrm{d}\bar{u}_i(x)/\mathrm{d}x$. Based on these definitions, the slip of the i^{th} steel bar, $u_b^i(x)$, can be described as the difference of the axial movement of the steel bar and the concrete fiber:

$$u_b^i(x) = \bar{u}_i(x) - (u_B(x) - \frac{dv_B(x)}{dx}\bar{y}_i) \tag{2-2}$$

where $\bar{y}_i$ is the y coordinate of the i^{th} steel bar. Therefore, the augmented section deformation vector $\mathbf{d}(x)$ and the slip vector $\mathbf{d_b}(x) = \{u_b^1(x)\ \ldots\ u_b^n(x)\}^T$ for an RC frame element with n steel bars can be written as Eqs. (2-3) and (2-4), respectively,

$$\mathbf{d}(x) = \partial\mathbf{N_u}(x)\mathbf{U} = \mathbf{B_u}(x)\mathbf{U} \tag{2-3}$$

$$\mathbf{d_b}(x) = \partial_\mathbf{b}\mathbf{N_u}(x)\mathbf{U} = \mathbf{B_b}(x)\mathbf{U} \tag{2-4}$$

with ∂, $\mathbf{B}_\mathrm{u}(x)$, $\partial_\mathbf{b}$, and $\mathbf{B}_\mathrm{b}(x)$ defined in Appendix A.

In this fiber-based frame element, the cross-section is discretized into uniaxial material fibers representing concrete and longitudinal steel bars. The strain of the concrete fiber at section height y_j is determined as $\bar{\varepsilon}_j(x) = \varepsilon_B(x) - y_j\ \kappa_B(x)$ from the section deformation vector $\mathbf{d}(x)$. In contrast, the strain for the i^{th} steel bar is directly taken from $\mathbf{d}(x)$, i.e., $\bar{\varepsilon}_i(x)$. Using the material behavior assigned to these concrete and steel fibers, the corresponding stress and tangent stiffness are obtained.

Similarly, following the bond-slip material behavior, the bonding stresses $t_i(x)$ between the i^{th} steel bar and the surrounding concrete, as well as the corresponding tangent stiffness $\bar{E}_b^i$, can be obtained in the fiber state determination process.

Corresponding to the augmented section deformation vector $\mathbf{d}(x)$ and the slip vector $\mathbf{d_b}(x)$, the augmented section force vector $\mathbf{D}(x)$ and bonding stress vector $\mathbf{D_b}(x)$ can be defined as follows. $\mathbf{D}(x)$ is defined as $\{N_B(x)\ M_B(x)\ \bar{N}_1(x)\ \ldots\ \bar{N}_i(x)\ \ldots\ \bar{N}_n(x)\}$, in which $N_B(x)$ = the axial force and $M_B(x)$ = the bending moment contributed from the concrete part, and $\bar{N}_i(x)$ = the axial force in the i^{th} steel bar. $\mathbf{D_b}(x)$ is the normalized bonding stress defined as $\{p_1t_1(x) \ldots p_it_i(x) \ldots p_nt_n(x)\}$, in which $t_i(x)$ = the bonding stresses between the i^{th} steel bar and the surrounding concrete, and p_i = the perimeter of the i^{th} steel bar. As such, the sectional stiffness matrix, denoted by $\mathbf{k_B}(x)$, can be derived to relate $\mathbf{D}(x)$ with $\mathbf{d}(x)$ in an incremental form, i.e., $\Delta\mathbf{D}(x) = \mathbf{k_B}(x)\ \Delta\mathbf{d}(x)$. Similarly, bond-slip stiffness, denoted as $\mathbf{k_b}(x)$, can be derived to relate $\mathbf{D_b}(x)$ and $\mathbf{d_b}(x)$ in an incremental form, i.e., $\Delta\mathbf{D_b}(x) = \mathbf{k_b}(x)\ \Delta\mathbf{d_b}(x)$.

Following the principle of virtual work, the element stiffness matrix $\mathbf{K}_{(6+2n)\times(6+2n)}$ and the resisting force vector $\mathbf{P}_{(6+2n)\times 1}$ for the displacement-based frame element considering bond-slip can be derived as Eq. (2-5) and (2-6), respectively [86]. Note that the element stiffness matrix $\mathbf{K}_{(6+2n)\times(6+2n)}$ is assembled by considering the contributions from both the concrete part and steel bars ($\mathbf{K_B}$), as well as from bond-slip ($\mathbf{K_b}$).

$$\mathbf{K} = \mathbf{K_B} + \mathbf{K_b} = \int_L \mathbf{B_u}^{\mathbf{T}}(x)\mathbf{k_B}(x)\mathbf{B_u}(x)dx + \int_L \mathbf{B_b}^{\mathbf{T}}(x)\mathbf{k_b}(x)\mathbf{B_b}(x)dx \tag{2-5}$$

Similarly, the element force vector increment $\Delta\mathbf{P}_{(6+2n)\times 1}$ can be assembled as the summation of $\Delta\mathbf{P_B}$ and $\Delta\mathbf{P_b}$. as shown in Eq. (2-6).

$$\Delta\mathbf{P} = \Delta\mathbf{P_B} + \Delta\mathbf{P_b} = \int_L \mathbf{B_u}^{\mathbf{T}}(x)\Delta\mathbf{D}(x)dx + \int_L \mathbf{B_b^T}(x)\Delta\mathbf{D_b}(x)dx \tag{2-6}$$

2.2.2. Geometric Nonlinearity

The element formulation above assumes small deformation without considering the geometric nonlinearity. To remedy this limitation without intervening in the element formulation, the corotational approach is used by introducing rigid body motion transformation that accounts for the geometric nonlinearity. In this approach, the motion of elements in the local coordinate system is decomposed into rigid body motion and pure deformational motion in the basic coordinate system, where rigid body motion modes are eliminated [88,92].

Unlike the conventional fiber-based frame element, the newly developed element has two groups of DOFs: 6 DOFs and $2n$ DOFs corresponding to the concrete part and n steel bars, respectively, in the local coordinate system. Thus, hybrid corotational transformation is proposed for the finite element described above to capture the effect of nonlinear geometry. In particular, this newly proposed transformation combines two corotational formulations of truss and beam within the newly developed element, respectively for steel bars and concrete. Note that the existing corotational transformation in *OpenSees* applies to the conventional fiber-based frame element without distinguishing the concrete and steel bars, which are assumed to be perfectly bonded to concrete. However, the new transformation proposed in this study applies to the new element, in which the steel bars can slip in concrete. Figure 2-2 shows the DOFs used to describe the movement of the element in the local and basic coordinate systems. The DOFs (i.e., u_1, u_2, u_3, u_4, u_5, u_6, $\bar{u}_1^i$ and $\bar{u}_2^i$ for the i^{th} steel bar) in the local system can be related geometrically through coordinate transformation with DOFs in the basic system (i.e., Δ_1, Δ_2, Δ_3, and d_i for the i^{th} steel bar) after the rigid body motion of concrete part and steel bars are removed, see Figure 2-2.

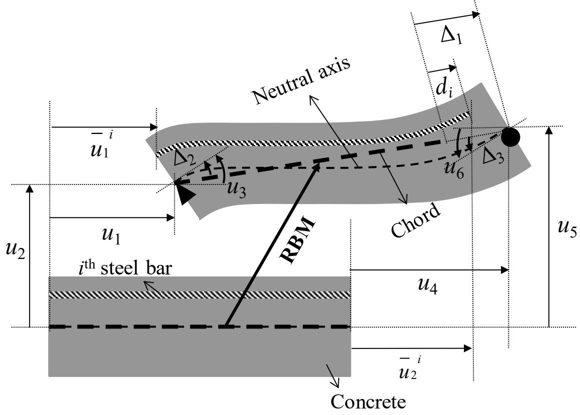

Figure 2-2: Corotational transformation: undeformed to deformed element configuration

To define such coordinate transformation, referred to as RBM (rigid body motion) transformation, the first group of DOFs of the newly developed element for the concrete part (i.e., u_1, u_2, u_3, u_4, u_5, and u_6) in the local system are related to the DOFs (i.e., Δ_1, Δ_2, and Δ_3) in the basic system per Eq. (2-7):

$$\begin{gathered}\Delta_1 = \sqrt{(L_0 + u_4 - u_1)^2 + (u_5 - u_2)^2} - L_0 \\ \Delta_2 = u_3 - \arctan(\frac{u_5 - u_2}{L_0 + u_4 - u_1}) \\ \Delta_3 = u_6 - \arctan(\frac{u_5 - u_2}{L_0 + u_4 - u_1})\end{gathered} \tag{2-7}$$

where L_0 denotes the undeformed element length.

The second group of DOFs in the newly developed element (i.e., $\bar{u}_1{}^i$ and $\bar{u}_2{}^i$ for the i^{th} steel bar, $i = 1, 2, \dots, n$) in the local system are related to the axial DOFs (i.e., d_i for the i^{th} steel bar, $i = 1, 2, \dots, n$) in the basic system per Eq. (2-8).

$$d_i = \sqrt{(L_0 + \bar{u}_2^i - \bar{u}_1^i)^2 + (u_5 - u_2)^2} - L_0, \quad i = 1,\ 2, \dots, n \tag{2-8}$$

Note that Eqs. (2-7) and (2-8) were used for the corotational formulation of conventional fiber-based frame elements without bond-slip [92] and truss elements [88], respectively. In this paper, they are integrated to derive corotational transformation matrix for the newly developed element to relate the nodal displacement vector in the local coordinate system ($\mathbf{U}_{\mathbf{local}}$) and the nodal displacement vector $\mathbf{U}_{\mathbf{basic}} = \{\Delta_1\ \Delta_2\ \Delta_3\ d_1 \ldots d_i \ldots d_n\}^{\mathrm{T}}$ in the basic coordinate system, per the RBM transformation matrix $\boldsymbol{\Gamma}_{\mathbf{RBM}}$; see Eq. (2-9):

$$\boldsymbol{\Gamma}_{\mathbf{RBM}} = \frac{\partial \mathbf{U}_{\mathbf{basic}}}{\partial \mathbf{U}_{\mathbf{local}}} = \left[\begin{array}{ccc:ccc:ccc:ccc} -c & -s & 0 & 0 & 0 & 0 & c & s & 0 & 0 & 0 & 0 \\ -s/L_e & c/L_e & 1 & \vdots & \vdots & \vdots & s/L_e & -c/L_e & 0 & \vdots & \vdots & \vdots \\ -s/L_e & c/L_e & 0 & 0 & 0 & 0 & s/L_e & -c/L_e & 1 & 0 & 0 & 0 \\ \hdashline 0 & -sb_1 & 0 & -cb_1 & \cdots & 0 & 0 & sb_1 & 0 & cb_1 & \cdots & 0 \\ \vdots & \vdots & \vdots & \vdots & \ddots & \vdots & \vdots & \vdots & \vdots & \vdots & \ddots & \vdots \\ 0 & -sb_n & 0 & 0 & \cdots & -cb_n & 0 & sb_n & 0 & 0 & \cdots & cb_n \end{array}\right] \quad (2\text{-}9)$$

in which

$$L_e = \sqrt{(L_0 + u_4 - u_1)^2 + (u_5 - u_2)^2};\ c = \frac{L_0 + u_4 - u_1}{L_e};\ s = \frac{u_5 - u_2}{L_e} \quad (2\text{-}10)$$

$$cb_i = \frac{L_0 + \bar{u}_2^i - \bar{u}_1^i}{\sqrt{(L_0 + \bar{u}_2^i - \bar{u}_1^i)^2 + (u_5 - u_2)^2}};\ sb_i = \frac{u_5 - u_2}{\sqrt{(L_0 + \bar{u}_2^i - \bar{u}_1^i)^2 + (u_5 - u_2)^2}} \quad i = 1,\ 2, \ldots, n \quad (2\text{-}11)$$

Consequently, the element end force vector for the basic system, i.e., $\mathbf{P}_{\mathbf{basic}} = \{P_1\ P_2\ P_3\ |\ P_r^1 \ldots P_r^i \ldots P_r^n\}$, can be related to the counterparts for the local system, i.e., $\mathbf{P}_{\mathbf{local}} = \{N_1\ V_1\ M_1\ |\ P_1^1 \ldots P_1^i \ldots P_1^n\ |\ N_2\ V_2\ M_2\ |\ P_2^1 \ldots P_2^i \ldots P_2^n\}$ with the effect of geometric nonlinearity taken into account through $\boldsymbol{\Gamma}_{\mathbf{RBM}}$. Specifically, the element force vector in the local system $\mathbf{P}_{\mathbf{local}}$ can be found using Eq. (2-12). Figure 2-3 summarizes the element nodal forces and displacements in both local and basic coordinate systems, as discussed above.

$$\mathbf{P}_{\mathbf{local}} = \boldsymbol{\Gamma}_{\mathbf{RBM}}{}^{\mathrm{T}} \mathbf{P}_{\mathbf{basic}} \quad (2\text{-}12)$$

As such, the local stiffness matrix ($\mathbf{K}_{\mathbf{local}}$) can be derived as the derivative of the local force vector $\mathbf{P}_{\mathbf{local}}$ with respect to the local nodal displacements $\mathbf{U}_{\mathbf{local}}$, see Eq. (2-13).

$$\mathbf{K}_{\mathbf{local}} = \frac{\partial \mathbf{P}_{\mathbf{local}}}{\partial \mathbf{U}_{\mathbf{local}}} = \frac{\partial (\boldsymbol{\Gamma}_{\mathbf{RBM}}{}^{\mathrm{T}} \mathbf{P}_{\mathbf{basic}})}{\partial \mathbf{U}_{\mathbf{local}}} \quad (2\text{-}13)$$

Since both $\mathbf{P_{basic}}$ and $\mathbf{\Gamma_{RBM}}$ depend on $\mathbf{U_{local}}$, the resultant stiffness matrix $\mathbf{K_{local}}$ is composed of two parts: the stiffness contributed from the material, i.e., $\mathbf{K_m}$, and the stiffness due to the geometric nonlinearity, i.e., $\mathbf{K_g}$, see Eq. (2-14).

$$\begin{aligned}\mathbf{K_{local}} &= \mathbf{K_m} + \mathbf{K_g} \\ &= \mathbf{\Gamma_{RBM}}^{\mathrm{T}}\mathbf{K_{basic}}\mathbf{\Gamma_{RBM}} + \frac{P_1}{L_e}\mathbf{K_{g1}} + \frac{P_2+P_3}{L_e^2}\mathbf{K_{g2}} + \sum_{i=1}^{n}\frac{P_r^i}{\sqrt{(L_0+\bar{u}_2^i-\bar{u}_1^i)^2+(u_5-u_2)^2}}\mathbf{K_{gr}}^{(i)}\end{aligned} \tag{2-14}$$

where

$$\mathbf{K_{g1}} = \left[\begin{array}{ccc|c|ccc|c}
s^2 & -sc & 0 & \underline{\mathbf{0}}_{1\times n} & -s^2 & sc & 0 & \underline{\mathbf{0}}_{1\times n} \\
-sc & c^2 & 0 & \underline{\mathbf{0}}_{1\times n} & sc & -c^2 & 0 & \underline{\mathbf{0}}_{1\times n} \\
0 & 0 & 0 & \underline{\mathbf{0}}_{1\times n} & 0 & 0 & 0 & \underline{\mathbf{0}}_{1\times n} \\ \hline
\underline{\mathbf{0}}_{n\times 1} & \underline{\mathbf{0}}_{n\times 1} & \underline{\mathbf{0}}_{n\times 1} & \underline{\mathbf{0}}_{n\times n} & \underline{\mathbf{0}}_{n\times 1} & \underline{\mathbf{0}}_{n\times 1} & \underline{\mathbf{0}}_{n\times 1} & \underline{\mathbf{0}}_{n\times n} \\ \hline
-s^2 & sc & 0 & \underline{\mathbf{0}}_{1\times n} & s^2 & -sc & 0 & \underline{\mathbf{0}}_{1\times n} \\
sc & -c^2 & 0 & \underline{\mathbf{0}}_{1\times n} & -sc & c^2 & 0 & \underline{\mathbf{0}}_{1\times n} \\
0 & 0 & 0 & \underline{\mathbf{0}}_{1\times n} & 0 & 0 & 0 & \underline{\mathbf{0}}_{1\times n} \\ \hline
\underline{\mathbf{0}}_{n\times 1} & \underline{\mathbf{0}}_{n\times 1} & \underline{\mathbf{0}}_{n\times 1} & \underline{\mathbf{0}}_{n\times n} & \underline{\mathbf{0}}_{n\times 1} & \underline{\mathbf{0}}_{n\times 1} & \underline{\mathbf{0}}_{n\times 1} & \underline{\mathbf{0}}_{n\times n}
\end{array}\right] \tag{2-15}$$

$$\mathbf{K_{g2}} = \left[\begin{array}{ccc|c|ccc|c}
-2sc & c^2-s^2 & 0 & \underline{\mathbf{0}}_{1\times n} & 2sc & -c^2+s^2 & 0 & \underline{\mathbf{0}}_{1\times n} \\
c^2-s^2 & 2sc & 0 & \underline{\mathbf{0}}_{1\times n} & -c^2+s^2 & -2sc & 0 & \underline{\mathbf{0}}_{1\times n} \\
0 & 0 & 0 & \underline{\mathbf{0}}_{1\times n} & 0 & 0 & 0 & \underline{\mathbf{0}}_{1\times n} \\ \hline
\underline{\mathbf{0}}_{n\times 1} & \underline{\mathbf{0}}_{n\times 1} & \underline{\mathbf{0}}_{n\times 1} & \underline{\mathbf{0}}_{n\times n} & \underline{\mathbf{0}}_{n\times 1} & \underline{\mathbf{0}}_{n\times 1} & \underline{\mathbf{0}}_{n\times 1} & \underline{\mathbf{0}}_{n\times n} \\ \hline
2sc & -c^2+s^2 & 0 & \underline{\mathbf{0}}_{1\times n} & -2sc & c^2-s^2 & 0 & \underline{\mathbf{0}}_{1\times n} \\
-c^2+s^2 & -2sc & 0 & \underline{\mathbf{0}}_{1\times n} & c^2-s^2 & 2sc & 0 & \underline{\mathbf{0}}_{1\times n} \\
0 & 0 & 0 & \underline{\mathbf{0}}_{1\times n} & 0 & 0 & 0 & \underline{\mathbf{0}}_{1\times n} \\ \hline
\underline{\mathbf{0}}_{n\times 1} & \underline{\mathbf{0}}_{n\times 1} & \underline{\mathbf{0}}_{n\times 1} & \underline{\mathbf{0}}_{n\times n} & \underline{\mathbf{0}}_{n\times 1} & \underline{\mathbf{0}}_{n\times 1} & \underline{\mathbf{0}}_{n\times 1} & \underline{\mathbf{0}}_{n\times n}
\end{array}\right] \tag{2-16}$$

$$\mathbf{K_{gr}}^{(i)} = \left[\begin{array}{c|c|c|c}
\left[cb_i^2\right]_{(2,2)}^{3\times 3} & \left[-sb_icb_i\right]_{(2,i)}^{3\times n} & \left[-cb_i^2\right]_{(2,2)}^{3\times 3} & \left[sb_icb_i\right]_{(2,i)}^{3\times n} \\ \hline
\left[-sb_icb_i\right]_{(i,2)}^{n\times 3} & \left[sb_i^2\right]_{(i,i)}^{n\times n} & \left[sb_icb_i\right]_{(i,2)}^{n\times 3} & \left[-sb_i^2\right]_{(i,i)}^{n\times n} \\ \hline
\left[-cb_i^2\right]_{(2,2)}^{3\times 3} & \left[sb_icb_i\right]_{(2,i)}^{3\times n} & \left[cb_i^2\right]_{(2,2)}^{3\times 3} & \left[-sb_icb_i\right]_{(2,i)}^{3\times n} \\ \hline
\left[sb_icb_i\right]_{(i,2)}^{n\times 3} & \left[-sb_i^2\right]_{(i,i)}^{n\times n} & \left[-sb_icb_i\right]_{(i,2)}^{n\times 3} & \left[sb_i^2\right]_{(i,i)}^{n\times n}
\end{array}\right] \quad i = 1, 2, \ldots, n \tag{2-17}$$

Note that $[\Theta]_{(\boldsymbol{s},\boldsymbol{t})}^{\boldsymbol{p}\times\boldsymbol{q}}$ means a zero matrix of dimension $p\times q$ with the element (s, t) replaced by Θ. Note that $\mathbf{P}_{\mathbf{basic}}$ and $\mathbf{K}_{\mathbf{basic}}$ can be deduced from the element force vector and the stiffness matrix derived in Eqs. (2-5) and (2-6), as a particular case with $u_1 = 0$, $u_2 = 0$, $u_5 = 0$, $\bar{u}_1{}^{\mathrm{i}} = 0$ ($i = 1, 2, \ldots, n$).

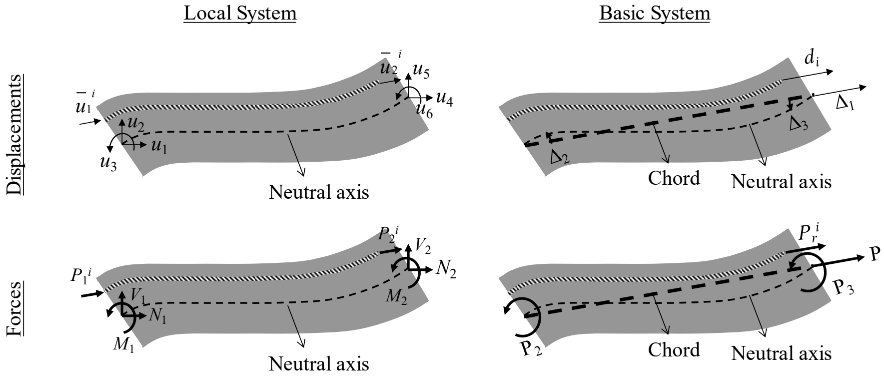

Figure 2-3: Schematic element nodal displacements and forces in local and basic coordinate systems

The combination of the described element and geometric nonlinearity forms the FE formulation developed in this study for RC structures with bond-slip. Figure 2-4 summarizes the proposed FE formulation for the fiber-based frame element, including the state determinations at the structure, element, section, and fiber levels. The stiffness matrix and resisting stress/force vector corresponding to each level are determined using the nodal displacements for all conventional and additional DOFs. As such, the imperfect bonding is incorporated in the RC structural modeling from the fiber to the structure level.

Following the element formulation, a displacement-based fiber-based frame element with bond-slip, denoted as *dispBeamColumnBS*, is implemented in *OpenSees*, in conjunction with the newly implemented fiber section for section state determination (i.e., *FiberBSele*) and bond-slip model (i.e., *BondSlip03*) for material state determination. To render it to account for geometric nonlinearity for large deformation problems, a new geometric transformation (i.e., *corotationalBS*) is implemented. Appendix B summarizes the implementation of these new capabilities in *OpenSees* framework.

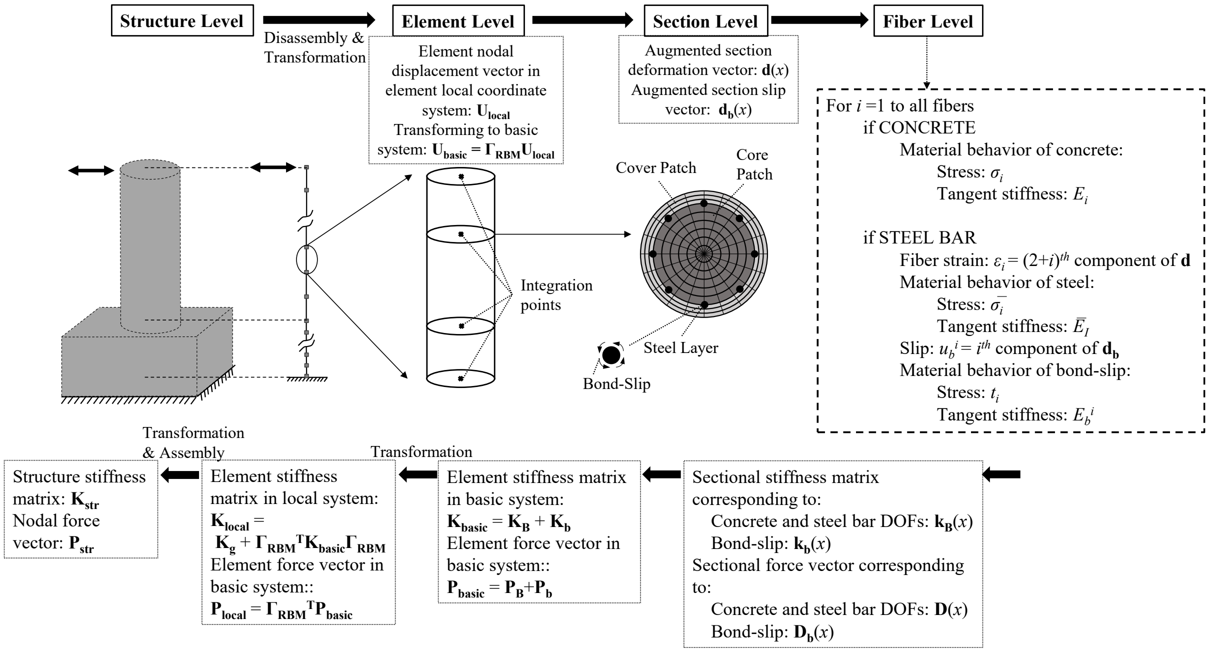

Figure 2-4: Schematic view of the FE formulation for the fiber-based frame element with bond-slip

2.3. FE MODEL DEVELOPMENT AND VALIDATION

In this section, the newly developed FE modeling capabilities in *OpenSees* are examined through numerical modeling and validation of four experimental RC columns tested in the literature, denoted as Low-Moehle column [93], Bousias column [94,95], Saatcioglu column [96,97], and UCSD column [79], respectively. The first three columns, with a constant axial load applied at the top, were tested statically under cyclic lateral displacement loading until flexural failure, and the fourth column was tested dynamically on a shake-table. Low-Moehle column considered here is specimen #1 from a series of RC cantilever columns presented in [93]. Bousias column is the specimen S0 tested at the ISPRA lab in Europe [94]. In these two columns, the longitudinal steel bars had hooked ends at the bottom in the anchorage zone. In contrast, Saatcioglu column, as the flexural-critical specimen BG-8 in [96], has unhooked longitudinal steel bars and is thus selected to validate the FE modeling tool further for a different anchorage scenario. The first three columns have rectangular cross-sections as schematically shown in Figure 2-5 (c) to (e), with properties presented in Table 2-1. The last column shown in Figure 2-6 had a circular cross-section and was tested on the shake table at the University of California, San Diego in 2010. The geometrical properties of this column are also provided in Table 2-1. In this study, the test of the column subjected to only one of earthquake ground motions (i.e., Loma Prieta 1989, Mw 6.9, recorded at Agnew State Hospital) is considered. In particular, this ground motion is the first one applied to the intact RC column, which can be used for the column with pristine material properties and no pre-existing damage [79].

These four experimentally tested RC columns are modeled using the conventional (without bond-slip) and newly developed (with bond-slip) fiber-based frame elements, respectively, for cases when assuming perfect bonding and considering imperfect bonding, as schematically shown in Figure 2-5 (b) with pertinent properties summarized in Table 2-1. To account for the strain penetration caused by the bar slips along the anchorage length, the anchorage zone was explicitly modeled in the same manner as the column body using the newly developed element, as shown in Figure 2-5 (b). This allows to consider the bar slippage along the anchorage length, or strain penetration, directly. Note that the number of elements for each RC column is so considered to achieve a balance between numerical efficiency and accuracy, and avoid localization issues by considering the length of the critical element (i.e., bottom element in the potential plastic hinge region of the column) to approximately equal to the potential plastic hinge length [98]. In each element, four Gauss-Lobatto integration points are used to achieve a balance between computational accuracy and efficiency [99–101].

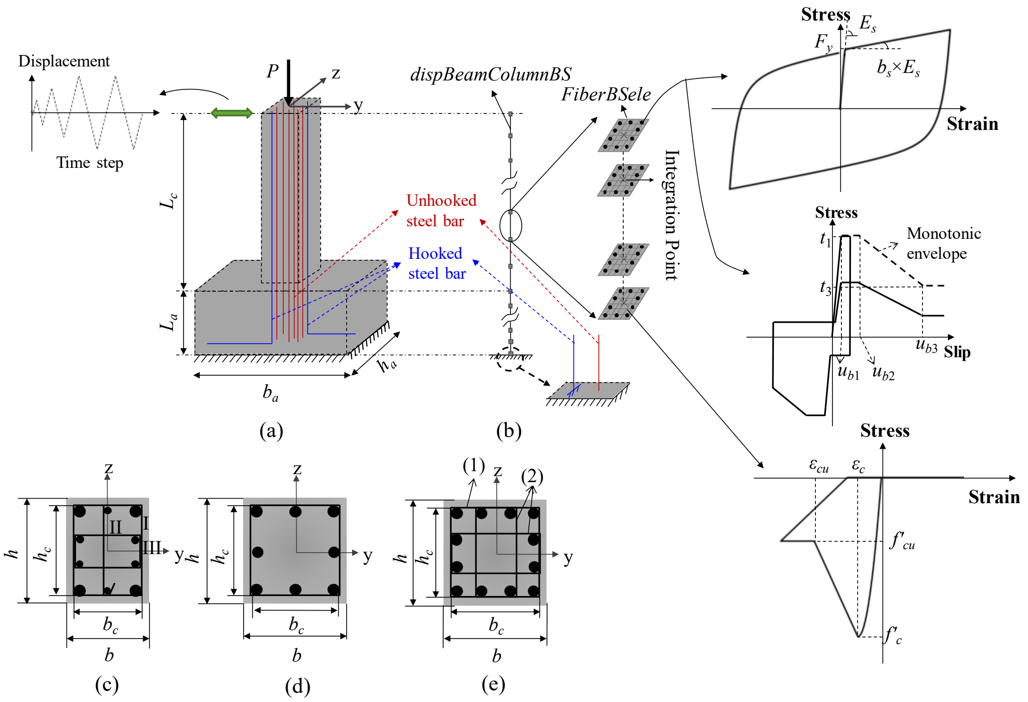

Figure 2-5: Schematic view of RC columns: (a) geometry and loads, (b) FE model, and sections of (c) Low-Moehle column, (d) Bousias column, and (e) Saatcioglu column

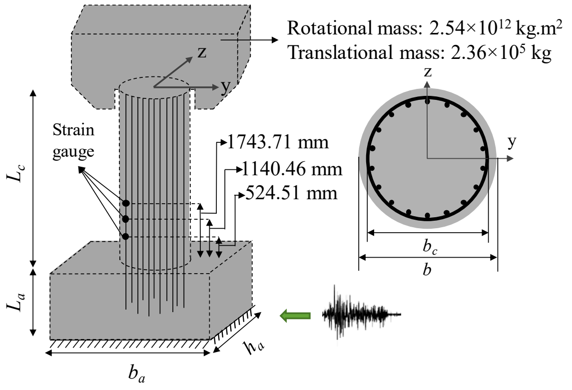

Figure 2-6: Schematic view of geometry of UCSD column tested and the strain gauges used

Due to lack of detailed cyclic stress-strain curves for concrete and steel from experimental programs considered, the stress-strain behaviors of concrete and steel in this study are represented by well-established uniaxial material models as widely used in the literature with proved accuracy based on the thorough comparative studies in [102,103]. Specifically, steel fibers are assigned with the Giuffre-Menegotto-Pinto (GMP) steel model, defined with yield stress F_y, strain hardening ratio b_s, and Young's module E_s. The parameters of the GMP model regarding the transition branches and isotropic hardenings are set to the recommendations presented in [102]. Using these model parameters, together with other material properties from material coupon tests, leads to an adequate accuracy in the material modeling, as shown later. For the concrete fibers, the Kent-Scott-Park concrete model is used, defined with concrete strength f'_c, strain at maximum strength ε_c, ultimate strength f'_{cu}, and strain at crushing strength ε_{cu}. The tensile strength of concrete is neglected in this material model, as its effect on the nonlinear behavior simulation of the RC columns was verified to be insignificant, which is consistent with the observation made in [86]. Note that the properties of the steel and unconfined concrete are determined based on the experimental data as reported in the literature; however, the properties related to the softening behavior of unconfined concrete are assumed from the practical range per [104–106]. Also, the confinement properties for the core concrete are determined using Mander's equations [45]. Note that for a fair comparison, the same concrete model parameters were used for the models with perfect and imperfect bonding. For the models with imperfect bonding, one of the pioneering bond-slip models proposed by Eligehausen et al. [107], shown in Figure 2-5 (b), is implemented in *OpenSees* and used to model local bonding stress-slip relationship. This material model requires peak bond stress t_1, slip at peak bond stress u_{b1}, slip at the end of plateau u_{b2}, bonding frictional stress t_3, and slip at bonding frictional stress u_{b3} as inputs. Table 2-2 presents the material properties used for the FE models of these four experimental columns. Note that the symbols used in Table 2-2 are shown as the schematic material models in Figure 2-5 (b). In UCSD column subjected to dynamic loading, the additional energy dissipation is required to be considered apart from the hysteretic energy existed in the nonlinear material model. To this end, a Rayleigh damping model is used in this study. This damping model has mass and initial stiffness proportional components defined based on the first and second modes of vibration with a damping ratio of 2% each, which is a common engineering assumption accepted for nonlinear dynamic analysis of civil structures subjected to earthquakes.

Table 2-1: Structural properties of experimental RC columns tested in the literature

Experimental Columns		**Low-Moehle** Quarter-scale Static cyclic	**Bousias** Full-scale Static cyclic	**Saatcioglu** Full-scale Static cyclic	**UCSD** Full-scale Dynamic
Column	L_c (mm)	514.4	1490.0	1645.0	7315.0
	# of elements	12	10	12	12
	P (kN)	44.5	300.0	961.0	2320.0
	h (mm)	165.0	250.0	350.0	N/A
	b (mm)	127.0	250.0	350.0	1219.2
	h_c (mm)	140.0	220.0	292.0	N/A
	b_c (mm)	92.0	220.0	292.0	1117.6
	Long. steel bar	Φ9.53 mm (I), Φ6.35 mm (II, III)	Φ16.00 mm	Φ19.50 mm	Φ35.81 mm
	Trans. reinforcement	Φ29.00 mm @ 31.75 mm	2×Φ8.00 mm @ 70.00 mm	Φ9.53 mm (1), Φ6.6 mm (2) @ 76.00 mm	2×Φ19.00 mm @ 152.00 mm
Footing & Anchorage	L_a (mm)	177.8	480.0	405.0	1219.2
	# of elements	5	5	8	8
	b_a (mm)	457.2	1000.0	1500.0	5486.4
	h_a (mm)	355.6	1000.0	1500.0	1828.8
	L_a/steel bar diameter	19 (I), 28 (II, III)	30	21	34
	Details of long. steel bar end	Hooked	Hooked	Free	Free

Table 2-2: Overview of the material properties of the RC columns

Test			**Low-Moehle**			**Bousias**	**Saatcioglu**	**UCSD**
Material		**Properties**	**Set I**	**Set II**	**Set III**			
Steel		F_y (MPa)	447.5	444.0	504.0	460.0	455.0	518.5
		b_s (−)	0.015	0.01	0.01	0.015	0.015	0.011
		E_s (MPa)	210000	210000	210000	210000	210000	200000
Concrete	**Unconfined**	f'_c (MPa)	−36.54			−30.75	−34.00	−40.30
		f'_{cu} (MPa)	−7.31			−6.15	−10.00	−8.06
		ε_c (−)	−0.0030			−0.0035	−0.0020	−0.0026
		ε_{cu} (−)	−0.0080			−0.0100	−0.0080	−0.0150
	Confined	f'_c (MPa)	−42.13			−38.44	−47.60	−49.60
		f'_{cu} (MPa)	−8.43			−15.37	−39.68	−8.00
		ε_c (−)	−0.0052			−0.0044	−0.0090	−0.0105
		ε_{cu} (−)	−0.0568			−0.1000	−0.0720	−0.0150
Bond-Slip		t_1 (MPa)	24.81	27.68	27.68	15.11	15.57	15.18
		t_3 (MPa)	6.90	7.43	7.43	5.05	4.88	5.11
		u_{b1} (mm)	1.10	1.10	1.10	1.01	1.06	1.16
		u_{b2} (mm)	3.00	3.00	3.00	3.00	3.00	3.00
		u_{b3} (mm)	4.76	3.18	3.18	8.00	9.75	17.91

For each of these columns, the loading protocol used in the experiment is applied to simulate the behavior of the column. These columns are modeled assuming perfect bonding and considering imperfect bonding for comparison. Figure 2-7 (a) to (c) show the comparison of the lateral load-drift ratio hysteresis between FE-predictions and experimental results for Low-Moehle column, Bousias column, and Saatcioglu column, respectively. For these three columns under cyclic loading, the FE-predicted lateral load-drift ratio hysteresis using the model with imperfect bonding correlates better with the experimental results compared with the model assuming perfect bonding. In particular, models with imperfect bonding can well capture the pinching effect induced by bond-slip, which indicates better characterization in terms of energy dissipation. This observation implies that considering bond-slip in FE modeling of RC columns improves the prediction accuracy (i.e., pinching effect) with less discrepancy between the FE-predictions and experimental results.

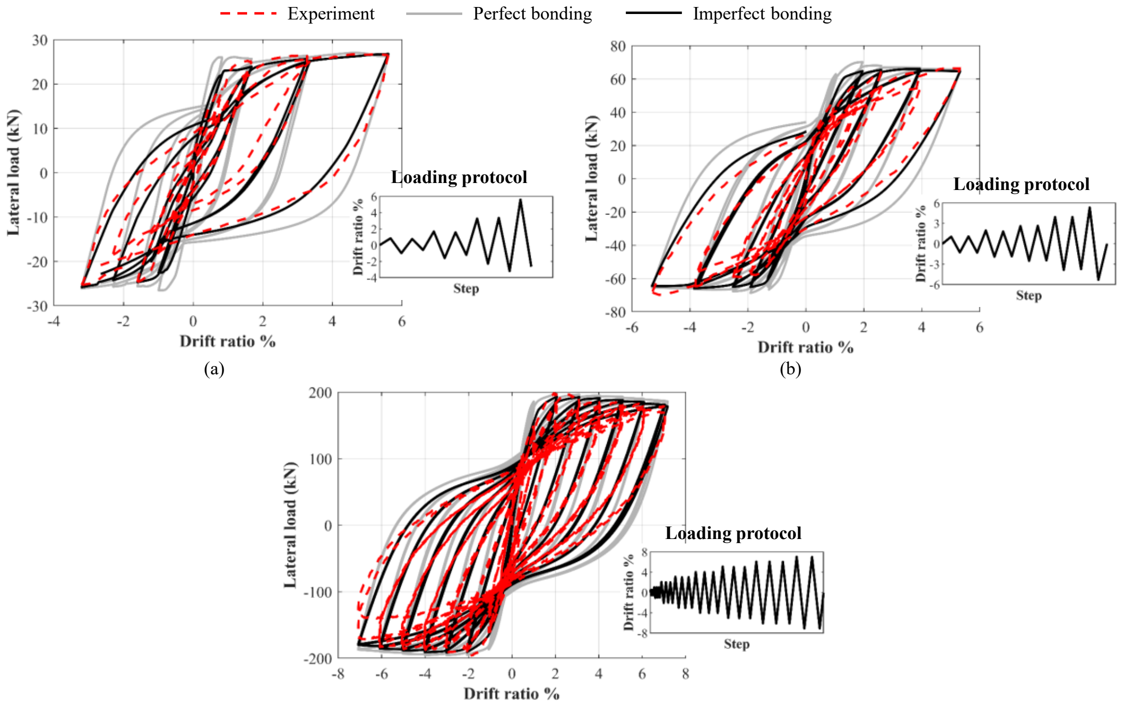

(a)

(b)

(c)

Figure 2-7: Comparison of lateral load-drift ratio hysteresis between FE predictions and experimental results for (a) Low-Moehle column, (b) Bousias column, and (c) Saatcioglu column

For UCSD column under dynamic loading, the inclusion of bond-slip leads to nearly perfect FE-prediction of drift ratio time-history measured at the top of the pier column, as shown in Figure 2-8 (b). In contrast, Figure 2-8 (a), which presents the comparison of the drift ratio time-history obtained from the FE model with perfect bonding and the experiment, shows the error arising from the assumption of perfect bonding. To further reveal the capability of the developed element for capturing the effect of bond-slip, Figure 2-9 presents the comparison between the experimental and numerical strain time-histories measured from three instrumented strain gauges for perfect bonding (in the left column) and imperfect bonding (in the right column) FE models, respectively. This figure reaffirms ignoring the effect of bond-slip would affect the response prediction of the RC column. Specifically, bond-slip barely affects the peak seismic response but significantly affects the dynamic response afterward. This is because the energy dissipation assuming perfect bonding suppresses the vibration, while the effect of less energy dissipation capability inherent with bond-slip is well exhibited. To sum up, considering bond-slip in FE modeling of RC columns can influence the prediction accuracy in both global and local responses. It is worth mentioning that such improvement in the prediction accuracy is remarkably important for constructing digital twins using the nonlinear FE model updating approach in structural health monitoring [108].

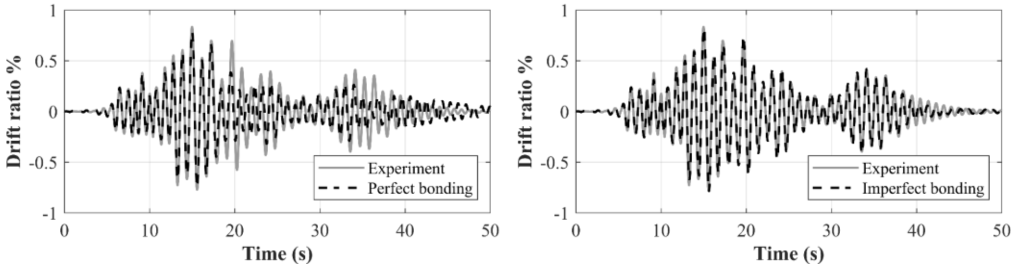

(a) (b)

Figure 2-8: Comparison of drift ratio time-history of the pier column top between experiment and FE prediction with (a) perfect bonding, and (b) imperfect bonding

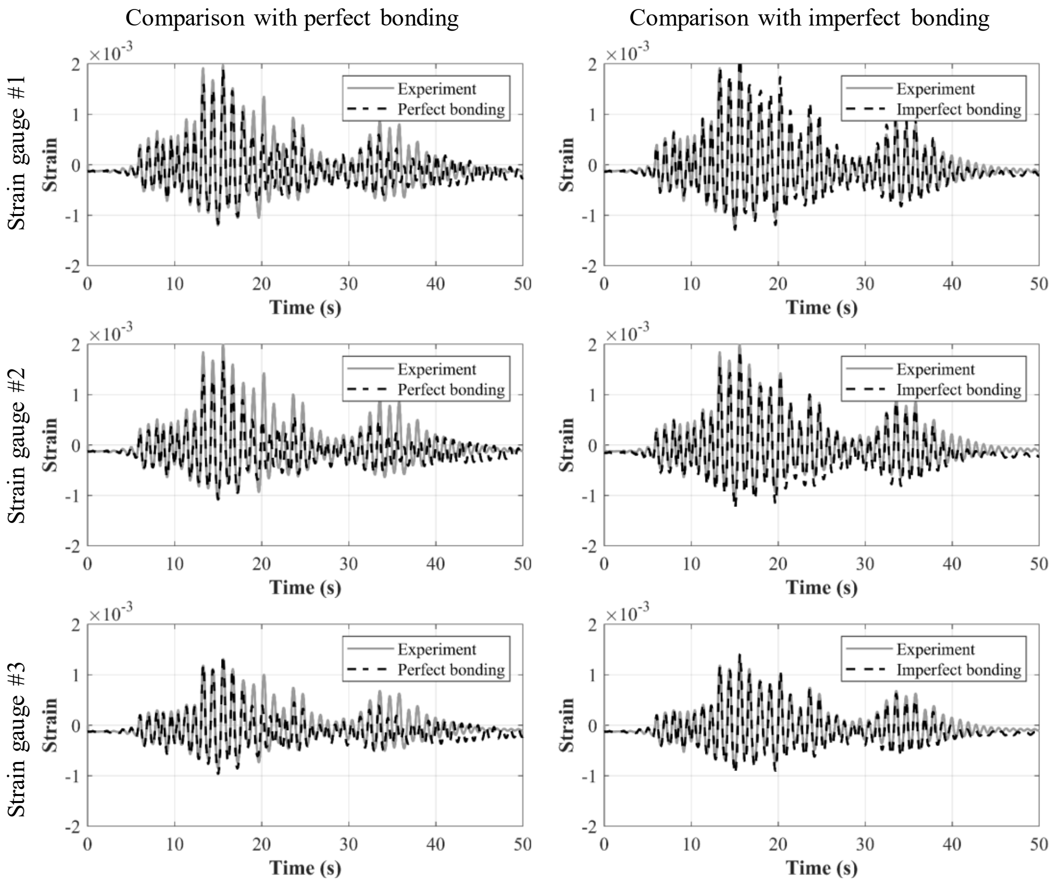

Figure 2-9: Comparison of local strain time-history of the pier column between experiment and FE prediction with perfect and imperfect bonding for three instrumented strain gauges

Note that in the FE-simulations above, the geometric nonlinearity is considered using the enhanced fiber-based frame element. To show the role of geometric nonlinearity captured using this enhancement, the RC columns are also simulated without considering geometric nonlinearity, i.e., using the original element formulation proposed by Spacone and Limkatanyu [86]. For the sake of space limitation, Low-Moehle and Bousias columns are used for demonstration here. Figure 2-10 describes the lateral load-drift ratio hysteresis of experimental results compared to FE prediction considering linear and nonlinear geometry. This comparison reveals the linear geometry leads to the strength overshooting for both columns. However, using the introduced hybrid corotational transformation resolves this issue and provides a reasonably better agreement with the experiments. This observation confirms the capability and importance of the introduced corotational transformation to capture the effect of nonlinear geometry in RC columns under large deformation levels. It is worth noting that the importance of considering geometric nonlinearity in FE predictions, especially for RC columns under large axial loads and lateral deformations, has been shown in the existing studies in the literature (e.g., [88,101,109]). This research verified this common knowledge to emphasize the importance of introducing geometric nonlinearity when bond-slip is considered, which is one of the novelties of this study.

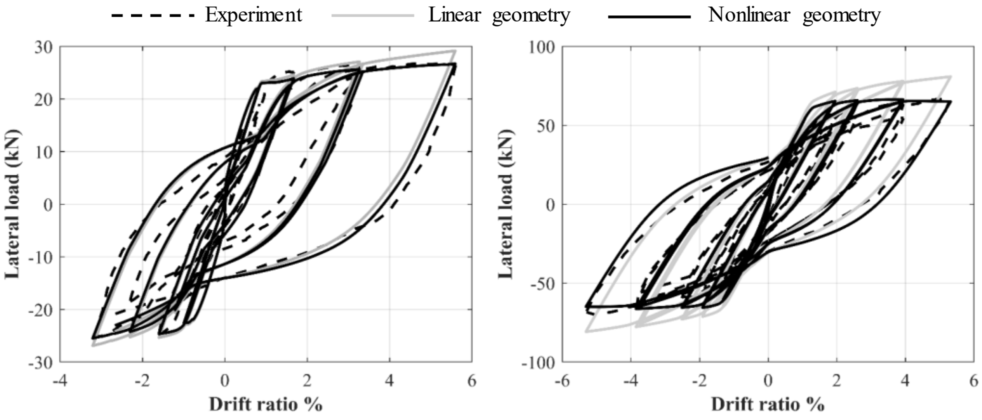

(a) (b)

Figure 2-10: Effect of nonlinear geometry on the lateral load-drift ratio hysteresis of (a) Low-Moehle column, and (b) Bousias column

To further investigate the effect of geometric nonlinearity on FE-simulations, Figure 2-11 (a) and (b) show the simulated lateral load-drift ratio behaviors for Low-Moehle column and Bousias column under monotonic loading, respectively, using FE models with imperfect bonding and considering linear and nonlinear geometry. Comparing the FE-predictions of models with linear and nonlinear geometry reaffirms that the geometric nonlinearity mainly affects the FE-predictions of column behavior (e.g., load capacity).

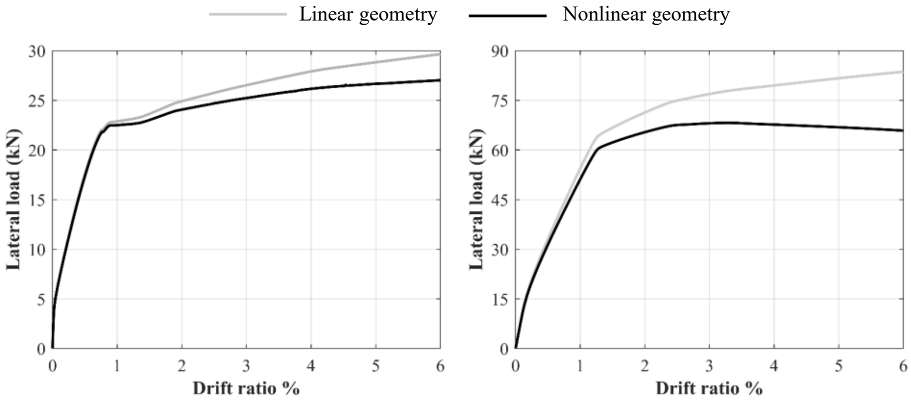

(a) (b)

Figure 2-11: Effect of nonlinear geometry on the lateral load-drift ratio monotonic envelops of (a) Low-Moehle column, and (b) Bousias column

2.4. BEHAVIOR OF RC COLUMNS WITH IMPERFECT BONDING

This section investigates the lateral behavior of RC columns considering imperfect bonding. To explore the effect of imperfect bonding, different scenarios are considered here, including (1) columns with different anchorage conditions for longitudinal steel bars (i.e., various anchorage lengths, with/without hooks), (2) columns with different axial load levels under static monotonic/cyclic pushover analysis, and (3) columns under dynamic seismic loading with earthquake ground motions characterized as short- or long-durations.

2.4.1. Columns with different anchorage conditions for steel bars

In RC columns, bond-slip of anchored steel bars is most likely to occur at the bottom of the column and/or in adjoining concrete members (e.g., column footings). Thus, one of the important parameters that can influence the role of bond-slip in RC columns is the anchorage condition, which is characterized by the details of steel bar ends (hooked or unhooked) and the anchorage length of longitudinal steel bars. In this paper, it is assumed that hooked ends are sufficiently effective such that no slip occurs where the steel bar bends due to its full embedment in the adjoining concrete member.

To show the effect of anchorage length on the behavior of RC columns, Saatcioglu column with straight (unhooked) steel bars is used here by varying the anchorage length $L_a = 10d_b$, $15d_b$, $20d_b$, $25d_b$, and $30d_b$, where d_b is steel bar diameter. Static pushover analyses are conducted for these five cases considering imperfect bonding. Figure 2-12 (a) and (b) present the monotonic and cyclic lateral load-drift ratio hysteresis of the columns subjected to monotonic and cyclic loading, respectively, compared to the counterpart assuming perfect bonding. As observed, the shorter anchorage length indicates more pronounced differences between the case with imperfect bonding and the case assuming perfect bonding. When the anchorage length is sufficient (e.g., $L_a/d_b = 21$ as in the test specimen), the difference between the behavior of the column is negligible in terms of peak strength and post-peak behavior up to 10% drift ratio, except for the slight difference in the post-cracking stiffness. However, when anchorage length is insufficient, e.g., $L_a/d_b = 10$, under low drift-ratio (or loading) levels, the RC column behaves similarly to the other cases with sufficient anchorage length. However, for higher loading levels, the effect of insufficient anchorage length gets dominant, and the column strength degrades significantly with an abrupt drop, resulting in the loss of ductility because of bonding failure. It is worth noting that the strength drop for the column is more severe (38% at drift ratio of 6%) under cyclic loading than monotonic loading (18% at drift ratio of 6%). This is because of the higher degradation of bond-slip under cyclic loading compared with monotonic loading, as indicated by Eligehausen et al. [107]. For the same reason, the strength degradation occurs for the case with $L_a/d_b = 15$ under cyclic loading at around 9% drift ratio, but not under monotonic loading. These conclusions reaffirm that for cases with straight steel bars, the anchorage length can remarkably influence bond-slip contribution. Therefore, when the anchorage length of steel bars is insufficient for RC columns subjected to high lateral loading levels, particularly during cyclic loading (e.g., earthquakes), the assumption of perfect bonding in FE modeling of RC columns is more problematic for response prediction.

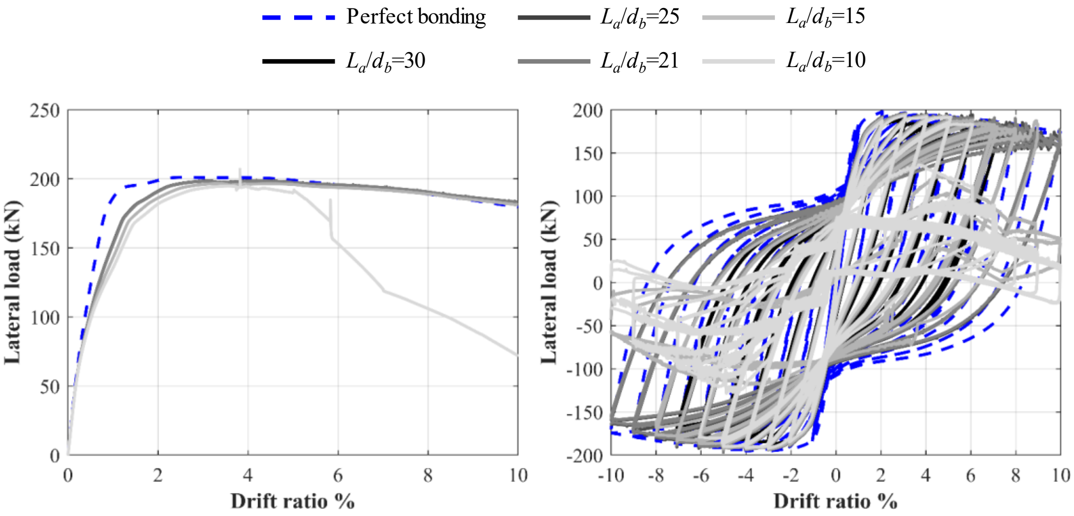

(a)

(b)

Figure 2-12: Effect of anchorage length of longitudinal steel bars on the behavior of Saatcioglu column subjected to (a) monotonic loading, and (b) cyclic loading

For RC columns with longitudinal steel bars hooked at the end, the effect of anchorage length is expected to be much less significant. To reveal this, Figure 2-13 compares the lateral load-drift ratio hysteresis using Saatcioglu column for three cases: sufficient anchorage length ($L_a/d_b = 21$) with steel bars unhooked, insufficient anchorage length ($L_a/d_b = 10$) with steel bars unhooked, and “insufficient” anchorage length ($L_a/d_b = 10$) with steel bars hooked. The comparison shows that the case of sufficient anchorage length with steel bars unhooked behaves similar to the case of steel bars hooked, even when $L_a/d_b = 10$ that is considered as “insufficient” for unhooked steel bars. This confirms that the hooking condition can remarkably affect the role of bond-slip in RC columns.

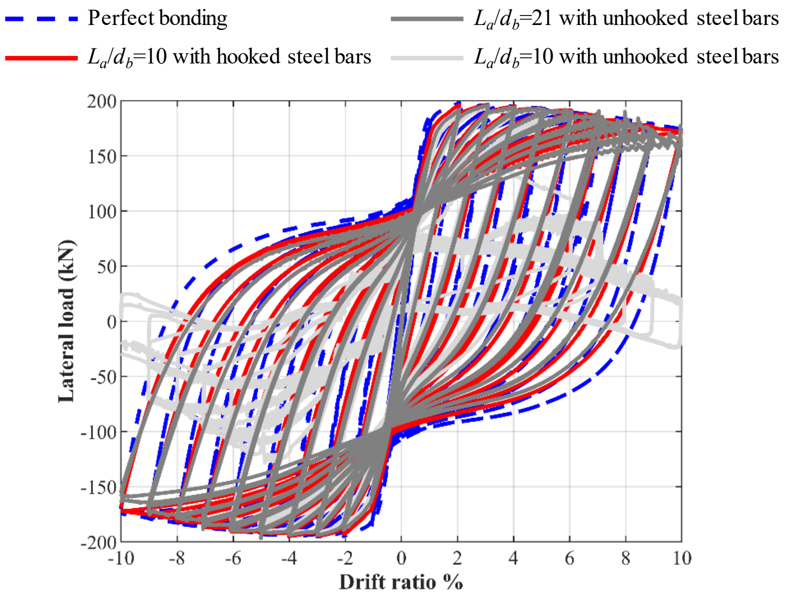

Figure 2-13: Effect of hooks at the end of longitudinal steel bars in Saatcioglu column on the role of anchorage length

2.4.2. Columns under different axial load levels

This section aims to investigate the relative importance of considering bond-slip in FE modeling for predicting the lateral behavior of RC columns under different axial load levels. For this purpose, Saatcioglu column is used with various axial load levels considered, i.e., P/f'_cA_g = 0.05, 0.10, 0.15, 0.20, 0.25, 0.30, 0.35, and 0.40, where P is the axial load imposed on the column, and f'_cA_g refers to the "nominal" axial load capacity of the column, defined as the product of the concrete compressive strength (f'_c) and the gross area of the column cross-section (A_g). Figure 2-14 shows the comparison of FE-predicted lateral load-drift ratio curves when assuming perfect bonding and considering imperfect bonding for the RC column subjected to monotonic and cyclic loading. Note that only two of eight cases considered (P/f'_cA_g = 0.1, 0.4) are shown here. The comparison indicates as the axial load ratio increases, the difference between lateral load-deformation behaviors predicted using the FE models with perfect and imperfect bonding increases. In particular, the RC column under larger axial load have higher demand under the lateral load, which imposes higher demand on the bonding between steel and concrete.

Furthermore, with a higher axial load ratio, the relative displacement between the steel bar and surrounding concrete (i.e., slip) is more significant due to assuming symmetric bond-slip behavior [107]. As a result, the bond-slip plays a more important role in the RC columns with a higher axial load ratio (i.e., higher level of loading), implying more discrepancy with the case assuming perfect bonding.

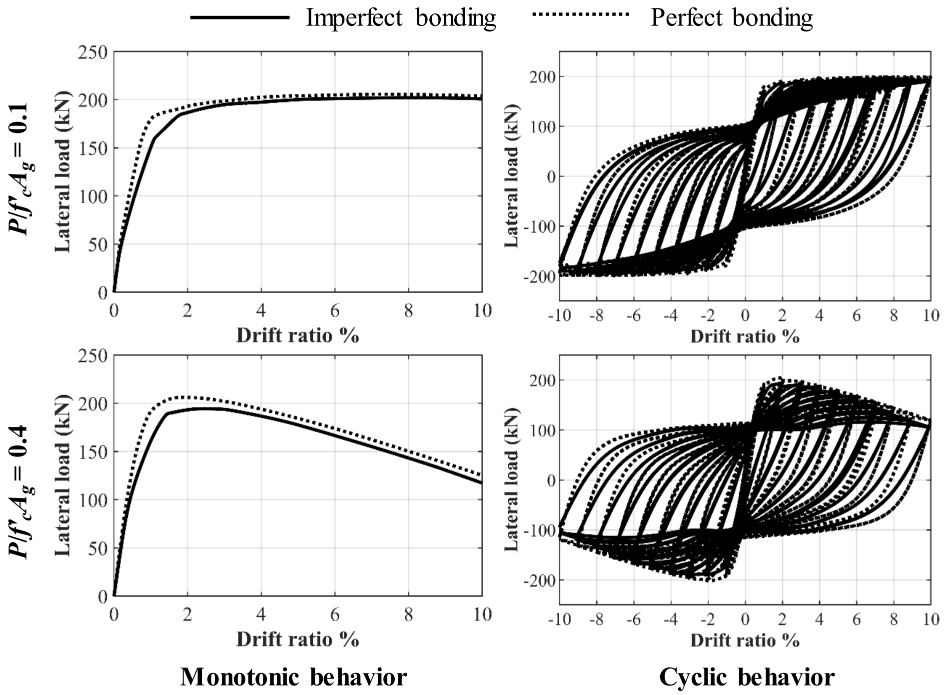

Figure 2-14: Comparison of FE-simulated lateral load-drift ratio responses considering imperfect and perfect bonding for Saatcioglu column with varying axial load levels

To quantify the difference in FE predictions arising from the bonding assumptions, three quantities extracted from the monotonic load-drift ratio curves are examined. They are the secant stiffness defined based on the point at which the tangent stiffness is reduced by 20%, the lateral strength capacity, and the deformation capacity measured by the ratio of the displacement corresponding to 20% drop in the strength to the displacement corresponding to the onset of steel yielding. The FE-prediction difference is measured by the discrepancy percentage when the case considering imperfect bonding is compared with the case assuming perfect bonding. Figure 2-15 presents the FE-prediction discrepancy percentages in the three considered quantities of RC columns under various axial load levels. Negative values of the discrepancy percentages here imply that the FE models assuming perfect bonding (i.e., neglecting bond-slip) over-predict the secant stiffness, the strength capacity, and the deformation capacity.

To be specific, Figure 2-15 (a) indicates that the secant stiffness is over-predicted slightly at low axial load levels; on the contrary, as the axial load level increases, the over-prediction of the secant stiffness gets more significant (e.g., up to 62%). Figure 2-15 (b) reveals that the strength capacity predictions differ little due to the negligible effect of bond-slip on the maximum strength. It is worth noting that the larger axial load levels in RC columns involve higher prediction errors for the strength capacity when perfect bonding is assumed. In contrast, the deformation capacity is highly affected by the assumption of perfect bonding, especially when the axial load level is low, as shown in Figure 2-15 (c).

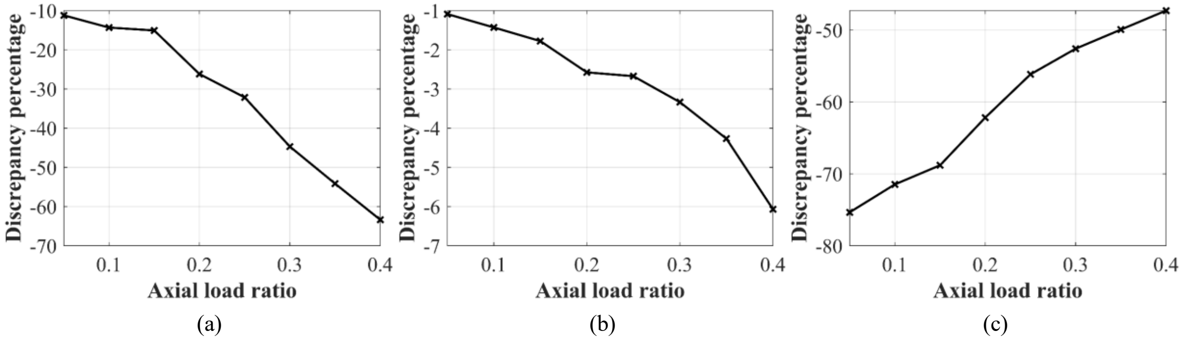

Figure 2-15: FE-prediction difference arising from bonding assumptions for Saatcioglu column at various axial load levels in terms of (a) secant stiffness, (b) strength capacity, and (c) deformation capacity

2.4.3. Columns subjected to short- and long-duration earthquakes

As shown earlier in this study, the newly developed FE element can capture the effect of bond-slip in RC columns under both static and dynamic loadings. In particular, under dynamic loading with a large number of unloading-reloading cycles, accurate modeling of RC columns requires more caution. This is because bonding degrades more due to cyclic loading, which leads to more pinching effect in the lateral load-deformation hysteresis of RC columns. Thus, it is worth investigating the impact of bond-slip on the RC column behavior subjected to short- and long-duration earthquakes. Examples of such earthquakes are crustal earthquakes, which lead to great damage from the rapid release of energy of shorter events [110,111], and subduction earthquakes, which are destructive due to longer-duration and more number of strong cycles [112,113], respectively. In this regard, this section employs the validated FE model of UCSD column introduced earlier to study the effect of earthquake duration on the role of bond-slip in RC columns. For a fair comparison, two pairs of spectrally equivalent short- and long-duration earthquake ground motions are used, which were well-established record sets used by other researchers [114,115] to quantify the earthquake duration effect. These two record sets taken from [70] are listed in Table 2-3. In addition, the acceleration time-histories and corresponding pseudo acceleration spectra for these two pairs are presented in Figure 2-16 and Figure 2-17, respectively, to show their difference in earthquake durations and their similarity in ground motion characteristics (i.e., amplitude, frequency content, elastic pseudo acceleration spectra).

Table 2-3: Spectrally equivalent pairs of short- and long-duration earthquake ground motions

Pair No.		#1	#2
Short duration record	Earthquake	1999 Chi-Chi, Taiwan-02	1999 Hector Mine
	Station	HWA059	Amboy
	Scale factor	5.1	2.8
Long duration record	Earthquake	1999 Kocaeli, Turkey	2010 El Mayor-Cucapah
	Station	Fatih	Chihuahua
	Scale factor	3.0	2.0

The seismic responses of UCSD column subjected to the two sets of earthquake ground motions are simulated and compared when considering imperfect bonding and assuming perfect bonding in the FE models. The corresponding drift ratio time-history responses are presented in Figure 2-18. Comparing the responses from the FE models assuming perfect bonding and those considering imperfect bonding, it shows that the effect of bond-slip on the overall dynamic response is significant for the RC columns under short- and long-duration earthquake ground motions. However, it can be observed that the bond-slip does not significantly affect the peak responses as found in other studies [81,82]. Specifically, the peak drift ratios are only slightly underestimated when assuming perfect bonding (see Table 2-4) for both cases under short- and long-duration earthquake ground motions.

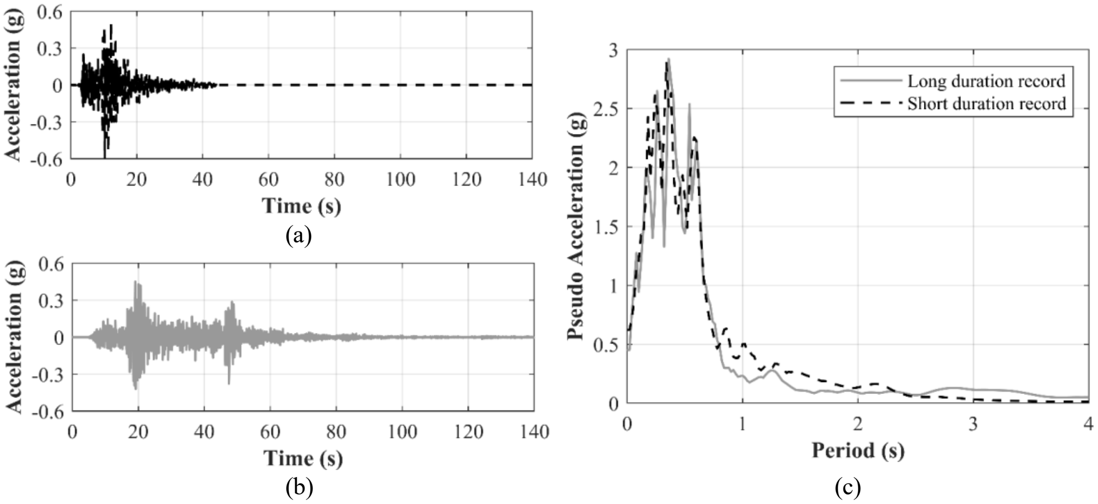

(a)

(b)

(c)

Figure 2-16: Spectrally equivalent record pair #1: (a) acceleration time history for the short-duration record, (b) acceleration time-history for the long-duration record, and (c) pseudo acceleration spectra of short- and long-duration records for 2% damping ratio

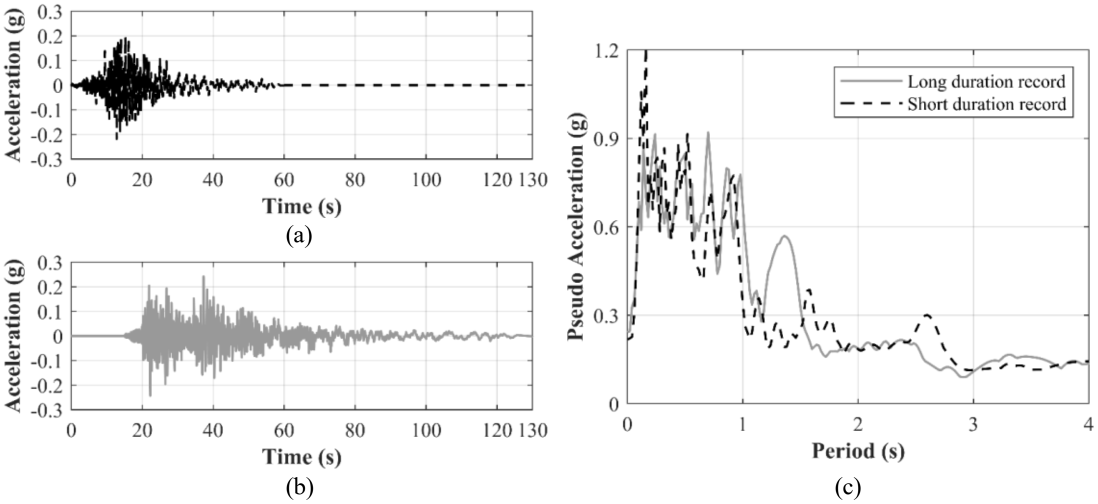

(a)

(b)

(c)

Figure 2-17: Spectrally equivalent record pair #2: (a) acceleration time history for the short-duration record, (b) acceleration time-history for the long-duration record, and (c) pseudo acceleration spectra of short- and long-duration records for 2% damping ratio

To further investigate the role of bond-slip in RC columns excited by short- and long-duration records, the energy dissipated during earthquakes through base-shear and drift-ratio hysteresis is examined. Table 2-4 shows that when imperfect bonding is considered, the energy dissipated is less due to pinching, compared to the case when perfect bonding is assumed. Such effect of bond-slip is more significant for long-duration earthquakes than short-duration earthquakes, e.g., (57.72% - 59.09%) and (12.30% - 14.64%) less energy dissipation compared to the perfect bonding case. Thus, this reaffirms the need to incorporate the effect of bond-slip in accurate FE modeling of RC structures for seismic analysis, particularly when long-duration earthquakes are considered and accumulative damage is of interest to engineers.

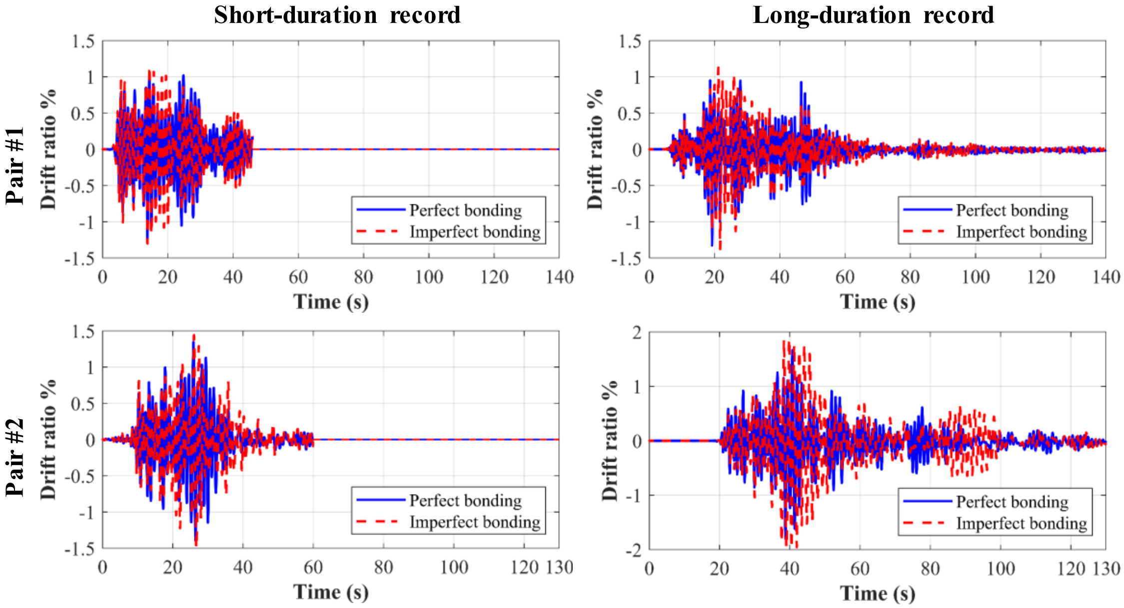

Figure 2-18: Drift ratio time-histories of UCSD column with perfect and imperfect bonding under short- and long-duration earthquake ground motions

Table 2-4: Comparison of FE-predicted structural responses considering imperfect bonding against perfect bonding for UCSD column under short- and long-duration earthquake ground motions

	Short-duration		**Long-duration**	
Ground motion set	Dissipated energy	Peak drift ratio	Dissipated energy	Peak drift ratio
Pair #1	−12.30%	+4.45%	−57.72%	+4.71%
Pair #2	−14.64%	+7.50%	−59.09%	+8.83%

2.5. CHAPTER CONCLUSIONS

This paper addresses the effect of imperfect bonding between the reinforcing steel and the surrounding concrete in RC structures. In order to investigate the actual behavior of RC structures considering imperfect bonding, this study enhances an existing displacement-based fiber frame element with bond-slip by accounting for the effect of geometric nonlinearity. Assuming the linear geometry would lead to strength overshooting in FE predictions. However, by introducing the hybrid corotational transformation for the element with bond-slip, the FE-predicted responses match well with the experiments in terms of strength and pinching. Hence, to incorporate the role of imperfect bonding in FE modeling of RC structures, this study develops and implements the required FE modeling capabilities, including element, section, and geometric transformation in *OpenSees*. Using this FE modeling approach, the bond-slip effect in the interior of the columns is also captured, which is particularly applicable to other circumstances such as in corroded RC columns, where the corroded bonding needs to be considered for the column above the footing.

Using the developed capabilities, this study indicates the effect of imperfect bonding on the behavior of the RC columns may be significant and cannot be blindly neglected. In addition, it shows that some factors, including steel bar anchorage scenario, load level, and duration of earthquake loading, can intensify the role of imperfect bonding in the nonlinear behavior of RC columns. Specifically, for RC columns with unhooked longitudinal steel bars, the anchorage length is an important factor. The response prediction error arising from perfect bonding assumption also depends on the response quantities of interest, the axial load level in the RC column, loading types (monotonic or cyclic), and the earthquake durations. Moreover, the bond-slip mainly affects the energy dissipation in RC columns. This study reveals that such observations are due to more contributions from bond-slip in cases with higher axial load levels and cases subjected to long-duration earthquakes rather than cases under short-duration earthquakes. These conclusions reaffirm the need to incorporate imperfect bonding in the advanced modeling of RC structures.

To summarize, the significant contributions of this study can be highlighted as follows: (1) enhancing a fiber-based frame element considering bond-slip with geometric nonlinearity taken into account through hybrid corotational transformation; (2) implementing the enhanced element in *OpenSees*, providing a powerful tool, which can be used for RC columns without presuming that the effect of bond-slip can be neglected; and (3) assessing the common assumption of perfect bonding in FE modeling of RC columns under different loading and anchorage scenarios, pointing out its validity depends on the responses of interest. In particular, the common perfect bonding assumption should be used with caution since considering imperfect bonding can be essential for accurate FE modeling of RC columns depending on the anchorage scenario and loading conditions.

Chapter 3. BOND-SLIP MODEL UNCERTAINTY QUANTIFICATION AND EFFECT ON NONLINEAR BEHAVIOR SIMULATIONS OF RC COLUMNS

3.1. INTRODUCTION

Advanced finite element (FE) modeling of reinforced concrete (RC) structures has been the focus of numerous studies in modern structural engineering with the rapid growth of computing technologies over the past decades. In RC structures, the composite action of steel and concrete has a crucial role, which allows the force transferring from the reinforcing steel to the adjoining concrete through bonding at the steel-concrete interface. Common FE modeling approaches for RC structures (e.g., using conventional fiber-based beam-column elements) assume perfect bonding between reinforcing steel and the surrounding concrete. Perfect bonding here implies that the deformation of reinforcing steel is fully compatible with the deformation of the surrounding concrete. However, this assumption can sometimes be questionable, as revealed by the historical and experimental observations of failures due to the de-bonding of reinforcement [71,72,76,77,79]. In particular, for RC structures subjected to severe loading or those of sub-standard design (e.g., steel bars with insufficient anchorage in seismic areas), the bond stress demand can lead to notable inelastic action within the steel-concrete interface, which significantly affects the stiffness and hysteretic energy dissipated of RC structures under cyclic loading [90,91,116]. To simulate the responses of such structures more accurately, the bond stress-slip relationship is required for representing the mechanical behavior of the steel-concrete interfaces. Also, the bond-slip properties suffer from various degrees of uncertainty as discussed later. In this regard, the objective of this study is to develop a probabilistic model for bonding properties and apply it to investigate the effect of bond-slip model uncertainties on the nonlinear behavior simulations of RC columns.

To incorporate the slippage between steel bar and surrounding concrete in FE models, different FE approaches can be used with various levels of sophistication and efficiency, including detailed continuum-based FE models [84,117] and fiber-based FE models [85–87,116,118]. In the detailed continuum-based FE modeling approach, zero-thickness interface elements are typically introduced between steel and concrete with appropriate bond-slip behavior models, where the focus is on the constitutive model development for interface elements [119]. However, this approach can aggravate the high computational cost (i.e., processing time) of continuum-based FE models for system-level modeling of frame-type RC structures. In contrast, the fiber-based modeling approaches are more common and efficient in terms of computational cost (i.e., less processing time) for frame-type structures, especially in the field of structural and earthquake engineering, providing an alternative venue to consider bond-slip in FE modeling of RC structures where only a uniaxial bond-slip model is required.

Therefore, several studies aimed to enhance the conventional fiber-based frame element formulation for considering the imperfect bonding. Among these developments, some approaches, such as using a zero-length element [118] and modifying the stress-strain behavior of steel [87], account for the imperfect bonding implicitly, which leads to limitations in their applicability. For instance, these methods are not general and thus incapable of modeling structures with the bonding behavior different from normal bonding conditions assumed in those studies. The FE modeling approach proposed in [85] incorporates the bond-slip explicitly by altering the composite behavior of steel and concrete at the fiber-section level but limited to the anchorage slippage only (e.g., in the column footing). On the contrary, the FE modeling approach developed in [86] proposed a fiber-based frame element, which explicitly considers the bonding between steel bars and concrete inside the entire structural member and the adjacent members by defining additional degrees of freedom for steel bar movements. However, this fiber-based frame element with bond-slip is limited to small deformation problems. To overcome this limitation, this element has been enhanced by considering the geometric nonlinearity via corotational transformation [116], and implemented in the open-source finite element software framework, *OpenSees* [65]. Hence, this newly developed geometrically nonlinear fiber-based frame element with bond-slip can be used for FE modeling of RC columns considering imperfect bonding under extreme loading conditions.

To model RC structures considering imperfect bonding, an explicit bond-slip material model is required. Such a bond-slip model is typically formulated with monotonic (i.e., back-bone curve) and cyclic (i.e., hysteretic rules) stress-slip patterns, which are characterized by relevant bonding properties. Several studies have proposed different bond-slip models but with similar patterns in the literature and minor differences. The pattern proposed by Eligehausen et al. [107] is one of the pioneering models for bond-slip behavior, which is developed based on several experimental tests and forms the basis of many other models [120,121]. Therefore, the main purpose of the other studies was to generate the bonding properties (i.e., bonding stress values and corresponding slips) based on the steel bar diameter, concrete strength, clear spacing between steel bars, lug properties, loading rate, etc. [84,85,107,120–124]. These models were developed based on limited test data, i.e., a certain test dataset with a relatively small sample size, and validated only for limited specimens. The comparison of these existing models, as revealed later in this study, showed large variations. The uncertainty quantification of bonding properties in RC structures under normal circumstances (i.e., with no corrosion) has not been thoroughly studied. Yu et al. [125] developed a probabilistic bond strength model to consider the uncertainties in the maximum bonding strength; however, no study has quantified uncertainties in the other bonding properties (e.g., parameters related to slip). In contrast, existing research on the role of bond-slip in the interface of steel bars and surrounding concrete (e.g., [84–86]) investigated the bond-slip effect by comparing three scenarios: strong (perfect), normal (imperfect), and no bonding (pure concrete) conditions. No research, to the best knowledge of the authors, has been devoted to studying normal (imperfect) bonding specifically after considering the potential variations in the "normal bonding" scenario. Hence, to address the gap, this study will explore the impact of bond-slip model uncertainties on the behavior simulations of RC columns using the recently developed geometrically nonlinear fiber-based frame element.

For this purpose, this study first describes the bond-slip behavior and assesses the goodness of eight existing bond-slip models by comparing model predictions with observations from the compiled experimental database from the literature. Then, a new model is proposed for bonding properties using Bayesian linear regression based on the compiled experimental database; the corresponding probabilistic model is utilized to predict the bonding properties with uncertainty quantified for steel bars in three experimental RC columns [79,94,96]. Finally, the three experimental RC columns tested in the literature are modeled using the recently developed fiber-based frame element considering bond-slip in *OpenSees* [116], and the newly implemented bond-slip material model in conjunction with bonding properties determined from nine different models aforementioned. The effect of bond-slip variations on the nonlinear behavior simulations of RC columns is investigated under static and dynamic loading, through (1) using different models to determine bonding properties to show the difference in the FE predictions and (2) using the newly developed probabilistic model for evaluating the relative importance of the uncertainty of bonding properties with comparison to that of the uncertainties in concrete/steel properties.

3.2. NONLINEAR MATERIAL MODELS FOR BOND-SLIP

The slippage between steel bars and the surrounding concrete can severely affect the behavior of RC structures. To capture this effect in computational modeling, such as using the geometrically nonlinear fiber-based frame element, the relationship between the bonding stress (t) and the slippage displacement (slip u_b) is required. As such, this section focuses on phenomenological nonlinear material models for bond-slip, describing the bonding stress and slip behavior. The bond-slip model comprises the pattern considered and associated bonding properties. Among available bond-slip models in the literature, similar patterns were observed with minor differences, while large variation exists in bonding properties, as revealed later in this section. In this regard, this study first discusses a typical bonding stress-slip pattern, followed by assessing the common prediction models for bonding properties in the literature. Then, a new prediction model for bonding properties is developed through Bayesian linear regression based on an experimental database compiled, together with the quantification of model errors or uncertainties.

3.2.1. Bonding stress-slip pattern

Many studies proposed different bond-slip relationships based on the experimental data [84,107,120–123,126]. Among all these relations, the commonly-used bonding stress-slip pattern originally proposed by Eligehausen et al. [107,126] is considered in this study, which is shown in Figure 3-1 (a) and (b) under monotonic and cyclic loading, respectively.

Under monotonic loading, the bond stress-slip pattern consists of four segments: the ascending branch (OA), a plateau (AB), a linear descending branch (BC), and the constant residual stress branch (CD), which are mathematically described in Eq. (3-1). The ascending branch OA can be characterized by a power-law relationship with a parameter α (e.g., α=1 for the linear case as considered in this paper), up to the yield point of bond-slip (u_{b1}, t_1), where t_1 = the peak bond stress and u_{b1} = the corresponding slip. The plateau AB aims to represent the bond-slip relationship during the gradual shearing off concrete keys between lugs or ribs on a steel bar without a noticeable reduction in bond resistance until slip u_{b2}. The linear descending segment BC is introduced to consider the drop of bond resistance up to the residual frictional stress t_3 at slip u_{b3} with the loss of the interlocking action, which is caused by crushing and shearing off the concrete keys between lugs or ribs. After slip u_{b3}, the constant residual stress is maintained.

$$t(u_b) = \begin{cases} \left(\dfrac{u_b}{u_{b1}}\right)^{\alpha} t_1 & u_b < u_{b1} \\ t_1 & u_{b1} \le u_b < u_{b2} \\ t_1 + \dfrac{t_3 - t_1}{u_{b3} - u_{b2}}(u_b - u_{b2}) & u_{b2} \le u_b < u_{b3} \\ t_3 & u_{b3} \le u_b \end{cases} \tag{3-1}$$

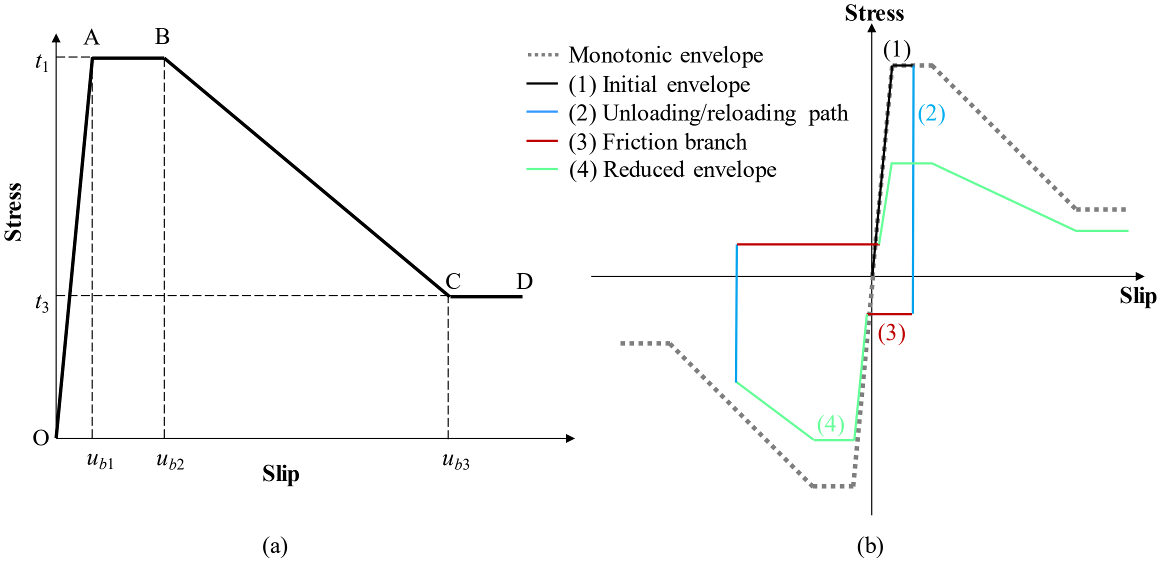

Figure 3-1: Schematic bond-slip material model: (a) monotonic, and (b) cyclic behavior

Under cyclic loading, the bond-slip behavior is schematically shown in Figure 3-1 (b) in terms of stress-slip hysteresis with comparison to the monotonic envelope. The cyclic bond-slip behavior is mainly characterized by (1) initial envelope, (2) unloading/reloading path, (3) friction branch, and (4) reduced envelope [107]. Before the first occurrence of unloading, the bond-slip behavior follows the initial envelope, which is the same as the monotonic envelope described earlier. When unloading occurs, there are three possible scenarios, as discussed later, for reloading in the opposite direction depending on the level of slip reversal. Note that between the unloading and reloading in the opposite direction, there is a friction branch within the gap formed between lugs and concrete before complete shearing off concrete keys.

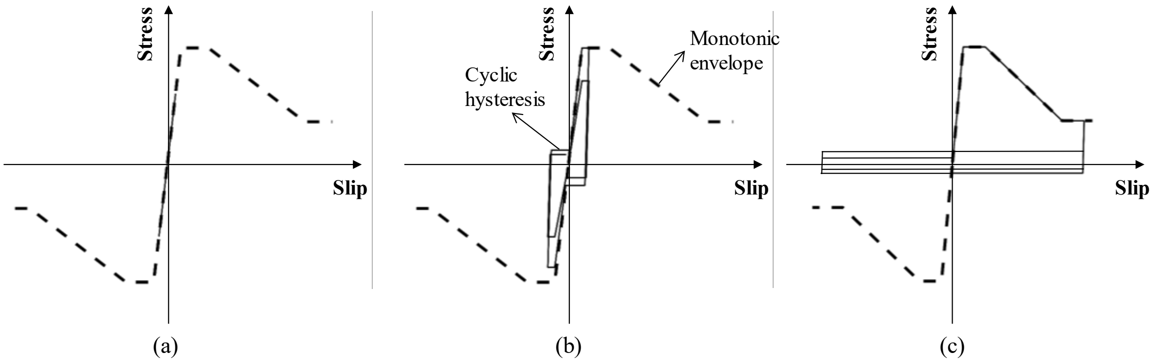

Figure 3-2: Schematic cyclic behavior for bond-slip: load reversals at (a) low, (b) moderate, and (c) high slip levels

Following the friction branch, if the slip reversal occurs at the early stage, i.e., before bond stress reaching 80% of the maximum bonding stress (i.e., t_1) [107,126], the bond-slip behavior under reloading follows the initial envelope closely. In this first scenario shown in Figure 3-2 (a), longitudinal shear cracks in concrete keys are not notably developed except for a few inclined cracks that would close under reloading. In the second scenario, if the slip reversal starts after stress reaching 80% of the yielding stress, i.e., when some longitudinal shear cracks initiate in the concrete keys, the bond-slip behavior under reloading reveals a lowered bond resistance, as illustrated in Figure 3-2 (b). Finally, suppose the load reversal occurs at a relatively large slip (e.g., after shearing off concrete keys between lugs). In that case, the bond-slip behaves more like a frictional model with bond resistance attributed from friction only, as shown in Figure 3-2 (c).

More details about the damage mechanisms and bond-slip behavior under cyclic loading are referred to [107].

This bond-slip material model is implemented in *OpenSees* as *BondSlip04*. This new material model with the newly developed fiber-based frame element considering bond-slip (i.e., *dispBeamColumnBS*), fiber section (i.e., *FiberBSele*), and geometrical transformation (i.e., *corotationalBS*) [116] provides *OpenSees* with a versatile and efficient FE modeling module. It is worth mentioning that it will benefit the FE modeling of corroded RC structures with corrosion-affected bonding, which will be studied by the authors but is beyond the research scope of this study.

3.2.2. Bonding property prediction models and uncertainty quantification

The bond-slip behavior for steel bars in RC structures is defined using the introduced pattern with corresponding bonding properties, i.e., t_1, t_3, u_{b1}, u_{b2}, and u_{b3}. To determine the bonding properties, eight sets of deterministic prediction models are available in the literature [84,85,107,120–124], as summarized in Table 3-1. These eight models predict the bonding properties for well-confined RC structures, which predominantly depend on the steel bar diameter d_b, peak concrete compressive strength f_c, lug properties (i.e., lug spacing l_s and lug height l_h), and clear spacing between steel bars c, shown schematically in Figure 3-3.

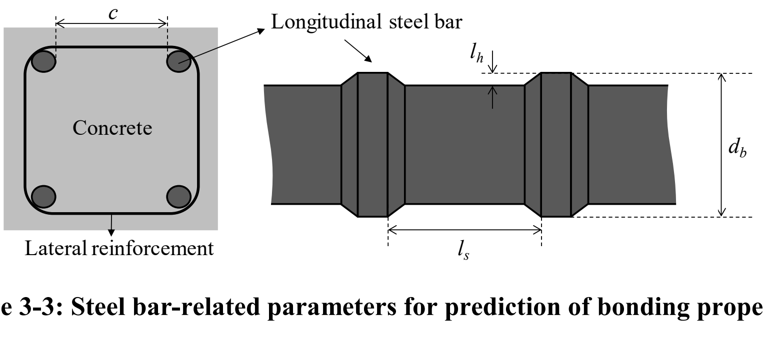

Figure 3-3: Steel bar-related parameters for prediction of bonding properties

The clear spacing is related to the confinement to bars in a RC column where a bar is surrounded by well-confined concrete except one side confined with concrete cover with limited thickness. It is worth noting that in well-confined RC structures, the propagation and width of possible splitting cracks are kept small so that the ultimate failure is caused by bar pull-out [107]. Furthermore, the bond-slip contribution in RC columns considered primarily stems from the bar slip in the anchorage zone of RC columns, where the confinement effect is significantly high due to the enormous concrete surrounding the bars in the column extending into the footing. Consequently, the concrete cover, which is critical in the bond-slip behavior of RC structures with no or insufficient confinement [127], is not considered in this work as an influential parameter. It is also worth mentioning that if the concrete in the vicinity of the bond zone is not well-confined, a splitting bond failure may occur instead of the pull-out failure, resulting in an abrupt drop in bond strength before reaching the plateau. Hence, in cases with insufficient confinement, the bonding properties would be different, which is not considered in this study. To consider the splitting bond failure, a number of existing models, such as the FIB model [124], introduce a modification factor to consider possible bond splitting failure, which is not presented in Table 3-1. Note that other factors, e.g., slip rate and external pressure, also affect the bonding properties according to some experiments [107,128]. Nevertheless, like many other studies (e.g., [85,122–124]), these factors were not included in the model developed to predict bonding properties due to the lack of sufficient data related to those factors, and this can partially explain the model errors. As implied in [128], further experiments and data are needed to facilitate the model development considering the effect of external pressure explicitly, and thus reducing the model uncertainty.

Table 3-1: Summary of existing prediction models for bonding properties

Model	**Model parameters for bond-slip**				
	t_1 (MPa)	t_3 (MPa)	u_{b1} (mm)	u_{b2} (mm)	u_{b3} (mm)
Eligehausen [107]	$13.5\times\sqrt{(f_c/30.0)}\times f_1(d_b)^{*}\times f_2(c)^{*}$	$5.0\times f_3(c)^{*}$	$\sqrt{(f_c/30.0)}$	3.0	l_s
Pochanart [122]	$(4.2-0.06(l_s/l_h))\times 6.9$	$(0.8-0.1(l_s/l_h))\times 6.9$	1.5	1.5	l_s
Soroushian [123]	$(20.0-d_b/4.0)\sqrt{(f_c/30.0)}\times$ $(1.0-0.8\exp(-1.6(c/d_b)^{0.8}))$	$(5.5-0.07l_s/l_h)\times$ $\sqrt{(f_c/27.6)}\times(1.0-0.8\times\exp(-1.6(c/d_b)^{0.8}))$	$\sqrt{(30.0/f_c)}$	3.0	l_s
Monti [85]	$0.2(100.0-d_b)$	$t_1/3.0$	$0.04(1.0+d_b)\geq 0.7$	$3.0\ u_{b1}$	$10.0\ u_{b1}$
Lowes [120]	$0.8\Gamma(d_b, c)^{**}$	$0.2\Gamma(d_b, c)^{**}$	$t_1/20.0$	$u_{b1}+1.0$	$u_{b1}+10.0$
Bamonte [121]	$f_c(0.5+(1.1\times 10.0/f_c)$ $\times(d_b/12.0)^{(-0.013fc)})$	$0.4t_1$	1.0	3.0	l_s
Delso [84]	$16.5(f_c/34.5)^{0.8}$	$0.25t_1$	$0.07d_b$	$1.1u_{b1}$	l_s
FIB [124]	$2.5\sqrt{(f_c)}$	$0.4t_1$	1.0	2.0	l_s

*For more details on the functions f_1, f_2, and f_3, see [107].
**For more details on the function Γ, see [120].

To investigate the accuracy of these prediction models for bonding properties, i.e., t_1, t_3, u_{b1}, u_{b2}, and u_{b3}, and the effect of model inaccuracy/uncertainty on the mechanical behavior simulations of RC columns, an experimental database is compiled in this study by collecting 93 bond-slip tests in the public literature [84,107,121–123,126,129]. This database consists of 93 data points for t_1, 30 data points for t_3, 64 data points for u_{b1}, 37 data points for u_{b2}, and 59 data points for u_{b3}, as summarized in Table 3-2. Detailed information of the database is reported in Appendix C, with the key parameter values used to develop bonding property prediction models.

Table 3-2: Source of experimental data for bonding properties

Parameter	Number of data from each source						Total
	[107,126]	[122]	[123]	[129]	[121]	[84]	
t_1	25	14	5	5	22	22	93
t_3	25	−	5	−	−	−	30
u_{b1}	25	3	5	5	4	22	64
u_{b2}	25	3	5	−	4	−	37
u_{b3}	25	3	5	−	4	22	59

This database is firstly used to assess those existing models for bonding property prediction. Comparison between the experimental data available (referred to as observations) in the literature and the bonding properties predicted based on the eight models mentioned above is presented, as shown in Figure 3-4 to Figure 3-8 for t_1, t_3, u_{b1}, u_{b2}, and u_{b3}, respectively. The deviation of the data points from the unity line (45° line) in these figures indicates the associated error, and the R-squared (R^2) value for each model is also reported; a value closer to 1.0 implies a better model generally. The data points originally used for developing the model are indicated by open gray diamonds in the plots, implying that only a fraction of this experimental database was used to develop each of those models. This partially explains why the models have such a huge prediction error or are limited to fitting only a portion of the data points within a certain parameter range.

To be specific, Figure 3-4 indicates the model predictions of t_1 correlate well with the experimental data used for the model development while the correlations between the model predictions with un-seen experimental data are significantly poor. This observation reaffirms the existing models for t_1 works well for a specific range of structures, and it is *not* proper to use one of the existing models for all RC structures. Similarly, Figure 3-5 shows the comparisons for t_3 and indicates that the model predictions and experimental observations are not in good agreement, and it is essential to develop a versatile model for all ranges of structures. In addition, Figure 3-6 to Figure 3-8 demonstrate the correlation between the model predictions and experimental observations of u_{b1}, u_{b2}, and u_{b3}. Some of the models for u_{b1} and u_{b2} propose constant values, which are close to the averages of the experimental data. However, these models neglect the variations of u_{b1} and u_{b2} due to their dependency on other effective parameters. Hence, it is essential to develop more accurate and versatile models to reduce the prediction error from model development, quantify the model uncertainty, and then assess the effect of model inaccuracy on predicting the mechanical behavior of RC structures.

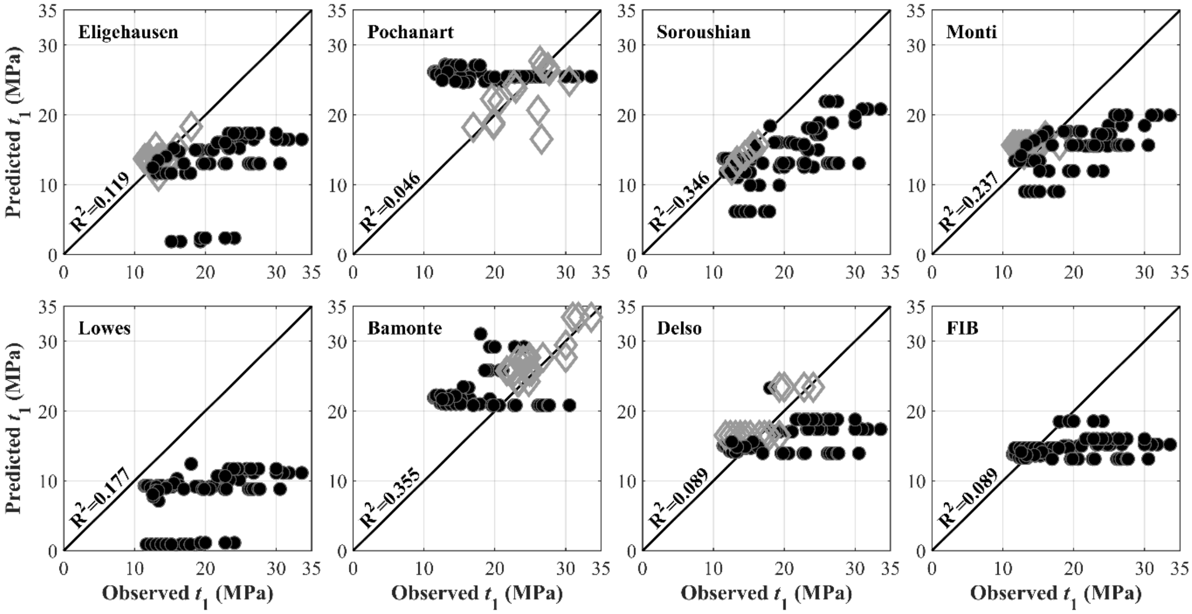

Figure 3-4: Observations vs. predictions using models for t_1

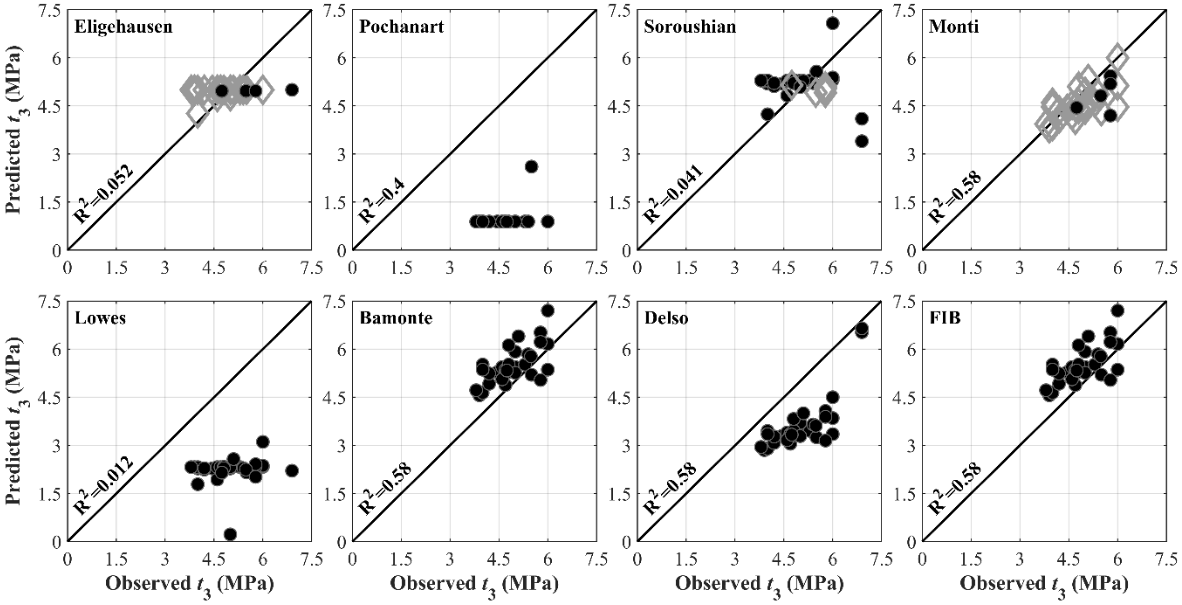

Figure 3-5: Observations vs. predictions using models for t_3

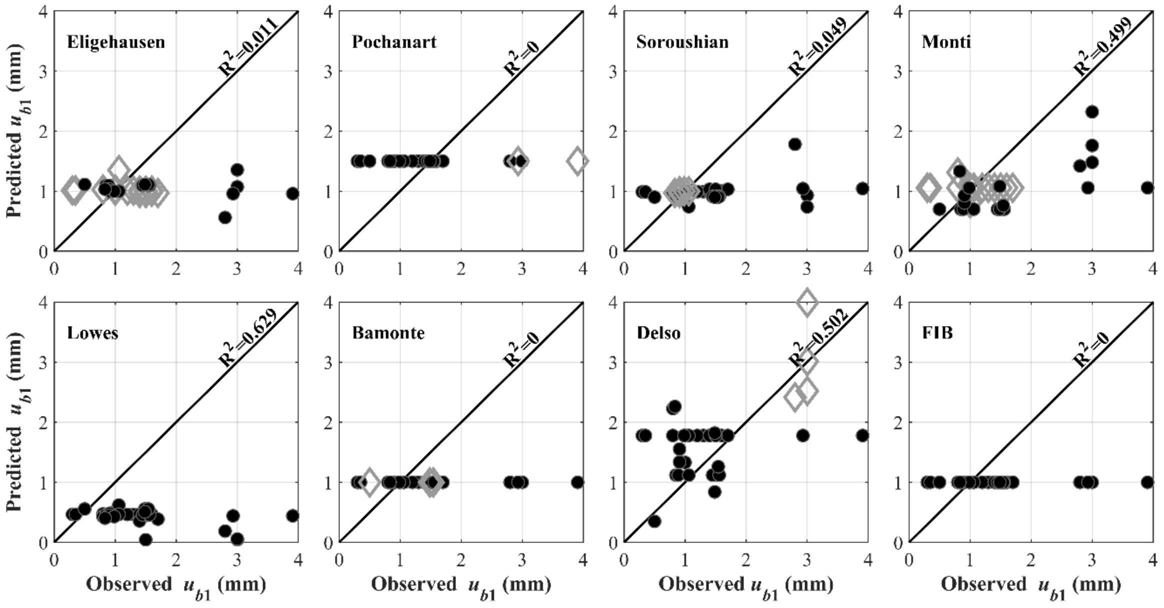

Figure 3-6: Observations vs. predictions using models for u_{b1}

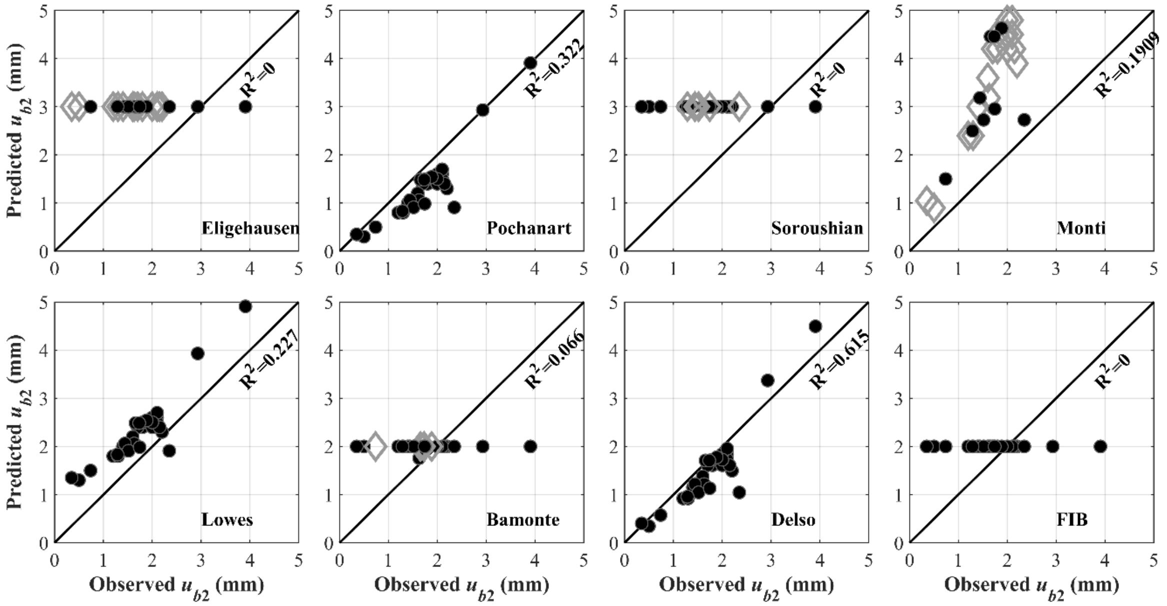

Figure 3-7: Observations vs. predictions using models for u_{b2}

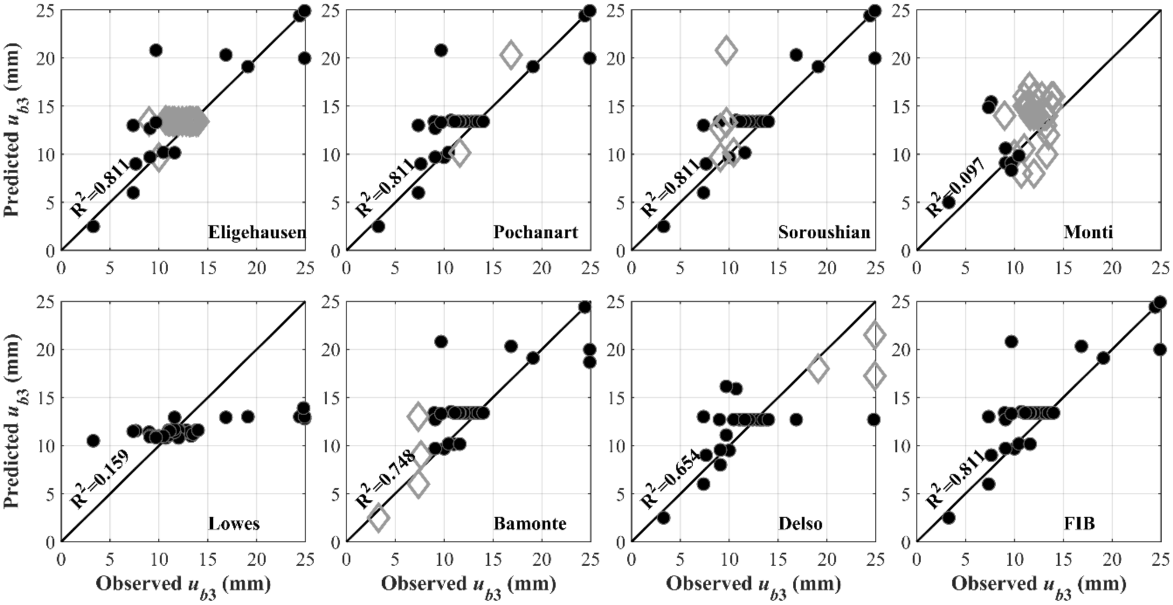

Figure 3-8: Observations vs. predictions using models for u_{b3}

Based on the experimental database compiled for bonding properties, a new prediction model is developed to predict the bonding properties, i.e., t_1, t_3, u_{b1}, u_{b2}, and u_{b3}, together with the prediction errors quantified probabilistically using Bayesian linear regression [130]. Note that in the context of Bayesian linear regression, all model parameters are estimated probabilistically. Therefore, in all proposed equations, mean values for the model parameters should be used in the newly proposed model when model uncertainties are not concerned.

(1) The maximum bonding stress, i.e., t_1

As shown in Table 3-1, the existing models for t_1 mainly depend on the steel bar diameter d_b (mm), concrete strength f_c (MPa), and the ratio of the space between bar lugs to the lug height S. This is because t_1 correlates with these influencing variables, and thus a group of candidate model forms considering these variables is examined using Bayesian Linear Regression, with 93 observations from the experimental data. It is worth mentioning that the candidate model forms include a wide variety of linear and nonlinear relationships between these parameters and the bonding property, taking into account all physical parameters used in the existing models with reference to existing model forms used by others; however, considering additional parameters results in high coefficients of variation for the corresponding model parameter, indicating that the physical parameter has a minor impact on the bonding property, and thus it is required to be removed. This serves a model selection process, which was common for other similar empirical equation or parametric regression model development. The final model form selected for t_1 (MPa) is presented in Eq. (3-2):

$$t_1 = \sqrt{f_c}\left(d_b^{\theta_1} \exp(\theta_2 S + \theta_3 + \varepsilon)\right) \tag{3-2}$$

where θ_1, θ_2, and θ_3 are model parameters and ε is the model error assumed as Gaussian with zero mean and standard deviation σ as a hyper-parameter. Note that the power of f_c was treated as an unknown parameter in the candidate model forms; however, the regression results revealed that using the square root of f_c, which has been utilized in the existing models [107,123,124], maintains the accuracy. As a result, the proposed model form employs the square root of f_c as a deterministic parameter to reduce the complexity in the proposed model. Table 3-3 provides the first- and second-moment statistics of these parameters (i.e., mean, coefficient of variation (CoV), and correlation coefficients). In accordance with Bayesian statistics, assuming the non-informative priors (i.e., locally uniform priors), the posterior distributions of model parameters (i.e., θ's) and the hyper-parameter σ would be the multivariate t-distribution and the inverse chi-squared distribution, respectively [130].

Table 3-3: Source of experimental data for bonding properties

			Correlation coefficients		
Parameter	Mean	CoV	θ_1	θ_2	θ_3
θ_1	−0.270	0.162	1.000	0.101	−0.940
θ_2	0.017	0.306	0.101	1.000	−0.398
θ_3	1.845	0.083	−0.940	−0.398	1.000
σ	0.228	0.076	–	–	–

(2) The residual frictional bonding stress, i.e., t_3

According to the models for t_3 as presented in Table 3-1, as well as the experimental data as shown in Figure 3-9 (a), there exists a linear correlation between t_3 and t_1. In view of this observation, a linear regression model shown in Eq. (3-3) is developed, with the model parameter θ_1 estimated to have a mean of 0.338 and a CoV of 0.267. The standard deviation of model error ε is estimated to have a mean and a CoV equal to 0.761 and 0.136, respectively.

$$t_3 = \theta_1 t_1 + \varepsilon \tag{3-3}$$

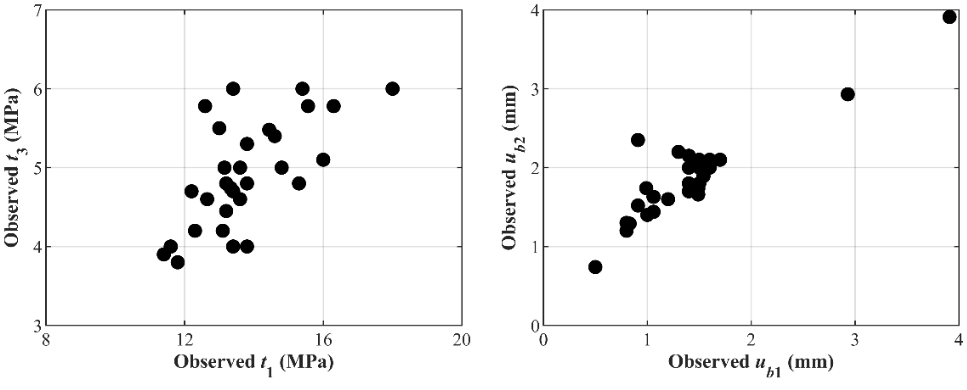

(a)

(b)

Figure 3-9: Linear relationship between experimental data of (a) t_3 and t_1, and (b) u_{b2} and u_{b1}

(3) The slip corresponding to maximum bonding stress, i.e., u_{b1}

The existing models presented for u_{b1} in Table 3-1 imply its relationship with the square root of f_c and linear dependency on d_b. Thus, a group of candidate model forms as a function of these terms with other variables, i.e., S and c, examined to find the best candidate. The model selected to describe u_{b1} is shown in Eq. (3-4), with the statistics of model parameters summarized in Table 3-4.

$$u_{b1} = \theta_1 + \theta_2 d_b + \frac{\theta_3}{\sqrt{f_c}} + \theta_4 \frac{c}{d_b} + \theta_5 S + \varepsilon \tag{3-4}$$

Table 3-4: Regression parameters for u_{b1} model

			Correlation coefficients				
Parameter	Mean	CoV	θ_1	θ_2	θ_3	θ_4	θ_5
θ_1	−2.565	0.121	1.000	−0.050	−0.767	−0.520	−0.389
θ_2	0.045	0.122	−0.050	1.000	−0.441	−0.625	0.284
θ_3	8.280	0.164	−0.767	−0.441	1.000	0.641	−0.120
θ_4	0.144	0.165	−0.520	−0.625	0.641	1.000	−0.078
θ_5	0.113	0.126	−0.389	0.284	−0.120	−0.078	1.000
σ	0.382	0.094	–	–	–	–	–

(4) The slip at the end of plateau, i.e., u_{b2}

Similar to the relationship between t_1 and t_3, the available models in Table 3-1 and experimental data for u_{b2} as shown in Figure 3-9 (b) imply that u_{b2} is constant or linearly related to u_{b1}. Therefore, a linear regression model for u_{b2} shown in Eq. (3-5) is developed with the model parameter θ_1 estimated to have a mean of 1.230 and a CoV of 0.310. The mean and CoV of the standard deviation of model error ε is estimated to be 0.366 and 0.121, respectively.

$$u_{b2} = \theta_1 u_{b1} + \varepsilon \tag{3-5}$$

(5) The slip corresponding to residual frictional bonding stress, i.e., u_{b3}

As shown in Table 3-1, this parameter can be related to u_{b1} and the spacing between bar lugs l_s (mm). Thus, different models considering l_s and the influencing variables of u_{b1} (e.g., f_c, c) are examined, and the model shown in Eq. (3-6) presents the model form proposed in this study for u_{b3}. The statistics of the model parameters are summarized in Table 3-5.

$$u_{b3} = \theta_1 + \frac{\theta_2}{\sqrt{f_c}} + \theta_3 c + \theta_4 l_s + \varepsilon \tag{3-6}$$

Table 3-5: Regression parameters for u_{b3} model

			Correlation coefficients			
Parameter	Mean	CoV	θ_1	θ_2	θ_3	θ_4
θ_1	−10.283	0.119	1.000	−0.791	−0.429	0.034
θ_2	62.583	0.108	−0.791	1.000	0.704	−0.594
θ_3	0.017	0.169	−0.429	0.704	1.000	−0.782
θ_4	0.702	0.094	0.034	−0.594	−0.782	1.000
σ	1.742	0.099	–	–	–	–

To show the performance of the newly proposed models for predicting bonding properties, Figure 3-10 presents the model predictions against all experimental observations for t_1, t_3, u_{b1}, u_{b2}, and u_{b3}, in which the model was developed based on the database compiled in this study (as reported in Appendix C).

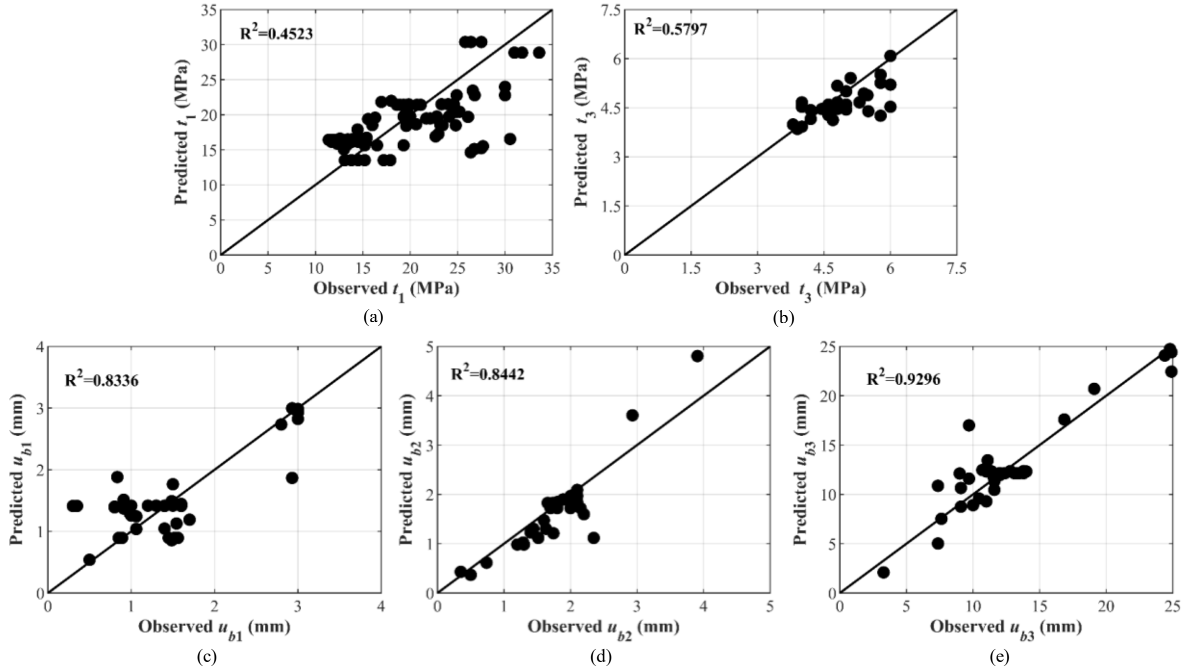

Figure 3-10: Observations vs. predictions via the newly proposed models for (a) t_1, (b) t_3, (c) u_{b1}, (d) u_{b2}, and (e) u_{b3}

Note that due to the limited number of data points, the entire database is employed to calibrate the model, similar to the development of existing models (e.g., [84,107]). Further validation of the developed model is presented through FE modeling of three experimental RC columns in the next sections. Compared to the observations vs. predictions shown in Figure 3-4 to Figure 3-8 for the existing models, Figure 3-10 reveals that the newly proposed model is more accurate and inclusive than the existing ones. The accuracy is also shown in Figure 3-11 by the test-to-prediction ratios for bonding properties. Despite the improvement of the new models of t_1 and t_3 compared to the existing models in the literature, the R-squared values are still low, implying the large scatter inherent uncertainty, whose effect will be examined later in this study. In contrast, models of u_{b1}, u_{b2}, and u_{b3} show good agreement between the predictions and observations with the R-squared values close to 1, which indicates the models are capable of properly predicting these bonding properties. Although not shown here for brevity, diagnostic tests were conducted for the generated models to evaluate normality and homoscedasticity of model residuals. In particular, the normality plots for each model show that model prediction residuals follow a Gaussian distribution, and the residuals plots indicate no sign of heteroscedasticity.

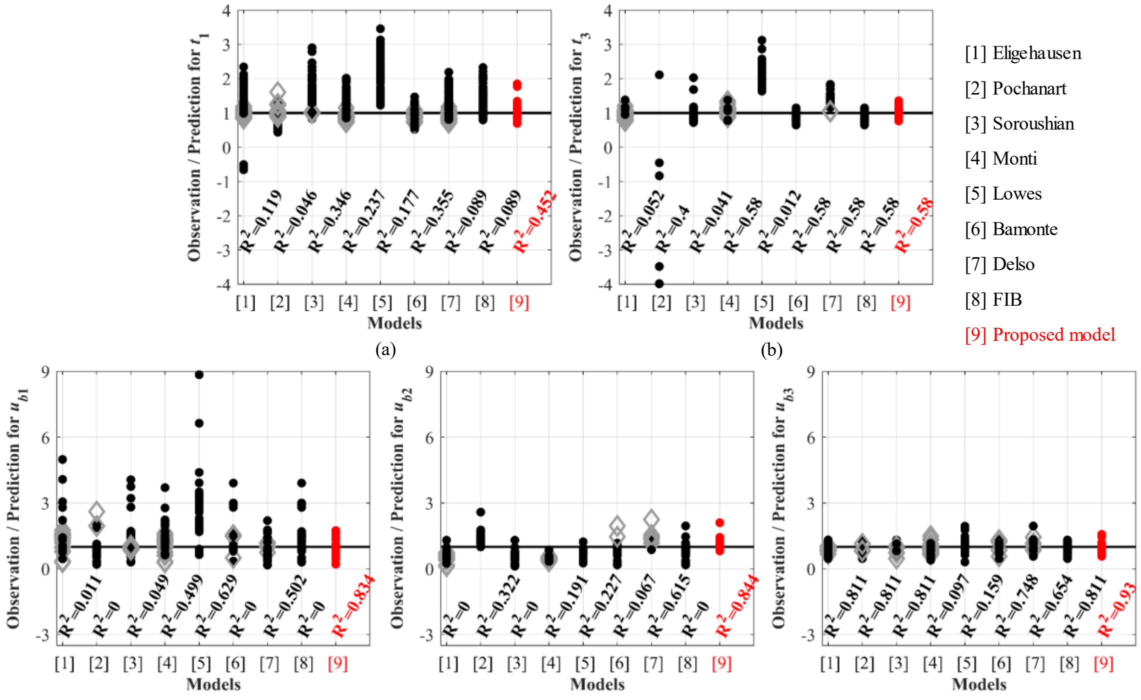

(a) (b)

(c) (d) (e)

Figure 3-11: Comparison of the test-to-prediction ratios using the newly proposed and eight existing models for bonding properties: (a) t_1, (b) t_3, (c) u_{b1}, (d) u_{b2}, and (e) u_{b3}

3.3. PROBABILISTIC BONDING PROPERTIES FOR STEEL BARS IN RC COLUMNS

This section examines the uncertainties of predicted bonding properties using the newly developed probabilistic models through their application to three experimental full-scale RC columns tested in the literature. The columns considered include: (1) Bousias column with a rectangular cross-section, which is specimen S0 in [94]; (2) Saatcioglu column with a rectangular cross-section, which is specimen BG-8 in [96]; and (3) UCSD column with a circular cross-section, which is a bridge pier column tested on the shake table in [79]. The first two columns with a constant axial load applied on the top were subjected to static cyclic lateral loading until flexural failure. In Bousias column, the longitudinal steel bars had hooked ends at the bottom in the anchorage zone. However, the longitudinal steel bars straightened to the bottom of the footing in Saatcioglu column and UCSD column were unhooked in the bar ends in the anchorage zone, as indicated in Figure 3-12 with the specified development length. The geometrical properties of these three columns are shown in Figure 3-12, and relevant variables as required to determine bonding properties are summarized in Table 3-6.

Table 3-6: Variables used to determine the bonding properties for steel bars in three RC columns considered

Input parameters	**Bousias column**	**Saatcioglu column**	**UCSD column**
Bar diameter (d_b)	16.00 mm	19.50 mm	35.81 mm
Peak concrete compressive strength (f_c)	30.75 MPa	34.00 MPa	40.30 MPa
Clear spacing between steel bars (c)	5.88d_b	2.97d_b	4.45d_b
Lug spacing (l_s)	0.50d_b	0.50d_b	0.50d_b
Lug height (l_h)	10.00d_b	10.00d_b	10.00d_b

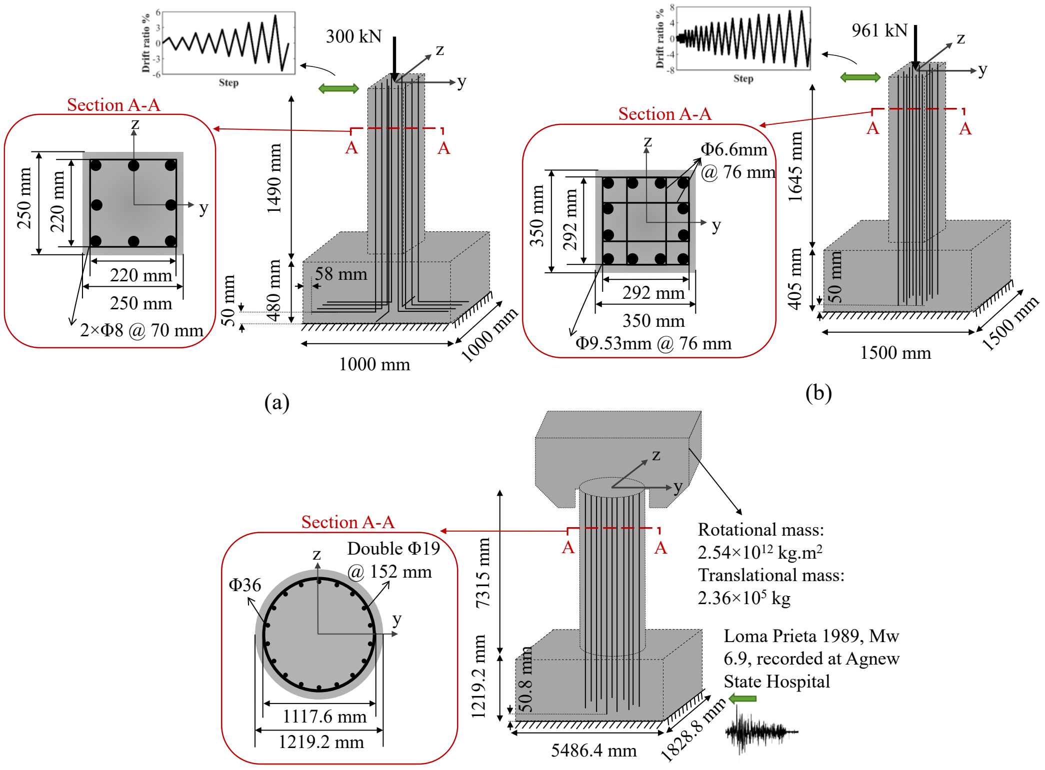

(a)

(b)

(c)

Figure 3-12: Schematic view of geometry and loads for (a) Bousias column, (b) Saatcioglu column, and (c) UCSD column

Figure 3-13 (a) to (e) presents the probability distribution functions (PDFs), as well as the mean, mean ± standard deviation, and mean ± 2×standard deviations, of t_1, t_3, u_{b1}, u_{b2}, and u_{b3} for steel bars in Bousias column, respectively. In addition, the bonding properties determined based on eight existing models are displayed to show the variety of bonding property predictions. Similarly, the probabilistic bonding properties for steel bars in Saatcioglu and UCSD columns are presented in Figure 3-14 and Figure 3-15, respectively. As indicated, the predictions of eight existing models are highly scattered; some of the predicted values lie outside the interval of mean ± 2×standard deviations. In addition, the predictions of existing models for some of the bonding properties (e.g., u_{b3}) are constant, while variations (being not constant) were observed in the experimental database collected in this study, as shown in Figure 3-8 for u_{b3}. These observations reveal that large uncertainty is inherent in the bonding properties. Therefore, it is essential to study the effect of the uncertainties in bonding properties as quantified in this study, as well as variations from different models, on the structural behavior simulation of RC columns.

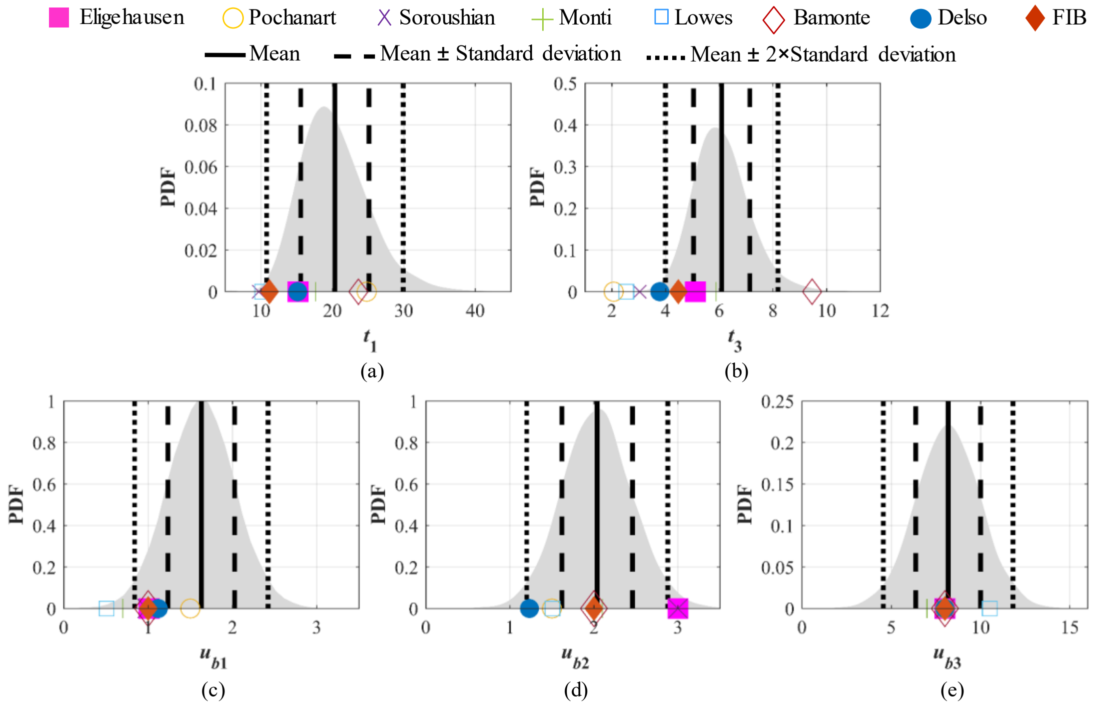

Figure 3-13: Uncertainties in predictions for bonding properties (a) t_1, (b) t_3, (c) u_{b1}, (d) u_{b2}, and (e) u_{b3} of steel bars in Bousias column

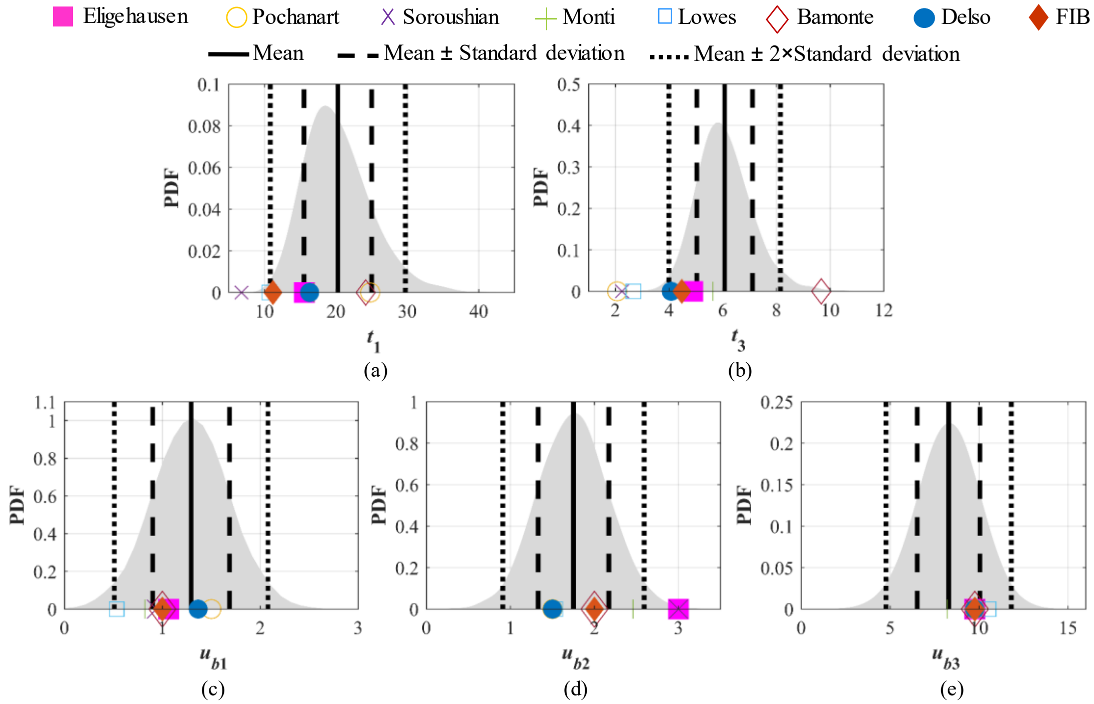

Figure 3-14: Uncertainties in predictions for bonding properties (a) t_1, (b) t_3, (c) u_{b1}, (d) u_{b2}, and (e) u_{b3} of steel bars in Saatcioglu column

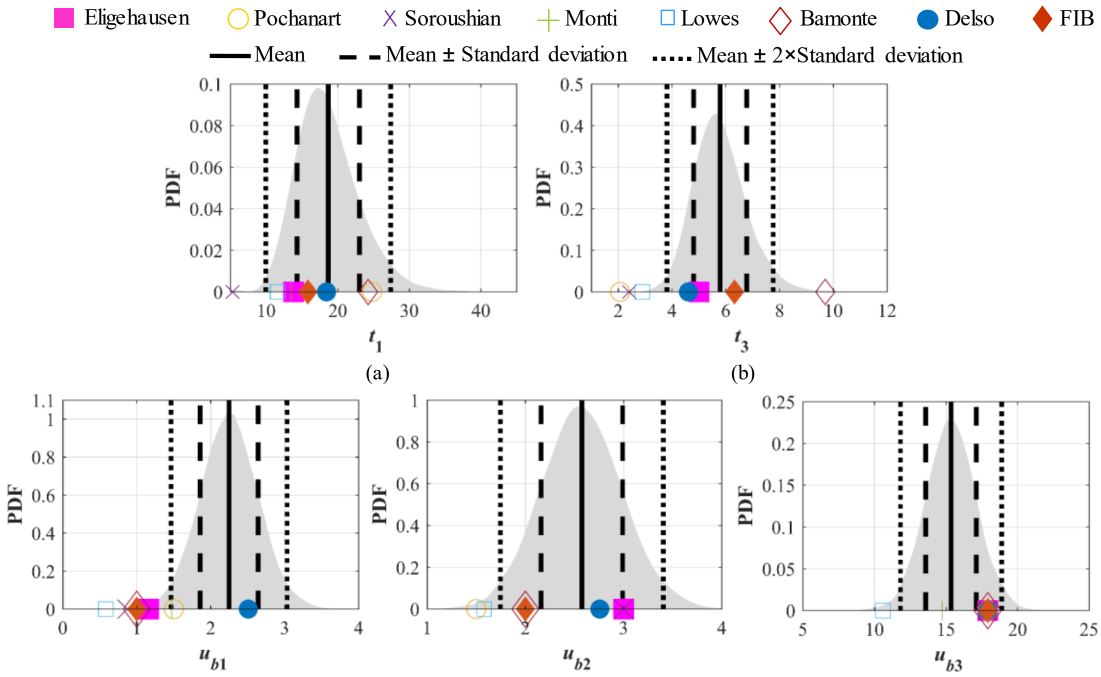

(a) (b) (c) (d) (e)

Figure 3-15: Uncertainties in predictions for bonding properties (a) t_1, (b) t_3, (c) u_{b1}, (d) u_{b2}, and (e) u_{b3} of steel bars in UCSD column

3.4. EFFECT OF BONDING UNCERTAINTIES ON RC COLUMN SIMULATION

This section examines the effect of variations or uncertainties in bonding properties on the nonlinear behavior simulation of RC columns subjected to static and dynamic loadings. The three RC columns considered in the previous section are used here.

3.4.1. FE modeling of RC columns

This section describes the FE models of the three RC columns, i.e., Bousias column, Saatcioglu column, and UCSD column. These three columns are so selected to cover different anchorage scenarios and loading types. Figure 3-16 (a) to (c) show the schematic view of the FE models for these columns.

To consider imperfect bonding in the FE model, the geometrically nonlinear fiber-based frame element with bond-slip implemented in *OpenSees* is employed here [116]. This element defines slip as the difference between the deformations of the steel bar and surrounding concrete in the axial direction, and thus it only explicitly models the bonding between the steel bar and concrete in the axial direction while the rib-concrete interactions in radial and orthoradial directions are not modeled. However, such effects on the axial bond-slip behavior are implicitly taken into account in the bond-slip material model developed based on the experimental data for deformed bars. Note that the bond-slip behavior for plain bars embedded in the concrete differs significantly from that of deformed bars [131,132].

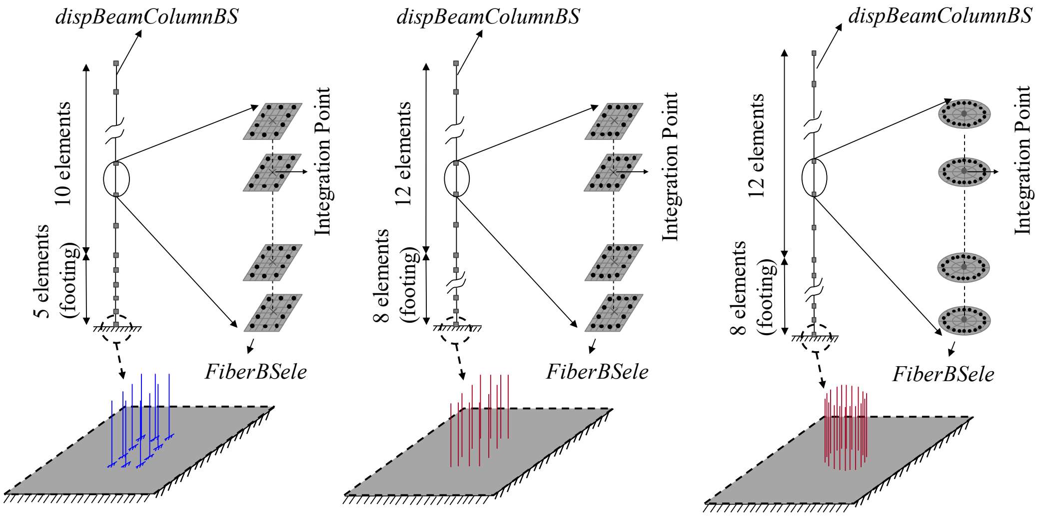

(a) (b) (c)

Figure 3-16: Schematic view of the FE models of (a) Bousias column, (b) Saatcioglu column, and (c) UCSD column

In the fiber section, steel fibers are represented by the Giuffre-Menegotto-Pinto steel model, as schematically shown in Figure 3-17 (a). This material model has been widely used and well developed to model the cyclic behavior of reinforcing steel by incorporating the effect of plastic deformations on the Bauschinger effect [133]. The yield stress f_y, strain hardening ratio b, and Young's modulus E_s are used to define this material model. The concrete fibers are assigned with the Kent-Scott-Park concrete model presented in Figure 3-17 (b), characterized by concrete compressive strength f_c and its corresponding strain ε_c, ultimate compressive strength f_{cu}, and its corresponding strain ε_{cu}. This material model has been also extensively used to represent the cyclic behavior of concrete by employing linear paths for unloading and reloading stiffness [106]. The steel and unconfined concrete properties are taken from the experimental data reported in the literature; however, the properties for the core concrete considering confinement effect are determined using Mander's equations [45]. The properties of the key model parameters are summarized in Table 3-7. In addition, the bond-slip is represented by the newly implemented model (i.e., *BondSlip04 in OpenSees*) as schematically shown in Figure 3-17 (c). The bonding properties can be determined using different models, including the eight existing ones and the newly developed model using the relevant variables summarized in Table 3-6. The bonding properties determined using the newly developed model in this study are also reported in Table 3-7. These FE models, together with bonding properties, are validated using experimental data as presented in Figure 3-18 [116]. Specifically, Figure 3-18 (a) and Figure 3-18 (b) demonstrate the comparisons of lateral load-drift ratio hysteresis for Bousias column and Saatcioglu column, respectively, indicating an outstanding correlation between experimental observations and FE predictions for the model considering imperfect bonding. In addition, the time-history of drift ratio for UCSD column is compared between experimental results and FE predictions in Figure 3-18 (c) for perfect and imperfect bonding cases, reaffirming the improvement in FE predictions due to the imperfect bonding consideration.

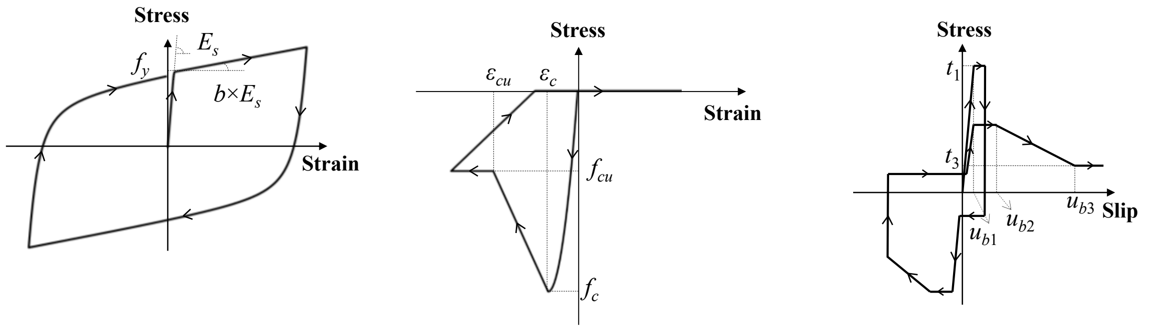

(a) (b) (c)

Figure 3-17: Schematic view of material models for (a) steel fibers, (b) concrete fibers, and (c) bond-slip

Table 3-7: Overview of the material properties of the three RC columns considered

Test			**Bousias**	**Saatcioglu**	**UCSD**
Material		**Properties**			
Steel		f_y (MPa)	460.0	455.0	518.5
		b (−)	0.015	0.025	0.011
		E_s (MPa)	210000	210000	200000
Concrete	Unconfined	f_c (MPa)	−30.75	−34.00	−40.30
		f_{cu} (MPa)	−12.30	−6.80	−8.00
		ε_c (−)	−0.0035	−0.0030	−0.0026
		ε_{cu} (−)	−0.0100	−0.0080	−0.0150
	Confined	f_c (MPa)	−38.44	−47.60	−49.60
		f_{cu} (MPa)	−15.37	−39.68	−8.00
		ε_c (−)	−0.0044	−0.0090	−0.0105
		ε_{cu} (−)	−0.1000	−0.0720	−0.0150
Bond-Slip		t_1 (MPa)	19.79	19.73	18.16
		t_3 (MPa)	5.99	5.98	5.70
		u_{b1} (mm)	1.63	1.30	3.01
		u_{b2} (mm)	2.03	1.74	3.22
		u_{b3} (mm)	8.16	8.26	17.78

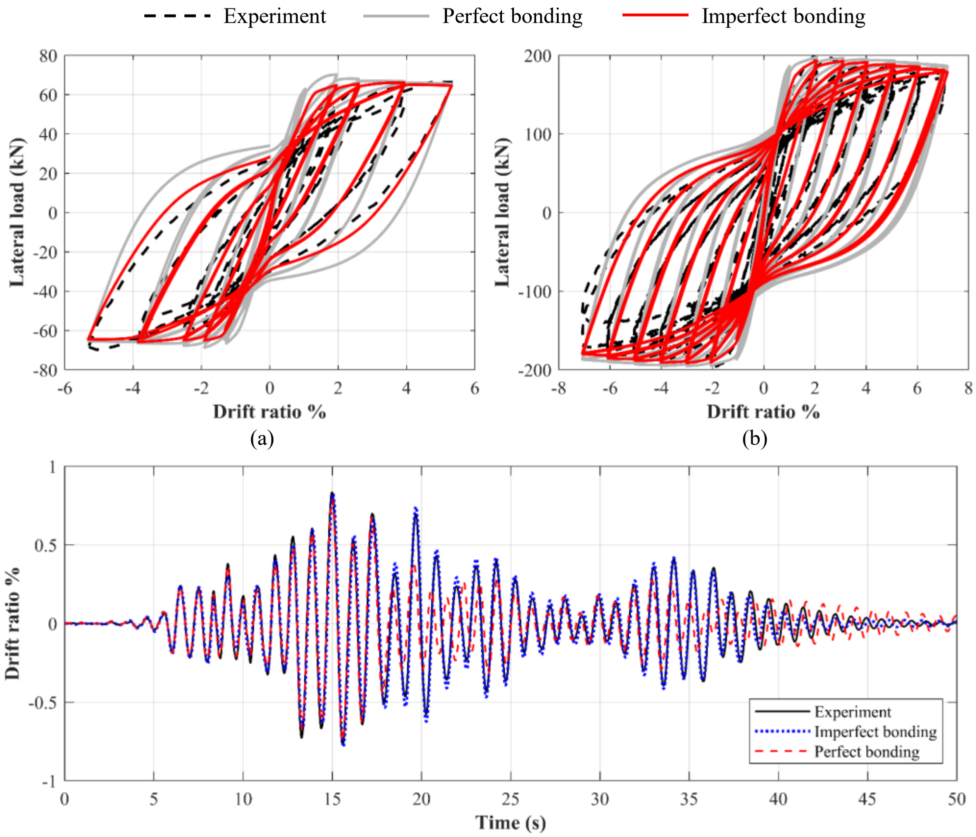

(a) (b)

(c)

Figure 3-18: Comparison of lateral load-drift ratio hysteresis between FE predictions and experimental results for (a) Bousias column and (b) Saatcioglu column, and (c) comparison of drift ratio time-history of UCSD column between experiment and FE prediction with perfect and imperfect bonding

Figure 3-19 shows the variation in the monotonic bond-slip behaviors due to different bonding properties predicted from different models for steel bars in the three RC columns. Significant variations in these bond-slip behaviors raise the need to investigate the effect of such variations on the nonlinear behavior simulations.

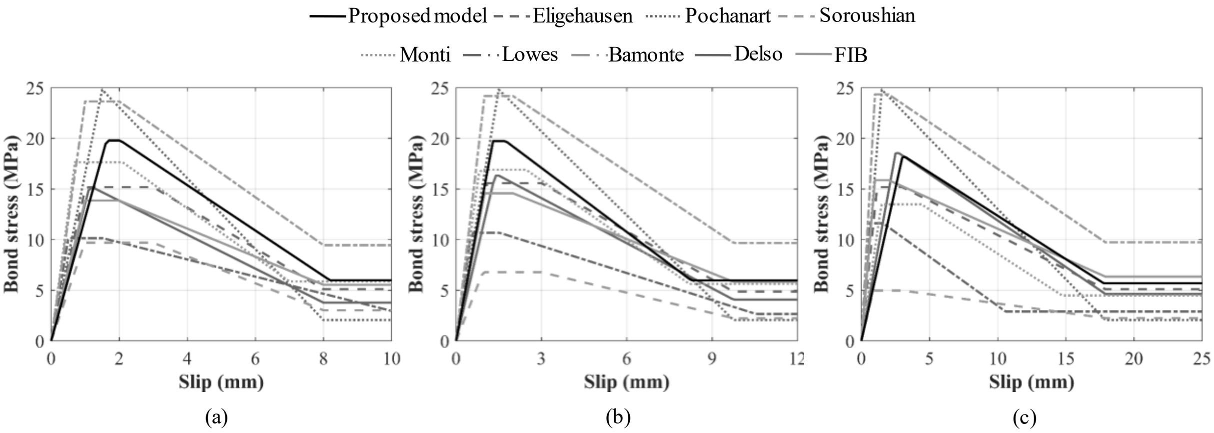

Figure 3-19: Monotonic bond-slip behavior using bonding properties predicted from the nine different models for steel bars in (a) Bousias column, (b) Saatcioglu column, and (c) UCSD column

3.4.2. Effect of variations of bonding properties on static behavior simulation

To investigate the effect of variations in bonding property prediction models on the static behavior simulation of RC columns, two representative RC columns with different anchorage scenarios are used: Bousias column with hooked steel bars and UCSD column with unhooked steel bars. It is worth noting that the anchorage scenario (i.e., hooked or unhooked bar ends) has a significant impact on the role of bond-slip in RC columns, as indicated in the literature [116]; however, it is unclear how variations in bonding properties affect the nonlinear behavior simulation of RC columns with these anchorage scenarios. In this regard, static pushover analyses following the same loading protocol are conducted using the FE models of RC columns considering different bonding properties predicted from nine different models. Figure 3-20 (a) and (b) show the lateral load-drift ratio hystereses of Bousias column and UCSD column, respectively, compared to the counterpart assuming perfect bonding and no bonding (i.e., pure concrete).

Figure 3-20 (a) reveals the difference between FE-simulated lateral load-drift ratio hystereses using these bonding property prediction models is negligible, despite significantly different bond-slip behaviors for Bousias column, as shown in Figure 3-19 (a). This observation indicates that the variations of bonding properties negligibly affect the static behavior simulation of this column, while the incorporation of bond-slip is imperative for more accurate simulation compared to the perfect bonding case, especially when hysteretic energy dissipation is concerned. In contrast, using different bonding properties for UCSD column leads to considerably different FE-predictions for the lateral load-drift ratio hystereses, as presented in Figure 3-20 (b). In particular, the simulation using the FE model with weak bonding properties, as predicted by Soroushian's model [123], behaves very closely to that of a purely concrete column. Therefore, variation in bonding properties from different bonding property prediction models can make a remarkable difference in simulating the nonlinear behavior of an RC column (e.g., UCSD column) with unhooked steel bars, which is different from Bousias column. This implies that the RC columns with straight steel bars are more sensitive to the variations of bonding properties than the RC columns with hooked steel bars. Note that the steel bar is assumed to be fully embedded in the adjoining concrete member in the hooked condition so that no slip occurs where it bends.

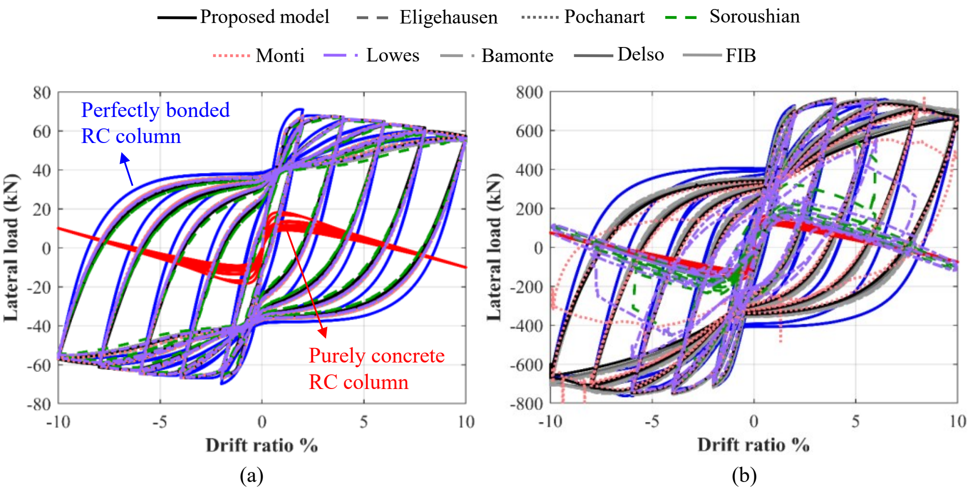

Figure 3-20: Effect of various bonding property prediction models on the nonlinear behavior simulation of RC columns: FE-predicted lateral load-drift ratio hysteresis for (a) Bousias column, and (b) UCSD column

An important factor affecting the role of bond-slip in RC columns with straight (i.e., unhooked) steel bars is the anchorage length. As such, RC columns with straight steel bars of insufficient anchorage length, such as a sub-standard designed RC column in a seismic area, are more susceptible to bond-slip. Therefore, it is required to explore the effect of variations of bonding properties on the nonlinear behavior simulations of RC columns with straight steel bars of different anchorage lengths.

For this purpose, the statically tested and validated Saatcioglu column with straight steel bars is used here by varying the anchorage length $L_a = 21d_b$ to $15d_b$ and $25d_b$, where d_b is the steel bar diameter. In addition, one case with the anchorage length $L_a = 21d_b$ but steel bars hooked is also considered for reference. For each of these four cases, static pushover analyses are conducted using FE models considering the eight existing and the newly proposed bonding property prediction models. The corresponding lateral load-drift ratio hystereses are presented in Figure 3-21 (a) to (d) for cases considering steel bars hooked, steel bars unhooked with $L_a = 25d_b$, $21d_b$, and $15d_b$, respectively. In addition, the simulated hystereses using the FE models with perfect bonding and no bonding (i.e., pure concrete) are also shown as two extreme cases.

Specifically, Figure 3-21 (a) reaffirms the effect of variations of bonding properties on the nonlinear behavior simulations of RC columns with steel bars hooked is negligible. In contrast, the nonlinear behavior simulation of RC columns with straight steel bars is significantly affected by such variations, especially when the anchorage length is insufficient. Comparing Figure 3-21 (a) to (d) reveals that in RC columns with straight steel bars, the variations of bonding properties can alter the nonlinear behavior simulation of sub-standard designed RC columns more considerably than RC columns with sufficient anchorage lengths (defined in accordance with design codes). In particular, the behavior simulations for RC columns with $L_a = 25d_b$ are negligibly affected by bonding property prediction models except for the model with extremely weak bonding prediction (e.g., Soroushian's model [123]). However, the behavior simulations of RC columns with $L_a = 21d_b$ and $15d_b$ begin to vary at higher loading levels, e.g., at a drift ratio of 6% and 5%, respectively. For higher loading levels, the effect of insufficient anchorage length gets dominant, making the behavior simulation of RC columns more sensitive to the bonding properties. For cases with insufficient anchorage length, the behavior simulation of the RC column can be significantly different when using different bonding property prediction models. For example, under-prediction of bonding properties (e.g., using Soroushian's model) can lead to significant underestimation of the behavior simulated, which is close to the purely concrete case. These observations indicate the remarkable effect of bonding property prediction models on the static behavior simulation of RC columns with straight longitudinal steel bars, especially for sub-standard designed columns with insufficient anchorage length. This further justifies the need to develop a reliable model using all the bond-slip data compiled in this study.

To further investigate the effect of variations of bonding properties on the static behavior simulations of RC columns, local sensitivity analyses are conducted here to examine the importance of uncertainty in bonding properties using Bousias column and UCSD column. In this regard, the local sensitivity analysis is selected to explore the impact of uncertainty in each parameter independently. It is worth noting that local sensitivity analysis reveals the importance to each parameter individually considering its uncertainty. To understand how the uncertainty is contributed by the uncertainty in each parameter as well as their interactions, variance-based global sensitivity analysis should be conducted, but outside the scope of this study.

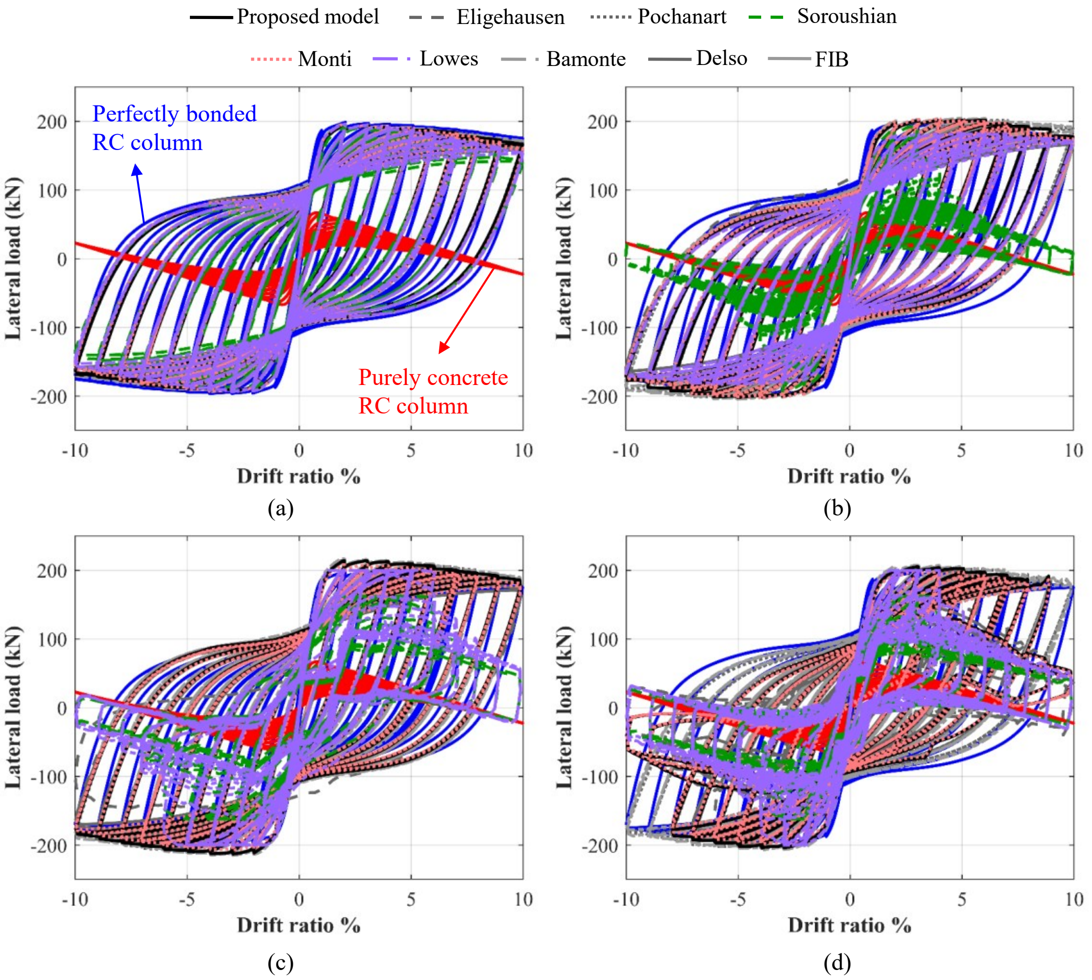

Figure 3-21: FE-predicted lateral load-drift ratio hystereses for Saatcioglu column using various bond-slip models considering (a) hooked steel bars with $L_a = 21d_b$, and straight steel bars with (b) $L_a = 25d_b$, (c) $L_a = 21d_b$, and (d) $L_a = 15d_b$

To provide a reference for the effects of uncertainty in bonding properties (i.e., t_1, t_3, u_{b1}, u_{b2}, and u_{b3}), the effects of uncertainty in other concrete and steel properties, such as elastic modulus of steel E_s, yield stress of steel f_y, and core concrete strength f_{cc}, are also considered. Note that the probability distributions of the bonding properties obtained in the previous section are used, while these three reference variables are considered to be normally distributed with the mean values shown in Table 3-7 and CoVs of 0.033, 0.093, and 0.175 for E_s, f_y, and f_{cc}, respectively [134]. In this regard, Latin Hypercube Sampling [135] is performed with 1000 samples for each of the eight random variables considered. Accordingly, a set of 1000 FE simulations are conducted with generated samples for the corresponding random variable and mean values for other parameters for each of these two RC columns considered subjected to the same cyclic static loading as earlier. Note that an FE model with these eight random variables set to their mean values is defined as the reference model. Using the FE-predicted lateral load-drift ratio hystereses, the sensitivity index for one sample is defined as the relative change in the total dissipated energy with respect to the reference model. Therefore, a set of 1000 sensitivity index values is established for each random variable, which shows the sensitivity of dissipated energy to the corresponding parameter. Figure 3-22 (a) and (b) present the mean and mean ± standard deviation of sensitivity indexes corresponding to the random variables considered here for Bousias column and UCSD column, respectively.

According to the mean values of sensitivity indexes in Figure 3-22 (a), the effect of variations of bonding properties is shown to be less significant in Bousias column in comparison with the reference parameters (i.e., f_y,). Specifically, t_1 and u_{b1} have the most effective variations among bonding properties due to their dominancy in the initial stiffness and yield point of bond-slip behavior. On the contrary, Figure 3-22 (b) indicates the uncertainty of t_1 can lead to a notable difference in the nonlinear behavior prediction of UCSD column compared to the reference parameters. To understand the underlying reason, the difference between the role of bond-slip in these two columns needs to be examined.

In Bousias column, the longitudinal steel bars have hooked ends, while UCSD column has straight (unhooked) longitudinal steel bars in the anchorage zone. Therefore, the anchorage scenario is the main difference between these two RC columns affecting the role of bond-slip. Observing higher sensitivity to the bonding properties in UCSD column with unhooked steel bars indicates this anchorage scenario (i.e., unhooked steel bars) leads to more sensitivity of the RC column behavior simulation to the variations of bonding properties. The literature has shown that the RC column with straight steel bars sufficiently developed in the anchorage zone would have the same performance as the RC column with hooked-end steel bars [116]. However, the variations of bonding properties can significantly affect the nonlinear behavior prediction of RC columns with unhooked steel bars.

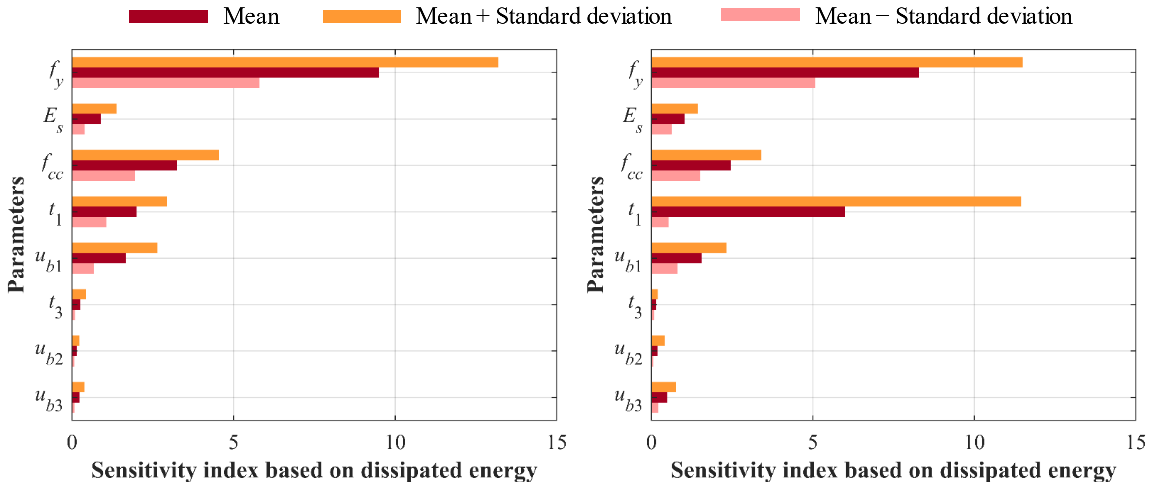

(a) (b)

Figure 3-22: Sensitivity of static behavior simulations of RC columns to the bonding, steel, and concrete properties: (a) Bousias column, and (b) UCSD column

3.4.3. Effect of variations of bonding properties on dynamic behavior simulation

Dynamic loading with a large number of unloading-reloading cycles can significantly affect the role of bond-slip in the behavior of RC columns [116]. This stems from bonding degradation due to cyclic loading, resulting in more hysteretic dissipated energy. Thus, it is vital to investigate how the variations in bonding property prediction models affect the dynamic behavior simulation of RC columns with different anchorage scenarios.

To this end, the FE models of Bousias column and UCSD column with hooked and unhooked steel bars in the anchorage zone, respectively, are used considering bonding properties predicted from eight existing models and the one newly developed. The seismic responses of these FE models subjected to the Loma Prieta earthquake recorded at Agnew State Hospital station [70] are simulated. For each RC column, the ground motion input is so scaled to reach the ductility demand (i.e., lateral drift ratio demand with respect to the yield drift ratio) of 2.0 for the FE model assuming perfect bonding. The FE-predicted drift ratio time-histories are presented in Figure 3-23 (a) and (b) for Bousias column and UCSD column, respectively, with markers identifying the peak response corresponding to each model. The comparison between these responses indicates the variations of bonding properties do not significantly affect the peak response of FE models when "sufficient" anchorage exists. This observation is in correlation with the insignificant effect of bond-slip on the peak response of RC columns as indicated in [116].

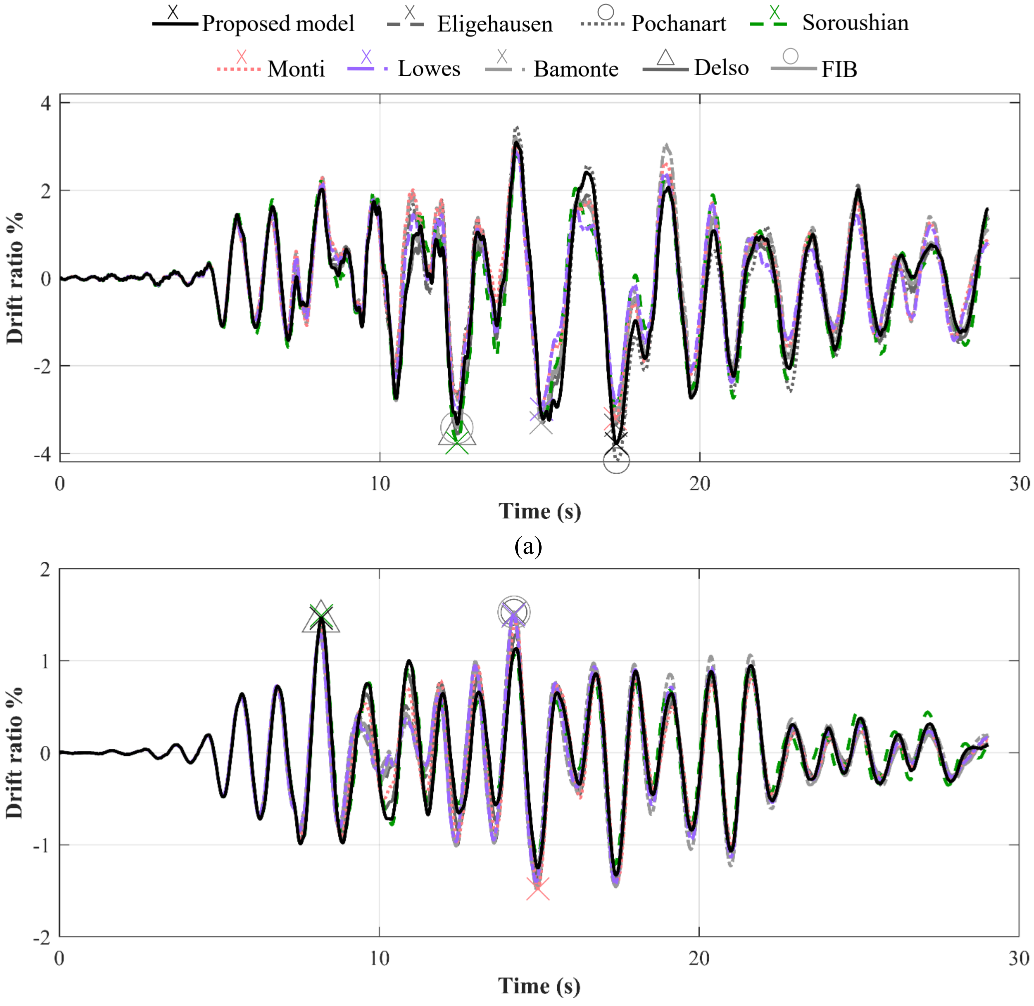

(a)

(b)

Figure 3-23: FE-predictions for drift ratio time-histories of (a) Bousias column, and (b) UCSD column

To further study the effect of variations of bonding properties on the RC column behavior simulations, a similar sensitivity analysis presented in the previous section is conducted here for RC columns subjected to dynamic loading. To this end, the Loma Prieta earthquake recorded at Agnew State Hospital station [70] is considered with two intensity levels. For Bousias column and UCSD column, this ground motion is so scaled that the corresponding FE model assuming perfect bonding reaches the ductility demand of 1.0, as "intensity level of 1", and 2.0, as "intensity level of 2". Defining the sensitivity index based on the peak response (i.e., the relative change of peak drift ratio with respect to the reference model), Figure 3-24 (a) and (b) present the mean and mean ± standard deviation of the sensitivity index established corresponding to each parameter for Bousias column and UCSD column subjected to earthquakes with the intensity level of 2. The results indicate the variations of bonding properties do not notably affect the peak response predictions for both RC columns compared to steel/concrete related properties, which reaffirms the observation shown in Figure 3-23.

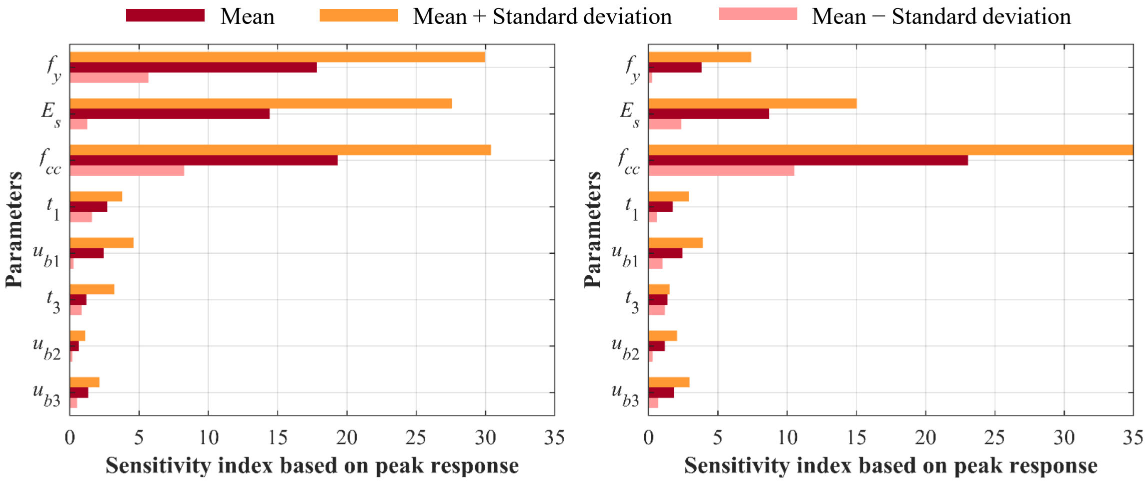

(a)

(b)

Figure 3-24: Sensitivity analysis based on peak drift ratio for (a) Bousias column, and (b) UCSD column under seismic loading with intensity level 2

Due to the significant effect of bond-slip on energy dissipation, as observed in the literature [116], the effect of bonding uncertainties on the dynamic behavior simulation of RC columns is investigated through defining a sensitivity index based on the dissipated energy (i.e., the relative change of dissipated energy with respect to the reference model). Figure 3-25 presents the mean and mean ± standard deviation of sensitivity index established corresponding to each parameter for Bousias column and UCSD column subjected to earthquakes with the two intensity levels considered.

Comparing Figure 3-25 (a) with Figure 3-25 (b), and Figure 3-25 (c) with Figure 3-25 (d), indicate that for both RC columns under seismic loading with a higher intensity level, the bonding properties related to the nonlinear behavior become more dominant due to bond-slip yielding and strength/stiffness degradation. In particular, the variations of t_1 and u_{b1} are the most important ones among bonding properties for intensity level 1 as these two parameters control the initial stiffness and yield point of bond-slip, while the effect of u_{b3} gets more significant for the higher intensity level. This stems from the dominancy of this parameter on the bonding degradation after the bond-slip yields. Furthermore, the variations in bonding properties can remarkably alter the nonlinear behavior simulation of RC columns under dynamic loading for both RC columns with different anchorage scenarios with more effect on the RC column with unhooked steel bars. Comparing Figure 3-25 (a) with Figure 3-25 (c), and Figure 3-25 (b) with Figure 3-25 (d), reaffirms the nonlinear behavior of the RC column with unhooked steel bars is more sensitive to bonding properties than the RC column with hooked steel bars. However, comparing Figure 3-22 with Figure 3-25 reveals the sensitivities of nonlinear behavior of RC columns to bonding properties are more significant when the columns are subjected to dynamic loading. This is mainly because of the large number of unloading-reloading cycles during earthquake loading, which results in more cyclic degradation of the bond-slip than the case under static loading with only a few cycles as considered here. Hence, it is vital to consider the uncertainties of the bonding properties in the probabilistic analysis of RC columns under dynamic loading, especially under large intensity levels.

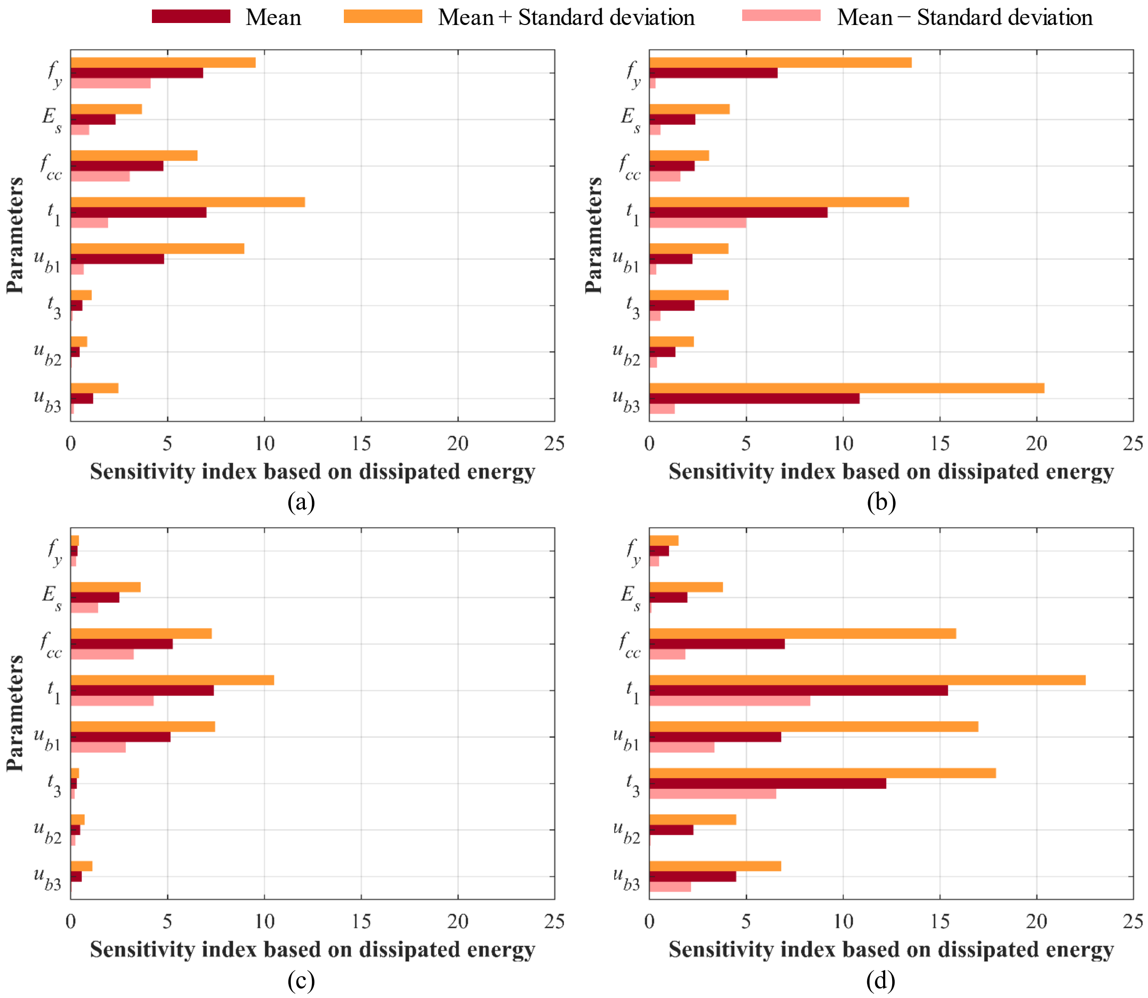

Figure 3-25: Sensitivity analysis based on dissipated energy for Bousias column under seismic loading with (a) intensity level 1 and (b) intensity level 2, and UCSD column under seismic loading with (c) intensity level 1 and (d) intensity level 2

3.5. CHAPTER CONCLUSIONS

To consider imperfect bonding between the steel bar and surrounding concrete in advanced structural modeling of reinforced concrete (RC) columns, an explicit bond-slip material model is required. However, various existing models to determine bonding properties were developed in the literature based on a limited dataset, and their predictions can be significantly different. The scattered bonding properties predicted based on the existing models highlighted the need to investigate the impact of variations in bonding properties on the nonlinear behavior simulations of RC columns. As such, this study compiled an experimental database for bonding properties. Using this experimental database, the authors developed a new model to better characterize the bonding properties and quantify the uncertainties at the same time. The newly developed probabilistic model for bonding properties provides mean values that are often needed for deterministic response simulations, as well as the statistics (e.g., variance) that are often needed for probabilistic response simulations. Together with the eight existing models in the literature, this study investigated the effect of bond-slip model uncertainties on the static and dynamic behavior simulations of RC columns, whereas previous studies had only explored the effect of bond-slip variation on the nonlinear behavior simulations by considering three scenarios, i.e., strong bonding condition (perfect bonding), normal bonding condition (imperfect bonding), and no bonding (purely concrete). Thus, this study shed more lights on the importance of uncertainty in bonding properties on RC column behavior simualtions when normal bonding condition (imperfect bonding) is considered.

By simulating three experimental RC columns from the literature with different anchorage scenarios (i.e., hooked and unhooked steel bars), this study highlights the following three findings. (1) The use of an inappropriate bonding property prediction model can lead to an unrealistic simulation of RC column behavior (e.g., when the anchorage for steel bars is insufficient). The model developed in this study for bonding property prediction proved to be appropriate, particularly because it was developed based on a larger database compared with existing ones. (2)

The variations/uncertainties of bonding properties significantly affect the hysteretic energy dissipation of RC columns with straight (unhooked) steel bars, particularly in the case with insufficient anchorage length. (3) The effect of variations of bonding properties are more important for simulations of RC columns subjected to earthquake loading in comparison to the importance of the uncertainties in concrete/steel properties, particularly in the case of high intensity levels. To summarize, it is essential to consider the pertinent uncertainties of the bonding properties, specifically in probabilistic dynamic analysis of RC columns under large intensity excitation levels, in which the probabilistic model for bonding properties as developed in this study can be used.

Chapter 4. CORRODED BOND-SLIP EFFECTS FOR RC COLUMNS UNDER CORROSION

4.1. INTRODUCTION

Corrosion due to carbonation attack or chloride penetration is common for aged reinforced concrete (RC) structures under aggressive environmental conditions. Corrosion in RC structures can cause a variety of deteriorations, such as reduction in cross-sectional area of steel bars and deterioration of the bonding between steel bars and the surrounding concrete. In particular, corrosion-induced bond deterioration in RC structures can change the composite action of concrete and steel, revealing that the perfect bonding assumption commonly used for pristine RC structures becomes invalid. Eventually, corrosion can severely affect the structural performance of RC structures, as evidenced in the experimental studies [136,137]. In this regard, the objective of this study is twofold: (1) to provide an efficient finite element (FE) modeling approach for corroded RC columns based on fiber-based frame elements that takes into account various aspects of corrosion; and (2) to investigate the corrosion effects on RC columns using the proposed modeling approach, with particular emphasis on corroded bond-slip. Specifically, this research mainly attempts to reveal how and to what extent the corroded bond-slip and its associated uncertainties affect the nonlinear behavior simulations of corroded RC columns. Additionally, the use of the fiber-based frame element and the probabilistic model for bonding properties is one of the novelties in this work.

Corrosion affects several structural properties such as steel bar cross-sectional area, strength, and ductility [138,139], vulnerability of steel bars to buckling [140], cover concrete spalling [43], confinement level for core concrete [141], and bonding between steel bars and surrounding concrete [47]. Several studies investigated the impact of corrosion-induced deterioration at the structural component or system level [26] by mainly considering steel bar cross-sectional area reduction, which is relatively easier to account for in the modeling process. However, these studies neglected some other aspects of corrosion, particularly corrosion-damaged bonding that is relatively challenging to consider. Presuming that the corroded reinforcing steel bars and the surrounding concrete are perfectly bonded can dramatically change the behavior prediction of RC structures, as mentioned in the literature [47]. As a result, in order to properly predict the structural behavior of corroded RC structures, it is vital to consider the effect of bond-slip in computational modeling. This is essential in the context of performance-based engineering [142], where post-peak behavior, such as ductility (the deformation capacity without significant loss of load capacity) and damage are of primary concerns.

To incorporate corrosion, particularly corroded bonding, in RC structural modeling, various approaches have been used in the literature [43,83]. However, in previous studies, corroded bonding was considered using either sophisticated or overly simplistic modeling approaches. For example, the continuum-based FE modeling approaches used in [43] are overly complicated and inefficient for frame-type structural systems in comparison to fiber-based FE modeling strategies. In contrast, the fiber-based FE modeling approach used in [83] over-simplifies the effect of corroded bond-slip by using zero-length elements that implicitly incorporate corroded bond-slip. This method limited the corroded bond-slip within the anchored region (e.g., in column footing), while corrosion in the unanchored region (e.g., column above the footing) is considerably more common and severe. As a result, a more accurate and efficient approach is needed to explicitly account for the corroded bond-slip in the RC column above the footing in addition to that inside the footing. In this regard, a geometrically nonlinear fiber-based frame element with bond-slip, which was recently developed by the authors [143] and implemented in the open-source finite element software framework, *OpenSees* [65], is employed in this study for FE modeling of corroded RC columns with corroded bond-slip.

To model corroded RC columns considering bond-slip, the effect of corrosion on the bonding at the steel-concrete interface needs to be captured. In the early stage of corrosion (i.e., minor corrosion), the corrosion products (i.e., steel rust) increase the roughness of the steel bar surface, which leads to higher bond strength due to increased friction in bond-slip. However, at greater levels of corrosion, expanding corrosion products cause radial pressure at the steel-concrete interface, which competes with the mechanical interlocking of bonding. Furthermore, steel bar corrosion greatly reduces the rib area of the steel, severely compromising the mechanical interaction at the steel-concrete interface. Both of these actions result in a substantial reduction in bond strength. Therefore, to account for such effects, a nonlinear material model for corroded bond-slip is needed, which is typically formulated using monotonic (i.e., back-bone curve) and cyclic (i.e., hysteretic rules) stress-slip patterns characterized by relevant properties (i.e., bonding stress values and corresponding slips). While the monotonic behavior of corroded bond-slip has been extensively studied in the literature (e.g., Lee et al. [144], Bhargava et al. [145], and Chung et al. [146]), only a few studies (e.g., Kivell et al. [147] and Zhou et al. [148]) investigated the effect of corrosion on the bond degradation under cyclic loading. As a result, the impact of corroded bonding on the nonlinear behavior of RC columns subjected to static cyclic or dynamic loads has rarely been explored. In addition, existing models for predicting corroded bonding properties were developed based on highly scattered and limited experimental data with no uncertainty quantifications. These gaps in the literature motivate this research to develop probabilistic models for predicting corrosion-affected bonding properties, which will be used in the proposed modeling approach for corroded RC structures and leveraged to investigate the effect of variations in corroded bonding properties on static and dynamic behavior simulations of corroded RC columns.

To this end, the remainder of this work is organized as follows. First, an FE modeling approach for corroded RC columns is provided, which considers various aspects of corrosion with particular emphasis on corroded bond-slip. In this regard, a probabilistic model is established for the corroded bonding properties based on compiled experimental data from the literature, together with the quantification of uncertainties. This new modeling approach is employed to model two experimental corroded RC columns tested in the literature using the newly implemented corroded bond-slip material model in *OpenSees* in conjunction with bonding properties determined from the proposed model. In addition, the importance of considering corrosion-affected bond-slip in FE modeling of corroded RC columns is examined and compared to the effect of corrosion-induced reduction of steel bar cross-sectional area, which is typically considered in existing studies of corroded RC structures. Before moving onto the conclusion section, this paper evaluates the effect of uncertainties in corroded bonding properties on the nonlinear behavior simulation of RC columns.

4.2. FE MODELING APPROACH FOR CORRODED RC COLUMNS

To predict the structural performance of corroded RC columns, a comprehensive approach for computational modeling of corroded RC columns is required to address different aspects of corrosion effects on structural properties (e.g., geometry and material). Corrosion, for example, can reduce the cross-sectional area, strength, and ductility of longitudinal steel bars [138,139]. As a result of the reduction of steel bar cross-sectional area, the longitudinal reinforcement would be slenderer than in the pristine condition, making the RC column more prone to steel bar buckling [140]. In addition, corrosion of lateral reinforcement would reduce the lateral confinement, resulting in lower maximum compressive strength and ultimate strain of core concrete [141]. More importantly, due to the radial pressure from the expansive corrosion products and reduced rib area of steel bar, the bonding at the concrete-steel interface is also deteriorated [47]. To capture the corrosion effects on these aspects at the structural level, this study presents an efficient FE modeling approach, schematically depicted in Figure 4-1, using the recently developed geometrically nonlinear fiber-based frame element [143] in *OpenSees*. Note that the material nonlinearity in steel, concrete, and bond-slip are considered using the material models used together with the fiber-based frame element [107,133,149]. This approach allows considering corrosion-induced cross-sectional area reduction and corrosion-affected material behavior for longitudinal steel bars, corrosion-affected material behavior for both cover and core concrete, as well as the corroded bond-slip. Below are descriptions of the modeling aspects (e.g., element, fiber section, and material or bond-slip models).

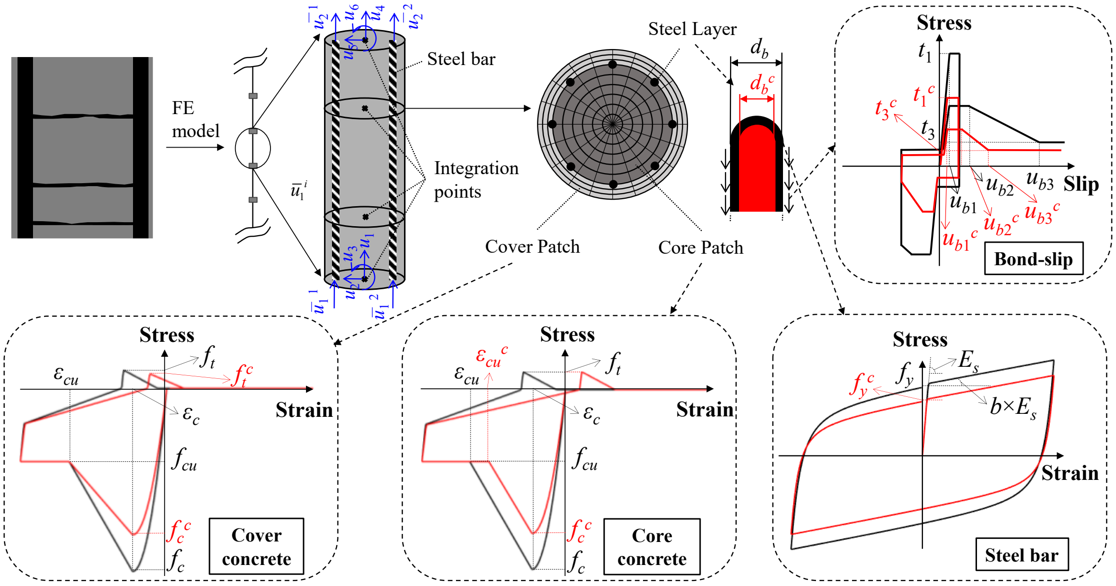

Figure 4-1: FE modeling approach for corroded RC columns (The superscript "*c*" for all symbols denotes the corresponding corroded properties.)

4.2.1. Element and section discretization

To model a corroded RC column, the recently developed geometrically nonlinear fiber-based frame element considering bond-slip [143] is used to discretize the column. This element with two nodes considers two sets of degrees of freedom (DOFs) (indicated by blue arrows): 6 conventional DOFs (i.e., u_1, u_2, u_3, u_4, u_5, and u_6) corresponding to the concrete part and $2n$ axial DOFs corresponding to n steel bars (i.e., $\overline{u}_1^i$ and $\overline{u}_2^i$ for i^{th} bar). Different axial DOFs are employed for the concrete and steel bars to allow steel bars to slip with regard to the surrounding concrete. Using these additional DOFs provides this element with the ability to capture the slip and thus its contribution to column deformation. It is worth noting that the shear deformation is neglected because the element formulation is based on the Euler-Bernoulli beam theory commonly used for slender columns. This element has been proven to capture the effect of imperfect bonding on the nonlinear behavior simulations of uncorroded RC columns when combined with an appropriate bond-slip material model in the nonlinear finite element framework of *OpenSees* [143]. As a result, this element is naturally selected in the proposed modeling approach for corroded RC columns with corrosion-affected bond-slip behavior. This fiber-based frame element employs a number of (typically 4 to 6) Gauss-Lobatto integration points, at which a fiber section is assigned. To represent the stress-strain relationships in the fiber section, well-established uniaxial material models widely used in the literature are selected. Corrosion-affected material model parameters need to be used for corroded RC columns, as elaborated below.

4.2.2. Modeling of corroded reinforcement

Corrosion in a steel bar is measured by the average reduction of the cross-sectional area based on the corrosion level K, which is defined as the percentage of mass loss. It is worth mentioning that corrosion barely affects the material strength of steel [150]. Thus, for uniform corrosion, corroded steel bars can be modeled by reducing the cross-sectional area. In contrast, in the case of pitting corrosion [139,151], the uncorroded steel strength (f_y) of steel bars should be reduced as (f_y^c) to model the negative effect of stress concentrations in pitting corrosion spots, in addition to reducing the cross-sectional area. Note that the corrosion can also lead to a loss of ductility, which can be modeled by reducing the ultimate strain [138], and increased risk to steel bar buckling [140]. The proposed FE modeling approach allows them to be considered if a proper material model is available. However, the steel bar buckling and ductility loss is not considered in this study, which mainly focuses on investigating the corroded bond-slip effect on the nonlinear behavior simulations of corroded RC columns, compared to the reduced steel bar cross-sectional area. Thus, the fibers corresponding to steel bars are assigned with the nonlinear steel model (i.e., *Steel02* in *OpenSees*) with a reduced cross-sectional area and impaired material properties for yield stress f_y (in case of pitting corrosion), strain hardening ratio b, and Young's modulus E_s according to [138,139,151].

4.2.3. Modeling of corroded cover concrete

Due to the volumetric expansion of corrosion products (i.e., steel rust), the splitting stresses can be developed in the cover concrete, resulting in cracking or spalling. This can be modeled by lowering the cover concrete strength to f_c^c, based on the corrosion level or corrosion-induced reduction of steel bar diameter [43], per Eq. (4-1):

$$f_c^c = \frac{f_c}{1+0.1\dfrac{\varepsilon_1}{\varepsilon_c}} \text{ where } \varepsilon_1 = \frac{\sum_{i=1}^{n} \pi(d_b - d_b^c)_i}{b_0} \tag{4-1}$$

in which f_c and ε_c are the concrete strength and corresponding strain in the pristine condition, respectively, n is the number of steel bars, d_b is the initial steel bar diameter, d_b^c is the reduced steel bar diameter due to corrosion, and b_0 denotes for the circumference of the cross-section of the RC column. Furthermore, the concrete tensile strength is affected by the cover concrete cracking and spalling induced by corrosion. According to [44], the concrete tensile strength (i.e., f_t) should be reduced by the same reduction factor as the compressive strength. Therefore, in each fiber section of a frame element in the FE model, the fibers corresponding to cover concrete are assigned with a nonlinear material model (*Concrete02* in *OpenSees*) using the corrosion-affected compressive and tensile strengths defined above, and uncorroded values for compressive strain ε_c, as well as ultimate compressive strength f_{cu} and its corresponding strain ε_{cu}.

4.2.4. Modeling of corroded confined concrete

To consider the effect of corrosion on the confinement, the confined (core) concrete properties are required to be modified based on the corroded longitudinal and transverse reinforcements using Mander's equations [45]. Accordingly, a nonlinear material model (*Concrete02* in *OpenSees*) with impaired concrete strength and ultimate strain due to corrosion is used for fibers corresponding to the core concrete [141].

4.2.5. Modeling of corroded bond-slip

The bonding between steel bars and the surrounding concrete is further affected by the reduction of rib areas of steel bars and cracks generated in concrete owing to corrosion. To capture this effect in the FE model, a corrosion-affected bond-slip material model in the fiber-based frame element is needed. In this regard, this work advances the bond stress-slip model of uncorroded bond-slip recently implemented in *OpenSees* by the authors [143], which is defined by five bonding properties (i.e., t_1, t_3, u_{b1}, u_{b2}, and u_{b3}), shown in the hysteretic bond-slip model in Figure 4-1. In this model, these bonding properties are estimated based on the concrete and steel bar properties. According to existing studies (e.g., Kivell et al. [147] and Lin et al. [47]), the monotonic and cyclic behavior of bond-slip is degraded by corrosion. To be specific, the corrosion effect on the cyclic bond-slip behavior can be considered through modifying the friction branch and reduced envelope in the corroded bond-slip model, based on the dissipated energy-related damage factors as a function of the corrosion level [147]. In contrast, the corrosion effect on the monotonic bond-slip behavior can be achieved by modifying the five bonding properties, or replacing them with corroded bonding properties (i.e., t_1^c, t_3^c, u_{b1}^c, u_{b2}^c, and u_{b3}^c) [144–148,152,153], which are summarized in Appendix D.

As implied by the aforementioned prediction models, inconsistency exists, particularly when it comes to modifying the maximum bonding stress (t_1) [47]. Furthermore, despite the fact that the experimental data used to develop the models in all of these studies reveals significant variability, none of the existing models has assessed the relevant uncertainties in corroded bonding properties. The uncertainties of bonding properties could affect the structural behavior simulations, according to the study conducted on uncorroded RC columns [143]. This finding highlights the need for further investigation of the impact of corroded bonding property uncertainties on the nonlinear behavior simulations of corrosion-affected RC structures. As a result, this research develops a probabilistic model to predict corroded bonding properties, i.e., t_1^c, t_3^c, u_{b1}^c, u_{b2}^c, and u_{b3}^c, with probabilistic quantification of the prediction errors.

To this end, an experimental database is compiled from the literature [145,147,148,154–159] in this study. This database is employed to develop a set of new prediction models for corroded bonding properties, i.e., t_1^c, t_3^c, u_{b1}^c, u_{b2}^c, and u_{b3}^c, using Bayesian linear regression [130]. Instead of using point estimates, all model parameters are estimated probabilistically with a distribution in Bayesian linear regression. Thus, mean values of the model parameters should be used in the proposed model to get deterministic forms of proposed equations. Table 4-1 summarizes the model forms of the newly developed model for corroded bonding properties, where K denotes for the percentage of mass loss ratio (i.e., corrosion level), and θ_i's and e_i's show model parameters defined in Table D-3 in Appendix D. Detailed information of the models developed using the compiled database is reported in Appendix D.

Table 4-1: Newly developed model for corroded bonding properties

Corroded bonding property	Proposed model	Corrosion level
t_1^c/t_1	1.0	$K \le 3$
	$\exp(\theta_1 + \theta_2 K + e_1)K^{\theta_3}$	$K > 3$
t_3^c/t_1^c	$\theta_4 + \theta_5 K + e_2$	$K \le 3$
	$\theta_6 + e_3$	$3 < K \le 12$
	$\theta_7 + \theta_8 K + e_4$	$K > 12$
u_{b1}^c/u_{b1}	1.0	$K \le 3$
	$\theta_9 + e_5$	$K > 3$
u_{b2}^c/u_{b1}^c	$\theta_{10} + e_6$	$K > 0$
u_{b3}^c/u_{b3}	1.0	$K \le 3$
	$K^{\theta_{11}} \exp(e_7)$	$K > 3$

To show the performance and importance of the proposed probabilistic model for corroded bonding properties, Figure 4-2 (a) to (e) present mean (indicated by solid curve) and mean ± standard deviation (indicated by dashed curves) of model predictions for t_1^c/t_1, t_3^c/t_1^c, u_{b1}^c/u_{b1}, u_{b2}^c/u_{b1}^c, and u_{b3}^c/u_{b3}, respectively, in addition to the experimental observations (indicated by gray dots). The newly proposed probabilistic model can be used to estimate the corroded bonding properties using mean predictions, and describe the uncertainty, the importance of which will be studied later in this work. As shown in Figure 4-2, the majority of the experimental measurements for these bonding properties fall within the mean ± standard deviation limits, indicating that the model can accurately predict the corroded bonding properties while accounting for the relevant uncertainties.

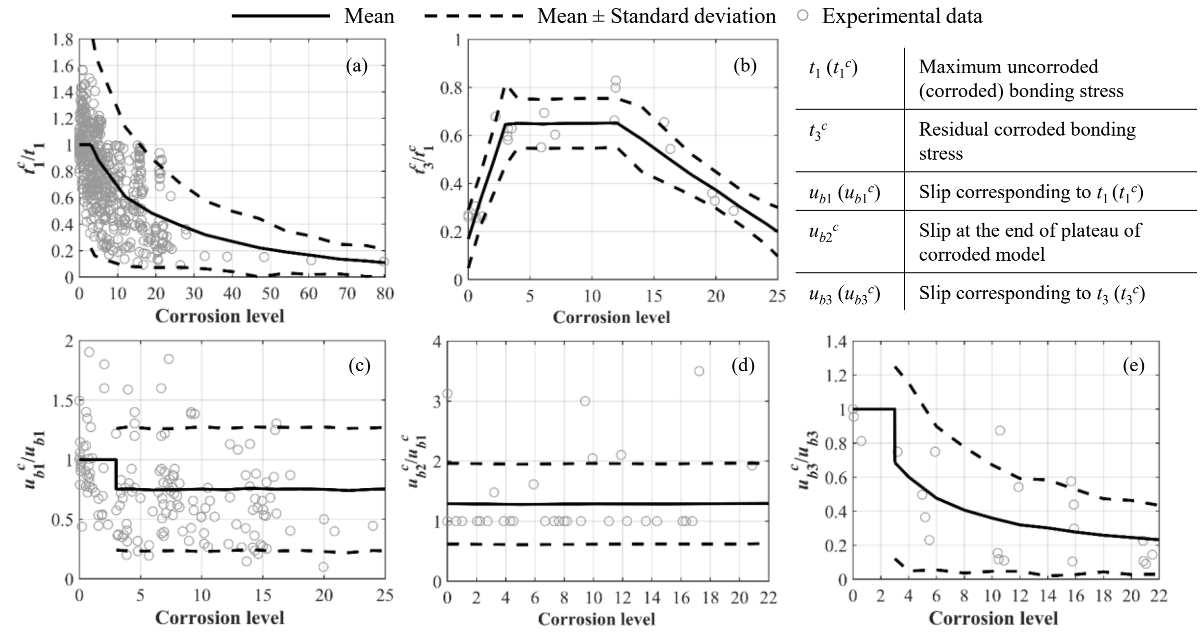

t_1 (t_1^c)	Maximum uncorroded (corroded) bonding stress
t_3^c	Residual corroded bonding stress
u_{b1} (u_{b1}^c)	Slip corresponding to t_1 (t_1^c)
u_{b2}^c	Slip at the end of plateau of corroded model
u_{b3} (u_{b3}^c)	Slip corresponding to t_3 (t_3^c)

Figure 4-2: Proposed models for (a) t_1^c/t_1, (b) t_3^c/t_1^c, (c) u_{b1}^c/u_{b1}, (d) u_{b2}^c/u_{b1}^c, and (e) u_{b3}^c/u_{b3} based on corrosion level

To compare the accuracy of the proposed model for corroded bonding properties with the existing models presented in Table D-1 of Appendix D, Figure 4-3 (a) to (e) show the test-to-prediction ratios for t_1^c/t_1, t_3^c/t_1^c, u_{b1}^c/u_{b1}, u_{b2}^c/u_{b1}^c, and u_{b3}^c/u_{b3}, respectively. The deviations of the experimental data points from the model predictions, i.e., the associated errors, are quantified by the R-squared (R^2) value shown in this figure. Note that the R^2 value closer to 1.0 implies a better model generally. Comparing the test-to-prediction ratios for these models indicates the accuracy of the proposed model has been only slightly improved with respect to the existing models in the literature. However, the uncertainties in these predictions are quantified in this study. The scattered test-to-prediction ratios reveal the large uncertainty associated with these models, which shows the need for probabilistic models considering such uncertainties.

This newly developed corroded bond-slip material model is implemented in *OpenSees* as *BondSlipCorC*, which requires the corroded bonding properties as input. This equips *OpenSees* with a versatile and efficient FE modeling module for corrosion-affected RC structures with imperfect bonding, together with the recently developed geometrically nonlinear fiber-based frame element with bond-slip (i.e., *dispBeamColumnBS*).

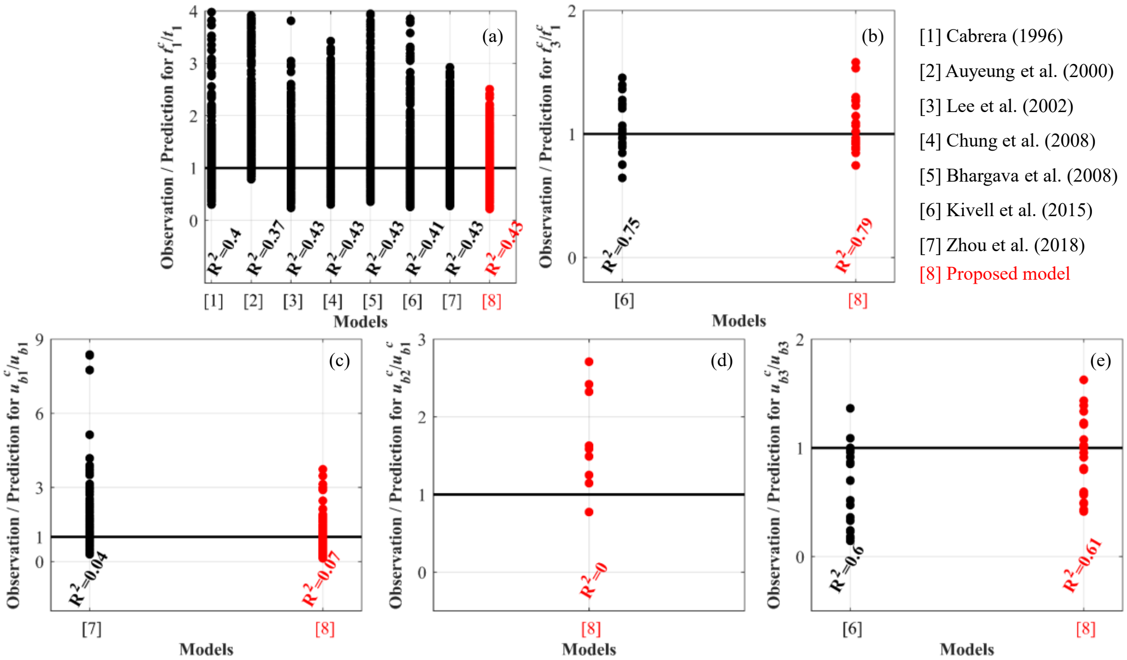

Figure 4-3: Comparison of the test-to-prediction ratios using the newly proposed and a group of existing models for corroded bonding properties: (a) t_1^c/t_1, (b) t_3^c/t_1^c, (c) u_{b1}^c/u_{b1}, (d) u_{b2}^c/u_{b1}^c, and (e) u_{b3}^c/u_{b3}

4.3. APPLICATION OF PROPOSED MODELING APPROACH TO TESTED COLUMNS

To examine the FE modeling approach presented above, two artificially corroded RC columns with their corresponding uncorroded RC columns tested in the literature are considered, referred to as Meda column [137] and Jia column [136]. According to [136], the bottom segment of Jia column, within 450 mm above the top of anchorage zone, was corroded with a corrosion level equal to 6% for longitudinal bars and 12.91% for lateral reinforcements. For Meda column, the whole column was under artificial corrosion with a corrosion level of 20% for longitudinal bars [137]. Note that the artificial corrosion in both of these columns was induced by accelerated chloride penetration, i.e., pitting corrosion. These two columns have hooked steel bars in the anchorage zone and a constant axial load applied on the top, and were subjected to static cyclic lateral loading until flexural failure during the tests. The geometrical properties and loading protocols of both corroded and uncorroded specimens of Meda column and Jia column are depicted in Figure 4-4 (a) and (b), respectively.

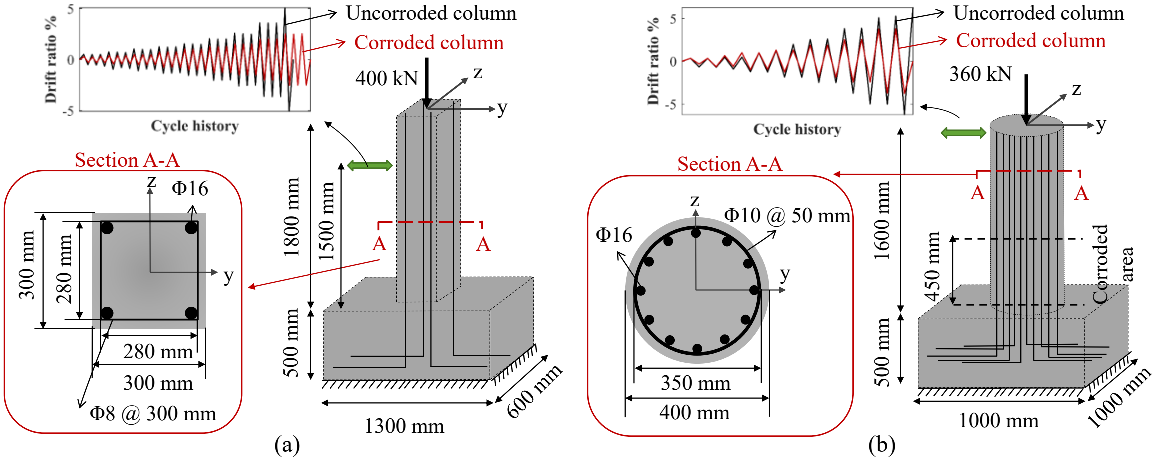

(a) (b)

Figure 4-4: Schematic view of geometry, loads, and cross-sections for (a) Meda column, and (b) Jia column

The two corroded RC columns are modeled using the proposed modeling approach employing the recently developed fiber-based frame elements (with bond-slip) considering corroded bonding, in comparison with the approach using conventional fiber-based frame elements (without bond-slip). The schematic view of the corresponding FE models with bond-slip developed in *OpenSees* is presented in Figure 4-5 (a) and (b) for Meda column and Jia column, respectively. It is worth noting that the foundations (i.e., anchorage zone) of these two columns, which will not be affected by corrosion in corroded columns, are also required to be modeled in order to consider the slip deformation in the anchorage zone. The key properties associated with the material models used in the FE models for RC columns under the corroded conditions are summarized in Table 4-2. Note that pitting corrosion effects on steel bars in these two columns are taken into account by reducing the strength and ultimate strain of steel bars, as well as the cross-sectional area [138,139]. It is worth mentioning that the reduced ultimate strain has no effect on the FE predictions for the two experimental RC columns since it is observed that the maximum strain level in steel is below the corrosion-affected ultimate strain. The corroded properties are computed following the approach presented earlier, by modifying the properties for the uncorroded condition. Note that the properties under the uncorroded condition, summarized in Table 4-2, are determined based on the experimental data reported in the literature [136,137] and Mander's equations [45] to consider the confinement effect for core concrete. For comparison purposes, the two control columns tested in [136,137] under pristine (uncorroded) conditions, which correspond to the two corroded columns, are also modeled assuming perfect bonding and considering imperfect bonding in pristine conditions. Thus, the corresponding static cyclic pushover analyses are conducted using the FE models for uncorroded and corroded columns. It is worth noting that the uncertainties of corroded bonding properties are not considered here; instead, the deterministic forms of the proposed bonding property models are used. The impact of the uncertainties in corroded bonding properties on the nonlinear behavior simulations will be explored later in this research.

Table 4-2: Summary of uncorroded and corroded properties for Meda column and Jia column

Test	**Corrosion level**	**Steel**		**Concrete**			**Bond-Slip**	
		Properties		**Properties**	**Unconfined**	**Confined**	**Properties**	
Meda Column	20% for both longitudinal bars and lateral reinforcements	d_b (mm)	16.0 (14.3)	f_c (MPa)	20.00 (16.4)	23.00 (22.00)	t_1 (MPa)	15.87 (6.35)
		f_y (MPa)	520.0 (468)	f_{cu} (MPa)	4.00 (4.00)	12.98 (12.98)	t_3 (MPa)	5.36 (2.34)
		b (−)	0.02 (0.02)	ε_c (−)	0.002 (0.002)	0.00875 (0.00875)	u_{b1} (mm)	1.71 (1.28)
		E_s (MPa)	210000.0 (210000.0)	ε_u (−)	0.008 (0.008)	0.013 (0.01)	u_{b2} (mm)	2.11 (1.65)
				f_t (MPa)	2.00 (1.64)	2.30 (2.30)	u_{b3} (mm)	10.41 (2.08)
Jia Column	6% for longitudinal bars and 12.91% for lateral reinforcements	d_b (mm)	16.0 (15.51)	f_c (MPa)	40.00 (37.26)	51.46 (47.31)	t_1 (MPa)	22.44 (15.47)
		f_y (MPa)	400.0 (388)	f_{cu} (MPa)	8.00 (8.00)	40.85 (40.85)	t_3 (MPa)	7.58 (10.05)
		b (−)	0.007 (0.007)	ε_c (−)	0.002 (0.002)	0.0049 (0.0049)	u_{b1} (mm)	1.42 (1.065)
		E_s (MPa)	210000.0 (210000.0)	ε_u (−)	0.008 (0.008)	0.0200 (0.0188)	u_{b2} (mm)	1.85 (1.37)
				f_t (MPa)	4.00 (3.73)	5.15 (5.15)	u_{b3} (mm)	6.76 (2.49)

Note: values in ( ) indicate the properties of the RC columns under the corroded condition.

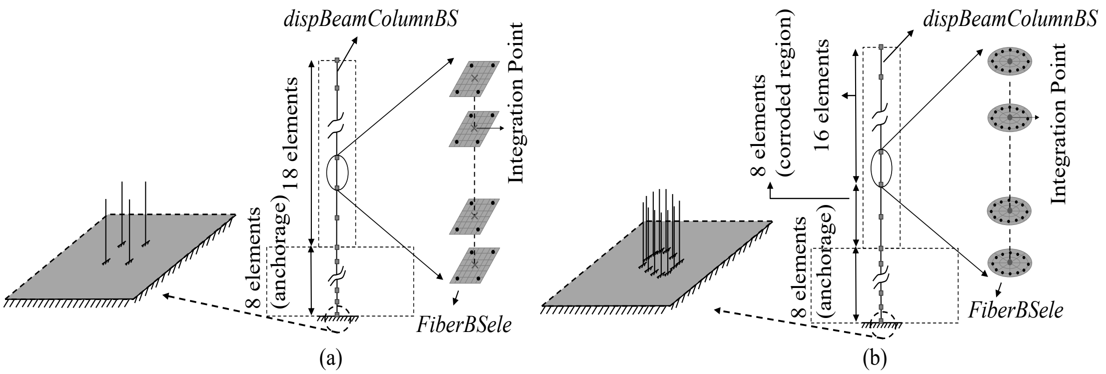

Figure 4-5: Schematic view of FE models of (a) Meda column, and (b) Jia column

Figure 4-6 (a) and (b) present the comparison of the FE-predicted lateral load-drift ratio hystereses with experimental results for uncorroded and corroded cases of Meda column, respectively. In both corroded and uncorroded cases, the FE predictions correlate well with the experimental results when the bond-slip effect is considered before reaching a certain deformation level (e.g., a drift ratio of 2.0% for Meda column designed for buildings). In particular, FE models with imperfect bonding (uncorroded and corroded) can well capture the pinching effect induced by bond-slip, which indicates better characterization in terms of energy dissipation. In contrast, the FE models assuming perfect bonding result in lateral load-drift ratio hystereses that differ significantly from the experiments in terms of energy dissipation. Similarly, Figure 4-6 6 (c) and (d) compare the lateral load-drift ratio hysteresis between FE predictions and experimental results for uncorroded and corroded cases of Jia column, respectively. This comparison reaffirms the improvement of FE predictions when imperfect bonding (i.e., the corroded and uncorroded bond-slip) is considered. These observations indicate that the improved FE modeling approach for corroded RC columns, which considers the corroded bond-slip, leads to better accuracy. It is worth emphasizing that more experimental tests with recorded local responses are required to better illustrate the performance of the provided FE modeling approach in capturing the corroded bonding, which are not readily available in the literature and beyond the scope of this study. In addition, note that the strength degradation at large deformation levels for both of these columns is not captured well. This is because the effect of buckling is not considered in this research, while the longitudinal steel bars were buckled in both of these columns according to the experimental reports [136,137]. In particular, the buckling impact is more severe in Meda column since the tests continued to increase the loading level after the buckling occurred (i.e., approximately after 2% drift ratio for the corroded column), whereas the level of loading in Jia column did not increase after the buckling point (i.e., approximately 3.9% drift ratio for the corroded column). This highlights the need to develop a proper material model for steel capable of capturing the effect of corroded steel bar buckling, which is beyond the scope of this research.

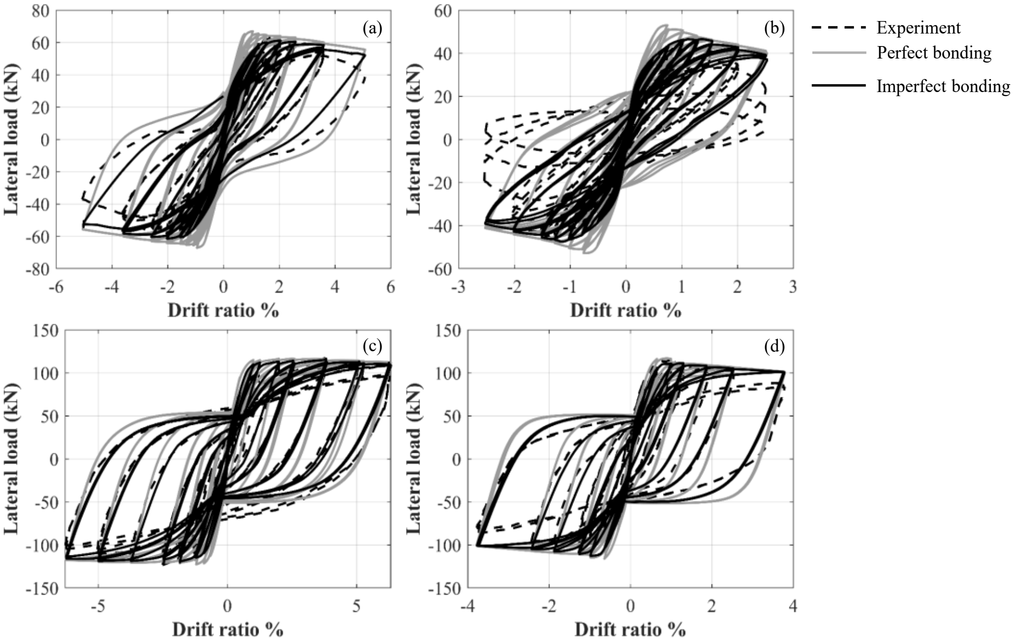

Figure 4-6: Comparison of lateral load-drift ratio hysteresis between FE predictions and experimental results for (a) uncorroded and (b) corroded Meda column, and (c) uncorroded and (d) corroded Jia column

4.4. IMPORTANCE OF CORRODED BONDING

This section investigates the role of corrosion-affected bond-slip in structural behavior simulation of corroded RC columns assuming uniform corrosion (typically induced by carbonation attack), considering a wide range of corrosion levels using the FE model developed for Meda column. For this purpose, the effect of corrosion-affected bond-slip is compared with the cross-section area reduction of steel bars, which is the most commonly considered corrosion aspect in the literature [26]. It is worth mentioning that the strength and ultimate strain of steel is not affected by corrosion since uniform corrosion is assumed here for the columns studied in this section. However, in case of pitting corrosion, the strength and ultimate strain reduction of steel might influence the structural responses, particularly if the ultimate strain level was reached and the strain increased further to the steel fracture point.

To this end, three different cases are studied: case (1) considering corrosion via only reducing the steel bar cross-sectional area, referred to as "corroded rebar"; case (2) considering corrosion via only degrading the bonding, referred to as "corroded bonding"; and case (3) considering corrosion via affecting both the bonding and steel bar cross-sectional area, referred to as "corroded rebar and bonding". Using these three cases, the FE-based parametric analyses are conducted to reveal how important it is to consider corroded bond-slip in FE modeling, as well as to indicate how and to what extent neglecting the corroded bond-slip might impair the nonlinear behavior simulations.

To model corrosion as an aging phenomenon, time-dependent corrosion models have been developed for different environmental conditions in the literature. This study employs the model developed by [26,40] to consider reasonable levels of corrosion. According to this model, the steel bar diameter at time t in years, $d_b{}^c(t)$, is estimated per Eq. (4-2):

$$d_b{}^c(t) = d_b - 2\lambda(t - T_i) \text{ for } T_i < t \leq T_i + \frac{d_b}{2\lambda}; 0 \text{ for } t > T_i + \frac{d_b}{2\lambda} \tag{4-2}$$

where T_i is the time of corrosion initiation, determined based on Fick's second law of diffusion and dependent on the cover concrete depth [26], and λ is the corrosion rate. Note that the bar diameter remains unchanged before reaching T_i. Assuming "medium corrosion intensity" situation, in which un-cracked concrete specimens are subjected to a medium level of contamination (e.g., salt spray condition) with visible corrosion products [40], the corrosion rate is 0.0348 mm/year on average in the case study considered. Note that this rate would be substantially higher in a very aggressive environment, which causes a high level of contamination. Accordingly, the corrosion level (i.e., K) defined as the percentage of mass loss of the corroded steel bar is calculated.

4.4.1. Deterministic Analysis

According to the age-dependent corrosion model in Eq. (4-2), 11 different corrosion levels are considered across a life span of 50 years (i.e., every 5 years), ranging from $K = 0$ for a newly built RC column with $t = 0$ to $K \approx 38$ for an aged RC column with $t = 50$ years, determined based on the cover concrete depth of Meda column. In the FE models corresponding to all these considered corrosion levels, the corroded bonding properties are estimated using deterministic forms of the newly proposed model. The importance of corroded bonding in structural response prediction is explored using these FE models under both static and dynamic loading scenarios.

(1) Static behavior simulation

To evaluate the importance of including the influence of corroded bonding in simulating the static behavior of RC columns, this research conducts static monotonic and cyclic pushover analyses. Figure 4-7 (a) to (c) show the FE-predicted lateral load-drift ratio responses under monotonic loading for the three cases considered, i.e., corroded rebar, corroded bonding, and corroded rebar and bonding, respectively. For comparison purposes, the responses assuming perfect bonding and no bonding (i.e., complete bond loss as it were pure concrete) are also presented. Furthermore, the four limit states as defined corresponding to steel bar yielding, cover concrete crushing, core concrete crushing, and bond-slip yielding are indicated.

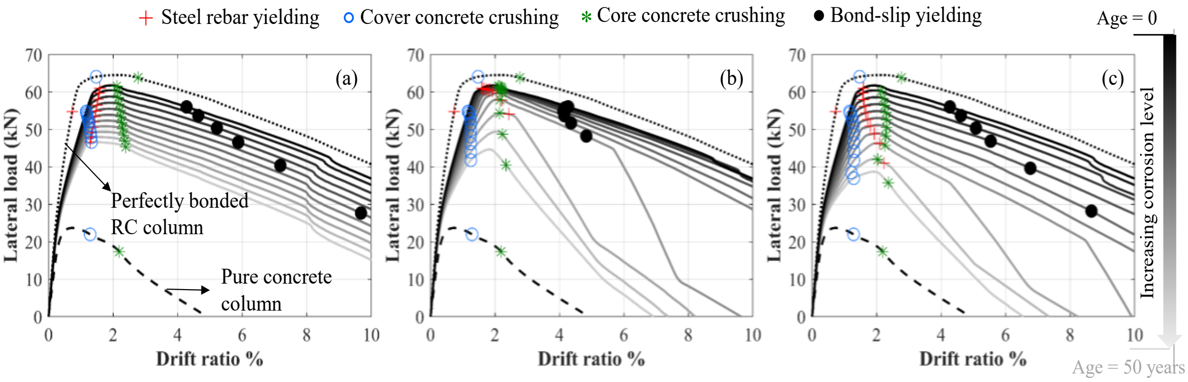

Figure 4-7: FE-predicted lateral load-drift ratio responses of the RC column with corrosion under monotonic loading considering (a) case 1: corroded rebar, (b) case 2: corroded bonding, and (c) case 3: corroded rebar and bonding

As shown in Figure 4-7, the corroded RC columns experience more performance degradation if the corroded bonding is considered in addition to the steel bar area reduction, particularly for more aged columns with higher corrosion levels. Specifically, as corrosion gets more severe as the age increases, the contribution of steel bars would be reduced. For a well-designed RC column under pristine condition, steel yielding occurs earlier than core concrete crushing. For an RC column under corroded condition, without considering corroded bonding, steel yield is predicted to occur even earlier in FE simulations. However, when considering corroded bonding, steel yielding can be postponed significantly, even after the core concrete crushing, e.g., for highly corroded columns. The rationale for this observation is that in corroded RC columns, the role played by steel bars is smaller due to corrosion-affected bonding between steel bars and surrounding concrete than in cases with normal (uncorroded) bonding. In other words, the stress transfer from concrete to steel bars would be weaker, resulting in less steel contribution. Comparing Figure 4-7 (a) with (b) and (c) reveals that such effects cannot be captured when corrosion is only considered via reducing the steel bar cross-sectional area. More important is that corroded bonding adversely affects the post-peak strength degradation to a considerable degree. As a result, neglecting the effect of corroded bonding in FE modeling of corroded RC columns under static monotonic loading (for capacity analysis) is problematic, particularly when the post-peak deformation capability (or ductility) is of concern.

To quantify the corrosion effect captured in the three cases considered, three different engineering quantities extracted from monotonic lateral load-drift ratio curves are examined. They include (1) the secant stiffness, which is defined based on the point at which the tangent stiffness is reduced by 20%; (2) the lateral load capacity, which is the maximum strength reached in the monotonic lateral load-drift ratio curves; and (3) the deformation capacity measured by the displacement corresponding to 20% drop in the lateral load capacity, which is normalized by the displacement corresponding to the onset of steel yielding in the uncorroded RC column. The corrosion impact is studied by comparing the FE-predictions for the corroded RC column case with that for the uncorroded RC column case, and measured by the discrepancy percentage in FE-predictions of the three quantities considered. Figure 4-8 (a) to (c) show how the corrosion impact changes as the corrosion level (indicated by ages) increases in terms of those three quantities for the cases considered. Note that negative values imply that the corroded RC columns have lower values than the uncorroded RC column for secant stiffness, lateral load capacity, and deformation capacity.

Specifically, Figure 4-8 (a) indicates that the secant stiffness reduction due to corrosion at the initial stage is mainly due to steel bar cross-sectional area reduction; in contrast, when the corrosion gets severe (i.e., more than 20 years old), neglecting the effect of corrosion on bond-slip leads to underestimation of the secant stiffness reduction, because the corroded bonding would contribute to the secant stiffness reduction considerably (e.g., up to 50%) by reducing the contribution of steel. Figure 4-8 (b) reveals that the lateral load capacity reduction due to corrosion is primarily governed by the steel bar cross-sectional area reduction rather than corroded bonding. However, when corrosion is severe (e.g., $K \approx 38$ at the age of 50 years), corroded bonding would reduce the lateral load capacity up to 25%. Note that in highly corroded RC columns (e.g., $K \approx 57$ at the age of 80 years), the lateral load capacity would be reduced significantly due to corroded bonding; if bonding is fully damaged due to corrosion, the RC column would behave as a pure concrete column (i.e., no steel contribution). In contrast, Figure 4-8 (c) shows the deformation capacity reduction due to corrosion is mainly affected by the corroded bonding after the initial stage (e.g., after 20 years). This observation reveals that corroded bonding can have a considerable impact on deformation capacity. It is worth noting that the simple approach, such as the one used in the case of "corroded rebar" that considers corrosion by only reducing the cross-sectional area of steel bars, is valid at an early age of the column with low corrosion, and the corrosion impact on lateral load and deformation capacity is nearly linear to age. However, the simple approach is problematic when corrosion severity increases with age because corroded bonding plays a significant role, causing corrosion impact to increase nonlinearly with age. Note that these three engineering quantities reflect how the contribution of steel bars affects the nonlinear behavior of RC columns. In particular, how strong the steel bar is bonded to the concrete can dramatically influence the secant stiffness and deformation capacity, namely, the ductile behavior of RC columns.

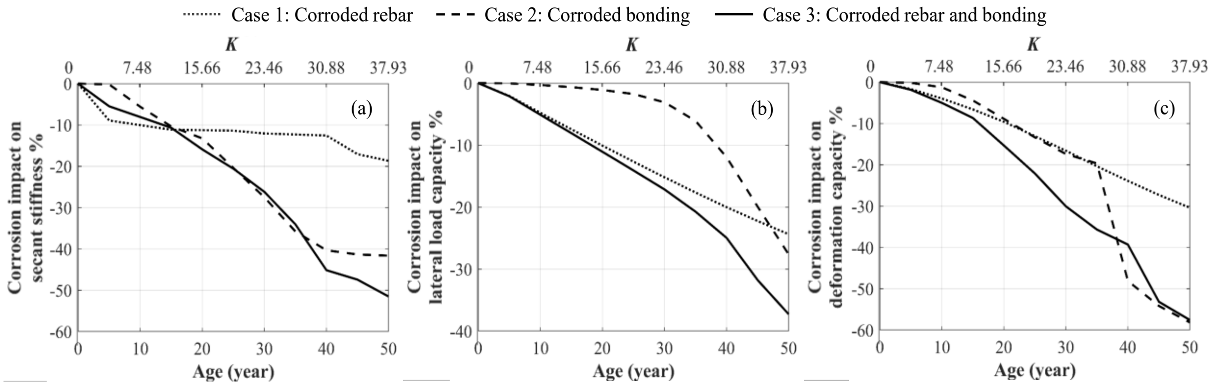

Figure 4-8: Corrosion impact as measured by the prediction difference between the behavior of corroded and uncorroded columns under monotonic loading in terms of (a) secant stiffness, (b) lateral load capacity, and (c) deformation capacity

In addition to the static monotonic pushover analyses, this research explores the effect of corroded bonding on the nonlinear behavior simulation of the RC column under cyclic loading. Figure 4-9 depicts the lateral load-drift ratio hysteresis for the three different cases considered at various corrosion levels. Note that the responses assuming perfect bonding and no bonding (i.e., pure concrete) are also shown with the dotted and dashed curves, respectively, for the purpose of comparison. Figure 4-9 (a) to (c) show that the role of corroded bonding increases as the corrosion level increases from mild to severe. This is consistent with the observations based on the behavior of corroded RC columns under monotonic loading. However, due to corroded bonding degradation under cyclic loading, heavily corroded RC columns behave as if they were pure concrete columns at high loading levels. This means that when the RC column is subjected to cyclic loading, the impact of corroded bonding on the structural behavior is more significant. This stems from the degradation of bonding under cyclic loading, which leads to less energy dissipated by steel bars (i.e., more pinching).

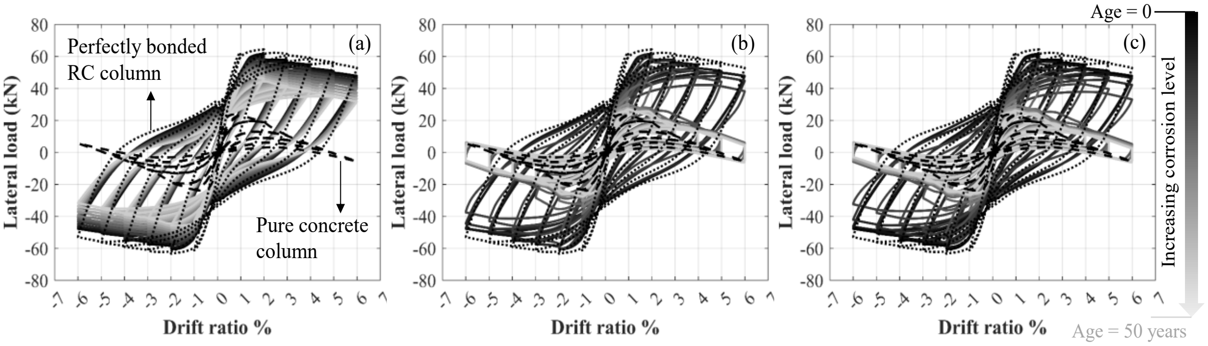

Figure 4-9: FE-predicted lateral load-drift ratio hysteresis of the RC column with corrosion for (a) case 1: corroded rebar, (b) case 2: corroded bonding, and (c) case 3: corroded rebar and bonding

When comparing Figure 4-9 (c) with Figure 4-9 (a) and (b), RC columns with higher corrosion levels exhibit more pinched hysteresis with less energy dissipation, mostly owing to the corroded bonding. To quantify the effect of corroded bonding on the reduction in hysteretic energy dissipation, Figure 4-10 shows the corrosion impact on FE-predicted hysteretic energy dissipation of the corroded RC column for different levels of drift ratios. The negative values in percentage here imply that neglecting the effect of corrosion on steel bar area reduction and/or bonding over-predicts the dissipated energy. When comparing Figure 4-10 (a) to (c) for the three cases considered, one can find that ignoring the corrosion effect on bonding greatly overestimates the dissipated energy by up to 80% under the loading protocol considered here, whereas ignoring the effect of corrosion on steel bar cross-sectional area over-predicts the dissipated energy by no more than 30%, specifically during hysteretic cycles at higher levels of deformations. In particular, stronger bonding (i.e., uncorroded) provides more stress transfer from concrete to steel bar, resulting in more energy dissipated by steel, while the corroded bonding reduces the contribution of steel. This observation further confirms the importance of considering the effect of corrosion on bonding in FE modeling of corroded RC columns subjected to cyclic loading.

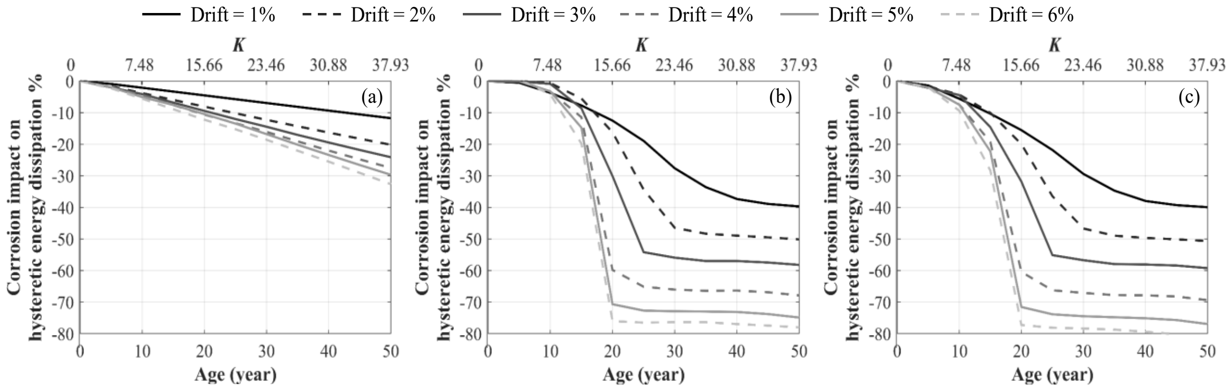

Figure 4-10: Corrosion impact as measured by the prediction difference between the behavior of corroded and uncorroded columns in terms of hysteretic energy dissipation for (a) case 1: corroded rebar, (b) case 2: corroded bonding, and (c) case 3: corroded rebar and bonding

(2) Dynamic behavior simulation

This section focuses on assessing the importance of considering corrosion-affected bonding in FE modeling of corroded RC columns subjected to dynamic loading. In this regard, the Loma Prieta earthquake recorded in 1989 at Agnew State Hospital station [70] is employed for illustration and scaled to reach different ductility demand levels (i.e., lateral drift ratio demand with respect to the yield drift ratio) for Meda column with no corrosion (i.e., $t = 0$). As a result, under these ground motions, the seismic responses of the RC columns with varying ages are simulated. Due to space limit, only the results for the ground motion scaled to achieve a moderate ductility demand level (i.e., 3.0) are reported here.

The FE-predicted drift ratio time-histories are presented in Figure 4-11 (a) to (c) for the three cases considered, including responses for the RC column assuming perfect bonding and no bonding as references. Figure 4-11 (a) shows that considering corrosion by reducing only steel bar cross-sectional area mainly affects the vibration amplitudes, when compared to the uncorroded case with age $t = 0$. Corroded bonding, on the other hand, has an impact on both the vibration periods and amplitudes, as illustrated in Figure 4-11 (b), by reducing the contribution of steel bars to the nonlinear behavior of the column. As a result, the corrosion effect is more severe when bar area reduction and corroded bonding are both considered, as shown in Figure 4-11 (c). This emphasizes the importance of considering corroded bonding in FE modeling of corroded RC columns, in addition to steel bar cross-sectional area reduction as commonly considered in the literature.

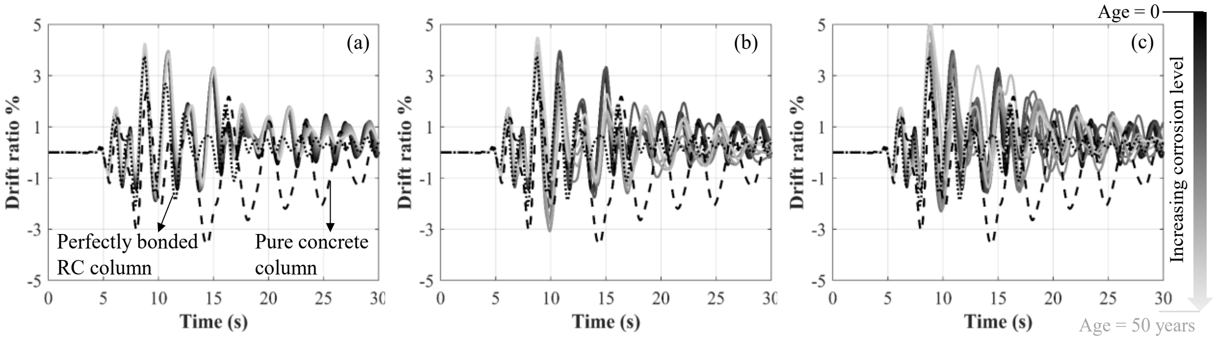

Figure 4-11: FE-predicted drift ratio time-histories of the RC column for (a) case 1: corroded rebar, (b) case 2: corroded bonding, and (c) case 3: corroded rebar and bonding

Figure 4-12 (a) and (b) show the impact of corrosion on predicting the peak drift ratio and hysteretic energy dissipation, respectively for the three cases considered. Similar to the corrosion impact mentioned earlier, the positive values of corrosion impact for the peak drift ratio, as shown in Figure 4-12 (a), suggest an underestimation if no corrosion effect is considered. For severely corroded RC columns, ignoring the effect of corroded bonding (i.e., considering bar area reduction only) can result in an even greater underestimation in peak drift ratio. In contrast, the negative values in corrosion impact for hysteretic energy dissipation, as shown in Figure 4-12 (b), indicate that the corroded RC column would have less energy dissipation during the earthquake excitation. When comparing the corrosion impact measures for the three cases considered, it is found that including the corrosion effect on bonding can lower the hysteretic energy dissipation up to 70% for the strong ground motion considered, compared to 20% when corrosion is considered only by steel bar cross-sectional area reduction. All these findings provide important insights into the demand of the corroded RC column under dynamic loading, which is exacerbated due to the diminishing contribution of steel bars to the nonlinear behavior of corroded RC column by deteriorated bonding.

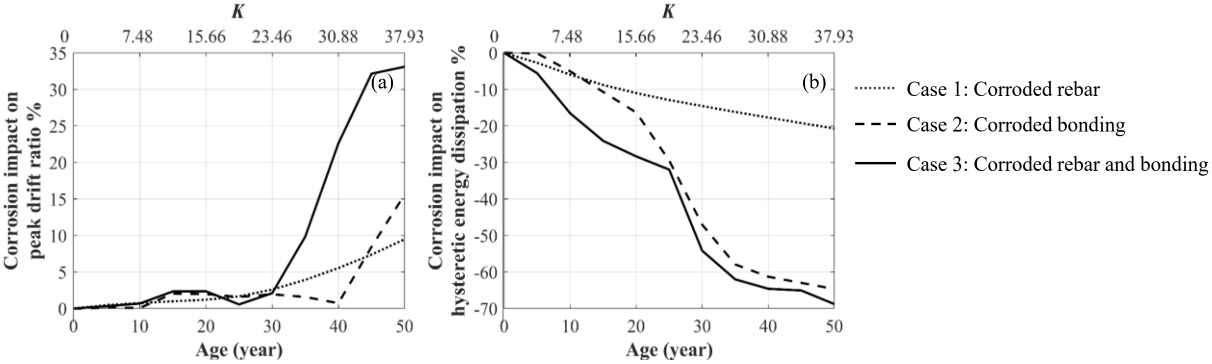

Figure 4-12: Corrosion impact as measured by the prediction difference between the dynamic behavior of corroded and uncorroded columns in terms of (a) peak drift ratio, and (b) hysteretic energy dissipated

4.4.2. Uncertainty Analysis

This section aims to investigate the importance of uncertainties in corroded bonding on the nonlinear behavior simulations of the RC column under static and dynamic loadings. The considered uncertainties associated with corroded bonding properties are derived from those in the uncorroded bonding properties (i.e., t_1, u_{b1}, and u_{b3}), as quantified in [143], and those originating from the corrosion-induced modification ratios (i.e., t_1^c/t_1, t_3^c/t_1^c, u_{b1}^c/u_{b1}, u_{b2}^c/u_{b1}^c, and u_{b3}^c/u_{b3}), as quantified earlier in this research. As a case study, Meda column is considered here, assuming the corrosion level of 20% affecting both the steel bar cross-sectional area and bonding. Figure 4-13(a) to (e) present the probability density functions (PDFs) of uncorroded and corroded bonding properties. It shows that the distributions shift to the left with lower values due to corrosion, which naturally increases the role of bond-slip in corroded RC columns and thus the importance of the corroded bonding uncertainties.

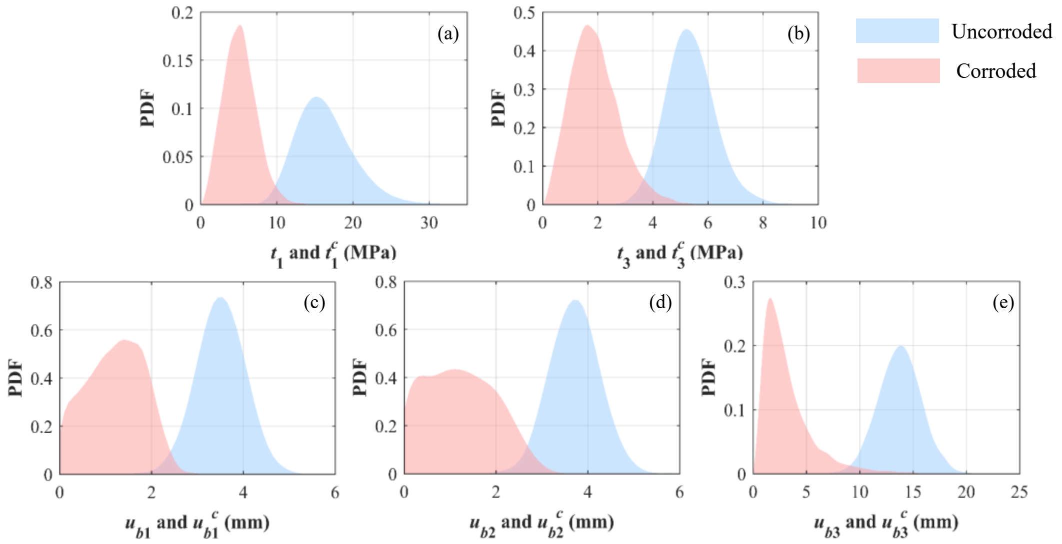

Figure 4-13: PDFs of uncorroded and corroded bonding properties for Meda column: (a) t_1 and t_1^c, (b) t_3 and t_3^c, (c) u_{b1} and u_{b1}^c, (d) u_{b2} and u_{b2}^c, and (e) u_{b3} and u_{b3}^c

To examine the importance of the uncertainties in corroded bonding properties for the column behavior, one-at-a-time sensitivity analyses are conducted here using perturbation analysis, i.e., varying one variable by one standard deviation at a time ($\theta_0 \pm \Delta\theta_0$). For comparison, three other random variables, i.e., elastic modulus of steel E_s, yield strength of steel f_y, and core concrete strength f_{cc}, are also considered. They are perturbed by 3.3%, 9.3%, and 17.5%, respectively, corresponding to one standard deviation [134]. A sensitivity index is used to measure the importance of uncertainty in that random variable by measuring the relative change of the response quantity of interest after perturbing that random variable with ± standard deviation.

Different response quantities of interest are considered, including the peak lateral strength, the hysteretic energy dissipation as obtained from static cyclic pushover analyses, as well as the maximum drift ratio and hysteretic energy dissipation obtained from dynamic analysis. Figure 4-14 (a) and (b) present the sensitivity indices for the static behavior of corroded RC columns in terms of peak lateral strength and hysteretic energy dissipation. It shows that the importance of the uncertainty in corroded bonding properties (i.e., t_1^c and u_{b1}^c) for the static behavior is comparable to the uncertainty in the two important variables: yield strength of steel (i.e., f_y) and core concrete compressive strength (i.e., f_{cc}). This is mainly attributed to variations in weak bonding properties for corroded RC columns.

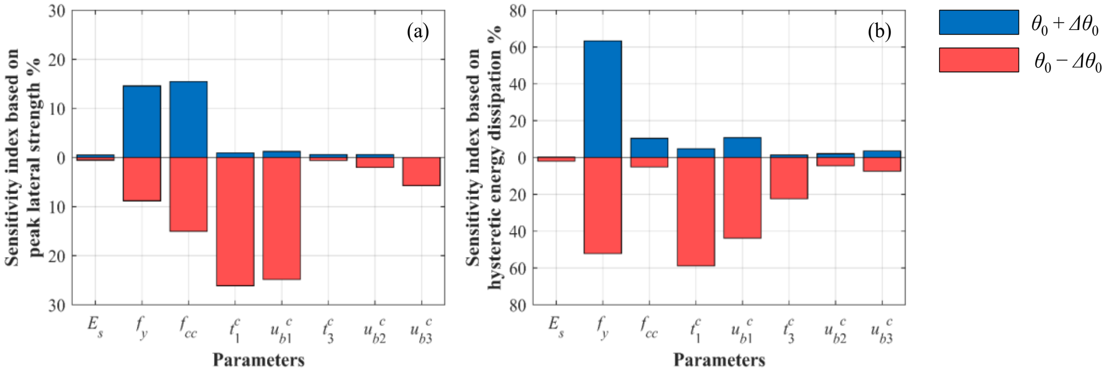

Figure 4-14: Sensitivity indices for the static behavior of corroded RC columns in terms of (a) peak lateral strength, and (b) hysteretic energy dissipation

Similarly, sensitivity analysis is also conducted to investigate the importance of the uncertainty in corroded bonding properties for the dynamic behavior of corroded RC columns. Figure 4-15 (a) to (b) present the sensitivity indices for the dynamic behavior of corroded RC columns in terms of maximum drift ratio and hysteretic energy dissipation, which are shown to be sensitive to the uncertainties in corroded bonding properties. Note that not only the uncertainties in t_1^c and u_{b1}^c, but also the uncertainties in other bonding properties are important. This is due to the large number of unloading-reloading cycles in dynamic loading and the resulted bonding degradation, particularly when the loading is of high intensity level. In fact, the relative importance of uncertain bonding properties is found to be less when the intensity level of the dynamic loading is lower. For instance, Figure 4-16 shows the sensitivity indices for the corroded column subjected to the same earthquake but with reduced intensity (e.g., scaled to reach the ductility demand of 1.0 instead of 3.0 as considered earlier). It reveals that role of the uncertainty in corroding bonding is less important under the dynamic loading with reduced intensity. However, it is worth emphasizing that the uncertainty in corroded bonding and its role on the dynamic characteristics (e.g., fundamental vibration period) of the corroded RC column is still not negligible due to the large uncertainty in the uncorroded bonding properties.

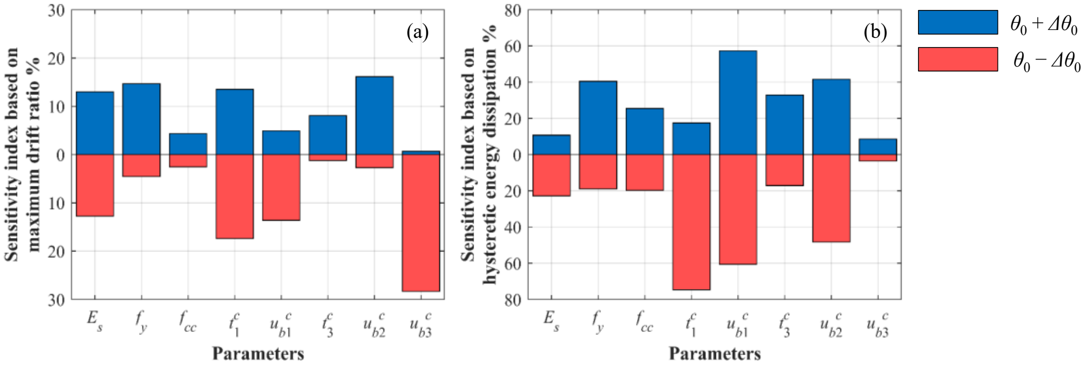

Figure 4-15: Sensitivity indices for the dynamic behavior of corroded RC columns in terms of (a) maximum drift ratio, and (b) hysteretic energy dissipation

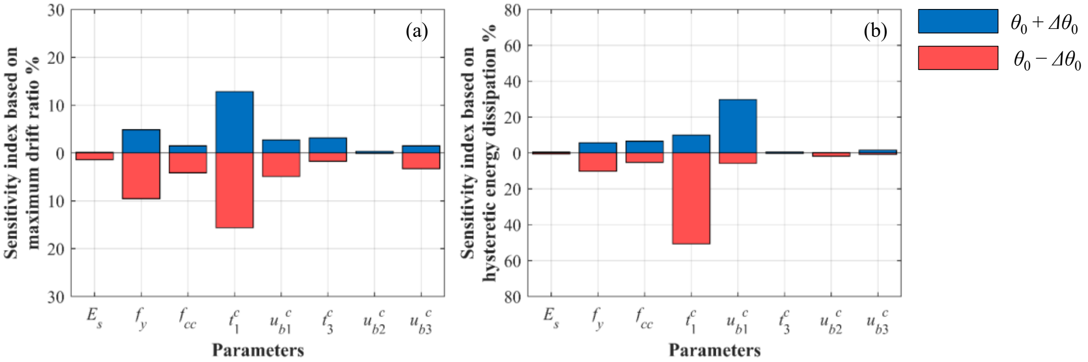

Figure 4-16: Sensitivity indices for the dynamic behavior of corroded RC columns subjected to reduced-intensity loading in terms of (a) maximum drift ratio, and (b) hysteretic energy dissipation

4.5. CHAPTER CONCLUSIONS

Corrosion of reinforcing steel is a primary environmental stressor with a negative impact on the performance of aged reinforced concrete (RC) structures. To explore the performance degradation of corroded RC structures, this study presented a comprehensive and efficient finite element (FE) modeling approach that accounts for various aspects of corrosion effect, especially corroded bond-slip. To this end, a geometrically nonlinear fiber-based frame element with bond-slip, recently developed by the authors, was used, for which a cyclic corroded bond-slip material model was implemented in the open-source FE software framework, *OpenSees*. Furthermore, a new probabilistic model for predicting corroded bonding properties was developed in this study based on the database compiled from the literature, which quantifies the prevailing uncertainties stemming from the wide dispersion of experimental data. Using two experimental RC columns under artificial corrosion, the presented FE modeling approach was proved to be a reliable tool for simulating the nonlinear behavior of corroded RC columns.

In comparison to the effect of reduced steel bar cross-sectional area due to corrosion, which is the most common corrosion aspect considered in the literature, this research deterministically investigated the role of corroded bonding in the static and dynamic behaviour simulations of corroded RC columns. Comparing the effects of these two corrosion aspects revealed that the lateral load capacity is governed by the steel bar cross-sectional area for low to medium levels of corrosion, while in severely corroded RC columns, the corroded bonding has a significant impact on the lateral load capacity. In contrast, the corroded bonding can notably alter the nonlinear behavior simulation of corroded RC columns in terms of secant stiffness, deformation capacity, peak drift ratio, and hysteretic energy dissipation for mildly to moderately corroded columns. As a result, using the conventional approach, which neglects the corroded bonding, would significantly bias the static and dynamic behavior simulations of corroded RC columns. Furthermore, this study examined the effect of uncertainty in corroded bonding properties on the nonlinear behavior simulations of RC columns. Findings revealed that the uncertainty in corroded bonding properties play equally important roles, if not more than other uncertainties, in FE predictions. Thus, in order to achieve reliable estimation of corrosion risk, it is essential to incorporate the uncertainties of the corroded bonding properties in the probabilistic analysis of corroded RC columns.

To summarize, the significant contributions of this work can be highlighted as follows: (1) providing a comprehensive and efficient FE modeling approach for corroded RC columns, with a focus on the integration of corroded bond-slip; (2) developing a probabilistic model for corroded bonding properties, with uncertainties quantified, based on the database compiled from the literature, and implementing a corroded bond-slip model in the open-source finite element software framework, *OpenSees*; (3) revealing the significant impact of corroded bonding on static and dynamic behavior simulations of corroded RC columns; and (4) evaluating the importance of uncertainties in corroded bonding properties in simulating corroded RC columns for probabilistic analysis. In particular, neglecting the corroded bonding and its associated uncertainties could result in notably biased predictions of corroded RC column behavior.

Chapter 5. UNIAXIAL CONSTITUTIVE MODEL OF STEEL BARS WITH BUCKLING CONSIDERING TRANSVERSE REINFORCEMENT FLEXIBILITY

5.1. INTRODUCTION

In performance-based engineering, rational seismic assessment of reinforced concrete (RC) structures requires a viable tool for nonlinear analysis, aiming at predicting the load capacity and post-peak behavior, such as strength degradation, deformation capability, and ductility. The purpose is to ensure targeted performance criteria are satisfied for the designed structures. To this end, fiber beam-column element has proved to be an effective and efficient analysis apparatus [160], and have taken a central role in assessing seismic performance of frame-type RC building or bridge structures [161]. This finite element (FE) approach can take advantage of macroscopic uniaxial material models for concrete [105,162], steel [102,133], and bond-slip between concrete and steel [107,143][107]. In turn, the capability of this approach highly relies on the accuracy of the macroscopic uniaxial material models.

Among existing uniaxial material models for steel, the most basic and commonly used ones include the bilinear steel material model with or without linear strain hardening, and its variants such as Giuffre-Menegotto-Pinto model with kinematic and/or isotropic hardening [133,163]. A common assumption behind these steel material models is that steel bar behaves identically in tension and compression in terms of engineering stress and strain. This assumption is valid under small and moderate strain levels, but questionable under large strain levels as experienced by RC columns during strong earthquakes, because the stress-strain behavior in compression differs from that in tension as a result of steel bar necking/fracture in tension and bar buckling in compression. In particular, buckling of steel bar, causing softening behavior of steel in compression, can dramatically reduce the ductility of the flexural RC members subjected to seismic loading

[164,165]. Consequently, neglecting the post-buckling behavior of steel bar can lead to overestimation of the ductility and underestimation of post-peak strength degradation in RC structures, acknowledging the fact that longitudinal steel bar play an important role in ensuring a ductile behavior of RC members. As such, realistic prediction of post-peak behavior of RC structures during strong earthquakes requires the steel constitutive model to consider the advanced aspects (e.g., buckling).

Numerous studies in the literature proposed constitutive models, i.e., average stress-strain relationships for steel bar including buckling, based on experimental and numerical observations [46,166–170]. All of these relationships implicitly or explicitly suggest the dependency of the compressive behavior on the critical buckling length-to-diameter ratio (i.e., slenderness ratio) of reinforcing bar. However, one major limitation in those constitutive models for steel including buckling is that their developments did not consider the finite flexibility of lateral reinforcements (i.e., stirrups or ties). To be specific, they were developed with a common setup in the experimental and numerical models, which represent a bare bar supported by double-rollers at both ends, assuming the steel bar is fixed against lateral deflection and rotation at the stirrup/tie locations [168,170]. In other words, it is assumed that steel bar buckles between two adjacent stirrups. However, analytical studies [171] showed that this assumption was not always true, because bar buckling length can be multiples of stirrup spacing as evidenced in experiments [172]. It is also important to point out that stirrups within the buckling length serve as flexible supports with finite stiffness and can interact with the lateral deformation of buckled bar, thus affecting the post-buckling behavior. To sum up, it is important to consider the effect of the finite stiffness of lateral supports provided by stirrups on both the critical buckling length/load and post-buckling behavior.

In order to account for the effect of lateral reinforcement on the critical buckling length/load of steel bar in RC members, several research works conducted theoretical, numerical, and experimental studies in this regard. Russo [173], as one of pioneering works in this field, determined the critical buckling length measured by the number of stirrup/tie spacing according to their stiffness. In that study, the buckling shape in each span (i.e., between two adjacent stirrups/ties) was assumed to follow a combination of sine and cosine functions and considered the single-sided boundary conditions for steel bar in RC structures. This work provided the theoretical basis of many other studies (Dhakal and Maekawa 2002; Sato and Ko 2007; Massone and López 2014, Minafò and Papia 2017) for estimating critical buckling length and load. In contrast, other studies assumed simpler buckling shapes to determine the critical buckling length [175,176]. The estimated critical buckling length was used to modify the slenderness ratio and correspoinding post-buckling behavior [175] in order to consider the effect of lateral reinforcements. Zong et al. (2014) also introduced modifications to the post-buckling behavior based on the stiffness of confining steel, which were assumed to be elastic. It is worth mentioning that there have been some studies on proposing simple bilinear models representing nonlinear behavior of lateral support provided by transverse reinforcement [177,178]. In spite of such efforts, no existing models for steel bar including buckling appropriately account for the effect of nonlinear supports from lateral reinforcements. It is also worth mentioning that the earlier work [179,180] also examined the relationship between longitudinal bar buckling and stirrups/ties, but their primary purpose was to define details for stirrups/ties to prevent steel bar buckling before its yielding.

The effect of the finite stiffness and nonlinear lateral supports provided by stirrups/ties becomes more important for steel bar in RC columns with sub-standard quality. Examples are under-designed or severely corroded RC columns, in which steel bars are more susceptible to buckling [36,140]. The reason behind this is three-folded: (1) increased slenderness of steel bar due to corrosion-induced reduction in their cross-sectional area; (2) reduced stiffness of stirrups due to corrosion-induced reduction in their cross-section areas; and (3) the possibly increased stirrup spacing due to corrosion-induced damage. Similar to the influence of corrosion-affected longitudinal steel bar on the buckling behavior [36,140], corrosion of lateral reinforcements can have a substantial impact on the steel bar buckling behavior. Furthermore, corrosion-induced concrete spalling, as caused by large compressive strain experienced during earthquakes [181], reduces the lateral restraint for longitudinal reinforcements and increase the tendency of steel bar buckling outwards. All of these factors highlight the need to develop a material model for steel bar including buckling considering lateral support flexibility with nonlinearity appropriately included. To the best of the authors' knowledge, no existing models have taken this into account.

To address the needs and gaps identified above, the objective of this study is to develop a constitutive model to represent average stress-strain behavior for steel bar with buckling considering the flexible lateral support provided by transverse reinforcement. Compared to similar models existing in the literature, the novelty of this developed model is its appropriate consideration of transverse reinforcement flexibility, which is particularly valuable for simulating RC columns with deficient transverse stirrups (e.g., those under-designed or with severe corrosion) under extreme loading conditions. To this end, this study firstly develops a FE model for a steel cage to simulate the buckling behavior of steel bar laterally supported by stirrups/ties and the core of an RC column. The capability of the FE model is then validated using experimental data acquired from the literature for bare steel bars that bucked between to two adjacent stirrups, at which the lateral deflection and rotation is fixed (e.g., assuming rigid stirrups/ties). To verify the need to consider the flexibility and nonlinearity of transverse reinforcement, their effect on critical buckling length/load and post-buckling behavior is further demonstrated using the developed FE model. In order to develop a new constitutive model for steel bar with buckling, the developed FE model, referred to as numerical buckling test, was used to generate a large database for the average stress-strain relationships of steel bar with buckling after considering different important influencing factors. Using this database, the new constitutive model is developed following two main steps: detecting the onset of buckling and modifying the stress-strain curve of the steel material model without buckling based on crucial influencing parameters. Before proceeding to the conclusion, the newly developed constitutive model is verified by numerical buckling tests, and applied in FE modeling of two RC columns (i.e., uncorroded and corroded).

5.2. NUMERICAL BUCKLING TEST

To develop a macroscopic uniaxial model for steel bar with buckling against flexible transverse reinforcement, this study designs a numerical test setup using fiber beam-column elements. Specifically, a FE model of a circular steel cage, consisting of longitudinal bar supported by transverse reinforcement and the single-sided support from the concrete core, is used to model the average stress-strain behavior of reinforcing bar including buckling. Note that it is assumed concrete cover has spalled off when steel bar buckles. This FE model is developed in *OpenSees* [65] by taking advantage of the nonlinear steel material model without buckling, e.g., *Steel02* [133] and *SteelDRC* [102], and the geometric nonlinearity. After FE validation, it is employed to generate a comprehensive database for the average stress-strain behavior of reinforcing bar including buckling, which is used for new constitutive model development in the next section.

5.2.1. FE model for a steel cage

The steel cage model developed can include adequate number of transverse reinforcement (e.g., stirrups), depending on the critical buckling length (i.e., L_{cr}) as detailed later. Figure 5-1 (a) describes the schematic view of an example steel cage model with one longitudinal bar laterally supported by the concrete core and four stirrups spaced by l. In this model, it is assumed that the first mode of buckling occurs along the critical length (i.e., $L_{cr} = 3l+2\eta l$), so that the boundary condition of the top and bottom of the steel bar is equivalent to the double-roller boundary condition, i.e., the steel bar is fixed against lateral deflection and rotation at the end of critical buckling length as commonly used at the end of buckling length in other studies [168,170]. Note that the length ηl used for the top and bottom spans is determined based on the ratio of L_{cr} and l with $0 \leq \eta < 1$. When the compressive force $\boldsymbol{P}$ is applied to both ends of the steel bar, lateral deformation may develop as a result of minor imperfections in the steel bar, leading to buckling which can be initiated in the model by applying a small amount of lateral deformation to the midpoint of the buckling length. Furthermore, due to the presence of confined concrete in the core of RC members, the lateral deflection of the longitudinal steel bar toward the core concrete is prohibited. Similarly, the transverse reinforcements are supported by the core concrete, which prevents their deformation toward the core concrete.

The described steel cage is modeled in *OpenSees*, as shown in Figure 5-1 (b) and (c). The longitudinal steel bar is discretized to a large number of *dispBeamColumn* elements, so that the element length is equal to steel bar diameter. Each element consists of four Gaussian-Lobatto integration points, at each of which a fiber section is assigned. The material model used for the steel fibers is the uniaxial material relationship for steel with no buckling effect considered, i.e., *SteelDRC* developed by [102,182]. This uniaxial material model can take into account the ultimate stress and strain of the steel behavior on the tension side, as schematically shown in Figure 5-1 (d). This model is defined with steel yield stress (σ_y), elastic modulus (E_s), strain at the onset of strain hardening branch (ε_{sh}), ultimate stress (σ_u) and strain (ε_u), and fracture strain ($\varepsilon_{\mathrm{fracture}}$). It is worth noting that the tensile stress will decrease after reaching the ultimate strain due to necking until fracture, while the magnitude of compressive stress will linearly increase after the ultimate point. More details about this uniaxial material model can be found in [102].

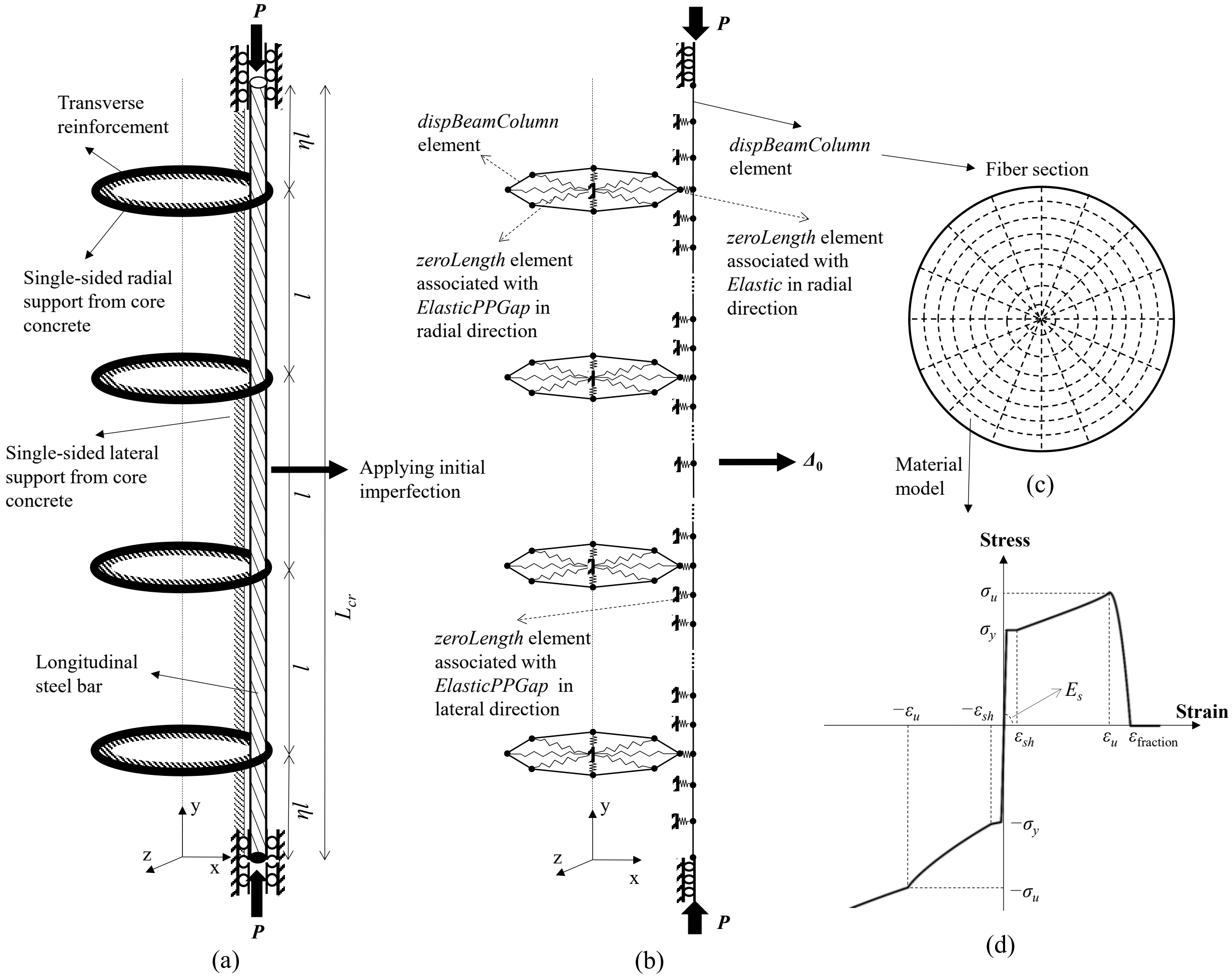

Figure 5-1: (a) Schematic view of the steel cage model, (b) corresponding FE model, (c) fiber section used for steel bar, and (d) material model assigned to fibers of steel bar

To model steel bar buckling appropriately, single-sided supports provided by the core concrete are represented by compression-only springs. These compression-only springs are defined by *zeroLength* elements and *ElasticPPGap* material with extremely high stiffness (quasi-rigid) in compression. To account for the flexibility of transverse reinforcements, the stirrups are modeled with a number (e.g., 16) of *dispBeamColumn* elements associated with four Gaussian-Lobatto integration points in a similar manner to longitudinal bar. Compression only springs are used to provide single-sided supports from core concrete for stirrups in the radial direction. The transverse stirrups are connected to the longitudinal steel bar using *zeroLength* elements with extremely high stiffness (quasi-rigid) assuming that the radial movement of stirrups is compatible with the outward movement of the longitudinal bar at their intersection point.

5.2.2. Critical buckling length determination

To develop the FE model of the steel cage model as described above, it is necessary to pre-determine the critical buckling length. As per the theoretical studies [171,173], a steel bar of infinite length with single-sided supports can buckle with the deflected shape consisting of non-interfering half-waves with equal length. Thus, it is sufficient to consider the deflected shape with a single half-wave as shown in Figure 5-2 (a), when the steel bar buckles with a number of elastic springs restraining the outwards buckling [171,173]. The half-wave between two adjacent springs (j^{th} span) contains a combination of sine and cosine functions in addition to the compressive force P and $M(j)$, which is the bending moment due to the reactions of the built-in end and the supports. With these presumptions, the critical buckling length (L_{cr}) can be estimated based on the stirrup/tie spacing (i.e., l) and the relative stiffness of lateral supports provided by transverse reinforcement with respect to the longitudinal bar (i.e., γ).

The stiffness of lateral supports provided by transverse reinforcement can be determined based on Eq. (5-1) [171]:

$$\alpha = \frac{2E_h(\pi d_h^{\,2}/4)}{D_{core}} \tag{5-1}$$

in which d_h is the diameter of transverse reinforcement (e.g., stirrups), E_h is the instantaneous modulus of the steel used for the transverse reinforcement, and D_{core} is the diameter of core concrete. The relative stiffness of lateral supports provided by transverse reinforcement with respect to the longitudinal steel bar (i.e., γ) can be defined in Eq. (5-2) [173]:

$$\gamma = \frac{\alpha l^3}{E_{sr} I} \tag{5-2}$$

in which, I denotes the moment of inertia of the longitudinal bar, and E_{sr} stands for the reduced elastic modulus of longitudinal steel, as estimated by Eq. (5-3) based on the initial elastic modulus E_s and the strain hardening ratio b [171]:

$$E_{sr} = E_s(2.13b^{0.88} - 4.11b^2) \tag{5-3}$$

To facilitate determining the critical length (i.e., L_{cr}) effectively, which is needed in the constitutive model of steel bar including buckling considering the transverse reinforcement flexibility, Eq. (5-4) is established by least-square curve fitting. The critical length for various values of γ is computed numerically (Russo 1988), a curve is fitted, as shown in Figure 5-2 (b). It is worth noting that the high R-squared (R^2) value presented in Figure 5-2 (b) indicates the high accuracy of the curve fitting.

$$L_{cr} = l(-0.04(\log\gamma)^3 + 0.72(\log\gamma)^2 - 3.13(\log\gamma) + 5.57) \tag{5-4}$$

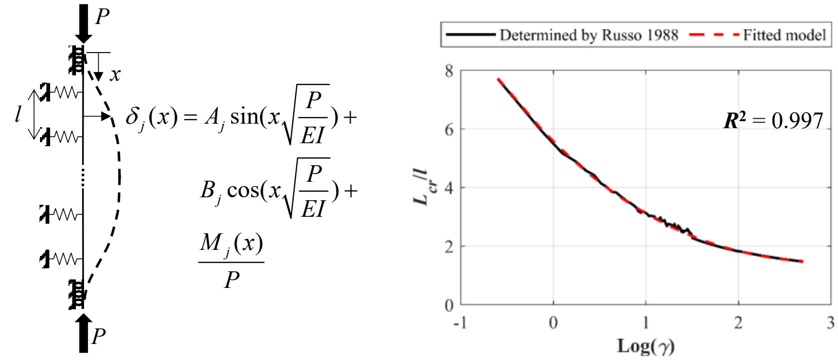

(a) (b)

Figure 5-2: (a) Deflected shape of steel bar along critical length, and (b) critical buckling length determination

5.2.3. FE model validation

Before using the FE model described above as a numerical test setup for bar buckling behavior prediction, it is first validated based on available experimental tests. However, the experimental tests conducted in the literature presupposed that that the lateral support offered by transverse reinforcement is rigid and buckling occurs within a single span, as evidenced by the double-roller boundary condition at the end of stirrup/tie spacing. Due to this limitation, those experimental tests are used to validate the FE model, when the lateral reinforcements in the FE model are extremely stiff, e.g., assuming large tie diameters (d_h).

For the purpose of validation, this study employs experimental tests of three bare steel bar supported by double rollers under static cyclic pushover tests [170]. Figure 5-3 (a) to (c) present the comparison of the FE-predicted and experimental (average) stress-strain hysteresis of the steel bar with slenderness ratios equal to 5, 8, and 11, respectively. Here, the slenderness ratio is defined as the ratio of the length of one span l to bar diameter d_b. Additionally, the uniaxial material behavior of steel with no effect of buckling is shown in this figure as a reference. Comparing FE predictions with experimental observations indicates the satisfactory correlation between these results and significant improvement in capturing the severe buckling effect, specifically in cases with relatively high slenderness ratios. This proves the capability of the numerical tests in accurately simulating the buckling behavior of steel bar. Although the stirrups/ties are considered to be highly strong, it is important to note that the flexibility of lateral reinforcements may alter the steel bar buckling behavior, necessitating conducting additional experimental steel cage that is beyond the scope of this study. However, since the developed FE model is capable of capturing this impact, it is employed as a numerical test setup in the following section to generate the data needed for the material model development.

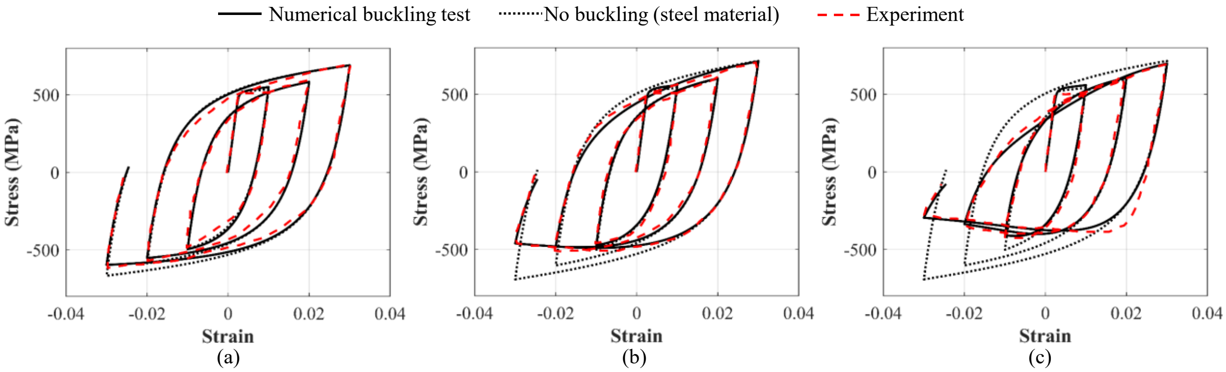

Figure 5-3: FE model validation of experimental steel bar [170] **with (a) l/d_b = 5, (b) l/d_b = 8, and (c) l/d_b = 11**

Furthermore, to demonstrate the effect of flexibility of transverse reinforcements on the buckling behavior of steel bars, Figure 5-4 presents two numerical tests with l/d_b = 10 laterally supported by flexible and rigid stirrups. Comparing the stress-strain behavior of numerical test with extremely weak stirrups and that of the test with rigid lateral supports shows that considering extremely weak transverse reinforcement, i.e., low stiffness of lateral supports, results in significantly different simulations. On the other hand, Figure 5-4 (b) indicates using extremely strong stirrups leads to the same simulations as the case with rigid stirrup assumption. This comparison reveals that it is necessary to account for the flexibility of transverse reinforcements in the steel bar buckling model,

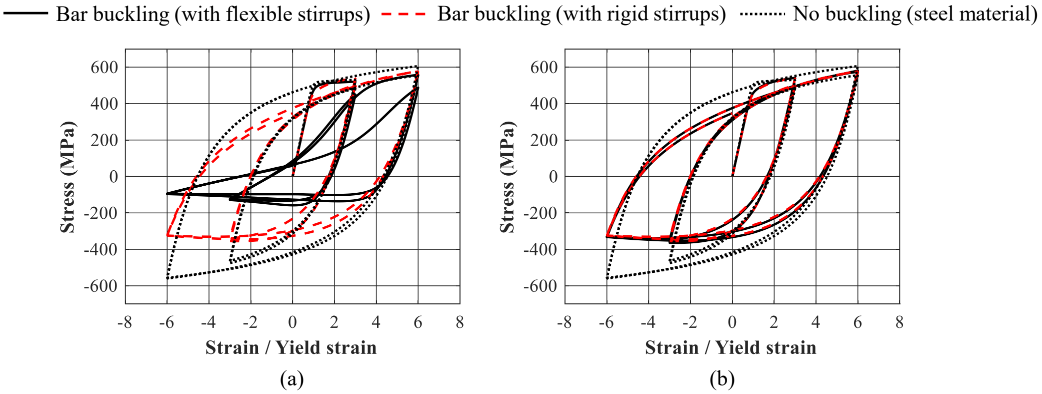

Figure 5-4: Effect of flexibility of transverse reinforcement for steel bar with l/d_b = 10 supported by (a) extremely weak and (b) extremely strong stirrups

5.3. NEW CONSTITUTIVE MODEL DEVELOPMENT

This section puts forward developing a constitutive model, i.e., average stress-strain relationship, for steel bar with buckling after accounting for the support flexibility provided by transverse reinforcements. To this end, a comprehensive database is generated using the validated FE model for the numerical buckling test. This database is employed to develop the new constitutive model, for which first the onset of buckling is determined and then the steel material model without buckling is modified to take the buckling effect into account. The newly developed constitutive model is verified using numerical buckling tests under different scenarios in this section.

5.3.1. Database generation

The numerical buckling tests discussed in the previous section is utilized here to generate a comprehensive database, considering realistic ranges for geometrical and material properties of a circular steel cage used in RC columns. Table 5-1 summarizes the considered geometrical properties such as slenderness ratio l/d_b, longitudinal bar diameter d_b, stirrup diameter d_h, and core concrete diameter D_{core}, as well as the relevant material model properties, such as yield stress (F_y for longitudinal steel bar and F_{yh} for transverse reinforcement), ultimate stress and strain of longitudinal steel bar (F_u and ε_u), and strain hardening ratio of lateral steel bar b_h. Note that the elastic modulus of both lateral and longitudinal steel bar (E_{sh} and E_s) are considered to be constant. The volumetric ratio of transverse reinforcement ρ_h, defined in Eq. (5-5), is also reported in this table, which shows that the ranges considered reflect the practical range as commonly used in engineering practice.

$$\rho_h = \frac{\pi d_h^{\,2}}{(l/d_b) d_b D_{core}} \tag{5-5}$$

Table 5-1: Parameters and their ranges considered for database generation

Longitudinal reinforcement		**Transverse reinforcement**	
l/d_b	6 – 22	d_h	4 – 12 mm
d_b	10 – 24 mm	D_{core}	400 – 1500 mm
F_y	300 – 600 MPa	F_{yh}	200 – 600 MPa
F_u	Calculated based on strain hardening ratio of 0.001 – 0.04	b_h	0.001 –0.04
ε_u	0.06 – 0.16	ρ_h	Calculated based on d_h and D_{core} (0.0001 – 0.09)
E_s	210,000 MPa	E_{sh}	210,000 MPa

In order to adequately consider different values for the properties from the introduced practical ranges, a Latin Hypercube Sampling [135] technique is used to generate 1000 cases, assuming the properties are uniformly distributed in the considered ranges. For each case, the critical buckling length is determined using Eq. (5-4), and the FE model is developed accordingly. Figure 5-5 describes the database generation process.Static cyclic pushover analysis is carried out for each FE model while adjusting the loading amplitude for each sample, taking into consideration one case with buckling and one case without buckling for each sample. The average stress-strain behavior (σ and ε) that resulted from these samples are included in the database, utilized later to develop the constitutive model for steel bar with buckling.

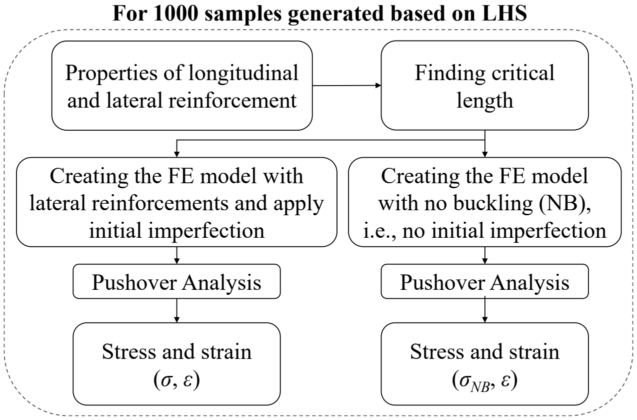

Figure 5-5: Database generation process

5.3.2. Proposed constitutive model

This section presents the development of new constitutive model for steel bar with lateral buckling, which takes into account the flexibility of transverse reinforcements. Prior to the onset of buckling at tensile or low compressive loading levels, the steel bar behave like a truss member with the local stress and strain distribution uniform over the cross section, and thus the average stress-strain coincide with that of the steel material. However, when compressive loading continues, the longitudinal bar tends to buckle outwards with reduced axial restoring force. After the buckling, the steel bar behaves like a beam, the local stress and strain over the cross section is non-uniform, and the average stress-strain behavior of the steel bar is altered. This leads to the need to a uniaxial constitutive model for steel bar with buckling.

The first step to develop the constitutive model for steel bar with buckling is by modifying the stress-strain behavior of steel material is to detect of the onset of buckling, which is supposed to occur at the instant that the steel bar within the critical length tends to deflect laterally. For simplicity, the deflected shape is assumed to follow a simple cosine function along the entire critical buckling length, as commonly adopted in the literature [168,176]. Figure 5-6 compares the cosine deflected shape with the shape function used for critical length determination [173], which demonstrates the adequate accuracy provided by the cosine shape function. However, this simplification greatly simplify the mathematical computations for detecting the onset of buckling.

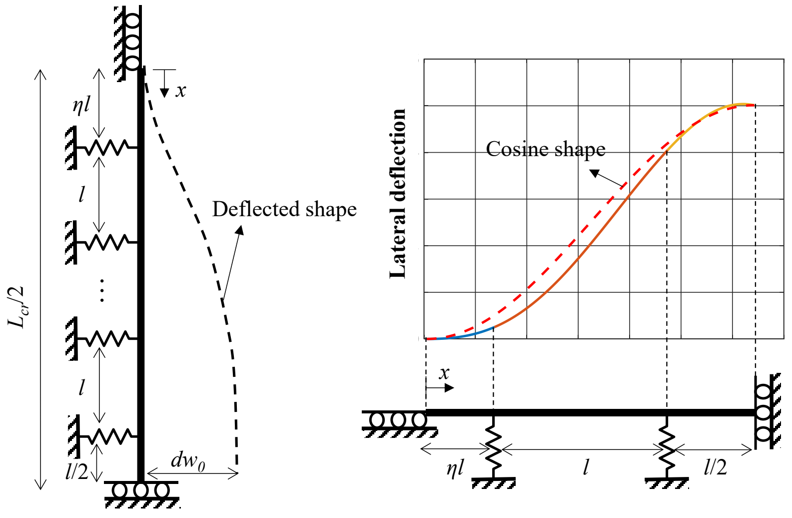

(a) (b)

Figure 5-6: Simplified schematic model for steel bar along the half of the critical length, and (b) comparison of deflected shape based on cosine function and shape function proposed by Russo (1988)

The deflection shape function can be described by the deflection at the mid-point (i.e., dw_0) using Eq. (5-6):

$$\delta(x) = \frac{dw_0}{2}\left(1-\cos\left(\frac{2\pi x}{L_{cr}}\right)\right) \tag{5-6}$$

The relationship between the moment and axial load can be determined using this deflected shape and the moment equilibrium for the half-length of steel bar, following the similar approach as [168]. Different from the derivation proposed in [168] for detecting the onset of buckling where a single span is considered with rigid ties at both ends, here m springs are used representing the lateral supports provided by transverse reinforcement along the critical length. The stiffness k_s for these springs are determined as the same sectional tangent stiffness presented in [168]. In the end, the average stress at the onset of buckling is determined according to Eq. (5-7):

$$\begin{aligned}
\sigma_{cr} &= \max(\sigma_{cr}^{1}, \sigma_{cr}^{2}) \\
\sigma_{cr}{}^{1} &= \frac{\pi}{(2n+1-\eta)^2 \left(l/d_b \right)^2}\left[\frac{\gamma_{12}\gamma_{21}\pi E_s}{\gamma_{11}} - \gamma_{22}\pi E_s - \frac{2k_s(2n+1-\eta)^2}{\pi^2 d_b}\left(l/d_b \right)^3 \right. \\
&\quad \left. \times \sum_{i=1}^{n}\left((\eta+i-1)\left(1-\cos\left(\frac{2\pi(\eta+i-1)}{2n+1-\eta}\right)\right)\right)\right] \\
\sigma_{cr}{}^{2} &= -\frac{\gamma_{22}\pi^2 E_s}{(2n+1-\eta)^2}\left(l/d_b \right)^{-2} - \frac{2k_s\left(l/d_b \right)}{\pi d_b} \times \sum_{i=1}^{n}\left((\eta+i-1)\left(1-\cos\left(\frac{2\pi(\eta+i-1)}{2n+1-\eta}\right)\right)\right)
\end{aligned} \tag{5-7}$$

where $n = m/2$. Once the average stress reaches the critical stress defined above, the strain ε_B corresponding to σ_{cr} is also obtained. Furthermore, since the critical stress found here coincides with the onset of buckling, indicating the ties are still in their initial linear elastic behavior, it is assumed that k_s is equal to the initial stiffness of the transverse reinforcement, presented in Eq. (5-8) [178]:

$$k_s = \frac{2E_{sh}(\pi d_h{}^2/4)}{D_{core}} \tag{5-8}$$

To model the post-buckling strength degradation for the steel bar, this study proposes a modification function, see Eq. (5-9). This function aims to modify the material stress $\sigma_{NB}(\varepsilon)$ derived from the uniaxial steel material model with no buckling.

$$\sigma_{buckled} = \sigma_{NB}\exp(b - a\varepsilon_N) \text{ with } \varepsilon_N = \frac{\varepsilon_B - \varepsilon}{\varepsilon_B + \varepsilon_u} \tag{5-9}$$

This functional form and the coefficients a and b are learned from the database within two steps. The first step is obtain the optimal values of a_i and b_i for case i (with i = 1 to 1000) by least-square curve fitting. The R-squared (R^2) values for all the 1000 cases are shown in Figure 5-7 (a), and the high values obtained for R-squared (R^2) indicate that the suggested functional form with the coefficients a_i and b_i represent the database well. The second step is to relate coefficients a and b to steel cage properties using the derived datasets for (a_i, b_i) with i = 1 to 1000 based on Bayesian linear regression [130]. Eq. (5-10) presents the posterior mean prediction of a based on the circular steel cage properties:

$$a = ({}^{l}\!/\!{}_{d_b})^{1.46}\rho_h^{-0.10}\varepsilon_u^{1.07}b_h^{-0.09}\times\exp(\frac{0.09F_y}{400\text{ MPa}} - \frac{0.07F_u}{400\text{ MPa}} - 0.88) \tag{5-10}$$

The predictive performance of Eq. (5-10) is examined with its comparison to the observations in derived datasets for (a_i, b_i), as shown in Figure 5-7 (b) with R^2 = 0.73. As seen, the data points are closer to the 45° line, indicating a high degree of agreement between the predicted and observed values. Similarly, the model parameter b is estimated as follows:

$$b = 0.017 + (e \sim \tag{5-11}$$

in which e is the error of the model following the normal distribution with zero mean and standard deviation of s, distributed by chi-squared with mean of 0.025 and standard deviation of 0.0055. The probabilistic estimation of b is depicted in Figure 5-7 (c) together with all the corresponding data points. This probabilistic form for model parameter *b* (and similarly for model parameter *a*) empowers the material model to consider the uncertainty inherent in this model in the probabilistic analysis; however, the mean value of *b* will be simply used in the deterministic model in this study.

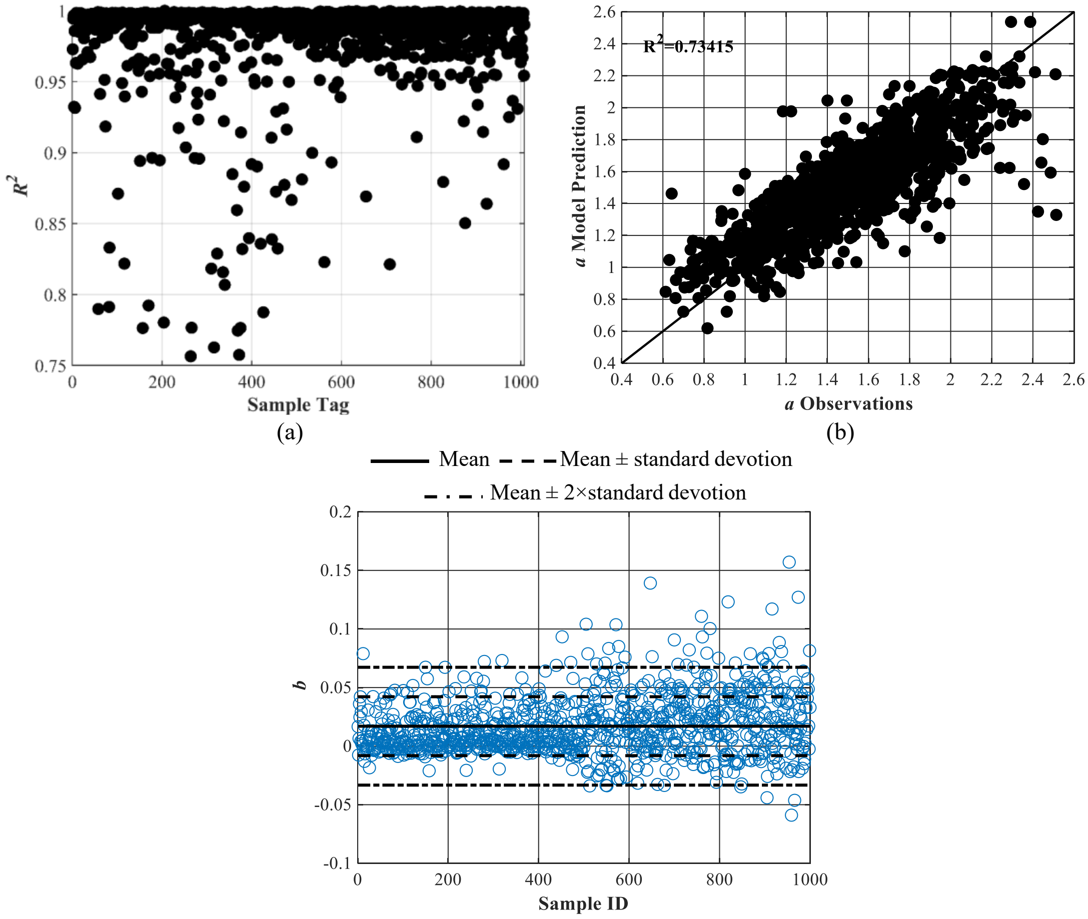

(a)

(b)

(c)

Figure 5-7: (a) Performance of proposed curve fitting for 1000 cases in step 1, (b) observation vs. prediction for model parameter *a* ins step 2, and (b) variations of model parameter *b* in comparison with data points

With the buckling stress determined in Eq. (5-7) and the modification factor in Eq. (5-9), together with associated model parameters stated in Eqs. (5-10) and (5-11), new constitutive model can be developed by modifying the material model for steel without buckling. To summarize, the framework for developing new constitutive models for steel with buckling can be as follows (see Figure 5-8). Firstly, the critical buckling length is evaluated based on the relative stiffness of the lateral reinforcement to the longitudinal steel bar, i.e., γ as shown in Eq. (5-2). Depending on the buckling state, the required modifications will be applied to a base steel material model $\sigma_{NB}(\varepsilon)$ without buckling. In particular, if the bar was not under the buckling stage, i.e., there is no stored ε_B, it should be assessed whether the current stress has reached the critical stress (σ_{cr}). In case of reaching the onset of buckling, the proposed modification function is used to reduce the material stress $\sigma_{NB}(\varepsilon)$ to find $\sigma_{buckled}(\varepsilon)$; otherwise, no modification is required. The strain at the onset of buckling (i.e., ε_B) is then stored until the strain exceeds ε_B. As long as $\varepsilon<\varepsilon_B$, the modifications are applied to the stress determined based on the steel material model $\sigma_{NB}(\varepsilon)$.

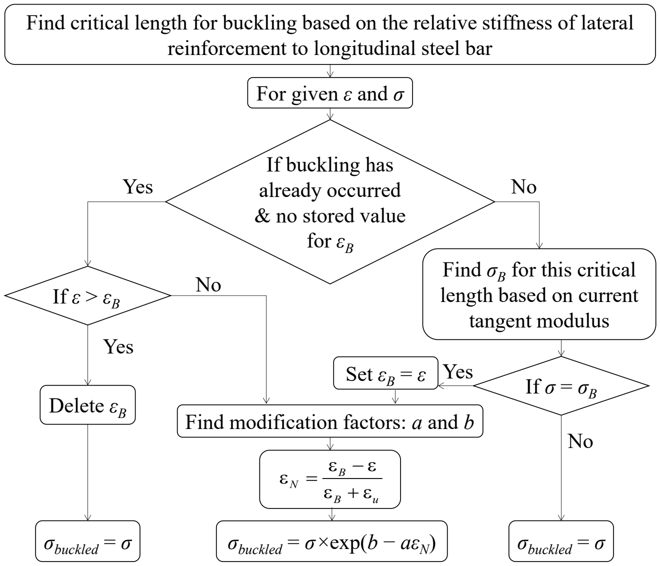

Figure 5-8: Flowchart of the proposed framework for developing a constitutive model for steel bar with buckling

It is worth noting that the above constitutive model considering the flexibility of transverse reinforcement enable it to incorporate corrosion effects more appropriately. As mentioned earlier, the increased vulnerability to buckling caused by corrosion must be taken into account in order to reflect the corrosion impact on computational modeling of RC structures [183]. The corrosion-induced reduction of longitudinal steel bar cross-sectional area can be readily adjusted by slenderness ratio by updating the critical buckling length/load and the bar diameter. More importantly, corrosion-induced reduction of cross-sectional area of transverse reinforcement can also be taken into account by updating the critical buckling length/load and corrosion-reduced volumetric reinforcement ratio.

5.3.3. Constitutive model verification

This proposed material model is implemented in *OpenSees* as *SteelBuck03*, which is based on *SteelDRC* with required modifications for buckling. To verify this material model, two unseen numerical tests (i.e., not used in the database generation for model development) are considered: one with $l/d_b = 8$ and $\rho_h = 0.004$, and the other one with $l/d_b = 12$ and $\rho_h = 0.01$.

Figure 5-9 presents the comparison between the average stress-strain of the buckled bar as acquired from the numerical buckling tests and the stress-strain determined using the new constitutive model proposed for the steel bar with buckling against flexible stirrups. As reference, the stress-strain relationship of the steel material behavior (no buckling) is also shown. It is observed that buckling effect is significant for these two cases considered because of the high slenderness ratios for longitudinal bar. However, the newly proposed constitutive model perform well when compared with the numerical buckling tests. In addition, the stress-strain for the steel bar with buckling against rigid stirrups, as similar to that proposed by [168], is presented for comparison. It shows that the rigid stirrup assumption leads to worse prediction results, especially for the case as shown in Figure 5-9 (a) with low ρ_h. The improvement obtained by the newly developed constitutive model shows it outperforms the existing buckling models developed assuming rigid stirrups. Using the proposed material model can potentially improve the accuracy of nonlinear behavior simulation of RC structures that are impacted by steel bar buckling, particularly for those cases with flexible stirrups (e.g., under-designed or severely corroded columns).

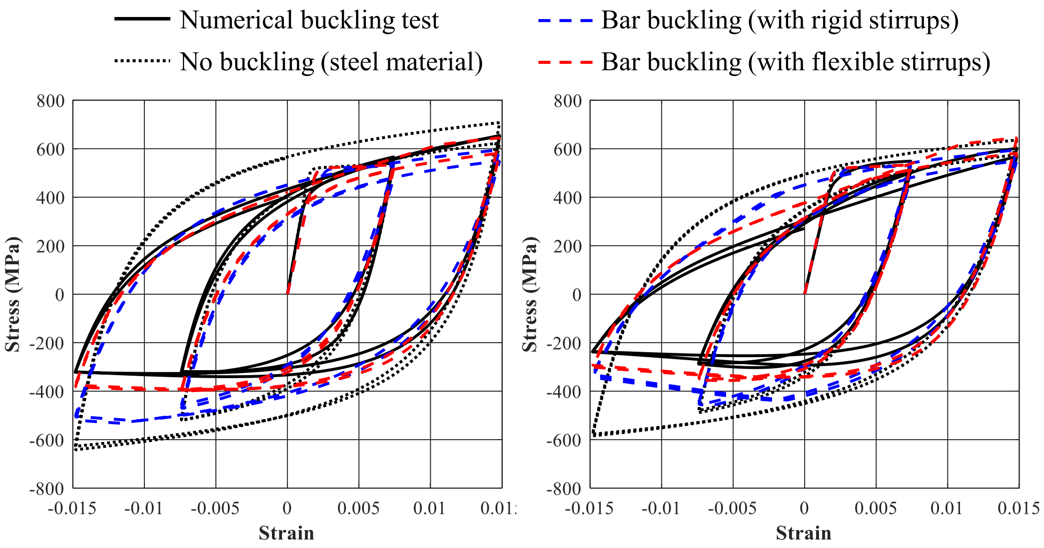

(a)

(b)

Figure 5-9: Steel bar buckling behavior with (a) l/d_b = 8 and ρ_h = 0.004, and (b) l/d_b = 12 and ρ_h = 0.01

The newly proposed constitutive model, implemented in *OpenSees* as *SteelBuck03* is also enhanced to be able to model the buckling behavior of corroded steel bar based on the percentage of mass loss ratios (defined as corrosion levels) of longitudinal and lateral reinforcements. To reveal the performance of this model with the additional feature for corroded steel bar, two more cases with longitudinal bar and lateral reinforcements with l/d_b= 10 and ρ_h = 0.008 before corrosion are considered here: one with corrosion level = 20% and the other one with corrosion level = 40%. Figure 5-10 presents the average stress-strain behavior of the steel bar in the numerical buckle tests, in comparison with the counterpart generated from proposed constitutive model. As reference, the stress-strain relationship of the steel material behavior (no buckling) is also shown. This comparison reveals the capability of the proposed constitutive model in capturing the impact of corroded longitudinal and lateral reinforcements on the buckling behavior of steel bar, even in cases with minor corrosion effects. This further verifies the proposed material model to be used in computational modeling of RC structures under severe corrosion.

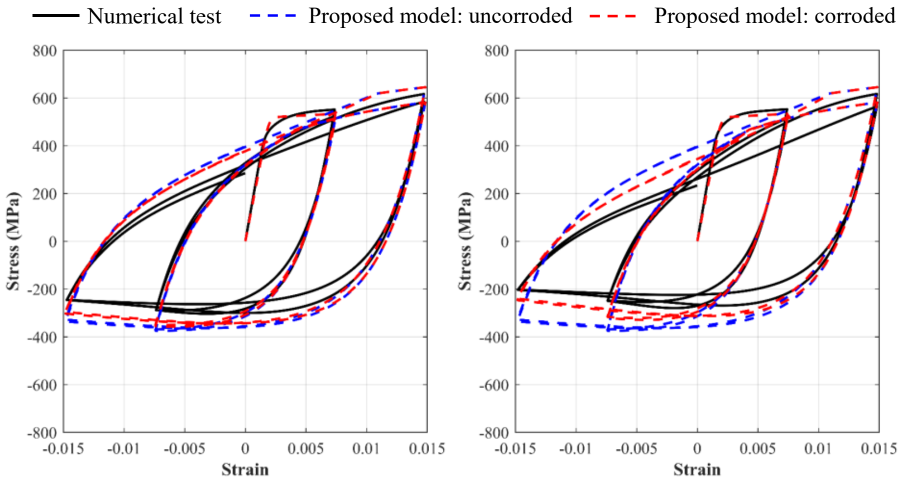

(a) (b)

Figure 5-10: Steel bar buckling behavior under corrosion effects: (a) 20% and (b) 40% mass loss ratio for longitudinal and lateral reinforcements

The framework used for constitutive model development to consider buckling effects can also be applied to a different base material model for steel, such as the widely used Giuffre-Menegotto-Pinto model, i.e., *Steel02*. To verify this, another constitutive model for steel bar with buckling is also developed and implemented in *OpenSees* as *Steel02BS*. Like *Steel02*, *Steel02BS* assumes indefinite strain hardening and is applicable when ultimate strain capacity is not concerned, and it is found that considering the ultimate strain on the tensile side or not does not affect the buckling behavior of steel on the compression side. When the tensile behavior of *Steel02* and *SteelDRC* are close before reaching the ultimate strain as shown in Figure 5-11 (a), except a minor difference in the plateau that is included in *SteelDRC* but neglected in *Steel02*, the compressive behavior of *Steel02BS* is comparable with *SteelBuck03*, see Figure 5-11 (b). To further clarify the similar behavior of these two material models (i.e., *Steel02BS* and *SteelBuck03*), Figure 5-11 (c) depicts the cyclic behavior of these models with minor differences in unloading/reloading stiffness.

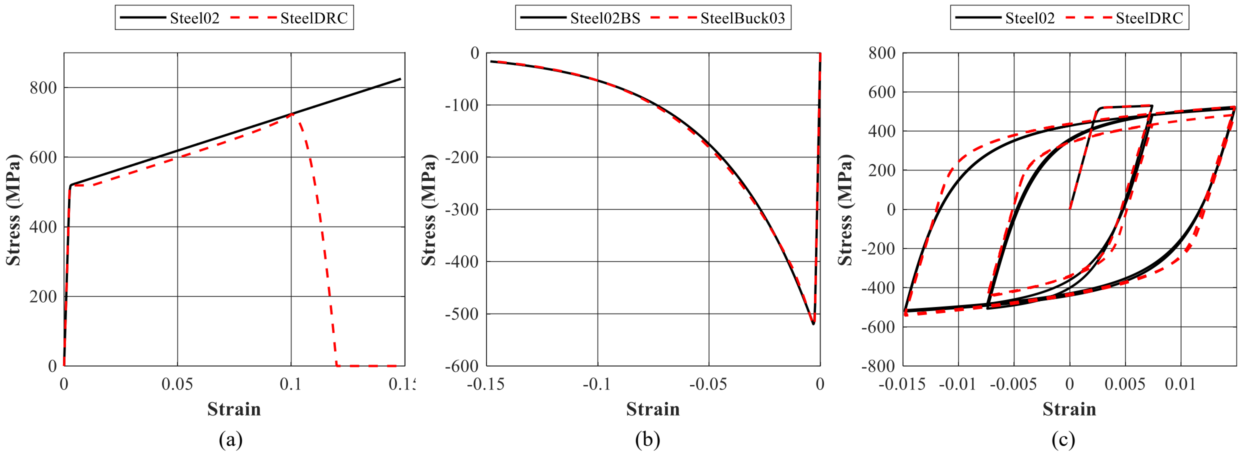

Figure 5-11: Comparison between *Steel02* and *SteelDRC* as the basis of the proposed material model: (a) monotonic stress-strain behavior of these two models (a) on tension side (without buckling) and (b) on compression side (with buckling) with l/d_b=10 and ρ_h=0.005, and (c) cyclic stress-strain behavior of these two models with buckling

5.4. APPLICATIONS OF PROPOSED CONSTITUTIVE MODEL

In this section, the proposed material model implemented in *OpenSees* (i.e., *Steel02BS*) is used for computational modeling of two experimental RC columns tested in the literature [136]: one with pristine condition and one under artificial corrosion. The bottom segment of the corroded RC column, i.e., within 450 mm above the top of anchorage zone, was affected by a corrosion level of 6% for longitudinal bars and 12.91% for lateral reinforcements. These two columns were subjected to static cyclic lateral loading until flexural failure with a constant axial load applied on the top. Figure 5-12 (a) presents the geometrical properties and loading protocols of both corroded and uncorroded columns.

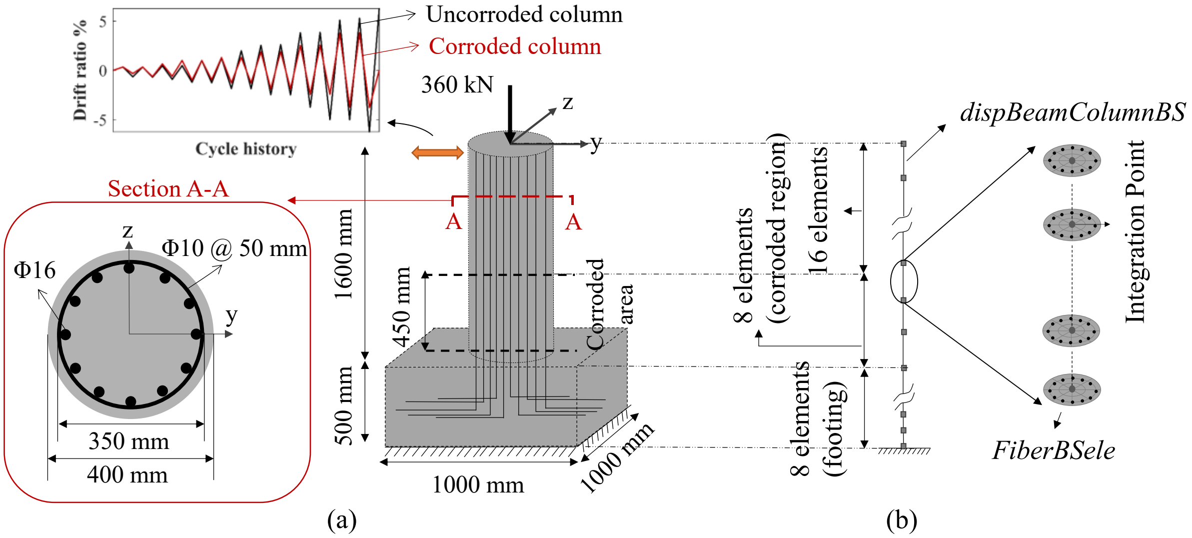

Figure 5-12: Schematic view of (a) geometry, loads, cross-section, and (b) FE model for RC columns

As revealed in [183], bond-slip played an important role for response simulation of these corroded RC columns, and thus the modeling approach employing the recently developed fiber-based frame elements with bond-slip (i.e., *dispBeamColumnBS*) is used. The schematic view of the corresponding FE model developed in *OpenSees* for these two columns is presented in Figure 5-12 (b). Table 5-2 summarizes the key properties associated with the material models employed in the FE model for both uncorroded and corroded columns. Note that the properties of uncorroded model are determined based on the experimental data reported in the literature [136] and Mander's equations [45] to consider the confinement effect for core concrete. As found by [183], steel bar buckling was also observed and thus considered in this study using the constitutive model developed. To capture the effect of steel bar buckling on the nonlinear behavior simulation of the RC columns, two FE models are defined for each column, one using the proposed constitutive model for steel bar with buckling, i.e., *Steel02BS*, and one with the material model for steel with no effect of buckling, i.e., *Steel02*. Static cyclic pushover analyses are conducted using these two FE models for each of the two RC columns (i.e., uncorroded and corroded).

Table 5-2: Summary of uncorroded and corroded properties for RC columns

Material		Properties				
		Symbol	**Description**	**Unit**	**Value**	**Source**
Steel		f_y	Yield stress	MPa	400.0 (388)	Material coupon test
		b	Strain hardening ratio	–	0.007 (0.007)	Material coupon test
		E_s	Young's modulus	MPa	210000.00 (210000.0)	Material coupon test
Concrete	Unconfined	f_c	Concrete compressive strength	MPa	−40.00 (−37.26)	Material coupon test
		f_{cu}	Ultimate compressive strength	MPa	−8.00 (−8.00)	[106]
		ε_c	Strain corresponding to f_c	–	−0.002 (−0.002)	Material coupon test
		ε_{cu}	Strain corresponding to f_{cu}	–	−0.008 (−0.008)	[106]
		f_t	Concrete tensile strength	MPa	4.00 (3.73)	[184]
	Confined	f_c	Concrete compressive strength	MPa	−51.46 (−47.31)	[45]
		f_{cu}	Ultimate compressive strength	MPa	−40.85 (−40.85)	[45]
		ε_c	Strain corresponding to f_c	–	−0.0049 (−0.0049)	[45]
		ε_{cu}	Strain corresponding to f_{cu}	–	−0.0200 (−0.0188)	[45]
		f_t	Concrete tensile strength	MPa	5.15 (5.15)	[184]
Bond-Slip		t_1	Peak bonding strength	MPa	22.44 (15.47)	[143]
		t_3	Residual bonding strength	MPa	10.05 (7.58)	[143]
		u_{b1}	Slip corresponding to t_1	mm	1.42 (1.065)	[143]
		u_{b2}	Slip at the end of plateau	mm	1.85 (1.37)	[143]
		u_{b3}	Slip corresponding to t_3	mm	6.76 (2.49)	[143]

Note: values in ( ) indicate the properties of the RC column under the corroded condition.

Figure 5-13 (a) and (b) present the comparison of the FE-predicted lateral load-drift ratio hystereses with experimental results for uncorroded and corroded cases, respectively. The FE predictions match the experimental observations well in both uncorroded and corroded cases. In particular, the strength reduction in the final cycle caused by steel bar buckling, as reported in [136], can be well captured by FE models utilizing the suggested constitutive model. In contrast, the FE models using *Steel02* (i.e., no buckling) result in lateral load-drift ratio hystereses that differ from the experiments in the last cycle in terms of strength. This comparison confirms that the proposed steel bar constitutive model with buckling improves FE predictions in both uncorroded and corroded scenarios.

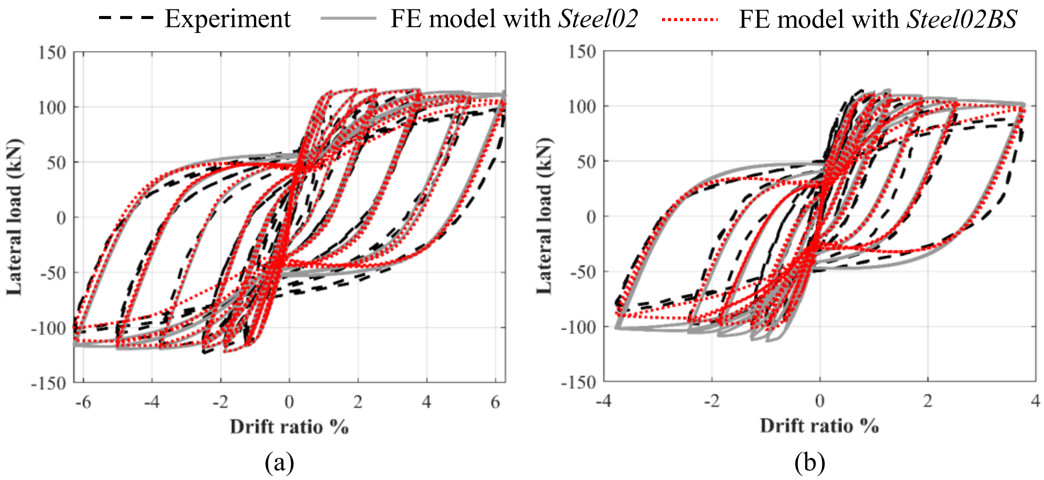

Figure 5-13: Comparison of lateral load-drift ratio hysteresis between FE predictions and experimental results for (a) uncorroded and (b) corroded RC column

5.5. CHAPTER CONCLUSIONS

To model reinforced concrete (RC) columns under extreme loading (e.g., strong earthquakes), particularly those columns under-designed or severely corroded, advanced modeling aspects such as steel bar buckling need to be taken into account. Thus, in fiber-based finite element approach, the constitutive model for steel bar needs to consider bar buckling, which is mainly restrained by flexible transverse reinforcement. In this regard, this study develops and validates a finite element (FE)-based steel cage model for numerical buckling tests, and generate a comprehensive database for steel buckling behavior under different scenarios, considering a wide range of steel cage properties (e.g., geometrical and material). Using this database, this study develops constitutive models for steel with buckling, following the framework proposed by modifying a base steel material model with no buckling effect considered. Two highlights of the developed constitutive model for steel bar with buckling are: (1) the model can consider the flexibility of stirrups on the critical buckling length/load and post-buckling behavior; and (2) the model can be used to take into account the corrosion effects in transverse and longitudinal steel on buckling.

Chapter 6. BAYESIAN CONDITION IDENTIFICATION FOR CORRODED RC STRUCTURES

6.1. INTRODUCTION

Reinforced concrete (RC) structures deteriorate with time and continuously accumulate damage during their lifetime due to aging in the aggressive environment and possible damaging events. Corrosion, being one of the most common causes of deteriorating RC structures, poses a serious threat to aged RC structures, especially in many coastal areas of the United States, Canada, and Japan, where strong seismicity is also a severe concern. The cumulative deterioration can affect substantially the seismic performance of aged RC structures in future earthquakes. Estimating the corrosion state through health monitoring and/or inspection can provide valuable information for seismic safety and performance assessment, avoiding or reducing potential human and economic losses. Thus, structural health monitoring and residual performance assessment of corroded RC structures have been a pressing need in the field of structural engineering to assist in decision-making on structural repair, retrofit, or demolition.

To evaluate the corrosion state in RC structures, non-destructive evaluation (NDE) technologies, such as ultrasonic waves, infrared imaging, ground penetrating radar, and implementing piezoelectric and fiber optic sensors, have been utilized extensively [185–187]. However, due to high-cost and time-consuming procedures of scanning the entire structure, these approaches are usually limited to local damage detection (e.g., mass loss of steel bars in a small area) and highly depend on the correlation between corrosion features and some other physical properties. More importantly, none of those methods can measure other important corrosion-affected variables (e.g., corroded bonding properties) that are highly needed for modeling because they can notably affect the structural behavior of corroded RC structures. As such, NDE methods can rarely assist in creating nonlinear finite element (FE) models of large-scale civil structural systems for seismic performance evaluation.

In contrast, model updating has been proven to be a promising technique for system identification and can be used to create a proper digital twin based on the vibration data of a structure. A digital twin, as a virtual representation of the structure, can assist in developing performance prediction models and thus a better-informed maintenance system [188]. This explains why many studies can be found in the literature, employing model updating to identify the unknown characteristics of a physics-based model of an existing structure via minimizing the discrepancy between the model-predicted responses and their measured counterparts [48,189–191]. Specifically for corroded RC structures, model updating on the basis of field measurement has been used to estimate the level of corrosion damage in RC structures (e.g., [192–196]). However, the majority of existing studies in the literature used low amplitude signals measured under ambient vibrations [195,196], free vibrations [192], or service loads [193,194]. Due to the relatively low levels of loading, elastic models were used in these studies for linear model updating. However, the capability of the linear model updating in estimating the corrosion condition is not applicable for corroded RC structures with significant nonlinearity under extreme loading conditions (i.e., earthquakes). One reason is that the updated model achieved based on linear model updating is incapable of describing the hysteretic damage or predicting the seismic response in future earthquakes (e.g., aftershocks). To address this issue, detailed mechanics-based nonlinear FE models considering corrosion-affected aspects and properties can be updated using seismic data. In this regard, the seismic measurement from an instrumented structure can be used to indirectly evaluate the corrosion state and to develop an updated model for a corroded RC structure. The updated model can be utilized for seismic performance assessment and risk analysis in the future.

To provide valuable information about the corrosion state through model updating, it is essential that the FE model used is capable of capturing various aspects of corrosion in a computationally efficient manner. Several studies have developed FE models to look into the corrosion-affected behavior of RC structures, considering the reduction of steel bar cross-sectional area as the main corrosion effect [25,26]. However, another important aspect, namely bonding deterioration at the concrete-steel interface caused by corrosion of longitudinal steel bars, is typically neglected but has a substantial impact on the composite action of steel bars with surrounding concrete [47]. To more realistically model corroded RC structures, nonlinear FE modeling needs to incorporate the corroded bond-slip behavior, as emphasized in other studies [27,147,183].

In order to perform nonlinear FE model updating (FEMU) using seismic measurement, different techniques can be utilized, including deterministic optimization (e.g., [197,198]) and Bayesian inference or stochastic filtering methods, such as unscented Kalman filter (UKF). Compared with deterministic optimization like the least squares method, Bayesian inference such as stochastic filtering methods has gained wide popularity in the past years for its proved capability [48–50]. Recent studies have successfully applied UKF to nonlinear FEMU problems using simulated seismic response data (e.g., [53,54,191]) for its robustness in solving nonlinear FEMU problems. However, to the best knowledge of the authors, stochastic filtering methods (e.g., UKF) have not been utilized for nonlinear FEMU of corroded RC structures for system identification or health condition assessment. Thus, the research work presented here is the first of its kind in the literature, proposing a methodology to estimate the corrosion state of RC structures by integrating detailed mechanics-based FE models and seismic data using a stochastic inference approach (i.e., UKF). This approach allows automatically tuning the corrosion-related model parameters, thus adjusting the nonlinear behavior of the corroded structure based on the measured response.

In the proposed methodology, the advanced fiber-based frame element that considers bond-slip [116], recently developed and implemented in *OpenSees* [65], is employed. Compared with the existing fiber-based frame element commonly used for non-corroded or corroded beam-columns without considering corroded bonding, this element takes into account the corrosion effect on the bonding properties. This approach leverages the knowledge embodied in FE models and the information hidden in the seismic data about the corrosion state of RC structures. Such a novel idea makes it possible to estimate corrosion-induced degradation of bonding properties, which cannot be measured directly through existing state-of-the-art NDE techniques. To demonstrate the validity of this methodology, an example RC column is considered using simulated seismic response data assuming different corrosion scenarios.

The remainder of this work is organized as follows. Firstly, the methodology proposed to estimate the corrosion state of RC columns is presented, followed by a brief description of the stochastic parameter estimation technique and the nonlinear FE modeling of corroded RC columns, as required in the proposed methodology. Secondly, the example column, which is a corroded RC column tested statically [137], is introduced. Thirdly, this methodology is examined using the simulated data by considering different measurement noise levels, corrosion levels, corroded features, excitation intensity levels, and types of measurement. In the end, this study was concluded with the promise of the proposed methodology that can be used to evaluate the corrosion state of corroded RC columns.

6.2. CORROSION STATE ESTIMATION METHODOLOGY

Lack of information regarding corrosion state or corroded mechanical properties of RC structures can compromise the predictability of the FE model developed and, in turn, bias the residual performance assessment of corroded RC structures for future earthquakes. As such, parameter estimation of the corrosion-affected mechanical characteristics is essential for developing a nonlinear FE model that can reliably predict structural responses. This can be achieved by nonlinear FEMU when measurements are available for a structural system (e.g., seismic measurements of an instrumented bridge during an earthquake). Nonlinear FEMU, also known as inverse FE modeling, is defined as the process of determining the optimal model parameters by minimizing the discrepancy between the FE predictions and experimental observations. This provides the basis for the proposed methodology as schematically shown in Figure 6-1, and briefly described as follows.

For an instrumented RC structure subjected to seismic excitation with measured responses during an earthquake, a mechanics-based nonlinear FE model considering unknown corrosion-affected parameters can be developed as a digital copy of the physical system. Without accurate information about the corrosion states or corrosion-affected model parameters (e.g., steel bar cross-sectional area reduction and corroded bonding), an initial FE model (digital copy) can be built with corrosion-affected model parameters simply determined based on experience or empirical models, or assumed with values based on the as-built condition. With seismic measurement, the predictions based on the FE model developed are compared with the field observations in the Bayesian estimation process (e.g., UKF). The FE model parametrized by corrosion-related parameters is updated so that FE predictions match well with the measurement, leading to statistical estimate of unknown corrosion-affected properties. It is worth noting that this framework necessitates advanced FE modeling capable of capturing different aspects of corrosion such as the corroded bond-slip. Before describing FE modeling of corroded RC columns, a brief overview of the UKF technique, which is used as an integral component in the corrosion state estimation methodology, is presented as follows. Note that more details about this technique is available in the literature (e.g., [53,191]). This paper will only introduce the essential ingredients to provide the context of its specific application in the proposed methodology.

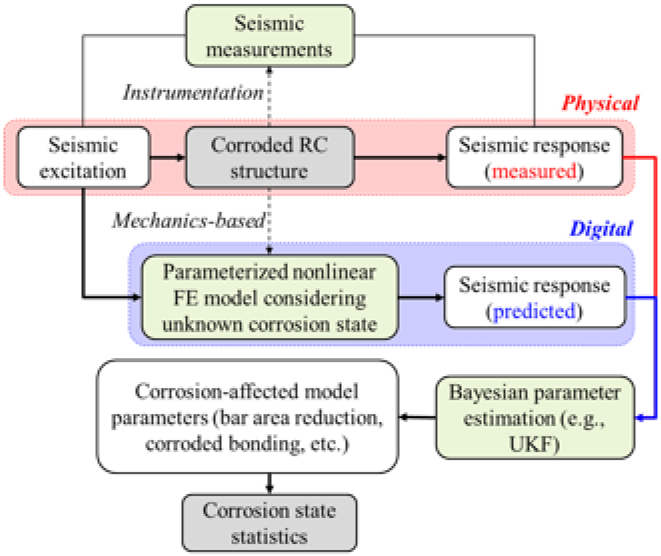

Figure 6-1: Schematic view of the proposed corrosion state estimation methodology using nonlinear FEMU

6.2.1. Unscented Kalman filter technique

In the UKF, the time-invariant unknown/uncertain model parameter vector $\boldsymbol{x}$ to be estimated is represented as a random walk process (i.e., a linear state-transition equation), as indicated in the state-transition equation, see Eq. (6-1):

$$\boldsymbol{x}_k = \boldsymbol{x}_{k-1} + \boldsymbol{w}_{k-1} \tag{6-1}$$

In the proposed methodology, $\boldsymbol{x}$ represents the unknown correlation-related properties (and other possibly unknown geometric or material parameters). The subscript k and $k-1$ denote the current and previous analysis step, respectively, and $\boldsymbol{w}$ is the process noise used to drive the estimate of $\boldsymbol{x}$, modeled as zero-mean additive white Gaussian noise (AWGN) with a diagonal covariance matrix $\boldsymbol{Q}$. The FE predictions relate the measurement (observation) vector of the structural response $\boldsymbol{y}$ to the unknown model parameter vector $\boldsymbol{x}$ through the measurement equation, as shown in Eq. (6-2). In this equation, $\boldsymbol{h}(\boldsymbol{x}_k, \ddot{u}^g_{1:k})$ represents the simulated structure response until analysis step k, which is evaluated by analyzing the nonlinear FE model with the current estimate of model parameter vector $\boldsymbol{x}_k$, subjected to the seismic input characterized by earthquake ground motion acceleration series until the current time step k, i.e., $\ddot{u}^g_{1:k}$. In addition, the inherent model uncertainty and the measurement noise in $\boldsymbol{y}$ is modeled using a prediction error vector $\boldsymbol{v}$, which is modeled by a zero-mean AWGN vector with a covariance matrix $\boldsymbol{R}$.

$$\boldsymbol{y}_k = \boldsymbol{h}(\boldsymbol{x}_k, \ddot{u}^g_{1:k}) + \boldsymbol{v}_k \tag{6-2}$$

When more observation data become available as time evolves during an earthquake, Bayesian inference can be utilized to estimate the posterior mean vector $\boldsymbol{\mu}_k^x$ and the corresponding covariance matrix $\boldsymbol{P}_k^{xx}$ of $\boldsymbol{x}_k$ recursively using the state-transition and measurement equations established above. This is to incorporate the information obtained from experimental observations in a Bayesian framework at time step k. Note that in UKF, it is assumed vectors $\boldsymbol{x}_k$ and $\boldsymbol{y}_k$ are Gaussian-distributed random vectors defined with first and second-order statistics ($\boldsymbol{\mu}$ and $\boldsymbol{P}$). Compared with other Bayesian methodologies, Kalman filter-based approach allows efficient updating through the Kalman gain matrix, which is introduced as a weight measure based on the difference between the FE prediction (i.e., $\boldsymbol{h}(\boldsymbol{x}_k, \ddot{u}^g_{1:k})$) and measurement $\boldsymbol{y}_k$ used for updating the posterior mean vector and covariance matrix of unknown parameter vector $\boldsymbol{x}_k$. The Kalman gain matrix $\boldsymbol{K}_k$ is calculated by the cross covariance matrix between $\boldsymbol{x}_k$ and $\boldsymbol{y}_k$, i.e., $\boldsymbol{P}_k^{xy}$, and the covariance matrix of $\boldsymbol{y}_k$, i.e., $\boldsymbol{P}_k^{yy}$.

By applying UKF, all the above-mentioned statistics related to $\boldsymbol{y}_k$ are estimated using the unscented transform [52], in which a series of sigma points (SPs) for $\boldsymbol{x}_k$ are deterministically defined by $\boldsymbol{\mu}_k^{\boldsymbol{x}}$ and $\boldsymbol{P}_k^{\boldsymbol{xx}}$. Then, the nonlinear FE model is analyzed in parallel at these SPs, resulting in a good approximation of the mean and covariance matrix of $\boldsymbol{y}_k$. The described procedure for nonlinear FEMU provides a tool to recursively update the mean vector and covariance matrix of the unknown parameter vector (i.e., $\boldsymbol{\mu}_k^{\boldsymbol{xx}}$ and $\boldsymbol{P}_k^{\boldsymbol{xx}}$) based on the measurement. Readers who are interested in more details about UKF can refer to the literature [191]. The other important component in the proposed methodology, represented as the nonlinear function $\boldsymbol{h}(\boldsymbol{x}_k, \ddot{\boldsymbol{u}}_{1:k}^{g})$ in Eq. (6-2), is detailed in tshe following section.

6.2.2. Nonlinear Finite Element Modeling of Corroded RC Columns

To predict the structural responses of corroded RC structures subjected to extreme loading (e.g., earthquakes), a nonlinear FE model for corroded RC structures is required to establish $\boldsymbol{h}(\boldsymbol{x}_k, \ddot{\boldsymbol{u}}_{1:k}^{g})$ in Eq. (6-2). In this regard, different aspects of corrosion effects on structural properties (geometry and materials) need to be considered, including reduction of steel bar cross-sectional area, degradation of cover concrete, decreasing confinement effect to core concrete, and corrosion-affected bond-slip [183].

Due to the significant role of bond-slip in the nonlinear behavior of corroded RC columns [183], the geometrically nonlinear fiber-based frame element (i.e., *dispBeamColumnBS*) that considers bond-slip was recently implemented by the authors in *OpenSees* [116] and is used in this study. This element contains additional degrees of freedom representing the axial movement of steel bars, which allows the steel bar to slip with respect to the surrounding concrete. Using an appropriate bond-slip material model with corroded bonding properties, this element can properly capture the effect of bond-slip on the nonlinear behavior simulations of corroded RC columns

[183]. For this purpose, a corroded bond-slip material model [183], i.e., *BondSlipCorC*, implemented in *OpenSees* is used. In this bond-slip material model, corrosion-affected degradation in the bonding properties and the hysteretic behavior is considered as elaborated below.

According to existing studies in the literature [145,147,152,199,200], corrosion mainly affects the bond-slip in terms of the peak bonding stress t_1 and the residual bonding stress t_3, while the corrosion effect on the other bonding properties is negligible. Therefore, in order to reduce the computational costs in the nonlinear FEMU, this study considers corroded t_1 and t_3 (i.e., t_1^c and t_3^c) as unknown in the FEMU process while assuming u_{b1}, u_{b2}, and u_{b3} can be determined empirically. To this end, Eqs. (6-3) and (6-4) are employed here to relate t_1^c and t_3^c with the corrosion level K (i.e., percentage of reinforcement mass loss ratio), respectively [147]. Given the corrosion level and corroded bonding properties, the cumulative damage factors can be calculated to characterize the corrosion-affected degradation in the hysterical behavior encoded in *BondSlipCorC*.

$$\frac{t_1^c}{t_1} = \begin{cases} 1.0 & K \le 3 \\ 1.2\exp(-0.076K) & K > 3 \end{cases} \tag{6-3}$$

$$\frac{t_3^c}{t_1^c} = \begin{cases} 0.26 + 0.13K & K < 3 \\ 0.65 & 3 \le K < 13 \\ 0.65 - 0.06(K-13) & 13 \le K < 20 \\ 0.23 & K \ge 20 \end{cases} \tag{6-4}$$

In addition to corrosion effect on bonding, other corrosion-affected geometric and material properties of RC columns can be readily considered in the fiber-based finite element models. For example, cover concrete strength should be reduced to consider concrete cracking or spalling due to volumetric expansion of corrosion products and the resulting splitting stresses. Specifically, the reduced concrete strength under compression for cover concrete f_c^c can be calculated in accordance with the corrosion level [43], as follows:

$$\frac{f_c^c}{f_c} = \frac{1}{1 + 0.1\left(\frac{\sum_{i=1}^{n} \pi (d_b - d_b^c)_i}{b_0 \varepsilon_c}\right)} \tag{6-5}$$

where f_c and ε_c are the pristine compressive strength and the corresponding strain of cover concrete, respectively; d_b and d_b^c represent the steel bar diameter in pristine and corroded conditions; n is the number of steel bars; and b_0 shows the circumference of the RC column cross-section. It is worth noting that d_b^c is calculated based on the corrosion level K (i.e., percentage of mass loss ratio). In addition, the tensile strength of concrete is also reduced by the same factor presented in Eq. (6-5) according to [44].

Furthermore, to account for the corrosion effects on the confinement to core concrete, the corroded properties of longitudinal and transverse reinforcements (i.e., corrosion levels of K and K_h, respectively) are employed in Mander's equations [45] to evaluate the impaired concrete strength and ultimate strain [141]. Using the corrosion-affected material behavior for cover concrete, core concrete, and bond-slip defined above, as well as reduced cross-sectional area of longitudinal steel bars, the FE model can be developed using the geometrically nonlinear fiber-based frame element that considers bond-slip to capture the important aspects of corrosion. Note that this FE modeling approach is effective in simulating the behavior of corroded RC columns, which has been validated by the authors [183].

6.3. APPLICATION EXAMPLE

To demonstrate the applicability of the proposed corrosion state estimation methodology, an example RC column is considered. Corrosion state estimation is carried out under a variety of scenarios. Note that due to lack of seismic measurement for corroded RC structures, this paper focuses on numerical investigations, in which the example RC column will be used to simulate seismic response measurements, based on which corrosion state will be estimated using the proposed corrosion state estimation methodology through nonlinear FEMU. In this section, the example RC column used is first described and followed by the seismic response measurements generation, and then the corroded cases studied using this column are introduced.

6.3.1. RC column

The example RC column is taken from the literature [137], in which the column was tested under uncorroded and corroded conditions. Figure 6-2(a) depicts the geometrical properties of this column. During the experimental test, this column was subjected to a constant axial load applied on the top and static cyclic lateral loading at the top until flexure failure; more information about this column can be found in [137].

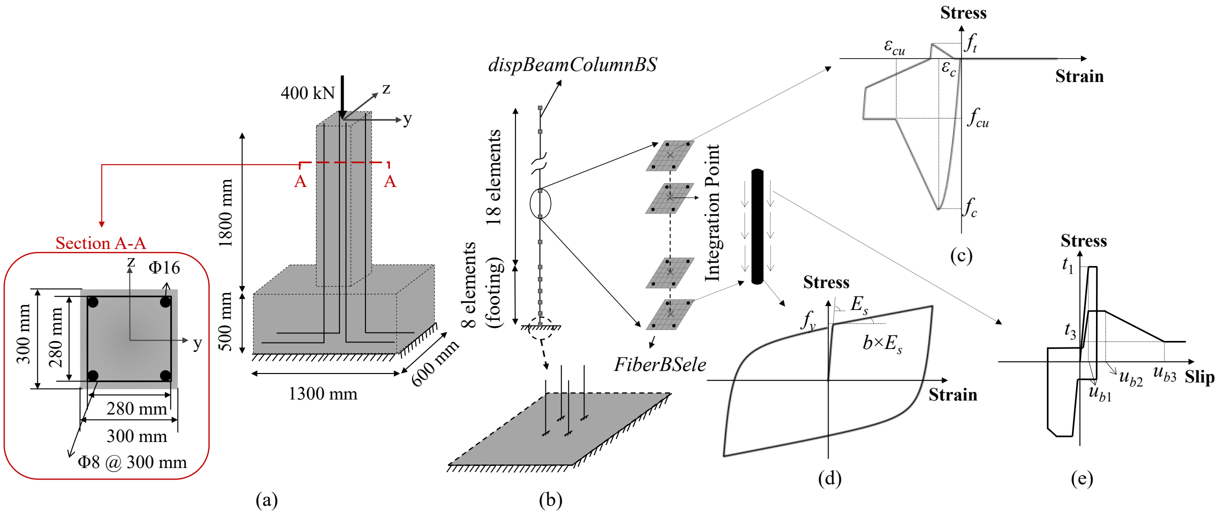

Figure 6-2: Schematic view of (a) geometry and (b) the FE model for Meda column, and material models used for (c) concrete fibers, (d) steel fibers, and (e) bond-slip

Table 6-1: Material properties of the example RC column considered under pristine condition

Material		Properties				
		Symbol	**Description**	**Unit**	**Value**	**Source**
Steel		f_y	Yield stress	MPa	520.00	Material coupon test
		b	Strain hardening ratio	–	0.020	Material coupon test
		E_s	Young's modulus	MPa	210000.00	Material coupon test
Concrete	Unconfined	f_c	Concrete compressive strength	MPa	−20.00	Material coupon test
		f_{cu}	Ultimate compressive strength	MPa	−4.00	[106]
		ε_c	Strain corresponding to f_c	–	−0.002	Material coupon test
		ε_{cu}	Strain corresponding to f_{cu}	–	−0.008	[106]
		f_t	Concrete tensile strength	MPa	2.00	[184]
	Confined	f_c	Concrete compressive strength	MPa	−23.00	[45]
		f_{cu}	Ultimate compressive strength	MPa	−12.98	[45]
		ε_c	Strain corresponding to f_c	–	−0.00875	[45]
		ε_{cu}	Strain corresponding to f_{cu}	–	−0.01300	[45]
		f_t	Concrete tensile strength	MPa	2.30	[184]
Bond-Slip		t_1	Peak bonding strength	MPa	15.87	[143]
		t_3	Residual bonding strength	MPa	5.36	[143]
		u_{b1}	Slip corresponding to t_1	mm	1.71	[143]
		u_{b2}	Slip at the end of plateau	mm	2.11	[143]
		u_{b3}	Slip corresponding to t_3	mm	10.41	[143]

Figure 6-2 (b) shows the schematic view of the FE model for this column, where bond-slip is taken into account, and the corrosion-affected properties can be readily incorporated for corroded conditions. This column is modeled with an appropriate number of elements determined based on mesh convergence analysis, and each fiber-based frame element is integrated with four Gauss-Lobatto integration points. At each integration point, a fiber section is assigned, where concrete fibers are represented with *Concrete02* material model in *OpenSees* shown in Figure 6-2 (c), characterized by concrete compressive strength f_c and its associated strain ε_c, ultimate compressive strength f_{cu} and its associated strain ε_{cu}, and tensile strength f_t. The steel fibers are represented by the Giuffre-Menegotto-Pinto steel model [133], as schematically shown in Figure 6-2 (d), which is defined by yield stress f_y, strain hardening ratio b, and Young's modulus E_s. The properties of steel and unconfined concrete are defined based on the experimental data from the literature [137]; the properties for the core concrete considering the confinement effect are determined using Mander's equations [45]. In addition, the bond-slip is modeled via the recently implemented *BondSlipCorC* in *OpenSees* [183]. This material model, shown in Figure 6-2 (e), is defined with the peak bonding stress t_1 and the corresponding slip u_{b1}, the slip at the end of plateau u_{b2}, and the residual bonding stress t_3 and the corresponding slip u_{b3}. Table 6-1 summarizes the properties of the key model parameters for this column under pristine condition. The FE model of this column using the aforementioned FE modeling strategy were validated under uncorroded and corroded conditions by the authors [183].

6.3.2. Seismic measurements simulation

Using the FE model developed for the example column, together with corrosion-affected properties as previously discussed, RC columns under different corrosion scenarios can be modeled. To employ these models for seismic simulation, the inertial effect in a dynamic system during earthquakes is represented using a lumped mass (mass = 4.08×10^4 kg) sitting at the top of the cantilever column, resulting in vibration periods of 0.91 and 0.15 seconds for the first and second modes, respectively. Furthermore, a Rayleigh damping model with mass and initial-stiffness proportional components is employed to represent the energy dissipation of the dynamic system in addition to hysteretic energy dissipation captured in nonlinear material models. These components are determined based on the first and second modes of vibration, each with a damping ratio of 2.0%, which is commonly employed in nonlinear dynamic analysis of RC structures [201].

Without loss of generality, this example column is assumed to be subjected to a seismic excitation with a short duration to minimize computational cost in this work with a large number of case studies. The Loma Prieta earthquake in 1989 recorded at Agnew State Hospital station [70] is selected in this study (considering 30 seconds for the seismic duration). To include structural response with low to high level of nonlinearity, two scale factors are used for this ground motion: (1) low-intensity ground motion excitation, which is so scaled to reach the ductility demand (i.e., deformation demand with respect to the yield deformation) of 2.0, and (2) high-intensity ground motion excitation, which is so scaled to reach the ductility demand of 3.5. This allows this study to investigate the effect of excitation intensity to reliably identify the various corrosion-affected properties (pre- and post-yielding parameters) corresponding to bond-slip and concrete.

The FE model of this RC column is used to simulate the structural response (i.e., time-histories of lateral displacement and acceleration at the column top) caused by seismic excitation, depending on the scenario selected for corrosion level, corroded features, and intensity level of ground motion. In addition, the simulated recorded data is then contaminated by different levels of measurement noise. It is worth mentioning that, in the real world, the column vibration data used as the measurement in the nonlinear FEMU can be obtained from a variety of sensor technologies, such as accelerometers, GPS, and unmanned aerial vehicles (UAVs) [202]. Note that this study does not employ the simulated strain gauge data to demonstrate the capability of the provided methodology in identifying the corrosion state based on the global behavior of the RC columns, considering that strain measurements for corroded structures are challenging. In the next section, more details on these various scenarios are provided, which are utilized to highlight the potential of the provided methodology that integrates stochastic filtering and efficient FE modeling for corroded RC columns in estimating corrosion-affected parameters.

6.3.3. Study cases

This section describes the cases examined in this study, using the example column, to explore the capability of the provided methodology in estimating the corrosion state of RC columns. These cases are summarized in Table 6-2 to consider a variety of factors that can affect the corrosion state estimation process. These factors include the measurement noise, the corrosion level, the corroded features (e.g., bonding, steel cross-sectional area, and concrete), the seismic excitation intensity, and the type of response measurement (e.g., displacement history, or acceleration history).

To begin, four cases are designed to demonstrate the capabilities of this methodology in finding corroded features related to bonding, which cannot be measured in engineering practice through the current technologies. Thus, it is assumed that the corrosion solely affects the bonding between the steel bar and the surrounding concrete in the example RC column. The first three cases consider low level of corrosion (i.e., 16%) for the RC column and the measurement during low-intensity ground motion excitation. The effect of noise levels contained in the measurement (i.e., displacement time-history) on the corrosion state identification is studied by comparing cases #1, #2, and #3, which consider zero, medium (2%), and high (5%) levels of noise (AWGN) [53], respectively. Next, the influence of corrosion level on the performance of provided methodology is investigated by considering this RC column with low (16%) and high (24%) levels of corrosion impacting bonding, i.e., cases #1 and #4, respectively.

In addition to bonding, corrosion can impact other aspects of an RC column, such as reducing the cross-sectional area of steel bar and degrading the properties of unconfined and confined concrete. To explore how well the provided methodology can identify these different corroded features, case #5 is defined for the RC column with high corrosion level (24%) impacting bonding, steel bar cross-sectional area, and concrete properties, with comparison to case #4. To reduce the computational cost in the case studies, corrosion is considered to exclusively impact the steel bar cross-sectional area and bonding in the remaining cases considered in this study for simplicity. This simplification is also based on the fact that various different techniques exist to measure corroded concrete properties [203], and also, the fact that the steel bar cross-sectional area reduction is the most common corrosion aspect used in FE modeling of RC structures in the literature [26]. Accordingly, before moving on to the next influential factor, two cases (#6 and #7) with zero and high-level (5%) noise in the measurements are considered. In these two cases, the RC column is assumed to have high corrosion level (24%) affecting bonding and bar cross-sectional area; the seismic measurement (i.e., displacement time-history) is available under low-intensity ground motion excitation. These two cases are used to further confirm that this methodology is able to estimate corroded bonding and bar properties even when the measurement is associated with high-level noise.

All of the cases discussed above are based on measurements during low-intensity ground motion excitation. To examine the applicability of the proposed methodology to stronger seismic events where there is a higher level of nonlinearity in structural responses, another two cases, i.e., #8 and #9, are studied considering high-intensity ground motions in contrast to cases #6 and #7, respectively. Note that the comparison between cases #6 and #8 is for the ideal scenario with no measurement noise, while the comparison between cases #7 and #9 is for the scenario with high-level noise.

It is worth mentioning that the measurement is assumed to be limited to the displacement time-history in the previous cases studied, while the type of measurement used in the nonlinear FEMU could be influential. To explore the impact of the type of measurement on the performance of the provided methodology, two more cases are studied: cases #10 (with time-history of acceleration measurement) and #11(with time-histories of both displacement and acceleration), which are in contrast to case #5 (time-history of displacement). Similarly, two more cases (#12, and #13) with high-level (5%) noise are also investigated with contrast to case #7, aiming to demonstrate the effect of measurement type when there is a high-level noise in the measurement.

The following section presents the corrosion state estimation results using nonlinear FEMU for the cases described above.

Table 6-2: Summary of cases examined in this study

Case identifier		Corroded features	Corrosion level	Measurement noise level	Ground motion intensity	Type of measurement
Different noise levels	#1	Corroded bonding	16%	0%	Low	Disp. Time Hist.
	#2	Corroded bonding	16%	2%	Low	Disp. Time Hist.
	#3	Corroded bonding	16%	5%	Low	Disp. Time Hist.
Different corrosion levels	#1	Corroded bonding	16%	0%	Low	Disp. Time Hist.
	#4	Corroded bonding	24%	0%	Low	Disp. Time Hist.
Different corroded features	#4	Corroded bonding	24%	0%	Low	Disp. Time Hist.
	#5	Corroded bonding, bar, and concrete	24%	0%	Low	Disp. Time Hist.
	#6	Corroded bonding and bar	24%	0%	Low	Disp. Time Hist.
	#7	Corroded bonding and bar	24%	5%	Low	Disp. Time Hist.
Different intensity levels for ground motion excitations	#6	Corroded bonding and bar	24%	0%	Low	Disp. Time Hist.
	#8	Corroded bonding and bar	24%	0%	High	Disp. Time Hist.
	#7	Corroded bonding and bar	24%	5%	Low	Disp. Time Hist.
	#9	Corroded bonding and bar	24%	5%	High	Disp. Time Hist.
Different types of measurements	#6	Corroded bonding and bar	24%	0%	Low	Disp. Time Hist.
	#10	Corroded bonding and bar	24%	0%	Low	Acc. Time Hist.
	#11	Corroded bonding and bar	24%	0%	Low	Disp. Time Hist. + Acc. Time Hist.
	#7	Corroded bonding and bar	24%	5%	Low	Disp. Time Hist.
	#12	Corroded bonding and bar	24%	5%	Low	Acc. Time Hist.
	#13	Corroded bonding and bar	24%	5%	Low	Disp. Time Hist. + Acc. Time Hist.

6.4. CORROSION STATE ESTIMATION

This section presents the results of the study cases introduced, aiming to investigate the capability of the proposed methodology in estimating the corrosion-affected parameters, with a particular focus on corroded bonding properties, i.e., t_1 and t_3. For this purpose, the UKF technique is used to identify unknown corroded features in the FE models based on seismic data. As mentioned earlier, different measurement noise levels, corrosion levels, corroded features, excitation intensity levels, and different types of measurement are all studied here to examine this proposed methodology using nonlinear FEMU.

6.4.1. FEMU with different noise levels

Assuming accurate measurement from high precision sensors (i.e., no noise) is unrealistic, since the measurements are typically contaminated by various levels of noise, which may affect the updating process. To show the robustness of the proposed methodology for corrosion-affected parameter estimation in RC columns, this section considers the contaminated measurement with different levels of noise in comparison to the case with zero noise in the measurement.

To begin, in cases #1, #2, and #3, it is assumed that corrosion has solely damaged the bonding properties, i.e., t_1 and t_3. According to Eqs. (6-3) and (6-4), the ratios of the corroded to initial (uncorroded) values for t_1 and t_3 are equal to 0.33 and 0.48, respectively, for the RC column with 16% corrosion. As stated earlier, seismic measurements are simulated using the nonlinear FE model of the column with corroded bond-slip, i.e., degraded t_1 and t_3 (denoted as true parameters). To pollute the predictions of column top displacement from the true FE model developed, a medium and a high level of AWGN, with a standard deviation of 2% and 5% of the maximum response (i.e., maximum displacement), respectively, are considered here.

Assuming the true parameter values are unknown, the proposed methodology is employed to identify corroded bonding parameters (t_1 and t_3) for this column, in which the initial guess for the bonding properties are assumed to be those for the uncorroded case. Figure 6-3 depicts drift ratio time-histories obtained from the initial FE analysis (FEA) and updated FEA (i.e. after updating), in comparison to the measurements for cases #1, #2, and #3 with 0%, 2%, and 5% noise levels, respectively. Comparing the before and after updating results with measurements shown in Figure

6-3 reveals that the FE predictions are significantly improved after updating unknown parameters (i.e., t_1 and t_3), even when a low- or high-level noise (i.e., 2% and 5%, respectively) exists. These findings demonstrate that the proposed methodology is able to effectively update the unknown features of the FE model regardless of measurement noise pollution.

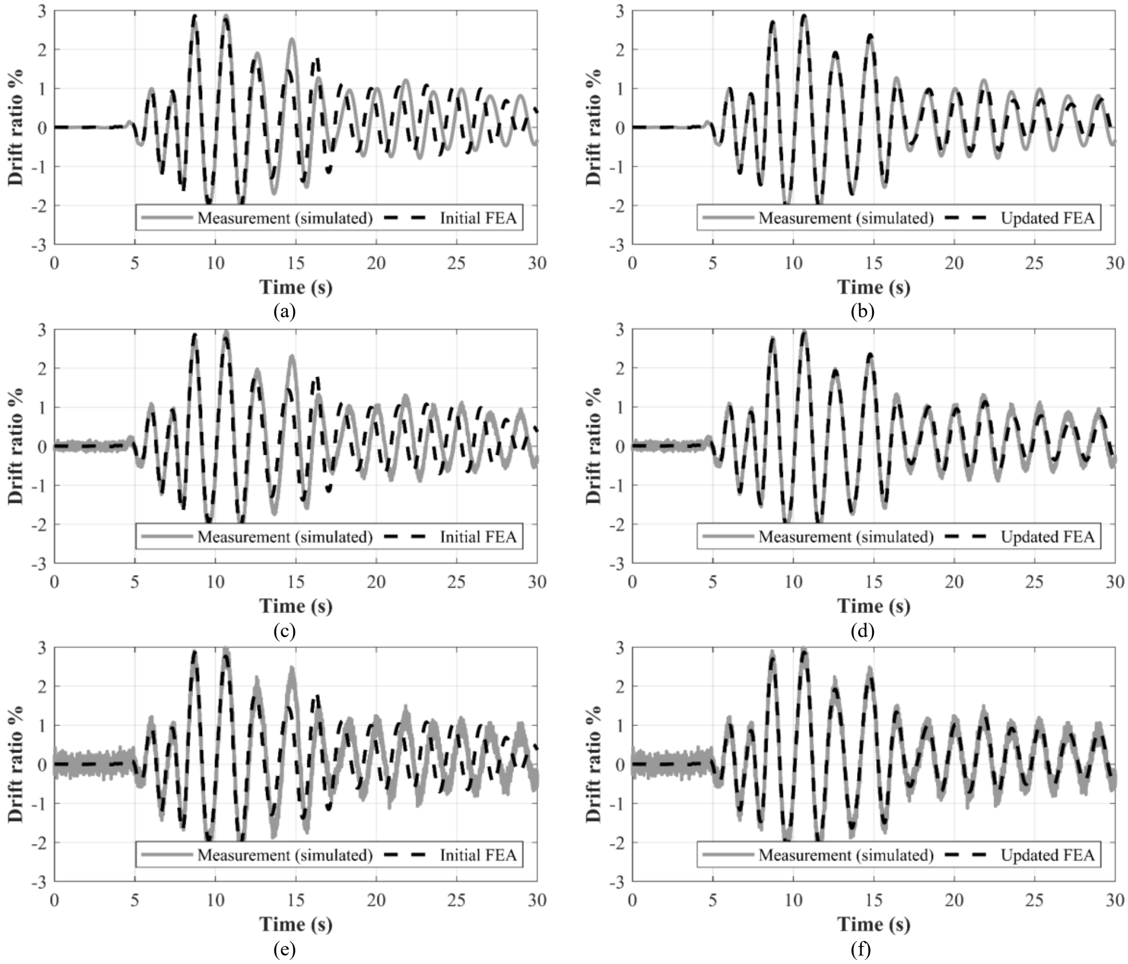

(a) (b) (c) (d) (e) (f)

Figure 6-3: Comparison of FE-predicted and measured time-histories of drift ratio for the RC column with 16% corrosion level for (a) before and (b) after updating in case #1 with zero noise, (c) before and (d) after updating in case #2 with 2% noise, and (e) before and (f) after updating in case #3 with 5% noise

To better illustrate the efficacy of nonlinear FEMU in estimating corroded bonding properties, Figure 6-4 shows the updating histories in terms of mean values of t_1 and t_3, as well as their 95% confidence intervals (CI) for cases #1, #2, and #3. The updating histories of peak bonding stress (i.e., t_1), shown in Figures 6-4 (a) to (c), indicate that the estimation of t_1 is converged quickly (right after 8.7 sec) to the true value, and the uncertainty in this parameter estimation decreases dramatically since it is closely related to the initial bonding stiffness and thus the column stiffness. Hence, the nonlinear FEMU can properly estimate t_1, even when there exists a relatively high level of noise (5%) in the measurement.

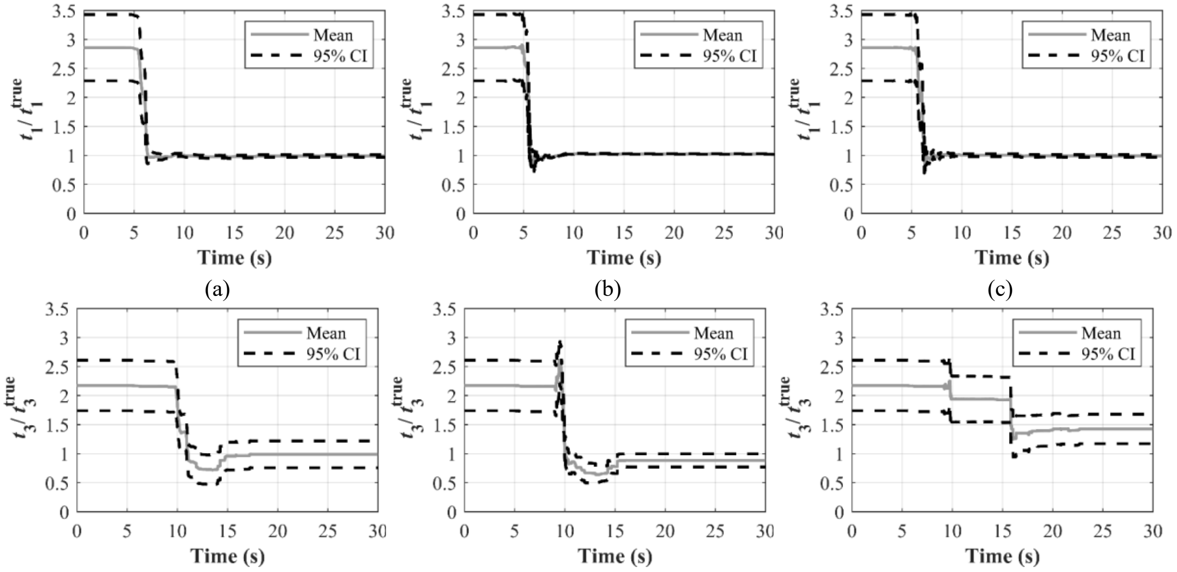

(a) (b) (c)

(d) (e) (f)

Figure 6-4: Parameter updating histories of the RC column with 16% corrosion level for t_1 in (a) case #1 with zero noise, (b) case #2 with 2% noise, and (c) case #3 with 5% noise; for t_3 in (c) case #1 with zero noise, (d) case #2 with 2% noise, and (e) case #3 with 5% noise

In contrast, the estimation of residual bonding stress (i.e., t_3) converges after 17 seconds to the true value, with only a slight reduction in the estimation uncertainty (95% CI) when no measurement noise exists, as shown in Figure 6-4 (d). The rationale behind this observation is that this parameter will only have an impact after the bond yielding, and thus, it occurs during the strong excitation phase and takes longer to update. Furthermore, when measurement noise exists, as shown in Figures 6-4 (e) and (f), the final estimated values for t_3 differ from the true value, implying that estimating t_3 is more challenging than t_1. This difference is primarily due to the additive noise in the measurements, which affects the accuracy of the parameter updating in these two examples. However, the global behavior of the column is not significantly sensitive to this parameter (i.e., t_3), and the FE-predicted drift ratio time-history from the updated model is still in good agreement with the measurement.

6.4.2. FEMU with high corrosion level

To further investigate the capability of the proposed methodology in identifying the corrosion-affected bonding properties, this study considers a higher corrosion level (i.e., 24%) for the RC column in case #4 in comparison to case #1 (i.e., 16%). The corresponding corroded to initial (uncorroded) ratios of t_1 and t_3 are 0.24 and 0.14, respectively, according to Eqs. (6-3) and (6-4). Similarly, their true values will be estimated using seismic measurement (simulated).

Figures 6-5 (a) and (b) show the time histories of the top drift ratio predicted from the FE model based on the bonding properties before and after updating in comparison with the measurement. As seen in the comparison, using nonlinear FEMU has resulted in a notable improvement in the FE prediction for this column with a high corrosion level. As a result, it can be concluded that nonlinear FEMU is capable of estimating corrosion-affected bonding properties at different corrosion levels. The updating histories of t_1 and t_3 in case #4 are shown in Figures 6-6 (a) and (b), respectively, similar to case #1. Due to the high level of corrosion in case #4, the bond yielding occurs at the earlier time step and thus both t_1 and t_3 would be updated earlier than in case #1 with a lower corrosion level.

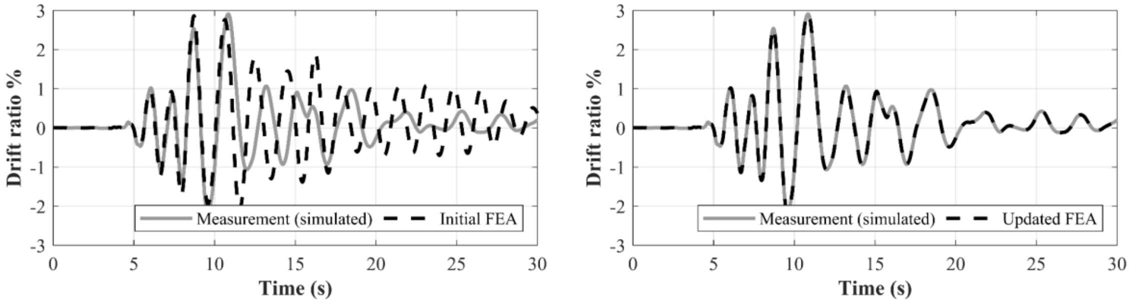

(a) (b)

Figure 6-5: Comparison of FE-predicted and measured time-histories of drift ratio for the RC column with 24% corrosion level in case #4 with zero noise: (a) before and (b) after updating

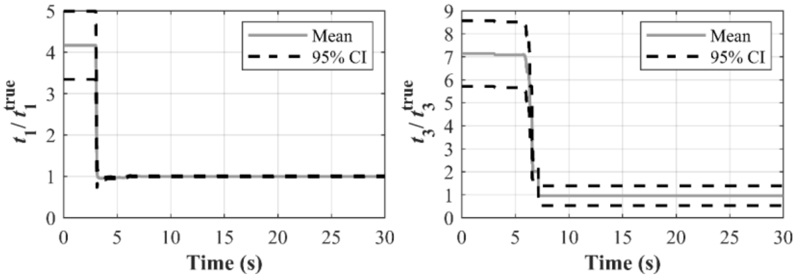

(a) (b)

Figure 6-6: Parameter updating histories of the RC column with 24% corrosion level for (a) t_1 and (b) t_3 in case #4 with zero noise

6.4.3. FEMU with different corroded features

In the preceding cases, the capability of the proposed methodology to estimate corroded bonding properties (i.e., t_1 and t_3) was examined. This section further investigates the capabilities of nonlinear FEMU in identifying the corrosion state of the RC columns by considering additional corrosion-affected parameters as unknowns. In this regard, the example RC column with various corroded features is used here (i.e., case #5). According to [183], corrosion can alter the cross-sectional area of steel bars, the properties of unconfined and confined concrete, and the bonding between steel bars and surrounding concrete. Hence, in addition to corroded t_1 and t_3 (i.e., t_1^c and t_3^c) taken into account in case #4, three additional corrosion-affected parameters are considered in case #5: (1) reduction percentage of cross-sectional area in longitudinal steel bars (e.g., $K_L = 24\%$); (2) reduction percentage of cross-sectional area in transverse reinforcement (e.g., $K_h = 45\%$), which is related to its corrosion effect on confined concrete; and (3) the corroded cover (unconfined) concrete strength f_c^c.

In the nonlinear FE model updating, the initial FE model is defined with uncorroded properties for bonding and cover concrete strength, and a 12% area reduction is assumed for both longitudinal and transverse reinforcements (i.e., K_L and $K_h = 12\%$). Figures 6-7 (a) and (b) compare the time-histories of drift ratio obtained from the FE model before and after updating to the counterpart measurement, respectively. The notable improvement in the FE predictions exhibited by this comparison confirms that nonlinear FEMU can also estimate unknown corroded properties when more corroded features are considered. However, identifying the true values of unknown parameters takes longer due to more unknown parameters and their interaction, as shown in Figures 6-8 (a) to (e), which present the updating histories of t_1, t_3, K_L, K_h, and f_c, respectively. Furthermore, the accuracy of estimated K_h and f_c is lower than that of other parameters, owing to the less corrosion effect of these parameters on the nonlinear behavior of RC column. These findings together provide important insights into the outstanding capabilities of nonlinear FEMU in estimating the corrosion state, as reflected by the corrosion-affected properties, of a corroded RC column.

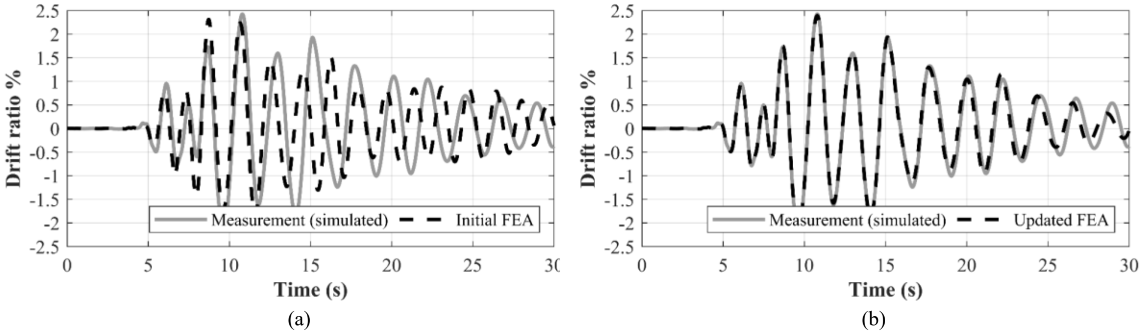

(a)
(b)

Figure 6-7: Comparison of FE-predicted and measured time-histories of drift ratio for the RC column with 24% corrosion level for (a) before and (b) after updating in case #5 with zero noise

In case #5, five unknown parameters pertaining to corrosion effects were considered. However, to reduce the computational cost of the nonlinear FEMU, only the corrosion level of longitudinal bars (i.e., K_L) will be considered unknown in the remaining study cases in addition to the two bonding properties (i.e., t_1 and t_3), and will be estimated throughout the updating process. Note that the corrosion-induced reduction of steel bar cross-sectional area, represented by K_L, is the most common corrosion aspect considered in the FE modeling of corroded RC structures [26].

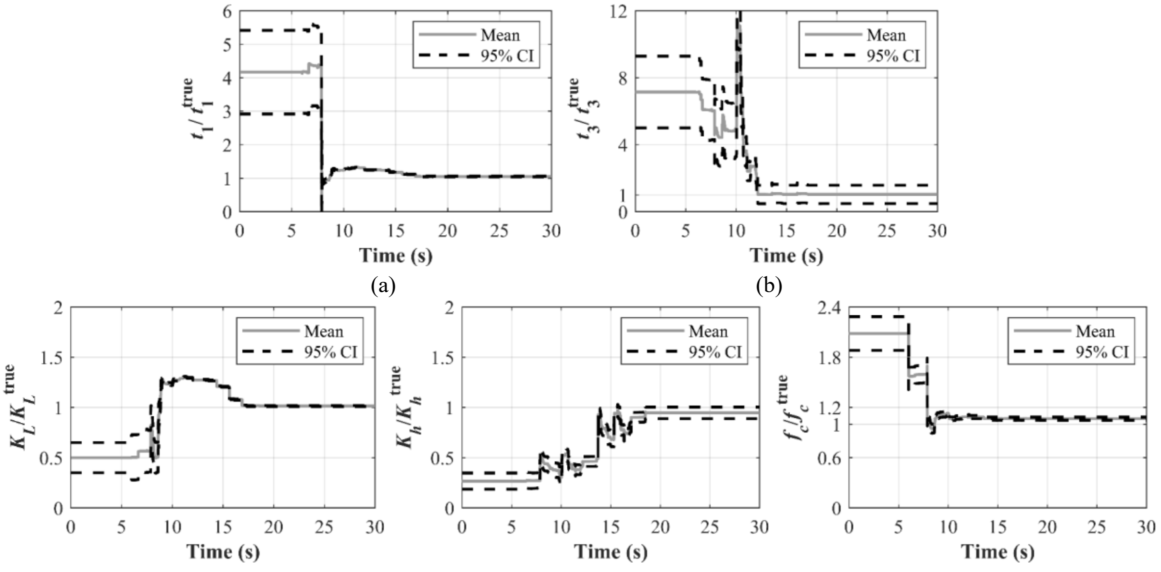

(a) (b)

(c) (d) (e)

Figure 6-8: Parameter updating histories of the RC column with 24% corrosion level for (a) t_1, (b) t_3, (c) K_L, (d) K_h, and (e) f_c in case #5 with zero noise

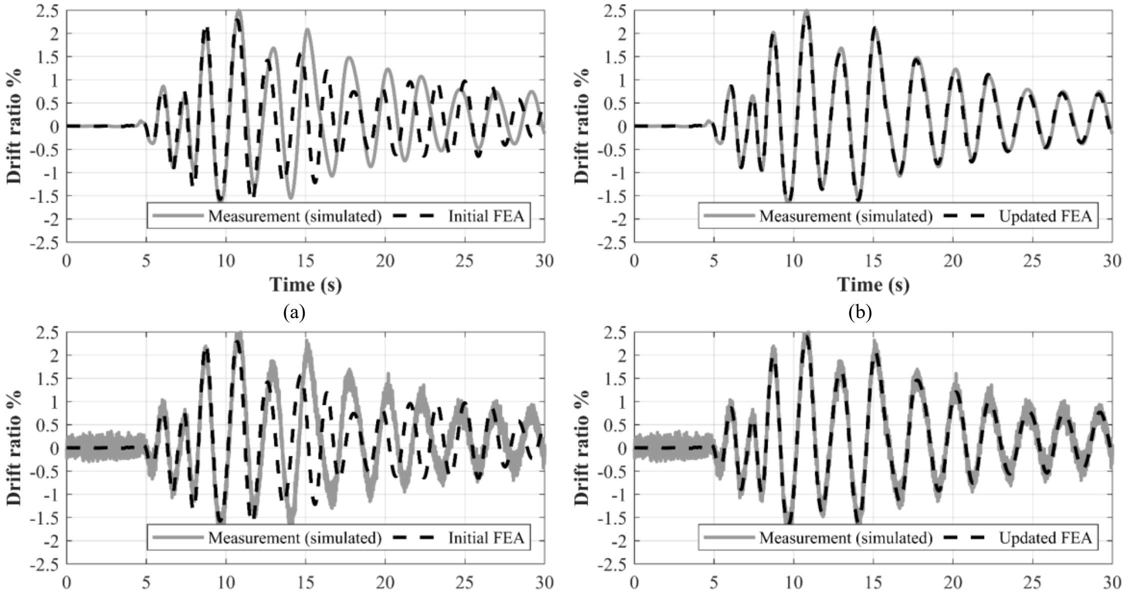

(a) (b)

(c) (d)

Figure 6-9: Comparison of FE-predicted and measured time-histories of drift ratio for the RC column with 24% corrosion level for (a) before and (b) after updating in case #6 with zero noise, and (c) before and (d) after updating in case #7 with 5% noise

Accordingly, cases #6 and #7 account for the corrosion impact on bonding and steel bar cross-sectional area with zero and 5% measurement noise, respectively. Figure 6-9 compares the time-histories of drift ratio before and after updating based on FE predictions to measurements with zero and 5% noise. The significant improvement in the FE-predicted drift ratio time-history demonstrates the capability of the nonlinear FEMU to estimate the unknown parameters (i.e., t_1, t_3, and K_L), even when additional corroded features are unknown. It is worth noting that the comparison between Figure 6-7 and Figure 6-9 reveals the corrosion effect on concrete only slightly altered the structural responses, confirming the significant role of these three corroded features comparing to concrete properties.

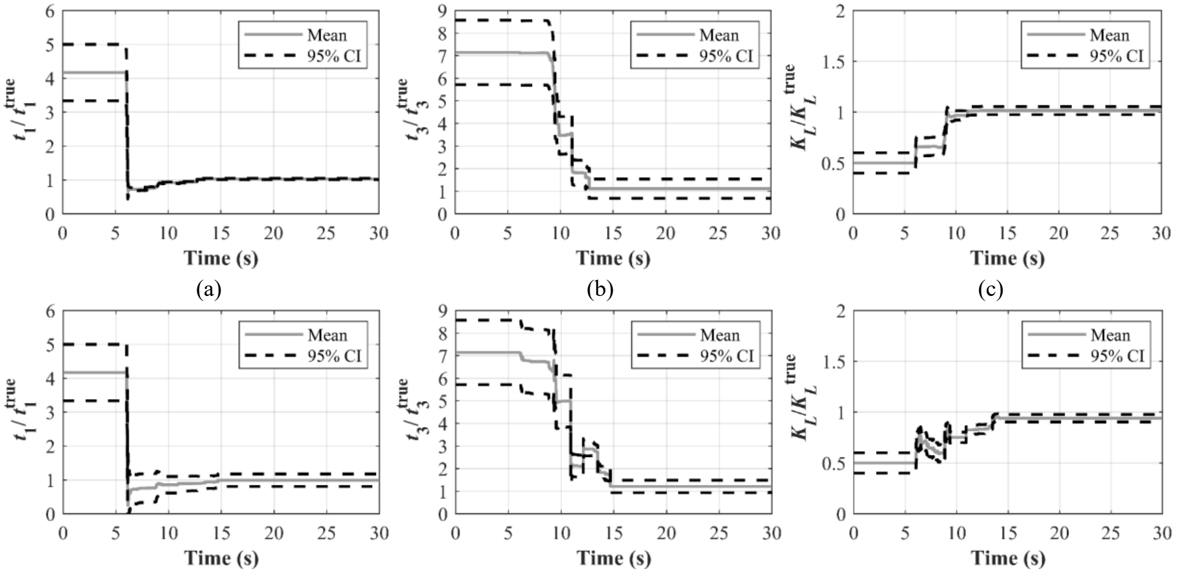

(a) (b) (c)

(d) (e) (f)

Figure 6-10: Parameter updating histories of the RC column with 24% corrosion level for (a) t_1, (b) t_3, and (c) K_L in case #6 with zero noise; for (d) t_1, (e) t_3, and (f) K_L in case #7 with 5% noise

Following the model updating results discussed above, Figure 6-10 presents the updating histories of t_1, t_3, and K_L in cases #6 and #7 with zero and 5% noise. As shown, the estimation of t_1 is converged to the true value in both cases, albeit with higher uncertainty in case #7 with 5% noise, which is consistent with the prior findings. In contrast, the updating histories of t_3 and K_L indicate that in case #7 with 5% noise, not only is the uncertainty of the estimated parameters higher, but also the accuracy of the estimated mean value is reduced due to the measurement contamination, when compared to case #6 with zero noise. However, the lower prediction accuracy does not affect the updated nonlinear behavior simulation of the corroded RC column, as illustrated in Figure 6-9, due to less sensitivity of the FE predictions to t_3 and K_L than t_1. As a result, the performance of the proposed methodology in estimating these corroded properties is satisfactory; in other words, the updated FE model can accurately replicate the nonlinear behavior of the corroded RC column. Note that the updating process has reduced the initial uncertainty assumed for all model parameters, as indicated by the 95% confidence interval in Figure 6-10.

6.4.4. FEMU of column under high-intensity excitation

To assess the performance of the proposed methodology for the columns with more nonlinearity in the structural responses, this section considers the RC column with 24% corrosion in cases #8 and #9, which are subjected to the high-intensity ground motion excitation, in comparison to cases # 6 and #7 with zero and 5% noise. Figure 6-11 presents the time-histories of drift ratio predicted from the FE model before and after updating compared to the measurement with zero and 5% noise.

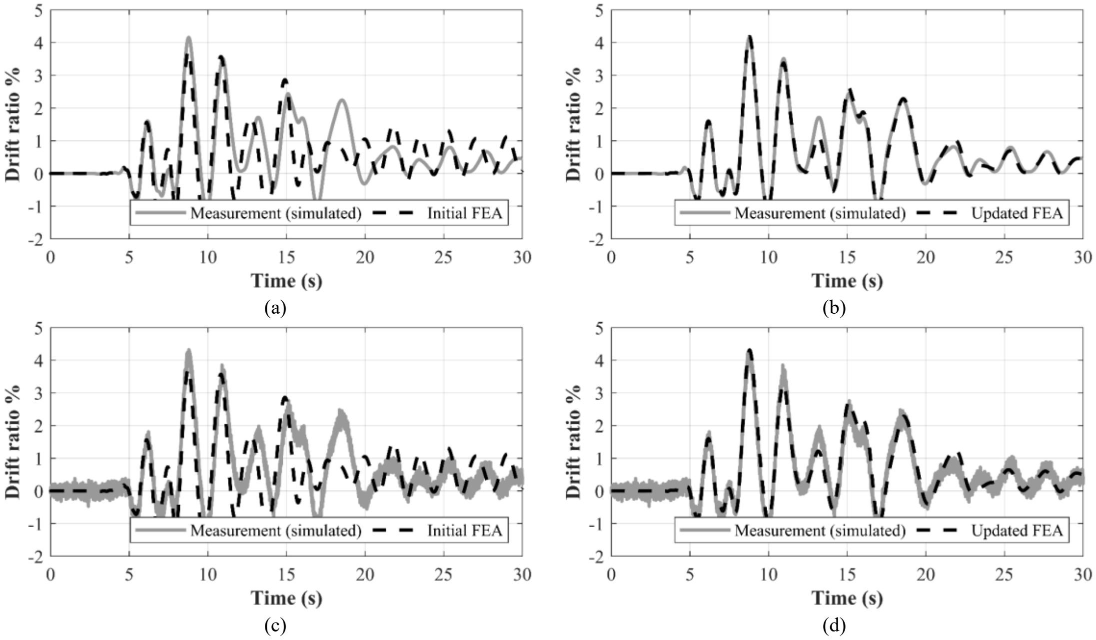

(a) (b)
(c) (d)

Figure 6-11: Comparison of FE-predicted and measured time-histories of drift ratio for the RC column with 24% corrosion level for (a) before and (b) after updating in case #8 with zero noise, and (c) before and (d) after updating in case #9 with 5% noise

Similar to cases #6 and #7 shown in Figure 6-9, comparing the before and after updating responses with the simulated measurement demonstrates a significant improvement in the FE predictions using the nonlinear FEMU. This finding confirms that the nonlinear FEMU can successfully update the FE model of the column subjected to the high-intensity ground motion excitation, resulting in more nonlinearity in the behavior of the RC column.

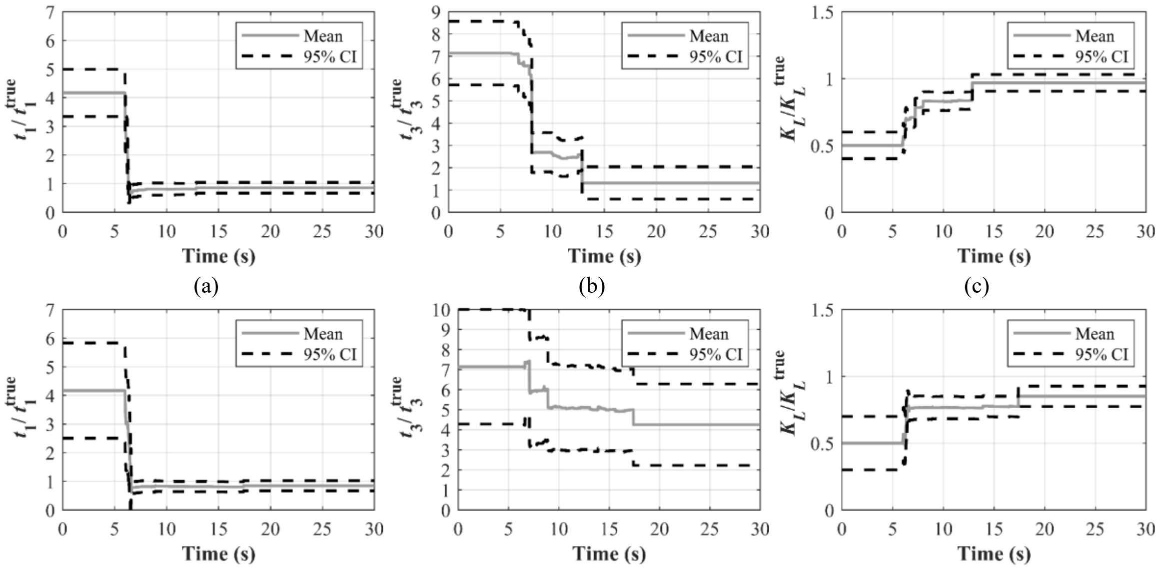

(a) (b) (c)

(d) (e) (f)

Figure 6-12: Parameter updating histories of the RC column with 24% corrosion level for (a) t_1, (b) t_3, and (c) K_L in case #8 with zero noise; for (d) t_1, (e) t_3, and (f) K_L in case #9 with 5% noise

To further illustrate the parameter estimation during the model updating process, Figure 6-12 presents the updating histories of t_1, t_3, and K_L for cases #8 and #9. As observed, the peak bonding stress (i.e., t_1) is estimated with high accuracy in both cases with zero and 5% noise. However, the predicted t_3 and K_L are less accurate than t_1, which is due to the complexity induced by the higher level of nonlinearity. Furthermore, comparing Figures 6-12 (b) and (c) with Figures 6-12 (e) and (f) reveals that the measurement noise has a significant impact on both parameter estimation accuracy and convergence time for t_3 and K_L in cases #8 and #9. In particular, the parameter estimations of t_3 and K_L do not converge to the true values, despite the fact that the overall behavior of the column matches the measurement relatively well. Additionally, in the absence of measurement noise (i.e., case #8), these parameters converge at $t \approx 13$ seconds, whereas the noise pollution extends the converging time (i.e., $t \approx 17$ seconds in case #9). These observations indicate that assessing the corroded characteristics becomes more challenging when the highly polluted measurement is obtained from the high-intensity excitation.

6.4.5. FEMU based on different types of measurement

The application examples described in the previous sections were all based on using the time-history of drift ratio as the measurement. However, it is necessary to prove the capability of the proposed methodology in identifying the corrosion state when other types of measurement are available. In this regard, three different sets of cases are considered: (1) using the time-history of drift ratio as the measurement in cases #6 and #7 for zero and 5% noise, respectively, (2) using the time-history of top acceleration as the measurement in cases #10 and #12 for zero and 5% noise, respectively, and (3) using both time-histories of top acceleration and drift ratio simultaneously as the measurements in cases #11 and #13 for zero and 5% noise, respectively.

Due to space limitation, the comparison of the FE-predicted displacement and acceleration histories with measurements (simulated) are not reported here. Instead, Figures 6-13 (a) and (b) show the updating history of the relative root mean square error (RRMSE) of drift ratio and top acceleration time-histories with respect to the corresponding noise-free measurements, respectively, for cases #6, #10, and #11. Eq. (6-6) presents the definition of RRMSE:

$$RRMSE = \sqrt{\frac{\sum_{i=1}^{N}\left(y_i - y_i^0\right)^2}{\sum_{i=1}^{N}(y_i^0)^2}} \tag{6-6}$$

where y_i corresponds to the response of the model after updating at the i^{th} step, y_i^0 denotes the response of the initial model at the i^{th} step, and N represents the total number of analysis steps for seismic response simulations. As seen in the comparison in Figure 6-13, the error in the FE predictions (i.e., RRMSE) has been substantially decreased in all three cases when compared to the initial responses. However, comparing the final RRMSE of these three cases indicates that using both top acceleration and drift ratio time-histories as measurements (i.e., case #11) leads to more accurate results than the other two cases (i.e., cases #6 and #10). In addition, comparing the accuracy of the updated FE predictions between cases #6 and #10 demonstrates that using the top acceleration time-history as the measurement may result in higher error in the updating findings due to high perturbation of the acceleration time-histories. Note that the updating results for similar cases with a 5% noise (i.e., cases #7, #12, and #13) indicate the same findings, which are not presented here for brevity.

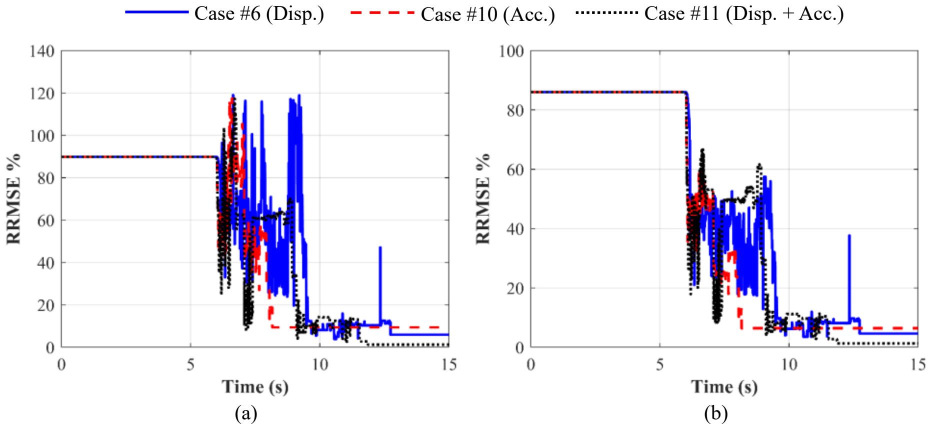

(a)
(b)

Figure 6-13: Updating history of RRMSE of (a) drift ratio and (b) top acceleration time-histories for the RC column with 24% corrosion level based on different types of noise-free measurement (cases #6, #10, and #11)

These observations are compatible with the updating histories of unknown parameters depicted in Figure 6-14. As shown, using both top acceleration and drift ratio time-histories as measurements results in more accurate parameter estimations with less uncertainty, i.e., a narrower 95% confidence interval. However, employing the top acceleration time-history provides the best performance among the others in terms of convergence time. This is due to the fact that the acceleration time-history contains more information in a short time frame. It is worth noting that the accuracy of updated responses resulting from the top acceleration time-history as the measurement is still satisfactory. Therefore, the findings suggest to use both the top acceleration and drift ratio time-histories as measurements, even though using each one individually results in acceptable and relatively reliable estimations.

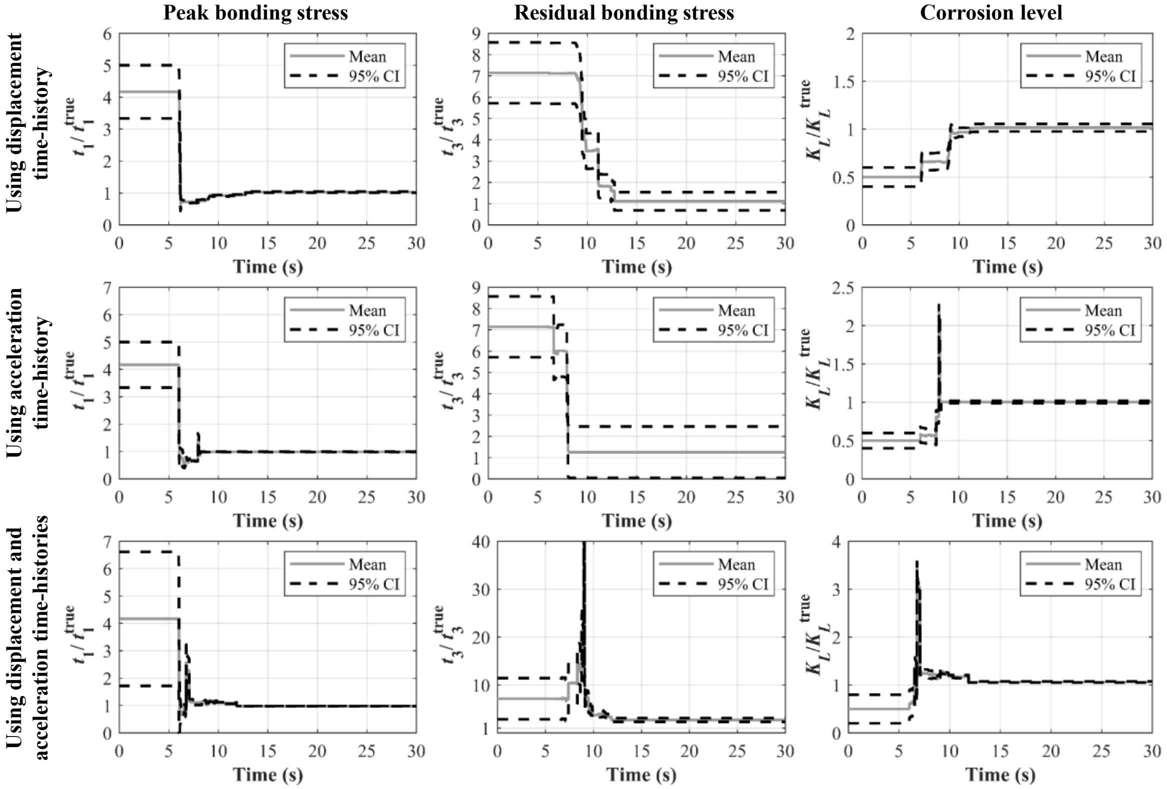

Figure 6-14: Parameter updating histories of the RC column with 24% corrosion level for t_1, t_3, and K_L in cases #6, #10, and #11 with zero noise

6.5. CHAPTER CONCLUSIONS

This study proposed a methodology to estimate the corrosion state, as reflected by the corrosion-affected proprieties of reinforced concrete (RC) structures, from seismic measurements. The idea behind was to integrate stochastic filtering, such as the unscented Kalman filtering (UKF) technique, with advanced nonlinear finite element (FE) modeling for corroded RC structures, to estimate the corroded properties based on global response measurement (e.g., displacement and/or acceleration time-history). For this purpose, an example RC column statically tested in the literature was modeled using a recently developed geometrically nonlinear fiber-based frame element with bond-slip and corrosion-affected features in the open-source FE framework (i.e., *OpenSees*). Due to the lack of experimental seismic observations for corroded RC structures, the measured responses used for parameter estimation in this study were simulated data from the nonlinear FE model of corroded RC columns under different scenarios. To the end, 13 different cases were studied using the proposed methodology to explore its capability.

Through case studies presented, the proposed approach was demonstrated to be capable of accurately estimating corrosion-affected properties, particularly the corroded bonding properties that cannot be measured directly, based on seismic measurements of global structural responses. Furthermore, different levels of corrosion, measurement noises, seismic excitation intensity, and various corroded features (e.g., corroded bonding properties, steel bar cross-sectional area reduction, corrosion level of transverse reinforcement, and degraded cover concrete strength) were all considered. The findings demonstrate that the presented methodology can successfully estimate the corroded properties and significantly improve the model prediction accuracy. In particular, the proposed methodology works well in estimating the corrosion state of RC columns despite the noise contamination of seismic measurements delaying the parameter identification and marginally lowering the accuracy. Additionally, the high nonlinearity in seismic responses, imposed by high corrosion and/or intensity level of ground motion excitation, cannot compromise the efficacy of the proposed methodology in estimating the corrosion-affected properties. Moreover, considering different types of measurement for system identification reveals that employing time-histories of both top acceleration and drift ratio together as the measurements can result in more precise parameter estimation. Together these results indicate that the methodology adopted in this study is promising to be used for condition assessment of corroded RC structures based on recorded seismic response data.

As the main limitation of the current work is using the simulated data to examine the capability of the proposed methodology, future research work is required to evaluate this methodology using real-world data on structures with corrosion effects. The updated FE model of the real-world corroded RC structure can be employed to assess their seismic performance, which assists in decision-making for repair or retrofit.

Chapter 7. PROBABILISTIC SEISMIC PERFORMANCE ASSESSMENT OF A CORRODED RC BRIDGE

7.1. INTRODUCTION

Reinforced concrete (RC) bridges, which are recognized as the most significant components of the transportation infrastructural system, are designed to remain operational for their design lifetime, during which the impacts of aging may cause performance degradation [26,28–30]. As one of the main environmental stressors that contributes to aging, corrosion of the reinforcing steel in RC bridges is more likely to occur, stemming from marine, airborne, and deicing sources [31]. Corrosion may affect the performance of RC bridges subjected to service loads or natural hazards, e.g., earthquake in seismic prone zones [32]. Specifically, numerous studies in the literature demonstrated that the impact of corrosion becomes more crucial when the bridges are subjected to seismic loading, since the corrosion of reinforcing steel can significantly reduce the lateral strength capacity [26,32–35]. Therefore, it is necessary to reliably estimate the safety and functionality of corroded RC bridges subjected to seismic loading by assessing their seismic performance during the course of their service life.

Due to the large variability in ground motion records and the corrosion process, it is expected that the seismic performance prediction entails a large uncertainty. To probabilistically assess the seismic performance of RC bridges, the performance-based earthquake engineering (PBEE) framework [14] can be used, which necessitates performing a large number of nonlinear time-history analyses using a suite of ground motions covering different levels of seismic intensity. In particular, the ground motion intensity measure (e.g., pseudo acceleration from elastic spectrum corresponding to the fundamental period or period of interest) is so adjusted to achieve different intensity levels associated with their corresponding seismic hazard levels. While this framework is specifically beneficial for precisely anticipating the seismic performance of structures (defined in terms of engineering demand parameters, a.k.a., EDPs) and has been widely used in the literature (e.g., [32,204–206]), it highly relies on the numerical model of the structure, which should be suitable and sufficient reliable for different structural health and seismic loading conditions considered. As a result, advanced computational modeling of the structure, which can represent various nonlinearities in the structural behavior, is essential to achieve reliable simulations of the nonlinear RC bridge responses.

Finite element (FE) modeling of RC structures can be accomplished through continuum-based and fiber-based approaches. Since the fiber-based FE modeling approach has been proven to be computationally more efficient for frame-type structural systems than the continuum-based approach with reasonable accuracy in the nonlinear structural behavior of interest, it has been widely applied in the field of structural earthquake engineering for RC bridges. The fiber-based FE model of corroded RC bridge is required to reflect different corrosion aspects, such as its impact on steel bar cross-sectional area, vulnerability of steel bars to buckling [140], cover concrete spalling [43], confinement level for core concrete [141], and bonding between steel bars and surrounding concrete [47]. By concentrating solely on the steel bar cross-sectional area reduction, which is relatively easier to account for in the modeling process for corroded RC structures, several studies investigated the impact of corrosion-induced deterioration on the structural reliability of the RC bridges [25,40]. The seismic performance of corroded RC bridges was later studied by accounting for the effect of corrosion on both the concrete and reinforcing steel [41,42]. These studies revealed that both strength and ductility of the structural members deteriorate over time by corrosion, affecting the seismic capacity of the bridge and eventually resulting in a shift to an undesirable mechanism of collapse. It is worth noting that other aspects of corrosion, particularly corrosion-damaged bonding and steel bar buckling that are relatively challenging to consider, were neglected in these studies. The impact of corrosion on seismic performance of RC bridges was further explored in [62,63] by capturing the strain penetration in the FE model of RC bridges using an oversimplified method, which lumps the bond-slip effect at the bottom of bridge column [64]. These studies showed that the deterioration in strain penetration increases the seismic fragility of corroded RC bridges, highlighting the importance of considering different aspects of corrosion. In particular, Bouazza et al. [207] investigated how incorporating bond-slip and steel bar buckling affected the seismic performance of uncorroded RC bridge piers. They found that neglecting these modeling aspects can lead to overestimation of the seismic performance. This highlights the need for integrating these aspects into the FE model of corroded RC bridges, in which corrosion may cause further degradation. To this end, this study employs advanced FE modeling approaches to simulate the seismic response of corroded RC bridges while incorporating various corrosion-related aspects, such as corrosion-affected bond-slip and buckling [183,208]. It is worth mentioning that the pristine RC bridge model that has been modified by corrosion is the basis for the seismic performance analysis discussed above.

However, in reality, there may be several earthquakes throughout the lifespan of the bridge, for which the recorded seismic measurements can be employed to estimate the current state of the RC bridge [209]. Namely, the seismic measurements can inform the current state of the bridge; therefore, an updated model of the corroded RC bridge can be used for re-assessing its seismic performance, which will be further studied in this research work.

The remainder of this work is organized as follows. Firstly, the description of the selected RC bridge is presented, followed by a brief description of the advanced FE modeling for this bridge under corrosion and the ground motion selection for seismic analysis. The corrosion process entails several significant sources of uncertainties, which are presented to illustrate the corrosion levels. Secondly, the probabilistic seismic capacity analysis is conducted on this RC bridge to evaluate the corrosion impact on the capacity of bridge columns. Additionally, the contributions of advancements in different aspects of the FE modeling approach to seismic capacity evaluation is studied. Thirdly, the probabilistic seismic demand analysis is performed to investigate the corrosion effects on the probabilistic demand hazard curves. Using the proposed probabilistic models for seismic capacity and the probabilistic demand hazard curves, the impact of corrosion on the seismic risk of this RC bridge is explored in terms of probability of demand exceeding the corresponding capacity. In the end, this study conducted a post-event analysis to reveal the importance of corrosion state estimation on the seismic performance prediction of RC bridges.

7.2. BRIDGE MODELING

7.2.1. Bridge description

This study considers an RC bridge as an application example to investigate the impacts of corrosion on its seismic performance assessment. To this end, the Jack Tone Road Overcrossing, located in Ripon, California, US, is selected. As illustrated in Figure 7-1, this bridge, built in 2001, has one single lane and two spans supported on a single column. The bridge deck, with a length of 67.18 m (33.10 m and 34.08 for two spans), is a three-cell continuous prestressed RC box girder with a total width of 8.27 m and a depth of 1.14 m. The bridge abutment, which is at a skew of 33°, is supported vertically by four elastomeric bearings (with height of 0.065 m and area of 0.09 m^2), and restrained horizontally by monolithic shear keys. The single column of this bridge, which is 8.5 m high with a circular cross-section with a diameter of 1.68 m, is reinforced by 22 double #36 longitudinal steel bars and lateral reinforcement of #19 spaced at 85 mm. The concrete used in this column has the nominal strength of 34.5 MPa, and the reinforcing steel is Grade 60 with the nominal yield stress of 468.84 MPa. This column is located on a foundation with a height of 1.37 m and the square cross-section of 5.18 m × 5.18 m, with hooked longitudinal steel bars at the bottom. It is also worth mentioning that the soil stratum predominantly made up of layers of sandy gravel and cobbles overlaid on a layer of dense gravel, and thus according to NEHRP site classification [210], this site is classified as stiff soil (class D) based on the average shear wave velocity in the top 30 m of 307 m/s.

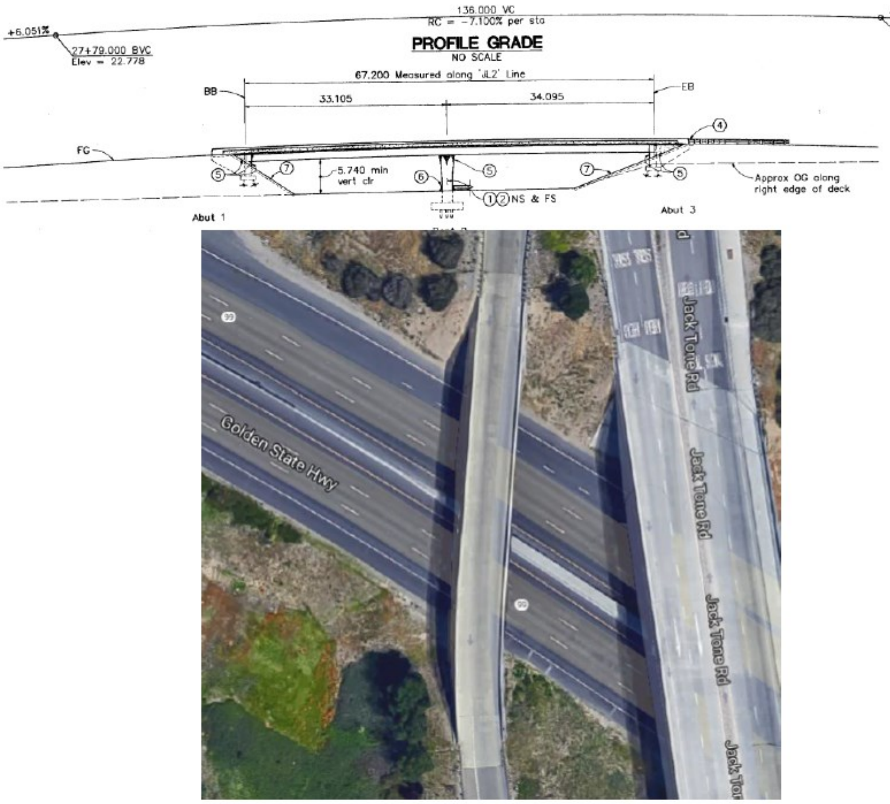

Figure 7-1: Profile and overview of considered RC bridge (adjacent to main Jack Tone Road) [211]

7.2.2. Advanced FE modeling of the RC bridge

To use this RC bridge for corrosion-affected seismic analysis, it is required to be modeled using an efficient and comprehensive approach. In this regard, a three-dimensional nonlinear FE model is developed in *OpenSees* [65]. This research work took the *OpenSees* models of this bridge from previous Caltrans/PEER funded projects [212,213], and improved them based on the advanced FE modeling approach proposed in this study in Chapters 2 to 5. A brief description of this FE model is presented in the following, with a schematic overview of the developed FE model shown in Figure 7-2.

Since the superstructure is protected by a capacity design and expected to remain within the elastic range [66], the bridge deck is modeled with ten linear elastic beam-column elements in each span for the composite actions of steel girders and bridge deck. To model the single column, 12 fiber-based frame elements with bond-slip (i.e., *dispBeamColumnBS*) is used. The foundation is similarly modeled with 5 elements to account for the imperfect bonding along anchorage zone. The sections assigned to these elements consist of a number of fibers representing cover concrete and core concrete (modeled by *Concrete02*) and steel bars (modeled by *Steel02BS* along the column and *Steel02* along the foundation). It is worth mentioning that the properties of core concrete are defined based on Mander's equations [45], and the bonding properties are estimated using the developed models in Chapter 3 [143]. Since the focus of this study is on the seismic behavior of corroded RC bridges, the FE model of the column accounts for the corrosion impacts through modifying the steel bar cross-sectional area, properties related to steel bar buckling, bond-slip model, and concrete properties, following the modeling approach provided in Chapters 4 and 5.

Furthermore, pre-existing analytical models are used [67–69] for modeling the abutments and bearings of the bridge. In particular, the coupled bidirectional shear force-deformation response is represented by modeling the longitudinal and transverse resistance of the bearing pads at the abutments using zero-length elements. Note that each bearing has a fixed connection at the base of the bearing element that supports it in the vertical direction. The transverse resistance of an exterior shear key is reflect by a translation compressive spring. Additionally, four translational compressive gap springs are employed along the width of the abutments to model the soil-structure interaction between the bridge deck and the embankment backfill. A nonlinear hysteretic force deformation relationship with a hyperbolic backbone curve is employed here to model the passive resistance of each backfill spring activated upon closure of gap. Readers who are interested in more details about abutment modeling for this bridge can refer to [211–213].

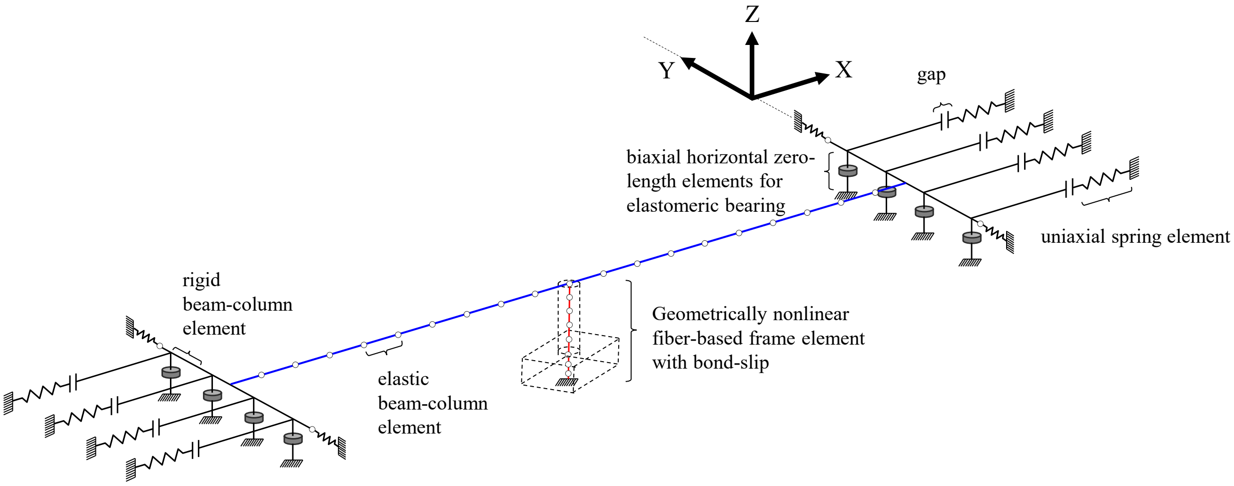

Figure 7-2: Schematic FE model of the RC bridge

7.2.3. Ground motion selection for seismic analysis

The probabilistic seismic hazard analysis integrates the contributions of all possible seismic sources corresponding to their likelihood. To consider a wide range of seismic hazard levels, this study uses the probabilistic seismic hazard curve for this RC bridge taken from [214] developed based on the uniform hazard spectrum. In this analysis, six seismic hazard levels are considered, defined as: level I with mean return period of 72 years (or 50% probability of exceedance in 50 years), level II with mean return period of 224 years (or 20% probability of exceedance in 50 years), level III with mean return period of 475 years (or 10% probability of exceedance in 50 years), level IV with mean return period of 975 years (or 50% probability of exceedance in 50 years), level V with mean return period of 2475 years (or 2% probability of exceedance in 50 years), and level VI with mean return period of 4975 years (or 1% probability of exceedance in 50 years). The seismic hazard curve yields a pseudo-acceleration (i.e., S_a(g)) that corresponds to each level of hazard and is used as an intensity measure. A randomly chosen record from a database collected from [70] is so scaled to reach the desired S_a based on the seismic hazard level. It is worth mentioning that the deaggregation data obtained from [214] is used to eliminate earthquakes with unlikely source-to-site distance at each hazard level. In addition, to avoid arbitrary scaling factors, the ground motion records with scaling factors greater than 4 and lower than 0.8 are not selected [215].

7.2.4. Corrosion Process

Time-dependent corrosion models have been created for various environmental situations in the literature to model corrosion as an aging phenomenon. This study employs the probabilistic models developed by [25,26,216] to consider reasonable levels of corrosion.

The main cause of steel corrosion is thought to be the entry of chloride ions through the concrete cover and into the reinforcing steel from the concrete surface. To determine the time required for chloride ions to reach the steel, i.e., the time of corrosion initiation T_i, this study employs the model presented in Eq. (7-1) [26]:

$$T_i = \frac{c}{4D_c}\left[\mathrm{erf}^{-1}\left(\frac{C_0 - C_{cr}}{C_0}\right)\right]^{-2} \tag{7-1}$$

where c is the cover depth in cm with a coefficient of variation (CoV) of 0.2, D_c is the diffusion coefficient with a mean of 1.29 cm^2/year and a CoV of 0.1, C_0 denotes for the surface chloride concentration with a mean of 0.1 and a CoV of 0.1, C_{cr} is the critical chloride concentration with a mean of 0.04 and a CoV of 0.1, and erf denotes the Gaussian error function. Assuming lognormal distributions for these parameters, the initiation time is estimated considering the prevailing uncertainties. Note that the mean values presented above depend on the environmental exposure conditions.

Following the corrosion initiation time, the time-dependent loss of cross-sectional area needs to be considered. Since the corrosion process has no memory of the past in the time-domain, the time-continuous state-separated Markov chain model is employed, which results in the Gumbel distribution for the ratio of the average cross-sectional area to the minimum one [216]. The reduced cross-sectional diameter is determined by Eq. (7-2) using this parameter, which is required to define the corrosion rate, i.e., λ [26]:

$$d_b^{\,c}(t) = d_b - 2\lambda(t - T_i) \text{ for } T_i < t \leq T_i + \frac{d_b}{2\lambda}; 0 \text{ for } t > T_i + \frac{d_b}{2\lambda} \tag{7-2}$$

where d_b is the initial bar diameter, d_b^c is the reduced bar diameter, and t denotes for time in years. Note that the bar diameter remains unchanged before reaching T_i. Assuming "medium-to-high corrosion intensity" situation, in which un-cracked concrete specimens are subjected to a relatively high level of contamination (e.g., salt spray condition) with visible corrosion products [40], the corrosion current density with a mean of 3 μA/cm^2 and CoV of 0.2 following a normal distribution is used to determine the corrosion rate. Accordingly, the corrosion level (i.e., K) defined as the percentage of mass loss of the corroded steel bar is calculated. Note that the corrosion level of transverse reinforcement, i.e., K_L, needs to be determined separately since the concrete cover for transverse reinforcement is different (smaller) than the one for longitudinal steel bar. Figure 7-3 presents the mean and mean ± standard deviation of K and K_L using the introduced model for the considered RC bridge.

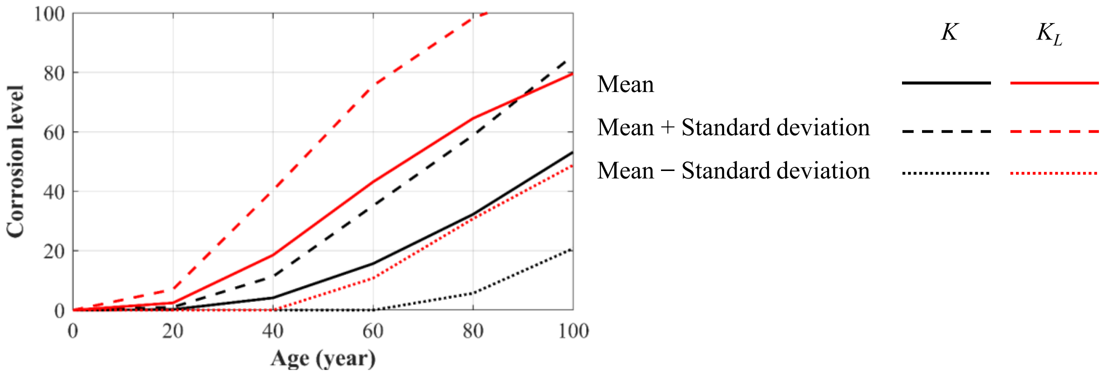

Figure 7-3: Time-dependent corrosion level for longitudinal and transverse reinforcement

7.3. PROBABILISTIC SEISMIC CAPACITY ANALYSIS

This section investigates the effect of corrosion on the seismic capacity of the RC bridge in a probabilistic framework. In RC bridges, the piers transfer the vertical loads from the superstructure to the foundation while also resisting all horizontal and transverse loads acting on the bridge [217]. The RC bridge considered in this study consists of a single column bent with a monolithic connection to the superstructure. As a result, the bridge behaves as a simple vertical column in transverse direction, which is represented in this section by a single-curvature column [218]. On the other hand, the bridge pier is subjected to double-bending in the longitudinal direction, which is modeled as a double-curvature column here [218]. These simplified models are used to study the seismic capacity of the RC bridge under various corrosion levels across a life span of 100 years (i.e., every 20 years). To account for the uncertainties associated with the corrosion process, the probabilistic model discussed in the previous section is employed in accordance with Latin Hypercube Sampling [135] to generate 100 samples at each age with random corrosion levels for longitudinal and lateral reinforcements (i.e., K and K_L, respectively). The seismic capacity of these samples is determined in terms of base shear V, base moment M, drift ratio Δ, and ductility μ by conducting static pushover analysis. The maximum values achieved in the monotonic behavior of the RC columns are defined as the base shear and base moment capacities. On the other hand, the maximum drift ratio is established in accordance with the point that the first core concrete crushing occurs. This is also used to define the ductility in addition to the yield deformation at the first cover concrete crushing.

To explore the contributions of modeling improvements on the seismic capacity prediction of the corroded RC bridge, the approach discussed above is applied to four groups of FE model:

(1) Case 1, which is the model with bond-slip and steel bar buckling;
(2) Case 2, which is the model with bond-slip but no steel bar buckling;
(3) Case 3, which is the model with perfect bonding and steel bar buckling; and
(4) Case 4, which is the model with perfect bonding but no buckling effect, referred to as the conventional modeling approach.

In each of these scenarios, the seismic capacity parameters are determined for the samples generated at each age by performing the static monotonic pushover analysis. Comparing the resulted seismic capacities demonstrates the contributions of the advancements in the FE modeling approach used in this study.

Figure 7-4 and Figure 7-5 present the impact of corrosion on the ratio of obtained capacity to the corresponding capacity estimated based on the conventional modeling approach used for pristine condition column, i.e., no corrosion, for double-curvature and single-curvature columns, respectively. Comparing the mean values for the ratio of base shear (i.e., V_c) to the corresponding initial value (i.e., V_0) in the double-curvature column indicates that neglecting corrosion-affected bond-slip in the FE models may lead to an overestimation of the base shear capacity, while the buckling behavior of steel bar has only slightly affected the base shear capacity. Due to the additional rotation in the base of the column that bond-slip causes, this effect is more significant in the double-curvature column than the single-curvature column. Note that the bond-slip plays more important role in double-curvature columns with restrained rotations on the top. Similar findings apply to the base moment capacity (i.e., M_c/M_0) with higher bond-slip effect on the base moment capacity. It is worth mentioning that the bars in Figure 7-4 and Figure 7-5 display the mean values, and thus in order to demonstrate the variations, the error bars are shown demonstrate the mean ± standard deviation, which indicate wider distributions (i.e., higher standard deviation) as corrosion increases.

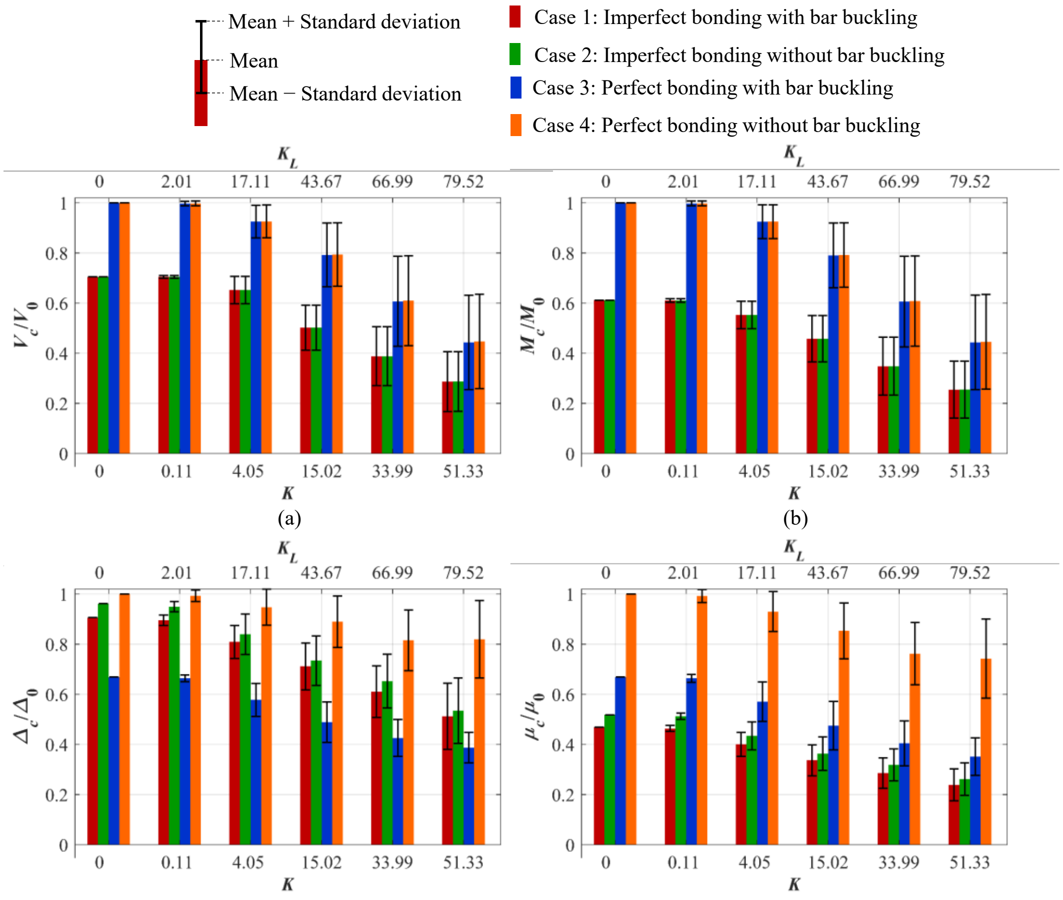

(a) (b)

(c) (d)

Figure 7-4: Corrosion impact on the ratio of seismic capacity of four cases defined with respect to that of conventional model for (a) base shear, (b) overturning moment, (c) drift ratio, and (d) ductility of double-curvature column (i.e., in longitudinal direction)

Comparing the drift ratio and ductility capacity predicted by cases 1 and 2 with those of cases 3 and 4, as shown in Figure 7-4, it reveals the significant impact of corroded bond-slip in these parameters, which gets more dominant as the corrosion level increases. The same comparison based on Figure 7-5 shows that the corroded bond-slip has a noticeable impact on drift ratio and ductility capacities, while the contribution of bond-slip is less in single-curvature columns than in double-curvature columns. Furthermore, neglecting the steel bar buckling results in overestimations of drift ratio and ductility capacities. It is worth mentioning that the corroded bond-slip leads to less contribution from the steel bar, and thus it lessens the steel bar buckling effect, as shown by comparing cases 2 and 3 in Figure 7-4 and Figure 7-5. As a result, using conventional modeling approach can significantly overestimate the seismic capacity of corroded RC bridges, specifically the parameters relating to their post-peak behavior, such as drift ratio and ductility, which may result in unsafe performance predictions for corroded RC bridges.

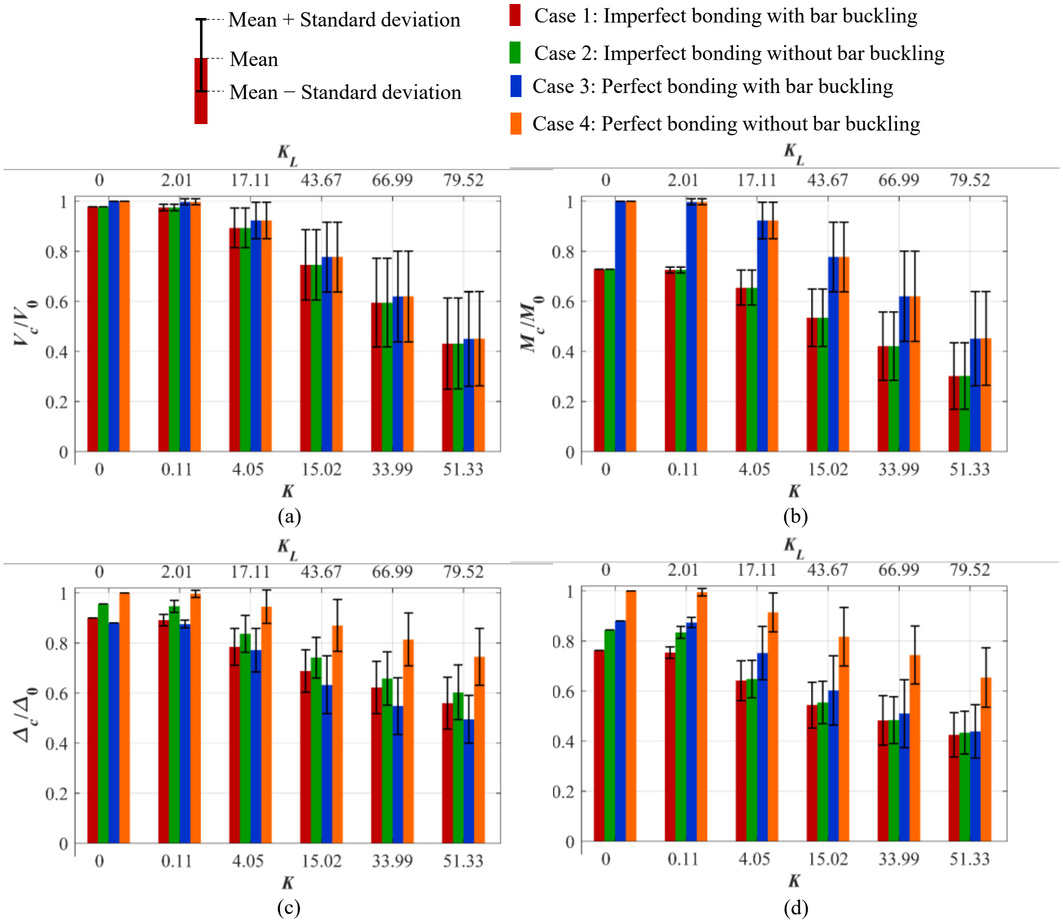

(a) (b)

(c) (d)

Figure 7-5: Corrosion impact on the ratio of seismic capacity of four cases defined with respect to that of conventional model for (a) base shear, (b) overturning moment, (c) drift ratio, and (d) ductility of single-curvature column (i.e., in transverse direction)

In order to assess the seismic performance of corroded RC bridges, the initial seismic capacity needs to be reduced due to corrosion. To this end, this study develops novel probabilistic models to modify the seismic capacity of uncorroded RC bridge based on the corrosion level. In this regard, Bayesian linear regression [130] is used to develop the probabilistic models utilizing the simulated data generated above for case 1 (i.e., with all advanced aspects considered in FE modeling). Eqs. (7-3) to (7-6) show the functional form presented for V_c, M_c, Δ_c, and μ_c based on their corresponding initial capacity. θ_i's are model parameters and ε is the model error, which is assumed to be Gaussian with zero mean and standard deviation σ_i as a hyper-parameter. Table 7-1 provides the first- and second-moment statistics of these parameters (i.e., mean, coefficient of variation (CoV), and correlation coefficients) for both single-curvature and double-curvature columns. In accordance with Bayesian statistics, assuming the non-informative priors (i.e., locally uniform priors), the posterior distributions of model parameters (i.e., θ_i's) and the hyper-parameter σ_i would be the multivariate t-distribution and the inverse chi-squared distribution, respectively [130].

$$\frac{V_c}{V_0} = \log(K^{\theta_1} K_h^{\theta_2}) + \theta_3 + \varepsilon(\sim N(0, \sigma_1)) \leq 1.0 \tag{7-3}$$

$$\frac{M_c}{M_0} = \log(K^{\theta_4} K_h^{\theta_5}) + \theta_6 + \varepsilon(\sim N(0, \sigma_2)) \leq 1.0 \tag{7-4}$$

$$\frac{\Delta_c}{\Delta_0} = \log(K^{\theta_7} K_h^{\theta_8}) + \theta_9 + \varepsilon(\sim N(0, \sigma_3)) \leq 1.0 \tag{7-5}$$

$$\frac{\mu_c}{\mu_0} = \log(K^{\theta_{10}} K_h^{\theta_{11}}) + \theta_{12} + \varepsilon(\sim N(0, \sigma_4)) \leq 1.0 \tag{7-6}$$

To show the accuracy of the proposed models, Figure 7-6 and Figure 7-7 compare the numerical simulations (referred to as observations) and the seismic capacity predicted based on the proposed models, for double-curvature and single-curvature columns, respectively. The deviation of the data points from the unity line (45° line) in these figures indicates the associated error, and the R-squared (R^2) value for each model is also reported; a value closer to 1.0 implies a better model generally. As indicated in these figures, the model predictions are in good agreement with the observations with the R-squared values close to 1, which implies the models are capable of properly predicting these corrosion-affected seismic capacities given the seismic capacity based on the pristine condition (i.e., uncorroded). Although not shown here for brevity, diagnostic tests were conducted for the generated models to evaluate normality and homoscedasticity of model residuals. In particular, the normality plots for each model show that model prediction residuals follow a Gaussian distribution, and the residuals plots indicate no sign of heteroscedasticity.

Table 7-1: Regression parameters for the proposed probabilistic models

Single-curvature column						**Double-curvature column**					
			Correlation coefficients						**Correlation coefficients**		
Parameters for V_c/V_0	**Mean**	**CoV**	θ_1	θ_2	θ_3	**Parameters for V_c/V_0**	**Mean**	**CoV**	θ_1	θ_2	θ_3
θ_1	−0.179	0.025	1.00	−0.77	−0.47	θ_1	−0.177	0.021	1.00	−0.73	−0.48
θ_2	0.0168	0.220	−0.77	1.00	−0.06	θ_2	0.013	0.232	−0.73	1.00	−0.09
θ_3	1.046	0.008	−0.47	−0.06	1.00	θ_3	1.045	0.007	−0.48	−0.09	1.00
σ_1	0.095	0.037	–	–	–	σ_1	0.086	0.037	–	–	–
Parameters for M_c/M_0	**Mean**	**CoV**	θ_4	θ_5	θ_6	**Parameters for M_c/M_0**	**Mean**	**CoV**	θ_4	θ_5	θ_6
θ_4	−0.257	0.016	1.00	−0.35	−0.84	θ_4	−0.186	0.017	1.00	−0.73	−0.48
θ_5	0.008	0.270	−0.35	1.00	−0.16	θ_5	0.014	0.175	−0.73	1.00	−0.09
θ_6	1.324	0.010	−0.84	−0.16	1.00	θ_6	1.037	0.006	−0.48	−0.09	1.00
σ_2	0.052	0.044	–	–	–	σ_2	0.072	0.037	–	–	–
Parameters for Δ_c/Δ_0	**Mean**	**CoV**	θ_7	θ_8	θ_9	**Parameters for Δ_c/Δ_0**	**Mean**	**CoV**	θ_7	θ_8	θ_9
θ_7	−0.090	0.025	1.00	−0.46	−0.23	θ_7	−0.104	0.026	1.00	−0.41	−0.27
θ_8	−0.017	0.124	−0.46	1.00	−0.59	θ_8	−0.011	0.223	−0.41	1.00	−0.59
θ_9	0.997	0.006	−0.23	−0.59	1.00	θ_9	0.995	0.008	−0.27	−0.59	1.00
σ_3	0.081	0.032	–	–	–	σ_3	0.098	0.032	–	–	–
Parameters for μ_c/μ_0	**Mean**	**CoV**	θ_{10}	θ_{11}	θ_{12}	**Parameters for μ_c/μ_0**	**Mean**	**CoV**	θ_{10}	θ_{11}	θ_{12}
θ_{10}	−0.120	0.017	1.00	−0.48	−0.23	θ_{10}	−0.132	0.016	1.00	−0.46	−0.33
θ_{11}	−0.009	0.208	−0.48	1.00	−0.58	θ_{11}	−0.006	0.308	−0.46	1.00	−0.51
θ_{12}	0.987	0.006	−0.23	−0.58	1.00	θ_{12}	0.982	0.006	−0.33	−0.51	1.00
σ_4	0.071	0.032	–	–	–	σ_4	0.073	0.033	–	–	–

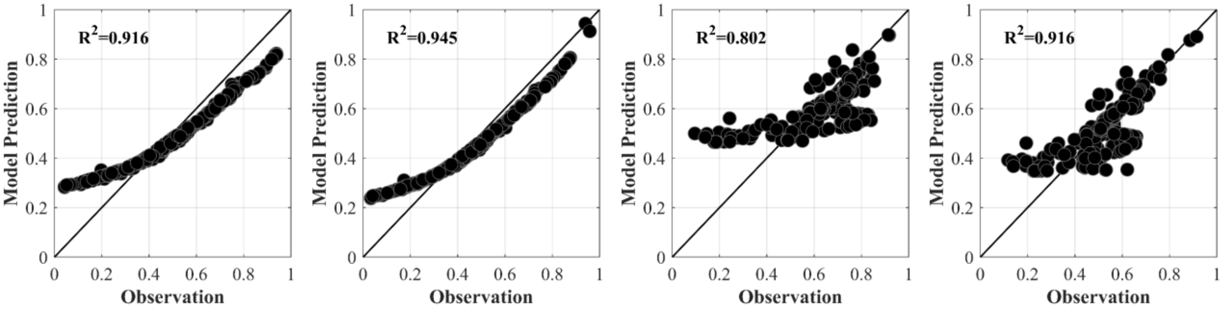

(a) (b) (c) (d)

Figure 7-6: Observations vs. predictions using models for seismic capacity of (a) base shear, (b) overturning moment, (c) drift ratio, and (d) ductility of double-curvature column

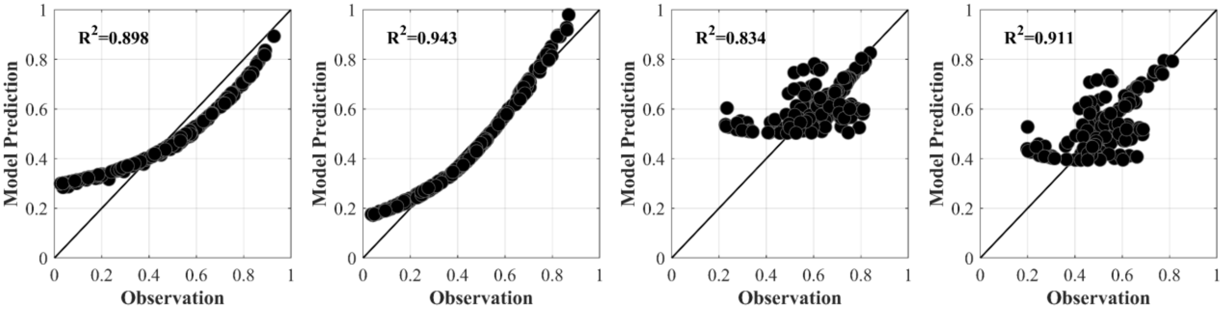

(a) (b) (c) (d)

Figure 7-7: Observations vs. predictions using models for seismic capacity of (a) base shear, (b) overturning moment, (c) drift ratio, and (d) ductility of single-curvature column

7.4. PROBABILISTIC SEISMIC DEMAND ANALYSIS

To evaluate the seismic performance of the RC bridge over time, i.e., as affecting by corrosion, this section examines the seismic demand under corrosion effect in a probabilistic framework with a goal of elucidating how the corrosion impacts the seismic risk. In this regard, it is first required to find the probabilistic demand hazard curve, i.e., $P(\text{EDP}\geq d_s)$, which shows the annual likelihood that the engineering demand parameter (EDP) exceeds any specified value d_s. The total probability theorem [219] is used to express this probability as Eq. (7-7):

$$P(\text{EDP} \geq d_s) = \int P(\text{EDP} \geq d_s \mid S_a = x) P(S_a = x) dx \tag{7-7}$$

in which $P(S_a = x)$ is the likelihood of a given level of spectral acceleration (S_a), employed as the intensity measure in this study. This term can be easily obtained from the standard hazard curve

[214], approximated by a linear function in the log-log plot in the region of interest [220], as shown in Eq. (7-8):

$$P(S_a = x_i) = |\, d(H(S_a)) \,| = |\, d(\exp(-8.4) S_a^{-2.4}) \,| \tag{7-8}$$

where d indicates the derivative of standard hazard curve ($H(S_a)$).

The first term in Eq. (7-7) expresses the likelihood that EDP exceeds d_s given the value of S_a, which is the conditional probability of EDP. This likelihood can be determined using structural time-history analysis. To this end, a series of aged RC bridges are considered across a life span of 100 years (i.e., every 20 years). To account for the uncertainties in ground motions and corrosion levels for longitudinal and lateral reinforcements (i.e., K and K_L, respectively), at each age level, 100 samples are generated using Latin Hypercube Sampling [135] for each of six different hazard levels considered. Conducting time-history analysis for these samples results in 600 time-history structural responses, which can provide estimations of desired EDPs, including maximum base shear, base moment, and drift ratio of the bridge column. Figure 7-8 demonstrates the conditional probability distribution of these EDPs in longitudinal and transverse directions for the uncorroded bridge (i.e., t=0) with respect to S_a. Note that the seismic hazard curve, i.e., $H(S_a)$, is also shown in these figures to reflect various hazard levels considered in this analysis. The mean and mean ± standard deviation of these responses are depicted in this figure together with the probability density functions (PDFs) at each S_a. This figure indicates intensity measures (i.e., S_a) result in greater seismic demands. Assuming that these seismic demands are distributed lognormally about their specified mean $\bar{D}$ and standard deviation $\bar{s}$ [221], a regression analysis is performed to find a relationship between the mean and standard deviation values with K, K_L, and $\mathrm{S_a}$ [220], following a functional form shown in Eq. (7-9):

$$\bar{D}(\text{or } \bar{s}) = c_1 S_a^{c_2} \exp(cK + c_4 K_L) \tag{7-9}$$

where c_1, c_2, c_3, and c_4 denotes for constant values obtained from regression analysis for each case. It is worth noting that the mean and standard deviation of the conditional probabilities have an extra term to adjust these parameters based on the corrosion level, i.e., K and K_L.

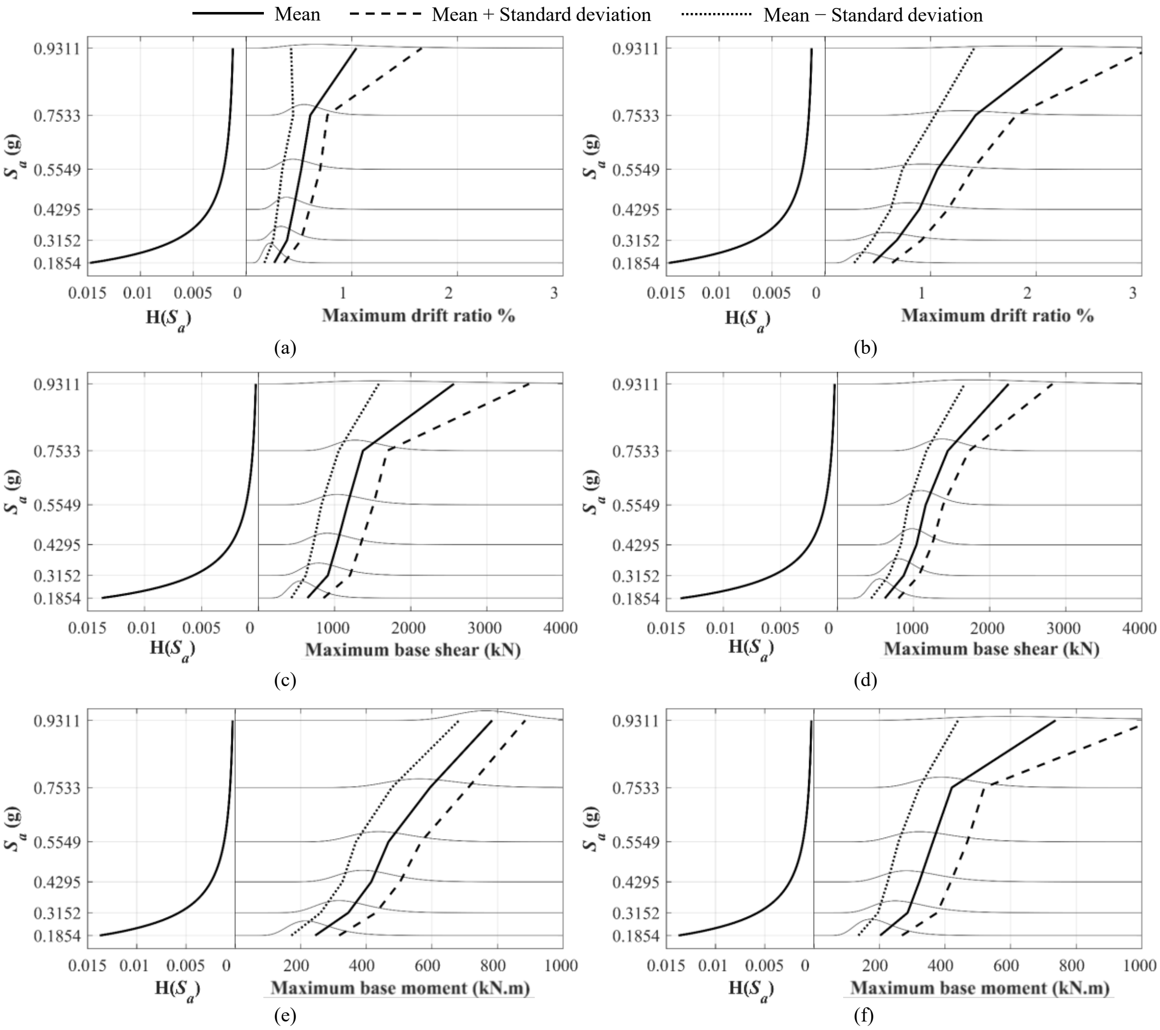

(a) (b) (c) (d) (e) (f)

Figure 7-8: Conditional probability distribution of seismic demands for uncorroded bridge, in terms of maximum drift ratio in (a) longitudinal and (b) lateral directions, maximum base shear in (c) longitudinal and (d) lateral directions, and maximum base moment in (e) longitudinal and (f) lateral directions

To demonstrate the corrosion impact on the conditional probability distribution of these EDPs, Figure 7-9 presents the PDFs of EDPs in longitudinal and transverse directions for various ages, analyzed based on hazard level III. Figure 7-9 (a) and (b) illustrate that the corrosion increases both mean and standard deviation of maximum drift ratio, resulting in wider distribution with higher mean values at a higher corrosion level. In contrast, the maximum base shear and base moment demands are reduced with corrosion. This observation implies that the corrosion may decrease or increase the seismic demands of the corroded RC bridges, despite the observation in the previous section that the corrosion considerably reduces the seismic capacity of the RC bridge. As a result, in order to fully understand the seismic performance of the corrosion-affected bridges, it is necessary to investigate the effect of corrosion on the likelihood that the seismic demand exceeds the corresponding capacity.

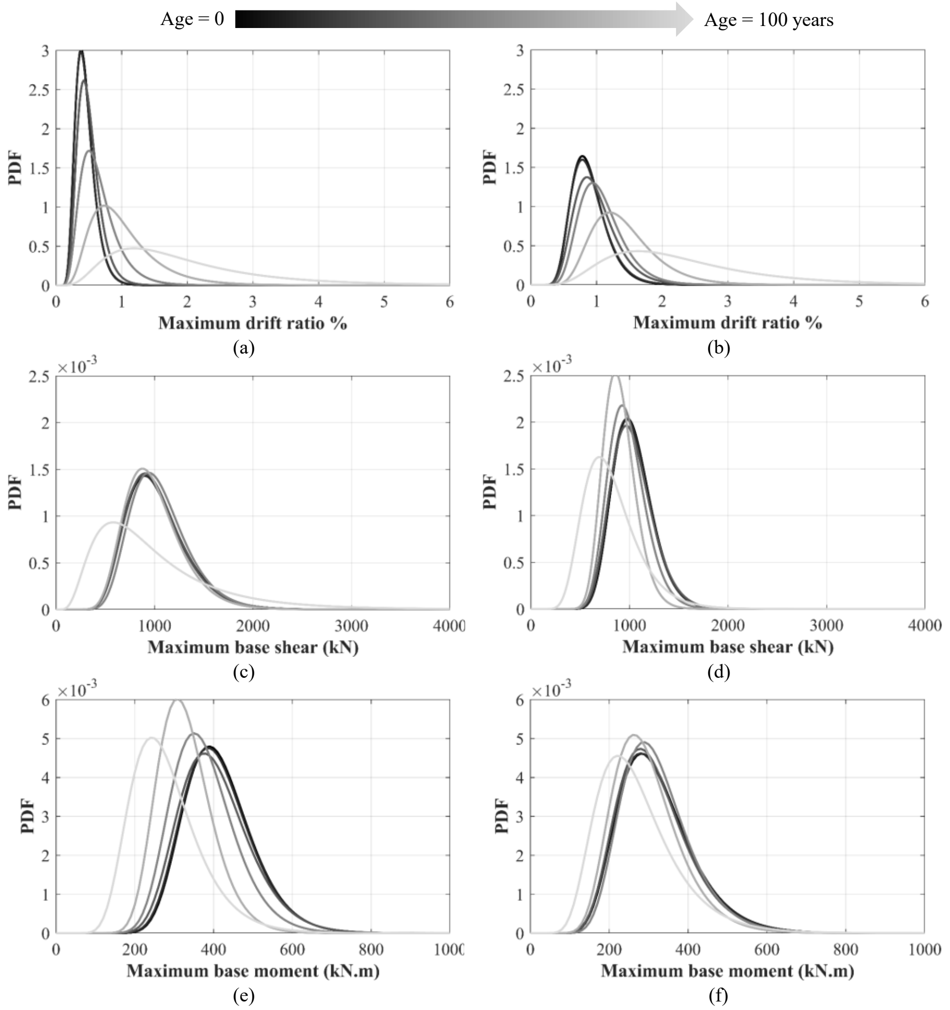

Figure 7-9: Comparison of conditional PDFs for seismic demands of the RC bridge at different ages corresponding to hazard level III, in terms of maximum drift ratio in (a) longitudinal and (b) lateral directions, maximum base shear in (c) longitudinal and (d) lateral directions, and maximum base moment in (e) longitudinal and (f) lateral directions

In order to determine the probability of demand exceeding the capacity, it is required to translate the conditional probability given above into the unconditional probabilistic demand hazard curve using Eq. (7-7). The resulted unconditional probabilistic demand hazard curve, which accounts for all seismic hazard levels, is measured in terms of annual probability of exceedance, i.e., $P(\text{EDP} \geq d_s)$, presented in Figure 7-10 for different seismic demands in longitudinal and lateral directions. Similar to the conditional probabilistic demand hazard curves, the corrosion may increase or decrease the probability of exceedance for different EDPs. These unconditional distributions will be used to evaluate the probability of demand exceeding the capacity.

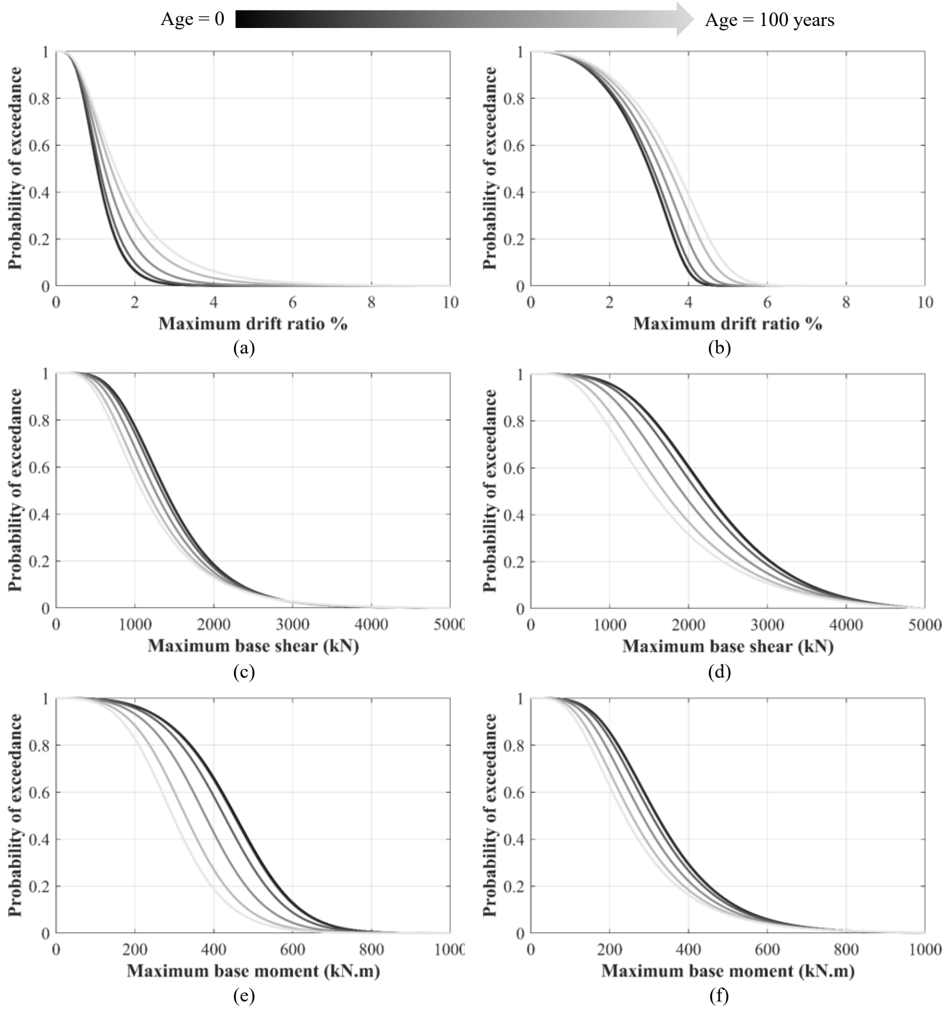

(a) (b)

(c) (d)

(e) (f)

Figure 7-10: Comparison of unconditional probabilistic demand hazard curves for RC bridges with different ages, in terms of maximum drift ratio in (a) longitudinal and (b) lateral directions, maximum base shear in (c) longitudinal and (d) lateral directions, and maximum base moment in (e) longitudinal and (f) lateral directions

The last step to assess the seismic performance of the RC bridge is to define the probability of performance not being met using the total probability theorem, as shown in Eq. (7-10):

$$P(C \leq \mathrm{EDP}) = \sum_{\text{all } d_s} P(C \leq \mathrm{EDP} \mid \mathrm{EDP} = d_s) P(\mathrm{EDP} = d_s) \tag{7-10}$$

in which *C* stands for the desired seismic capacity parameter. The first term in this equation shows the likelihood that the capacity is less than the demand given that the demand is equal to d_s. However, it can be assumed that this probability is independent of the information regarding the demand level [220], and thus Eq. (7-10) can be approximated as follows:

$$P(C \leq \mathrm{EDP}) = \sum_{\text{all } d_s} P(C \leq d_s) P(\mathrm{EDP} = d_s) \tag{7-11}$$

Similar to the previous step, the second term can be obtained from the unconditional probabilistic demand curve determined above. To compute $P(C \leq d_s)$, the probabilistic models developed in the previous section for different seismic capacity parameters are employed. Using these models with Eq. (7-11) results in the probability of demand exceeding the capacity in terms of age represented by corrosion levels, i.e., K and K_L. Figure 7-11 (a) to (c) presents the impact of corrosion level K on the probability of demand exceeding the capacity defined based on the drift ratio, base shear, and base moment, respectively, in both longitudinal and transverse directions. As shown in Figure 7-11 (a), the corrosion can extremely increase this probability based on the drift ratio, demonstrating the need to take corrosion effects into account when predicting in the seismic performance. In particular, the drift ratio of the bridge column is significantly affected by corrosion due to its impact on the bond-slip and steel bar buckling, which play essential roles in the post-peak behavior of the RC bridge.

Furthermore, the corrosion can influence the seismic performance of the RC bridge in terms of demand exceeding the base shear and base moment capacities in the bridge column, as shown in Figure 7-11 (b) and (c), respectively. The impact of corrosion on these two limit states is significant, but less notable than on the drift ratio, which stems from the less corrosion effect on the lateral strengths than the deformation. Additionally, the higher effect of corrosion on the probability of demand exceeding the capacity based on these parameters in the transverse direction is in agreement with the corrosion effect on the corresponding capacities discussed in the preceding section.

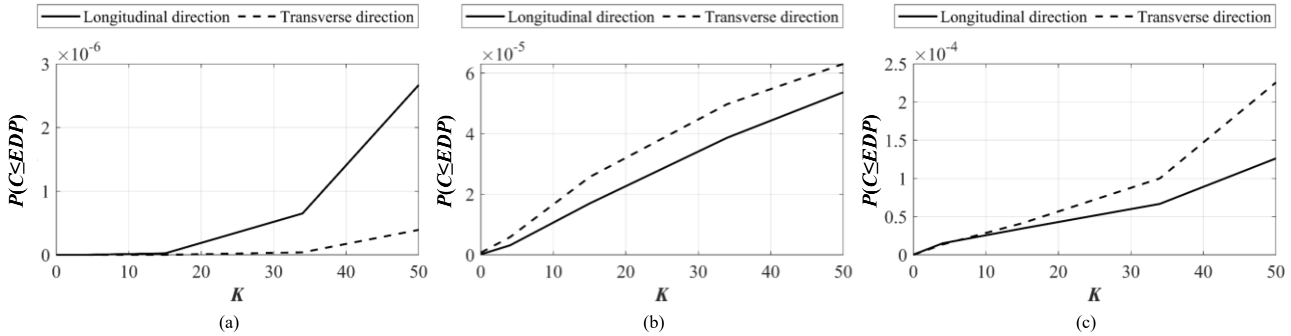

(a) (b) (c)

Figure 7-11: Pre-event estimations of corrosion impact on the probability of the seismic demand exceeding the corresponding capacity in terms of (a) drift ratio, (b) base shear, and (c) base moment

The corrosion levels used in Figure 7-11 are estimated based on the numerical models, while these estimations can entail large uncertainties. In case of availability of seismic measurements after a seismic event, the corroded properties and corresponding corrosion level can be estimated with more accuracy using the corrosion state estimation methodology provided in [209]. To further demonstrate the role of corrosion state estimation, two cases are defined here based on the seismic measurement obtained at age 60 years: (1) K is measured to be equal to its mean + standard deviation at this age, and (2) K is measured to be equal to mean – standard deviation at this age. Using the probabilities of failure developed based on the pre-event analysis, the performance of this corroded bridge can be updated at this age and from this point forward. Figure 7-12 (a) to (f) present the updated probabilities of failure based on drift ratio, base shear, and base moment in longitudinal and transverse directions for these two cases. As shown, the updated corrosion level at this age can dramatically alter the performance prediction for the corroded RC bridge. This observation reveals the importance of combining the FE modeling and Bayesian estimation strategies developed in this research work to assess the seismic performance of corroded RC bridges.

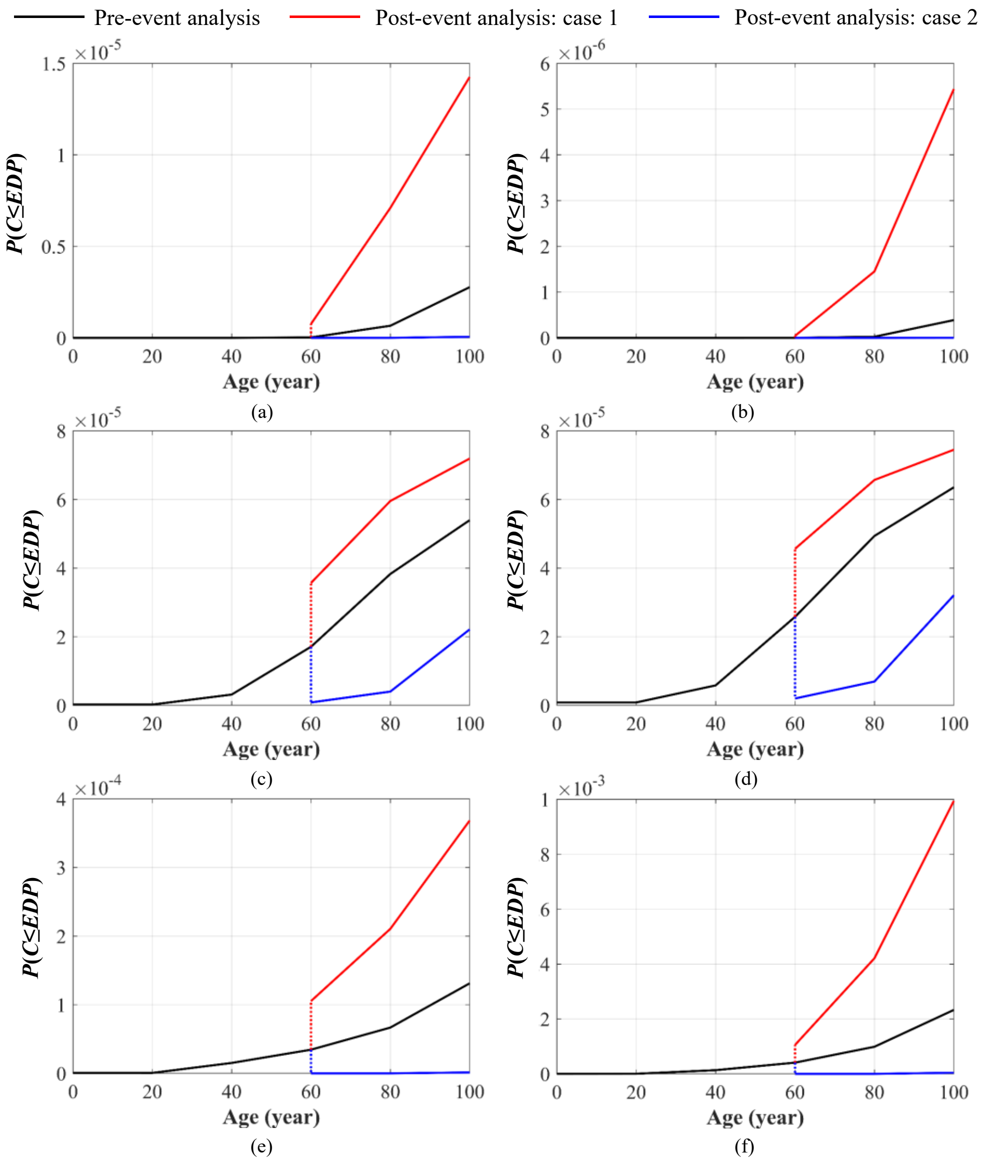

Figure 7-12: Post-event estimations of corrosion impact on the probability of the seismic demand exceeding the corresponding capacity in terms of drift ratio in (a) longitudinal and (b) transverse directions, base shear in (a) longitudinal and (b) transverse directions, and base moment in (a) longitudinal and (b) transverse directions

7.5. CHAPTER CONCLUSIONS

The FE modeling and Bayesian estimation strategies developed in this study provide the capability to evaluate the seismic performance of corroded RC bridges. In this context, the seismic performance of an RC bridge was investigated under varying corrosion levels over the course of its lifetime, which is modeled by the advanced FE modeling approach proposed in this study. This bridge model was used to study the role of advanced modeling aspects (i.e., bond-slip and steel bar buckling) in evaluating the seismic capacity of corroded RC bridges. Considering the uncertainties associated with the corrosion process, the probabilistic models were developed to modify the seismic capacity of the corroded RC bridge based on the corrosion level of longitudinal and transverse reinforcements. These models were applied in conjunction with the probabilistic seismic demands to investigate the impact of corrosion on the seismic risk of the corroded RC bridge. Additionally, to further highlight the contributions of this study, the effect of applying corrosion state estimation tool on the seismic performance prediction was explored.

With the aid of these developments, it has been demonstrated that corrosion can severely reduce the seismic capacity of the RC bridges. To be more specific, overestimating the seismic capacity, particularly the ductility, is a result of employing the conventional FE modeling approach, which neglects the bond-slip and steel bar buckling. In addition, estimating the seismic demands based on the advanced FE model of the RC bridge and comparing with the corresponding predicted seismic capacity indicate that the corrosion will increase the seismic risk of RC bridges, specifically in terms of limit states defined based on the post-peak behavior. This highlights the need to incorporate corrosion effects when assessing the seismic performance of RC bridges rather than relying on the predictions based on the pristine model. It is also worth mentioning that the post-event estimated corrosion state through seismic measurements can notably provide more confident estimation of the performance prediction, which indicates the importance of the condition state identification.

Chapter 8. CONCLUSIONS

8.1. SUMMARY OF RESEARCH WORK

Reinforced concrete (RC) structures, as one of most common types of infrastructure systems, are susceptible to deterioration brought on by environmental stressors, such as corrosion of reinforcing steel. Corrosion may alter the performance of RC structures subjected to extreme loading conditions, such as strong earthquakes. Specifically, it can severely affect the post-peak behavior of these structures during seismic events. To reliably estimate the safety of corroded RC structures subjected to seismic loading, this study focused on developing finite element (FE) modeling and Bayesian parameter estimation strategies for corroded RC structures, considering an application example of corroded RC bridges, in order to probabilistically assess their seismic performance.

To explore the nonlinear behavior of corroded RC bridges subjected to earthquakes, the computational model needs to account for all aspects of corrosion effects. In this regard, this study provided a comprehensive and efficient FE modeling approach that takes into consideration various aspects of corrosion impacts on reinforcing steel bars, concrete, and bonding between steel bars and surrounding concrete. In order to investigate the behavior of RC structures considering imperfect bonding, this study developed a geometrically nonlinear fiber-based frame element with bond-slip, which requires an explicit bond-slip material model defined based on the bonding properties. In order to determine bonding properties, this study first examined the goodness of existing models; however, due to limited dataset used for developing these models and scattered predictions, this study compiled an experimental database for bonding properties and developed a new probabilistic model to better characterize the bonding properties and quantify the uncertainties. Additionally, to incorporate the corrosion impacts on the bond-slip, a new probabilistic model for predicting corroded bonding properties was developed in this work based on the database compiled from the literature, which quantifies the prevailing uncertainties resulting from the wide dispersion of experimental data.

The post-peak behavior of under-designed or severely corroded RC columns subjected to extreme loading may be significantly influenced by steel bar buckling. To account for such effects in the FE modeling of RC structures, this study developed a constitutive model for steel bar buckling behavior considering flexible restraints provided by transverse reinforcement, which is capable of considering corrosion effects on both longitudinal and transverse reinforcements. In this regard, a FE-based steel cage model was developed and validated to generate a database of numerical buckling tests. Using this database, the constitutive model was proposed by modifying a base steel material model with no buckling effect.

The newly established constitutive model for steel bar buckling behavior and the newly developed element and material models for considering bond-slip empower this research work to efficiently model corrosion-affected RC structures. This study implemented the required FE modeling capabilities for considering bond-slip and steel bar buckling, including element, section, geometric transformation, and material models in the open-source FE software framework, *OpenSees*. Using experimental RC columns taken from the literature in both uncorroded and corroded conditions, the presented FE modeling approach was examined for the nonlinear behavior simulation of corroded RC columns. In addition, this study further investigated the importance of uncertainty in bonding properties on the simulations of the static and dynamic behavior of RC columns when uncorroded and corroded bonding condition is considered.

To estimate the corrosion state of RC structures, this study proposed a methodology to integrate stochastic filtering, such as the unscented Kalman filtering (UKF) technique, with the advanced FE modeling approach presented before. By combining this methodology with simulated seismic measurements (e.g., displacement and/or acceleration time-history), the corrosion state of RC structures, which has affected the geometrical and material properties, can be estimated. The capability of this methodology was proved using simulated data from the nonlinear FE model of corroded RC columns under different scenarios.

The FE modeling and Bayesian estimation strategies developed in this study provide the capability to evaluate the seismic performance of corroded RC bridges. In this context, the seismic performance of an RC bridge was investigated under varying corrosion levels over the course of its lifetime, which is modeled by the advanced FE modeling approach proposed in this study. This bridge model was used to study the role of advanced modeling aspects (i.e., bond-slip and steel bar buckling) in evaluating the seismic capacity of corroded RC bridges. Considering the uncertainties associated with the corrosion process, the probabilistic models were developed to modify the seismic capacity of the corroded RC bridge based on the corrosion level of longitudinal and transverse reinforcements. These models were applied in conjunction with the probabilistic seismic demands to investigate the impact of corrosion on the seismic risk of the corroded RC bridge. Additionally, to further highlight the contributions of this study, the effect of applying corrosion state estimation tool on the seismic performance prediction was explored. The findings of different parts of this work are briefly presented in the next section.

8.2. CONCLUSIONS OF RESEARCH WORK

The development of advanced FE modeling and Bayesian estimation capabilities for corrosion-affected RC structures and assessing their seismic performance in a probabilistic framework has made this thesis to arrive at a solution for the stated problem, i.e., how the corrosion affects the seismic performance of RC structures, particularly RC bridges.

In terms of FE modeling capabilities, the newly developed fiber-based frame element with bond-slip enables this study to capture the bond-slip effect in the interior of the columns. This is particularly relevant to corroded bridge piers, where the corroded bonding needs to be taken into account for the column above the foundation. According to the findings of this, the impact of imperfect bonding on the behavior of the RC columns in both corroded and uncorroded conditions may be substantial and cannot be blindly neglected. This research shows that using the conventional approach for modeling corroded RC columns, which commonly neglects the corroded bonding, would significantly bias the static and dynamic behavior simulations of corroded RC columns. Additionally, simulating the nonlinear behavior of RC columns using an inappropriate bonding property prediction model can lead to an unrealistic results. The models developed in this study for bonding property prediction in both corroded an uncorroded conditions proved to be adequate through the satisfactory agreement between FE-predicted and experimental results of validation tests. Furthermore, it has been demonstrated that the newly developed constitutive model for steel bar buckling behavior can incorporate the flexibility of ties as well as corrosion effects on both transverse and longitudinal reinforcements. Therefore, the presented FE modeling approach is a reliable tool for simulating the nonlinear behavior of corroded RC bridges under extreme loadings (e.g., strong earthquakes).

In terms of corrosion state estimation strategy, the findings show that the presented methodology can successfully estimate corrosion-affected properties, specifically corroded bonding properties that cannot be measured directly. In particular, the efficacy of the proposed methodology for estimating the properties impacted by corrosion cannot be jeopardized by noise contamination or the high nonlinearity in seismic responses caused by high corrosion and/or intensity level of ground motion stimulation. As a result, the methodology adopted in this study is promising to be employed for condition assessment of corroded RC bridges based on recorded seismic response data, which will significantly improve the model prediction accuracy.

With the aid of these developments, it has been demonstrated that corrosion can severely reduce the seismic capacity of the RC bridges. To be more specific, overestimating the seismic capacity, particularly the ductility, is a result of employing the conventional FE modeling approach, which neglects the bond-slip and steel bar buckling. It is worth mentioning that the enhancements of FE modeling mainly impact the performance prediction of RC structures in extreme scenarios, such as severe corrosion, under-designed structures, or extreme loading (e.g., strong earthquakes). In addition, estimating the seismic demands based on the advanced FE model of the RC bridge and comparing with the corresponding predicted seismic capacity indicate that the corrosion will raise the seismic risk of RC bridges. This highlights the need to incorporate corrosion effects when assessing the seismic performance of RC bridges rather than relying on the predictions based on the pristine model. It is also worth mentioning that the post-event estimated corrosion state through seismic measurements can notably alter the performance prediction, which indicates the importance of the condition state identification.

8.3. CONTRIBUTIONS AND HIGHLIGHTS

The main contributions and highlights of this research work, which focuses on probabilistically evaluating the seismic performance of corroded RC bridges, are summarized, as follows:

(1) This study provides a comprehensive and efficient FE modeling approach for corroded RC structures, with a focus on the integration of corroded bond-slip and steel bar buckling behavior. These FE modeling capabilities are implemented in the open-source FE software framework, *OpenSees*, which are demonstrated in Figure 8-1.

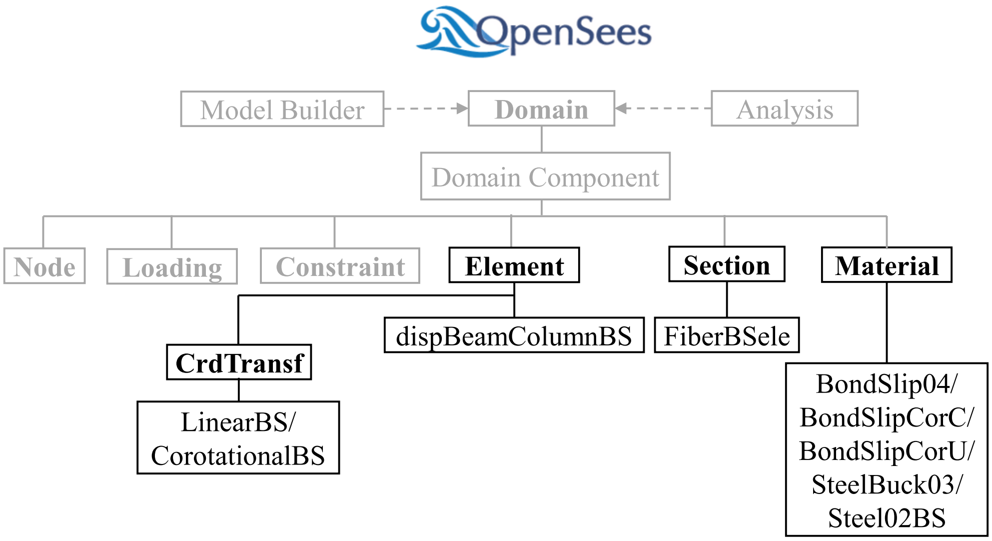

Figure 8-1: Contributions to *OpenSees*

(2) This research work has developed probabilistic models for uncorroded and corroded bonding properties, with uncertainties quantified, based on the database compiled from the literature. These models can be employed to simulate the nonlinear behavior of RC structures in a probabilistic framework.

(3) The proposed constitutive model for steel bar buckling behavior is novel in capturing the effect of flexibility of transverse reinforcement on the steel bar buckling. In particular, the proposed model accompanied by an advanced steel base model with capability of capturing ultimate stress and strain (e.g., *SteelDRC*) can result in more accurate predictions of the post-peak behavior in RC structures subjected to extreme loading.

(4) Another innovative contribution of this study is the corrosion state estimation methodology used for corroded RC structures. Using this tool, the corroded properties, which cannot be measured directly, will be identified through global structural responses.

(5) In addition to the two tools developed in this study, the probabilistic seismic performance assessment provides more insight into the seismic risk of corroded RC bridges. Specifically, the increased seismic risk by corrosion highlights the importance of including corrosion effects

in the seismic performance assessment. In light of these findings, the most efficient and reliable repair or retrofit strategy can be selected. It is worth mentioning that the developed strategies used for the probabilistic seismic performance assessment of corroded RC bridges can be similarly applied to other RC structures with corrosion effects.

(6) The development and implementation of FE modeling and condition identification strategies for corroded RC structures, which will be used for the probabilistic seismic performance assessment, have been the main focus of this research work. These developed tools can be potentially used for corroded RC structures subjected to dynamic loading, e.g., earthquakes, wind, etc. In summary, this study contributes to developing an updated performance-based engineering framework by integrating condition identification strategy for corroded RC structures.

8.4. LIMITATIONS AND RECOMMENDATIONS

Although this research work develops novel strategies for FE modeling and corrosion state estimation of corroded RC bridges, there are more challenges that need to be resolved in order to establish a thorough methodology that could be applied to all corroded RC bridges. These limitations and recommendations are listed as follows:

(1) As the main limitation of the current work, the FE modeling approach developed in this study neglects the shear deformations. In particular, where the failure mode (flexure or shear) is uncertain, this approach needs to be improved to account for the shear failure mode as well.

(2) The constitutive model for steel bar buckling is developed based on the cylindrical RC columns, and thus it can only be applied to those types of columns. In this regard, a constitutive model needs to be established using similar analysis framework before this model can be widely applied in RC structures (e.g., building structures with non-cylindrical columns).

(3) Irregular and asymmetrical reductions in the steel bar cross-section can be a consequence of the corrosion of steel bars brought on by chloride penetration. Although the spatial variability of the pit can severely affect the buckling behavior of steel bars, this study assumed that the cross-sectional area would be reduced uniformly by corrosion. To capture such impacts, more experimental data and numerical models are needed.

(4) The main limitation of the corrosion state estimation chapter is using the simulated data to examine the capability of the proposed methodology. When updating using real-life data, the UKF performance is satisfactory but sensitive to the selection of the initial algorithm variables. Therefore, future research work is required to evaluate this methodology using real-world data on structures with corrosion effects. The updated FE model of the real-world corroded RC structure can then be employed to assess their seismic performance, which assists in decision-making for repair or retrofit.

(5) The performance-based earthquake engineering (PBEE) context used in the last step of this study for a corroded RC bridge mainly considered the first two steps of PBEE framework, i.e., hazard analysis and structural analysis. As the recommendation for the future work, this research can be extended to the next steps PBEE, i.e., damage analysis and loss analysis, for corrosion-affected RC structures.

BIBLIOGRAPHY

[1] Brundtland GH. World commission on environment and development. *Environment Policy Law* 1985; 14: 26–30.

[2] CSA. Canadian highway bridge design code. *CAN/CSA-S6-06*, Toronto 2006.

[3] Mitchell D, Paultre P, Tinawi R, Saatcioglu M, Tremblay R, Elwood K, et al. Evolution of seismic design provisions in the National building code of Canada. *Canadian Journal of Civil Engineering* 2010; 37: 1157–70.

[4] Canadian Infrastructural Report Card (CIRC). Informing the future: assessing the health of our communities' infrastructure. 2019.

[5] Bastidas-Arteaga E, Schoefs F, Stewart MG, Wang X. Influence of global warming on durability of corroding RC structures: A probabilistic approach. *Engineering Structure* 2013; 51: 259–66.

[6] Stewart MG, Wang X, Nguyen MN. Climate change impact and risks of concrete infrastructure deterioration. *Engineering Structure* 2011; 33: 1326–37.

[7] Talukdar S, Banthia N, Grace JR, Cohen S. Carbonation in concrete infrastructure in the context of global climate change: Part 2-Canadian urban simulations. *Cement and Concrete Composites* 2012; 34: 931–5.

[8] Enright MP, Frangopol DM. Probabilistic analysis of resistance degradation of reinforced concrete bridge beams under corrosion. *Engineering Structure* 1998; 20: 960–71.

[9] Government of Canada. Retrieved from http://www.publicsafety.gc.ca.

[10] Ghofrani H, Atkinson G. Distinguishing Cryoseisms from Earthquakes in Alberta, Canada. *Canadian Journal of Earth Sciences* 2018.

[11] Melanta S, Miller-Hooks E, Avetisyan HG. Carbon footprint estimation tool for transportation

construction projects. *Journal of Construction Engineering Management* 2013; 139: 547–55.

[12]Trade World Bank. Greenhouse Gas Emissions Mitigation in Road Construction and Rehabilitation, a toolkit for developing countries. 2010.

[13]Sánchez-Silva M, Frangopol DM, Padgett J, Soliman M. Maintenance and operation of infrastructure systems. *ASCE Journal of Structural Engineering* 2016; 142: F4016004.

[14]Porter KA. An overview of PEER's performance-based earthquake engineering methodology. *In Proceedings of 9th International Conference of Application of Statistics and Probability in Civil Engineering* 2003, p. 1–8.

[15]Barbato M, Petrini F, Unnikrishnan VU, Ciampoli M. Performance-based hurricane engineering (PBHE) framework. *Structural Safety* 2013; 45: 24–35.

[16]Winget DG, Marchand KA, Williamson EB. Analysis and design of critical bridges subjected to blast loads. *ASCE Journal of Structural Engineering* 2005; 131: 1243–55.

[17]Wang Y, Burgess I, Wald F, Gillie M. *Performance-based fire engineering of structures*. CRC press; 2012.

[18]Attary N, Unnikrishnan VU, van de Lindt JW, Cox DT, Barbosa AR. Performance-based tsunami engineering methodology for risk assessment of structures. *Engineering Structure* 2017; 141: 676–86.

[19]Federal Highway Administration (FHWA). Seismic retrofitting manual for highway structures. *US Department of Transportation*, Federal Highway Administration, 2006.

[20]Cai H, Liu X. Freeze-thaw durability of concrete: ice formation process in pores. *Cement and Concrete Research* 1998; 28: 1281–7.

[21]Penttala V. Causes and mechanisms of deterioration in reinforced concrete. *Failure, distress*

and repair of concrete structures 2009; p. 3–31.

[22]Baboian R. Environmental conditions affecting transportation infrastructure. *Material Performance* 1995; 34: 48–52.

[23]Fitzpatrick RA. Corrosion of concrete structures in coastal areas. *Concrete International* 1996; 18: 46–7.

[24]Vaysburd AM. Some durability considerations for evaluating and repairing concrete structures. *Concrete International* 1993; 15: 29–35.

[25]Vu KAT, Stewart MG. Structural reliability of concrete bridges including improved chloride-induced corrosion models. *Structural Safety* 2000; 22: 313–33.

[26]Ghosh J, Padgett JE. Aging considerations in the development of time-dependent seismic fragility curves. *ASCE Journal of Structural Engineering* 2010; 136: 1497–511.

[27]Vu NS, Yu B, Li B. Prediction of strength and drift capacity of corroded reinforced concrete columns. *Construction and Building Materials* 2016; 115: 304–18.

[28]Wang Z, Padgett JE, Duenas-Osorio L. Risk-consistent calibration of load factors for the design of reinforced concrete bridges under the combined effects of earthquake and scour hazards. *Engineering Structure* 2014; 79: 86–95.

[29]Ellingwood BR. Risk-informed condition assessment of civil infrastructure: state of practice and research issues. *Structure and Infrastructure Engineering* 2005; 1: 7–18.

[30]Biondini F, Frangopol DM, others. Life-cycle performance of deteriorating structural systems under uncertainty. *ASCE Journal of Structural Engineering* 2016; 142: F4016001.

[31]Rao AS, Lepech MD, Kiremidjian AS, Sun X-Y. Simplified structural deterioration model for reinforced concrete bridge piers under cyclic loading. *Structure and Infrastructure Engineering* 2017; 13: 55–66.

[32]Choe D-E, Gardoni P, Rosowsky D, Haukaas T. Seismic fragility estimates for reinforced concrete bridges subject to corrosion. *Structural Safety* 2009; 31: 275–83.

[33]Akiyama M, Frangopol DM, Matsuzaki H. Life-cycle reliability of RC bridge piers under seismic and airborne chloride hazards. *Earthquake Engineering and Structural Dynamics* 2011; 40: 1671–87.

[34]Alipour A, Shafei B, Shinozuka MS. Capacity loss evaluation of reinforced concrete bridges located in extreme chloride-laden environments. *Structure and Infrastructure Engineering* 2013; 9: 8–27.

[35]Kumar R, Gardoni P, Sanchez-Silva M. Effect of cumulative seismic damage and corrosion on the life-cycle cost of reinforced concrete bridges. *Earthquake Engineering and Structural Dynamics* 2009; 38: 887–905.

[36]Afsar Dizaj E, Madandoust R, Kashani MM. Exploring the impact of chloride-induced corrosion on seismic damage limit states and residual capacity of reinforced concrete structures. *Structure and Infrastructure Engineering* 2018; 14: 714–29.

[37]Darmawan MS, Stewart MG. Spatial time-dependent reliability analysis of corroding pretensioned prestressed concrete bridge girders. *Structural Safety* 2007; 29: 16–31.

[38]Pettigrew CS, Barr PJ, Maguire M, Halling MW. Behavior of 48-year-old double-tee bridge girders made with lightweight concrete. *ASCE Journal of Bridge Engineering* 2016; 21: 4016054.

[39]Spacone E, Filippou FC, Taucer FF. Fibre beam-column model for non-linear analysis of RC frames: Part I. Formulation. *Earthquake Engineering and Structural Dynamics* 1996; 25: 711–25.

[40]Stewart MG, Rosowsky D V. Time-dependent reliability of deteriorating reinforced concrete

bridge decks. *Structural Safety* 1998; 20: 91–109.

[41]Alipour A, Shafei B, Shinozuka M. Performance evaluation of deteriorating highway bridges located in high seismic areas. *ASCE Journal of Bridge Engineering* 2011; 16: 597–611.

[42]Biondini F, Camnasio E, Palermo A. Lifetime seismic performance of concrete bridges exposed to corrosion. *Structure and Infrastructure Engineering* 2014; 10: 880–900.

[43]Coronelli D, Gambarova P. Structural assessment of corroded reinforced concrete beams: modeling guidelines. *ASCE Journal of Structural Engineering* 2004; 130: 1214–24.

[44]Zandi Hanjari K, Kettil P, Lundgren K. Analysis of mechanical behavior of corroded reinforced concrete structures. *ACI Structural Journal* 2011; 108: 532–41.

[45]Mander JB, Priestley MJN, Park R. Theoretical stress-strain model for confined concrete. *ASCE Journal of Structural Engineering* 1988; 114: 1804–26.

[46]Kashani MM, Crewe AJ, Alexander NA. Nonlinear cyclic response of corrosion-damaged reinforcing bars with the effect of buckling. *Construction and Building Materials* 2013; 41: 388–400.

[47]Lin H, Zhao Y, Feng P, Ye H, Ozbolt J, Jiang C, et al. State-of-the-art review on the bond properties of corroded reinforcing steel bar. *Construction and Building Materials* 2019; 213: 216–33.

[48]Astroza R, Ebrahimian H, Conte JP. Material parameter identification in distributed plasticity FE models of frame-type structures using nonlinear stochastic filtering. *ASCE Journal of Engineering Mechanics* 2015; 141: 4014149.

[49]Chatzi EN, Smyth AW. Particle filter scheme with mutation for the estimation of time-invariant parameters in structural health monitoring applications. *Structural Control and Health Monitoring* 2013; 20: 1081–95.

[50]Van Der Merwe R, Wan E, Julier S. Sigma-point Kalman filters for nonlinear estimation and sensor-fusion: Applications to integrated navigation. *In Proceedings of AIAA Guidance, Navigation, and Control Conference and Exhibit*, 2004, p. 5120.

[51]Ebrahimian H, Astroza R, Conte JP. Extended Kalman filter for material parameter estimation in nonlinear structural finite element models using direct differentiation method. *Earthquake Engineering and Structural Dynamics* 2015; 44: 1495–522.

[52]Wan EA, Van Der Merwe R. The unscented Kalman filter for nonlinear estimation. *In Proceedings of the IEEE 2000 Adaptive Systems for Signal Processing, Communications, and Control Symposium (Cat. No. 00EX373)*, Lake Louise, AB, Canada, 1–4 October 2000; pp. 153–158.

[53] Astroza R, Ebrahimian H, Li Y, Conte JP. Bayesian nonlinear structural FE model and seismic input identification for damage assessment of civil structures. *Mechanical Systems and Signal Processing* 2017; 93: 661–87.

[54]Astroza R, Barrientos N, Li Y, Flores EIS, Liu Z. Bayesian updating of complex nonlinear FE models with high-dimensional parameter space using heterogeneous measurements and a batch-recursive approach. *Engineering Structure* 2019; 201: 109724.

[55]Liu Z, Li Y, Astroza R. Parameter estimation of a shake-table tested bridge column with bond-slip effect using stochastic inference. *In Proceedings of CSCE national conference*, Saskatoon, Saskatchewan, Canada: 2020.

[56]Han R, Li Y, van de Lindt J. Assessment of seismic performance of buildings with incorporation of aftershocks. *ASCE Journal of Performance of Constructed Facilities* 2015; 29: 4014088.

[57]Mirzaie F, Mahsuli M, Ghannad MA. Probabilistic analysis of soil-structure interaction effects

on the seismic performance of structures. *Earthquake Engineering and Structural Dynamics* 2017; 46: 641–60.

[58]Abtahi S, Mahsuli M, Ali Ghannad M. Probabilistic Evaluation of Soil-Structure Interaction Effects on Strength Demands of Shear Buildings. *ASCE Journal of Structural Engineering* 2020; 146: 4019166.

[59]Mander JB. Fragility curve development for assessing the seismic vulnerability of highway bridges. *Technical Report*, University at Buffalo, State University of New York, 1999.

[60]Astriana L, Sangadji S, Purwanto E, Kristiawan SA. Assessing seismic performance of moment resisting frame and frame-shear wall system using seismic fragility curve. *Procedia Engineering* 2017; 171: 1069–76.

[61]Zhou H, Xu Y, Peng Y, Liang X, Li D, Xing F. Partially corroded reinforced concrete piers under axial compression and cyclic loading: An experimental study. *Engineering Structure* 2020; 203: 109880.

[62]Deng P, Zhang C, Pei S, Jin Z. Modeling the impact of corrosion on seismic performance of multi-span simply-supported bridges. *Construction and Building Materials* 2018; 185: 193–205.

[63]Xu J-G, Cai Z-K, Feng D-C. Life-cycle seismic performance assessment of aging RC bridges considering multi-failure modes of bridge columns. *Engineering Structure* 2021; 244: 112818.

[64]Zhao J, Sritharan S. Modeling of strain penetration effects in fiber-based analysis of reinforced concrete structures. *ACI Structural Journal* 2007; 104: 133–41.

[65]Mazzoni S, McKenna F, Scott MH, Fenves GL, Jeremic B. Open system for earthquake engineering simulation, User Command Manual. *Pacific Earthquake Engineering Research*

Center, Berkeley, California, USA 2006.

[66]Aviram A, Mackie KR, Stojadinovic B. Guidelines for Nonlinear Analysis of Bridge Structures in California. *Pacific Earthquake Engineering Research Center*, Berkeley, California, USA: 2008.

[67]Mander JB, Kim DK, Chen SS, Premus GJ. *Response of steel bridge bearings to reversed cyclic loading*. 1996, NCEER, Buffalo.

[68]Nielson BG. Analytical fragility curves for highway bridges in moderate seismic zones. *PhD dissertation*, Georgia Institute of Technology, 2005.

[69]Wilson JC, Tan BS. Bridge abutments: formulation of simple model for earthquake response analysis. *ASCE Journal of Engineering Mechanics* 1990; 116: 1828–37.

[70]Chiou B, Darragh R, Gregor N, Silva W. NGA Project Strong-Motion Database. *Earthquake Spectra* 2008; 24: 23–44.

[71]Penzien J, Clough RW. Observations on the Damages of Highway Bridge Structures, San Fernando, California, Earthquake, February 9, 1971. University of California, Berkeley, Report to Division of Structural Engineers, Federal Highway Administration; 1971.

[72]Architectural Institute of Japan. Report on the Damage Investigation of Urakawa-Oki Earthquake 1982 and Nihonkai-Chubu Earthquake 1983; 1984.

[73]Gates JH, Mellon S, Klein G. The Whittier Narrows, California Earthquake of October 1, 1987-Damage to State Highway Bridges. *Earthquake Spectra* 1988; 4: 377–88.

[74]Astaneh A, Bertero VV, Bolt BA, Mahin SA, Moehle JP, Seed RB. Preliminary report of the seismological and engineering aspects of the October 17, 1989 Santa Cruz (Loma Prieta) earthquake. *Earthquake Engineering Research Center*, University of California, Berkeley, Calif., Report UCBIEERC-89/14; 1989.

[75]Housner GW, Masri SF. Performance of the base-isolated USC University Hospital under the 1994 Northridge earthquake. *Nuclear Engineering and Design* 1994; 148: 509–13.

[76]Yang JN, Wu JC, Kawashima K, Unjoh S. Hybrid control of seismic-excited bridge structures. *Earthquake Engineering and Structural Dynamics* 1995; 24: 1437–51.

[77]Reinhardt HW, Balazs GL. Steel-concrete interfaces: Experimental aspects. *Studies in Applied Mechanics* 1995; vol. 42, p. 255–79.

[78]Lehman DE, Moehle JP. Seismic Performance of Well-Confined Bridge Columns. University of California, Berkeley: 2000.

[79]Schoettler M, Restrepo J, Guerrini G, Duck DE, others. A full-scale, single-column bridge bent tested by shake-table excitation. *Report No. 258*, Center for Civil Engineering Earthquake Research, Dept. of Civil Engineering, University of Nevada, Reno, NV; 2012.

[80]Alavi-Dehkordi S, Mostofinejad D, Alaee P. Effects of high-strength reinforcing bars and concrete on seismic behavior of RC beam-column joints. *Engineering Structure* 2019; 183: 702–19.

[81]Saatcioglu M, Alsiwat JM, Ozcebe G. Hysteretic behavior of anchorage slip in R/C members. *ASCE Journal of Structural Engineering* 1992; 118: 2439–58.

[82]Sezen H, Setzler EJ. Reinforcement slip in reinforced concrete columns. *ACI Structural Journal* 2008 ;105: 280–9.

[83]Cheng H, Li H-N, Yang YB, Wang D-S. Seismic fragility analysis of deteriorating RC bridge columns with time-variant capacity index. *Bulletin of Earthquake Engineering* 2019; 17: 4247–67.

[84]Murcia-Delso J, Shing PB. Bond-slip model for detailed finite-element analysis of reinforced concrete structures. *ASCE Journal of Structural Engineering* 2015; 141: 4014125.

[85]Monti G, Spacone E. Reinforced concrete fiber beam element with bond-slip. *ASCE Journal of Structural Engineering* 2000; 126: 654–61.

[86]Spacone E, Limkatanyu S. Responses of reinforced concrete members including bond-slip effects. *ACI Structural Journal* 2000; 97: 831–9.

[87]Braga F, Gigliotti R, Laterza M, D'Amato M, Kunnath S. Modified steel bar model incorporating bond-slip for seismic assessment of concrete structures. *ASCE Journal of Structural Engineering* 2012; 138: 1342–50.

[88]Criesfield MA. *Nonlinear finite element analysis of solids and structures*, vol. 1, Wiley, New York; 1991.

[89]Engstrom B, Magnusson J, Huang Z. Pull-out bond behavior of ribbed bars in normal and high-strength concrete with various confinements. *Special Publications* 1998; 180: 215–42.

[90]Saadatmanesh H, Ehsani MR, Jin L. Seismic strengthening of circular bridge pier models with fiber composites. *ACI Structural Journal* 1996; 93: 639–738.

[91]Mazzarolo E, Scotta R, Berto L, Saetta A. Long anchorage bond-slip formulation for modeling of RC elements and joints. *Engineering Structure* 2012; 34: 330–41.

[92]Filippou FC, Fenves GL. Methods of analysis for earthquake-resistant structures. *Earthquake Engineering: From Engineering Seismology to Performance-Based Engineering* 2004; 6:1–6.

[93]Low SS, Moehle JP. Experimental study of reinforced concrete columns subjected to multi-axial cyclic loading. *EERC Report 87-14*, Earthquake Engineering Research Center, University of California, Berkeley, California, USA; 1987.

[94]Bousias SN, Verzeletti G, Fardis MN, Gutierrez E. Load-path effects in column biaxial bending with axial force. *ASCE Journal of Engineering Mechanics* 1995; 121: 596–605.

[95]Ayoub A. Nonlinear Analysis of Reinforced Concrete Beam-Columns with Bond-Slip. *ASCE Journal of Engineering Mechanics* 2006; 132: 1177–86.

[96]Saatcioglu M, Grira M. Confinement of reinforced concrete columns with welded reinforced grids. *ACI Structural Journal* 1999; 96: 29–39.

[97]Feng D-C, Xu J. An efficient fiber beam-column element considering flexure-shear interaction and anchorage bond-slip effect for cyclic analysis of RC structures. *Bulletin of Earthquake Engineering* 2018; 16: 5425–52.

[98]Scott MH, Fenves GL. Plastic hinge integration methods for force-based beam-column elements. *ASCE Journal of Structural Engineering* 2006; 132: 244–52.

[99]Conte JP, Barbato M, Spacone E. Finite element response sensitivity analysis using force-based frame models. *International Journal for Numerical Methods in Engineering* 2004; 59: 1781–820.

[100] Barbato M, Conte JP. Finite element response sensitivity analysis: a comparison between force-based and displacement-based frame element models. *Computer Methods in Applied Mechanics and Engineering* 2005; 194: 1479–512.

[101] Al-Aukaily A, Scott MH. Response sensitivity for geometrically nonlinear displacement-based beam-column elements. *Computers and Structures* 2019; 220: 43–54.

[102] Carreno R, Lotfizadeh KH, Conte JP, Restrepo JI. Material Model Parameters for the Giuffrè-Menegotto-Pinto Uniaxial Steel Stress-Strain Model. *ASCE Journal of Structural Engineering* 2020; 146: 4019205.

[103] Yang Z, Li C, Liu L, Yang H, Zhong T. Study on Modeling Method of Reinforced Concrete Pier Based on OpenSees. *Journal of Physics: Conference Series* 2021; vol. 1838, p. 12034.

[104] Roy HHE, Sozen MA. Ductility of concrete. *In Proceedings of International Symposium of*

Flexural Mechanical Reinforced Concreter, ASCE-ACI, Miami: 1964, p. 213–24.

[105] Kent DC, Park R. Flexural members with confined concrete. *ASCE Journal of the Structural Division* 1971; 97: 1969–90.

[106] Scott BD, Park R, Priestley MJN. Stress-strain behavior of concrete confined by overlapping hoops at low and high strain rates. *Journal of Proceedings* 1982; vol. 79, p. 13–27.

[107] Eligehausen R, Popov E, Bertero V. Local bond stress-slip relationships of deformed bars under generalized excitations. *EERC Report 83-23*, Earthquake Engineering Research Center, University of California, Berkeley, California, USA; 1983.

[108] Wagg DJ, Worden K, Barthorpe RJ, Gardner P. Digital Twins: State-of-the-Art and Future Directions for Modeling and Simulation in Engineering Dynamics Applications. *ASCE-ASME Journal of Risk and Uncertainty in Engineering Systems, Part B: Mechanical Engineering* 2020; 6.

[109] Scott MH, Filippou FC. Response gradients for nonlinear beam-column elements under large displacements. *ASCE Journal of Structural Engineering* 2007; 133: 155–65.

[110] Bommer JJ, Udias A, Cepeda JM, Hasbun JC, Salazar WM, Suarez A, et al. A new digital accelerograph network for El Salvador. *Seismological Research Letters* 1997; 68: 426–37.

[111] Iyama J, Kuwamura H. Application of wavelets to analysis and simulation of earthquake motions. *Earthquake Engineering and Structural Dynamics* 1999; 28: 255–72.

[112] Tremblay R. Development of design spectra for long-duration ground motions from Cascadia subduction earthquakes. *Canadian Journal of Civil Engineering* 1998; 25: 1078–90.

[113] Hancock J, Bommer JJ. A state-of-knowledge review of the influence of strong-motion

duration on structural damage. *Earthquake Spectra* 2006; 22: 827–45.

[114] Chandramohan R, Baker JW, Deierlein GG. Quantifying the influence of ground motion duration on structural collapse capacity using spectrally equivalent records. *Earthquake Spectra* 2016; 32: 927–50.

[115] Barbosa AR, Ribeiro FLA, Neves LAC. Influence of earthquake ground-motion duration on damage estimation: application to steel moment resisting frames. *Earthquake Engineering and Structural Dynamics* 2017; 46: 27–49.

[116] Abtahi S, Li Y. Efficient Modeling of Steel Bar Slippage Effect in Reinforced Concrete Structures using a Newly Implemented Nonlinear Element. *Computers and Structures* 2022 (under review).

[117] Salem HM, Maekawa K. Pre-and postyield finite element method simulation of bond of ribbed reinforcing bars. *ASCE Journal of Structural Engineering* 2004; 130: 671–80.

[118] Zhao J, Sritharan S. Modeling of strain penetration effects in fiber-based analysis of reinforced concrete structures. *ACI Structural Journal* 2007; 104: 133.

[119] Mang C, Jason L, Davenne L. A new bond slip model for reinforced concrete structures: Validation by modelling a reinforced concrete tie. *Engineering with Computers* 2015.

[120] Lowes LN, Moehle JP, Govindjee S. Concrete-steel bond model for use in finite element modeling of reinforced concrete structures. *ACI Structural Journal* 2004; 101: 501–11.

[121] Bamonte PF, Gambarova PG. High-bond bars in NSC and HPC: Study on size effect and on the local bond stress-slip law. *ASCE Journal of Structural Engineering* 2007; 133: 225–34.

[122] Pochanart S, Harmon T. Bond-slip model for generalized excitations including fatigue. *Materials Journal* 1989; 86: 465–74.

[123] Soroushian P, Choi K-B. Local bond of deformed bars with different diameters in confined concrete. *ACI Structural Journal* 1989; 86: 217–22.

[124] FIB. *fib model code for concrete structures 2010*. Berlin, Germany: Ernst & Sohn; 2013.

[125] Yu B, Tang R, Li B. Probabilistic bond strength model for reinforcement bar in concrete. *Probabilistic Engineering Mechanics* 2020; 61: 103079.

[126] Eligehausen R, Popov E, Bertero V. Local bond stress-slip relationships of deformed bars under generalized excitations. *In Proceedings of the 7th European Conference on Earthquake Engineering*, vol. 4. Athens : Techn. Chamber of Greece 1982; S. 69–80.

[127] Torre-Casanova A, Jason L, Davenne L, Pinelli X. Confinement effects on the steel--concrete bond strength and pull-out failure. *Engineering Fracture Mechanics* 2013; 97: 92–104.

[128] Turgut C, Jason L, Davenne L. Structural-scale modeling of the active confinement effect in the steel-concrete bond for reinforced concrete structures. *Finite Elements in Analysis and Design* 2020; 172: 103386.

[129] Lundgren K. Pull-out tests of steel-encased specimens subjected to reversed cyclic loading. *Materials and Structures* 2000; 33: 450–6.

[130] Box GEP, Tiao GC. *Bayesian inference in statistical analysis*. vol. 40. New York: Wiley; 2011.

[131] Verderame GM, De Carlo G, Ricci P, Fabbrocino G. Cyclic bond behaviour of plain bars. Part II: Analytical investigation. *Construction and Building Materials* 2009; 23: 3512–22.

[132] Melo J, Rossetto T, Varum H. Experimental study of bond--slip in RC structural elements with plain bars. *Materials and Structures* 2015; 48: 2367–81.

[133] Giuffrè A. Il comportamento del cemento armato per sollecitazioni cicliche di forte

intensità. *G. Del Genio Civ.* 28 1970: 1–20.

[134] Mirza SA, MacGregor JG. Probabilistic study of strength of reinforced concrete members. *Canadian Journal of Civil Engineering* 1982; 9: 431–48.

[135] McKay MD, Beckman RJ, Conover WJ. A comparison of three methods for selecting values of input variables in the analysis of output from a computer code. *Technometrics* 2000; 42: 55–61.

[136] Jia J, Zhao L, Wu S, Wang X, Bai Y, Wei Y. Experimental investigation on the seismic performance of low-level corroded and retrofitted reinforced concrete bridge columns with CFRP fabric. *Engineering Structure* 2020; 209: 110225.

[137] Meda A, Mostosi S, Rinaldi Z, Riva P. Experimental evaluation of the corrosion influence on the cyclic behaviour of RC columns. *Engineering Structure* 2014; 76: 112–23.

[138] Du YG, Clark LA, Chan AHC. Effect of corrosion on ductility of reinforcing bars. *Magazine of Concrete Research* 2005; 57: 407–19.

[139] Du YG, Clark LA, Chan AHC. Residual capacity of corroded reinforcing bars. *Magazine of Concrete Research* 2005; 57: 135–47.

[140] Kashani MM, Lowes LN, Crewe AJ, Alexander NA. Phenomenological hysteretic model for corroded reinforcing bars including inelastic buckling and low-cycle fatigue degradation. *Computers and Structures* 2015; 156: 58–71.

[141] Ou Y-C, Fan H-D, Nguyen ND. Long-term seismic performance of reinforced concrete bridges under steel reinforcement corrosion due to chloride attack. *Earthquake Engineering and Structural Dynamics* 2013; 42: 2113–27.

[142] Bozorgnia Y, Bertero V V. *Earthquake engineering: from engineering seismology to performance-based engineering*. CRC Press: Boca Raton, FL.

[143] Abtahi S, Li Y. Bond-Slip Model Uncertainty Quantification and Effect on Nonlinear Behavior Simulations of Reinforced Concrete Columns. *Engineering Structure* 2022; 266: 114525.

[144] Lee H-S, Noguchi T, Tomosawa F. Evaluation of the bond properties between concrete and reinforcement as a function of the degree of reinforcement corrosion. *Cement and Concrete Research* 2002; 32: 1313–8.

[145] Bhargava K, Ghosh AK, Mori Y, Ramanujam S. Suggested empirical models for corrosion-induced bond degradation in reinforced concrete. *ASCE Journal of Structural Engineering* 2008; 134: 221–30.

[146] Chung L, Kim J-HJ, Yi S-T. Bond strength prediction for reinforced concrete members with highly corroded reinforcing bars. *Cement and Concrete Composites* 2008; 30:603–11.

[147] Kivell A, Palermo A, Scott A. Complete model of corrosion-degraded cyclic bond performance in reinforced concrete. *ASCE Journal of Structural Engineering* 2015; 141: 4014222.

[148] Zhou HJ, Zhou YF, Xu YN, Lin ZY, Xing F, Li LX. Regression Analysis of Bond Parameters between Corroded Rebar and Concrete Based on Reported Test Data. *International Journal of Corrosion*, Hindawi 2018; 5309243.

[149] Yassin MHM. Nonlinear analysis of prestressed concrete structures under monotonic and cyclic loads. *PhD Dissertation*, Department of Civil Engineering, University of California, Berkeley, 1994.

[150] Palsson R, Mirza MS. Mechanical response of corroded steel reinforcement of abandoned concrete bridge. *ACI Structural Journal* 2002; 99: 157–62.

[151] Stewart MG. Mechanical behaviour of pitting corrosion of flexural and shear reinforcement

and its effect on structural reliability of corroding RC beams. *Structural Safety* 2009; 31: 19–30.

[152] Cabrera JG. Deterioration of concrete due to reinforcement steel corrosion. *Cement and Concrete Composites* 1996; 18: 47–59.

[153] Auyeung Y, Balaguru P, Chung L. Bond behavior of corroded reinforcement bars. *Materials Journal* 2000; 97: 214–20.

[154] Al-Sulaimani GJ, Kaleemullah M, Basunbul IA, others. Influence of corrosion and cracking on bond behavior and strength of reinforced concrete members. *ACI Structural Journal* 1990; 87: 220–31.

[155] Berto L, Simioni P, Saetta A. Numerical modelling of bond behaviour in RC structures affected by reinforcement corrosion. *Engineering Structure* 2008; 30: 1375–85.

[156] Fang C, Lundgren K, Chen L, Zhu C. Corrosion influence on bond in reinforced concrete. *Cement and Concrete Research* 2004; 34: 2159–67.

[157] Lin H, Zhao Y, Ozbolt J, Hans-Wolf R. The bond behavior between concrete and corroded steel bar under repeated loading. *Engineering Structure* 2017; 140: 390–405.

[158] Ma Y, Guo Z, Wang L, Zhang J. Experimental investigation of corrosion effect on bond behavior between reinforcing bar and concrete. *Construction and Building Materials* 2017; 152: 240–9.

[159] Stanish KD. Corrosion effects on bond strength in reinforced concrete. *MSc thesis*, Department of Civil Engineering, University of Toronto 1999.

[160] Japan Society of Civil Engineers. *Recommended code and manual for seismic performance verification of out-door important structures of nuclear power plants*. 2002.

[161] Taucer F, Spacone E, Filippou FC. A fiber beam-column element for seismic response

analysis of reinforced concrete structures. *EERC Report 91/17*, Earthquake Engineering Research Center, University of California, Berkeley, 1991.

[162] Popovics S. A numerical approach to the complete stress-strain curve of concrete. *Cement and Concrete Research* 1973; 3: 583–99.

[163] Menegotto M. Method of analysis for cyclically loaded RC plane frames including changes in geometry and non-elastic behavior of elements under combined normal force and bending. *In Proceedings of IABSE Symposium on Resistance and Ultimate Deformability of Structures Acted on by Well Defined Repeated Loads* 1973; p. 15–22.

[164] Lopes A V, Lopes SMR, do Carmo RNF. Effects of the compressive reinforcement buckling on the ductility of RC beams in bending. *Engineering Structure* 2012; 37: 14–23.

[165] Yang H, Sun P, Deng Y. Experiment investigation of the influence of reinforcing bar buckling on seismic behavior of RC columns. *Engineering Structure* 2020; 220: 110923.

[166] Bae S, Mieses AM, Bayrak O. Inelastic buckling of reinforcing bars. *ASCE Journal of Structural Engineering* 2005; 131: 314–21.

[167] Gomes A, Appleton J. Nonlinear cyclic stress-strain relationship of reinforcing bars including buckling. *Engineering Structure* 1997; 19: 822–6.

[168] Kim SH, Koutromanos I. Constitutive model for reinforcing steel under cyclic loading. *ASCE Journal of Structural Engineering* 2016; 142: 4016133.

[169] Kunnath SK, Heo Y, Mohle JF. Nonlinear uniaxial material model for reinforcing steel bars. *ASCE Journal of Structural Engineering* 2009; 135: 335–43.

[170] Monti G, Nuti C. Nonlinear cyclic behavior of reinforcing bars including buckling. *ASCE Journal of Structural Engineering* 1992; 118: 3268–84.

[171] Papia M, Russo G, Zingone G. Instability of longitudinal bars in RC columns. *ASCE*

Journal of Structural Engineering 1988; 114: 445–61.

[172] Sato Y, Ko H. Experimental investigation of conditions of lateral shear reinforcements in RC columns accompanied by buckling of longitudinal bars. *Earthquake Engineering and Structural Dynamics* 2007; 36: 1685–99.

[173] Russo G. A buckling model for reinforcing bars. *International Journal of Mechanical Sciences* 1988; 30: 3–11.

[174] Dhakal, R.P., Maekawa, K. reinforcement stability and fracture of cover concrete in reinforced concrete members. *ASCE Journal of Structural Engineering* 2002: 128(10), pp. 1253-1262.

[175] Su J, Wang J, Bai Z, Wang W, Zhao D. Influence of reinforcement buckling on the seismic performance of reinforced concrete columns. *Engineering Structure* 2015; 103: 174–88.

[176] Zong Z, Kunnath S, Monti G. Material model incorporating buckling of reinforcing bars in RC columns. *ASCE Journal of Structural Engineering* 2014; 140: 4013032.

[177] Dhakal RP, Su J. Design of transverse reinforcement to avoid premature buckling of main *Earthquake Engineering and Structural Dynamics* 2018; 47: 147–68.

[178] Zong Z, Kunnath S, Monti G. Simulation of Reinforcing Bar Buckling in Circular Reinforced Concrete Columns. *ACI Structural Journal* 2013; 110.

[179] Bresler B, Gilbert PH. Tie requirements for reinforced concrete columns. *Journal of Proceedings* 1961; vol. 58, p. 555–70.

[180] Scribner CF. Reinforcement buckling in reinforced concrete flexural members. *Journal of Proceedings* 1986; vol. 83, p. 966–73.

[181] Pantazopoulou SJ. Detailing for reinforcement stability in RC members. *ASCE Journal of Structural Engineering* 1998; 124: 623–32.

[182] Carreno Vallejos R. Characterization of large diameter reinforcement under large strain cyclic reversals. *PhD Dissertation*, UC San Diego, 2018.

[183] Abtahi S, Li Y. Investigation of Corroded Bond-Slip Effects for Corroded RC Columns. *ASCE Journal of Structural Engineering* 2022 (under review).

[184] Raphael JM. Tensile strength of concrete. *Journal of Proceedings* 1984; vol. 81, p. 158–65.

[185] Fildes, J. M., Chen, P., and Zhan, X. Application of electrochemical impedance spectroscopy, color visible imaging, and infrared imaging for non-destructive evaluation of anti-corrosion coatings. *Infrastructure Technology Institute Technical Rep. 14*, Infrastructure Technology Institute, Northwestern University, Evanston, IL, 1995.

[186] Casas JR, Cruz PJS. Fiber optic sensors for bridge monitoring. *ASCE Journal of Bridge Engineering* 2003; 8: 362–73.

[187] Simmers Jr GE, Sodano HA, Park G, Inman DJ. Detection of corrosion using piezoelectric impedance-based structural health monitoring. *AIAA Journal* 2006; 44: 2800–3.

[188] Shim C-S, Dang N-S, Lon S, Jeon C-H. Development of a bridge maintenance system for prestressed concrete bridges using 3D digital twin model. *Structure and Infrastructure Engineering* 2019; 15: 1319–32.

[189] Hoshiya M, Saito E. Structural identification by extended Kalman filter. *ASCE Journal of Engineering Mechanics* 1984; 110: 1757–70.

[190] Chatzi EN, Smyth AW. The unscented Kalman filter and particle filter methods for nonlinear structural system identification with non-collocated heterogeneous sensing. *Structural Control and Health Monitoring* 2009; 16: 99–123.

[191] Liu Z, Abtahi S, Astroza R, Li Y. Test data-informed nonlinear finite element model updating and damage inference of a shake-table tested bridge column considering bond-slip

under multiple earthquakes. *Journal of Earthquake Engineering* 2022; 1−25.

[192] Jang S, Li J, Spencer Jr BF. Corrosion estimation of a historic truss bridge using model updating. *ASCE Journal of Bridge Engineering* 2013; 18: 678–89.

[193] Faroz SA, Pujari NN, Ghosh S. Reliability of a corroded RC beam based on Bayesian updating of the corrosion model. *Engineering Structure* 2016; 126: 457–68.

[194] Heitner B, Obrien EJ, Yalamas T, Schoefs F, Leahy C, Décatoire R. Updating probabilities of bridge reinforcement corrosion using health monitoring data. *Engineering Structure* 2019; 190: 41–51.

[195] Panchireddi B, Ghosh J. Cumulative vulnerability assessment of highway bridges considering corrosion deterioration and repeated earthquake events. *Bulletin of Earthquake Engineering* 2019; 17: 1603–38.

[196] Vereecken E, Botte W, Lombaert G, Caspeele R. A Bayesian inference approach for the updating of spatially distributed corrosion model parameters based on heterogeneous measurement data. *Structure and Infrastructure Engineering* 2021; 18: 30–46.

[197] Li Y, Astroza R, Conte JP, Soto P. Nonlinear FE model updating and reconstruction of the response of an instrumented seismic isolated bridge to the 2010 Maule Chile earthquake. *Earthquake Engineering and Structural Dynamics* 2017; 46: 2699–716.

[198] Girardi M, Padovani C, Pellegrini D, Robol L. A finite element model updating method based on global optimization. *Mechanical Systems and Signal Processing* 2021; 152: 107372.

[199] Lundgren K, Kettil P, Hanjari KZ, Schlune H, Roman ASS. Analytical model for the bond-slip behaviour of corroded ribbed reinforcement. *Structure and Infrastructure Engineering* 2012; 8: 157–69.

[200] Blomfors M, Zandi K, Lundgren K, Coronelli D. Engineering bond model for corroded reinforcement. *Engineering Structure* 2018; 156: 394–410.

[201] Sakai J, Unjoh S. Shake table experiment on circular reinforced concrete bridge column under multidirectional seismic excitation. *Frontiers of Structural and Civil Engineering* 2007; p. 1–12.

[202] Sony S, Laventure S, Sadhu A. A literature review of next-generation smart sensing technology in structural health monitoring. *Structural Control and Health Monitoring* 2019; 26: e2321.

[203] McCarter WJ, Vennesland Ø. Sensor systems for use in reinforced concrete structures. *Construction and Building Materials* 2004; 18: 351–8.

[204] Deb A, Zha AL, Caamano-Withall ZA, Conte JP, Restrepo JI. Updated probabilistic seismic performance assessment framework for ordinary standard bridges in California. *Earthquake Engineering and Structural Dynamics* 2021; 50: 2551–70.

[205] Mosleh A, Jara J, Razzaghi MS, Varum H. Probabilistic seismic performance analysis of RC bridges. *Journal of Earthquake Engineering* 2020; 24: 1704–28.

[206] Nielson BG, DesRoches R. Analytical seismic fragility curves for typical bridges in the central and southeastern United States. *Earthquake Spectra* 2007; 23: 615–33.

[207] Bouazza H, Djelil M, Matallah M. On the relevance of incorporating bar slip, bar buckling and low-cycle fatigue effects in seismic fragility assessment of RC bridge piers. *Engineering Structure* 2022; 256: 114032.

[208] Abtahi S, Li Y. Material Model of Corroded Reinforcing Bars with Buckling Considering the Effects of Stirrups. *ASCE Journal of Structural Engineering* 2022 (in preparation).

[209] Abtahi S, Liu Z, Li Y. Corrosion State Estimation for RC Structures Based on Bayesian

Nonlinear Finite Element Model Updating with Seismic Data. *Mechanical Systems and Signal Processing* 2022 (under review).

[210] Building Seismic Safety Council. NEHRP recommended provisions for seismic regulations for new buildings and other structures, Part 1-Provisions. *Report No. FEMA 302*, for the Federal Emergency Management Agency, Washington, D.C, 1997.

[211] Deb A. Risk-targeted performance-based seismic assessment and design of bridges. *PhD Dissertation*, University of California, San Diego; 2021.

[212] Kaviani P, Zareian F, Taciroglu E. Performance-based seismic assessment of skewed bridges. *Pacific Earthquake Engineering Research Center*, Technical Report No. PEER 2014/01, 2014.

[213] Omrani R, Mobasher B, Liang X, Gunay S, Mosalam KM, Zareian F, et al. Guidelines for nonlinear seismic analysis of ordinary bridges: Version 2.0. *Caltrans Final Report* 2015.

[214] Frankel AD, Mueller CS, Barnhard TP, Leyendecker E V, Wesson RL, Harmsen SC, et al. USGS national seismic hazard maps. *Earthquake Spectra* 2000; 16: 1–19.

[215] Watson-Lamprey J, Abrahamson N. Selection of ground motion time series and limits on scaling. *Soil Dynamic and Earthquake Engineering* 2006; 26: 477–82.

[216] Zhang W-P, Chen J-P, Yu Q-Q, Gu X-L. Corrosion evolution of steel bars in RC structures based on Markov chain modeling. *Structural Safety* 2021; 88: 102037.

[217] Lin W, Yoda T. *Bridge engineering: classifications, design loading, and analysis methods*. Butterworth-Heinemann; 2017.

[218] Priestley MJN, Seible F, Calvi GM. *Seismic design and retrofit of bridges*. John Wiley & Sons; 1996.

[219] Benjamin JR, Cornell CA. *Probability, statistics, and decision for civil engineers*. McGraw-

Hill, New York; 2014.

[220] Cornell CA, Jalayer F, Hamburger RO, Foutch DA. Probabilistic basis for 2000 SAC federal emergency management agency steel moment frame guidelines. *ASCE Journal of Structural Engineering* 2002; 128: 526–33.

[221] Shome N, Cornell CA, Bazzurro P, Carballo JE. Earthquakes, records, and nonlinear responses. *Earthquake Spectra* 1998; 14: 469–500.

Appendix A. ELEMENT FORMULATION

The following equation demonstrates the shape function matrix used in the element formulation:

$$\mathbf{N}_{\mathbf{u}}(x)=\left[\begin{array}{c:c:c:c}\mathbf{N}_B^1(x)_{2\times 3} & \underline{\mathbf{0}}_{2\times n} & \mathbf{N}_B^2(x)_{2\times 3} & \underline{\mathbf{0}}_{2\times n} \\ \hdashline \underline{\mathbf{0}}_{n\times 3} & \mathbf{N}_b^1(x)_{n\times n} & \underline{\mathbf{0}}_{n\times 3} & \mathbf{N}_b^2(x)_{n\times n}\end{array}\right] \tag{A-1}$$

where

$$\mathbf{N}_B^1(x)=\begin{bmatrix}1-\dfrac{x}{L_0} & 0 & 0 \\ 0 & 2(\dfrac{x}{L_0})^3-3(\dfrac{x}{L_0})^2+1 & \dfrac{x}{L_0}(\dfrac{x}{L_0}-1)^2\end{bmatrix} \tag{A-2}$$

$$\mathbf{N}_B^2(x)=\begin{bmatrix}\dfrac{x}{L_0} & 0 & 0 \\ 0 & -2(\dfrac{x}{L_0})^3+3(\dfrac{x}{L_0})^2 & \dfrac{x^2}{L_0}(\dfrac{x}{L_0}-1)\end{bmatrix} \tag{A-3}$$

$$\mathbf{N}_b^1(x)=\begin{bmatrix}-\dfrac{x}{L_0}+1 & & \underline{\mathbf{0}} \\ & \ddots & \\ \underline{\mathbf{0}} & & -\dfrac{x}{L_0}+1\end{bmatrix} \tag{A-4}$$

$$\mathbf{N}_b^2(x)=\begin{bmatrix}\dfrac{x}{L_0} & & \underline{\mathbf{0}} \\ & \ddots & \\ \underline{\mathbf{0}} & & \dfrac{x}{L_0}\end{bmatrix} \tag{A-5}$$

in which L_0 is the undeformed element length and n is the number of steel bars. To find the augmented section vector and slip vector, it is required to define the following equations:

$$\partial = \left[\begin{array}{cc|ccc} {d}/{dx} & 0 & & \underline{\mathbf{0}}_{2\times n} & \\ 0 & {d^2}/{dx^2} & & & \\ \hline & & {d}/{dx} & & \underline{\mathbf{0}} \\ \underline{\mathbf{0}}_{n\times 2} & & & \ddots & \\ & & \underline{\mathbf{0}} & & {d}/{dx} \end{array}\right] \tag{A-6}$$

$$\partial_b = \left[\begin{array}{cc|ccc} -1 & \overline{y}_1 \dfrac{d}{dx} & 1 & & \underline{\mathbf{0}} \\ \vdots & \vdots & & \ddots & \\ -1 & \overline{y}_n \dfrac{d}{dx} & \underline{\mathbf{0}} & & 1 \end{array}\right] \tag{A-7}$$

Correspondingly, $\mathbf{B_u}(x)$ is defined as follows:

$$\mathbf{B_u}(x) = \partial \mathbf{N_u}(x) = \left[\begin{array}{c|c|c|c} \mathbf{B}_1(x)_{2\times 3} & \underline{\mathbf{0}}_{2\times n} & \mathbf{B}_2(x)_{2\times 3} & \underline{\mathbf{0}}_{2\times n} \\ \hline \underline{\mathbf{0}}_{n\times 3} & \mathbf{B}_3(x)_{n\times n} & \underline{\mathbf{0}}_{n\times 3} & \mathbf{B}_4(x)_{n\times n} \end{array}\right] \tag{A-8}$$

where

$$\mathbf{B}_1(x) = \begin{bmatrix} -\dfrac{1}{L_0} & 0 & 0 \\ 0 & -\dfrac{6(L_0 - 2x)}{L_0^{\,3}} & -\dfrac{2(2L_0 - 3x)}{L_0^{\,2}} \end{bmatrix} \tag{A-9}$$

$$\mathbf{B}_2(x) = \begin{bmatrix} \dfrac{1}{L_0} & 0 & 0 \\ 0 & \dfrac{6(L_0 - 2x)}{L_0^{\,3}} & -\dfrac{2(L_0 - 3x)}{L_0^{\,2}} \end{bmatrix} \tag{A-10}$$

$$\mathbf{B}_3(x) = \begin{bmatrix} -\dfrac{1}{L_0} & & \underline{\mathbf{0}} \\ & \ddots & \\ \underline{\mathbf{0}} & & -\dfrac{1}{L_0} \end{bmatrix} \tag{A-11}$$

$$\mathbf{B}_4(x) = \begin{bmatrix} \frac{1}{L_0} & & \underline{\mathbf{0}} \\ & \ddots & \\ \underline{\mathbf{0}} & & \frac{1}{L_0} \end{bmatrix} \tag{A-12}$$

Similarly, $\mathbf{B_b}(x)$ reads:

$$\mathbf{B_b}(x) = \partial_{\mathbf{b}} \mathbf{N_u}(x) = \left[\mathbf{B}_{b1}(x)_{n\times 3} \;\vdots\; \mathbf{B}_{b2}(x)_{n\times 3} \;\vdots\; \mathbf{B}_{b3}(x)_{n\times 3} \;\vdots\; \mathbf{B}_{b4}(x)_{n\times 3} \right] \tag{A-13}$$

where

$$\mathbf{B}_{b1}(x) = \begin{bmatrix} \frac{x}{L_0} - 1 & \frac{6xy_1(L_0 - x)}{L_0{}^3} & \frac{y_1(L_0 - x)(L_0 - 3x)}{L_0{}^2} \\ \vdots & \vdots & \vdots \\ \frac{x}{L_0} - 1 & \frac{6xy_n(L_0 - x)}{L_0{}^3} & \frac{y_n(L_0 - x)(L_0 - 3x)}{L_0{}^2} \end{bmatrix} \tag{A-14}$$

$$\mathbf{B}_{b2}(x) = \begin{bmatrix} 1 - \frac{x}{L_0} & & \underline{\mathbf{0}} \\ & \ddots & \\ \underline{\mathbf{0}} & & 1 - \frac{x}{L_0} \end{bmatrix} \tag{A-15}$$

$$\mathbf{B}_{b3}(x) = \begin{bmatrix} -\frac{x}{L_0} & \frac{6xy_1(L_0 - x)}{L_0{}^3} & \frac{xy_1(2L_0 - 3x)}{L_0{}^2} \\ \vdots & \vdots & \vdots \\ -\frac{x}{L_0} & \frac{6xy_n(L_0 - x)}{L_0{}^3} & \frac{xy_n(2L_0 - 3x)}{L_0{}^2} \end{bmatrix} \tag{A-16}$$

$$\mathbf{B}_{b4}(x) = \begin{bmatrix} \frac{x}{L_0} & & \underline{\mathbf{0}} \\ & \ddots & \\ \underline{\mathbf{0}} & & \frac{x}{L_0} \end{bmatrix} \tag{A-17}$$

Appendix B. ELEMENT IMPLEMENTATION IN OPENSEES

To show the framework of the new capabilities implemented in *OpenSees*, Figure B-1 presents the newly added subclasses (i.e., new element, section, and material state determinations as well as new geometric transformation) with respect to the existing software architecture of *OpenSees*. Note that these subclasses enable *OpenSees* to model RC members considering imperfect bonding, which was not achievable by using existing fiber-based frame elements in *OpenSees* [65].

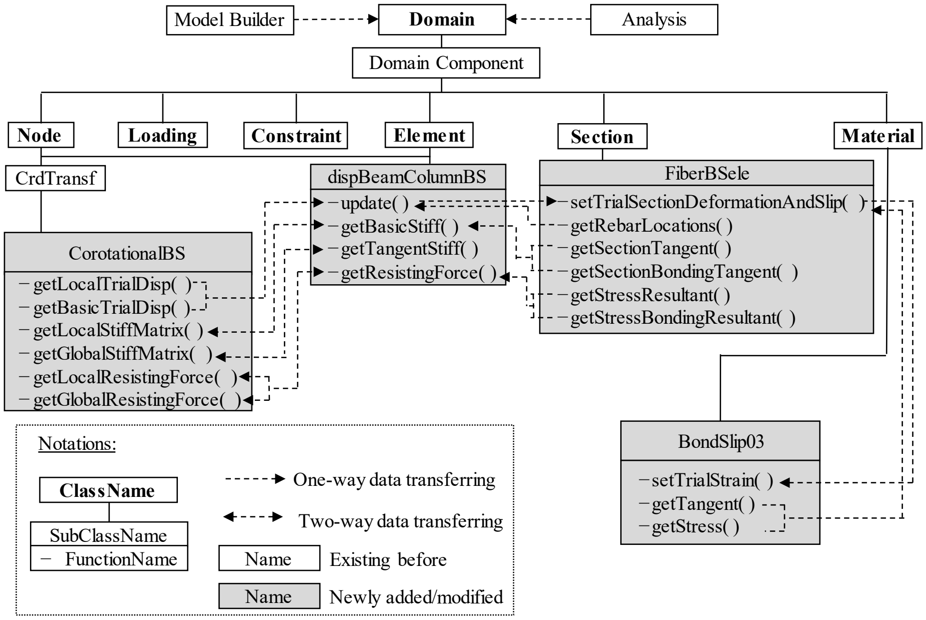

Figure B-1: Implementation of newly developed finite element modeling capabilities for RC structures considering bond-slip in *OpenSees* framework

Appendix C. EXPERIMENTAL DATA FOR BONDING PROPERTIES

Table C-1: Experimental data for bonding properties for steel bars in concrete

No.	Source	Inputs						Outputs				
		d_b	f_c	c/d_b	l_s/d_b	l_h/d_b	l_s/l_h	t_1	t_3	u_{b1}	u_{b2}	u_{b3}
1	[107,126]	25.40	29.40	4.00	0.53	0.08	6.70	13.60	5.00	1.60	2.00	13.80
2		25.40	29.40	4.00	0.53	0.08	6.70	13.20	4.45	1.60	2.00	13.80
3		25.40	29.40	4.00	0.53	0.08	6.70	13.80	4.00	1.60	2.00	12.80
4		25.40	30.50	4.00	0.53	0.08	6.70	13.60	4.60	1.40	1.80	12.40
5		25.40	30.50	4.00	0.53	0.08	6.70	13.80	5.30	1.40	1.80	13.30
6		25.40	30.50	4.00	0.53	0.08	6.70	13.40	4.70	1.00	1.40	13.30
7		25.40	30.50	4.00	0.53	0.08	6.70	11.40	3.90	1.30	2.20	13.20
8		25.40	30.50	4.00	0.53	0.08	6.70	11.60	4.00	1.50	1.80	13.80
9		25.40	30.50	4.00	0.53	0.08	6.70	12.20	4.70	1.50	2.00	12.00
10		25.40	30.50	4.00	0.53	0.08	6.70	13.20	4.80	1.40	2.00	13.10
11		25.40	30.50	4.00	0.53	0.08	6.70	14.80	5.00	1.40	1.70	12.00
12		25.40	30.50	4.00	0.53	0.08	6.70	11.80	3.80	1.20	1.60	13.50
13		25.40	28.50	4.00	0.53	0.08	6.70	12.30	4.20	1.50	2.10	11.00
14		25.40	30.70	4.00	0.53	0.08	6.70	13.40	6.00	1.40	2.00	9.00
15		25.40	30.70	4.00	0.53	0.08	6.70	13.80	4.80	1.60	2.10	12.00
16		25.40	29.60	4.00	0.53	0.08	6.70	14.60	5.40	1.60	2.10	11.00
17		25.40	29.60	4.00	0.53	0.08	6.70	15.30	4.80	1.50	2.10	11.40
18		25.40	29.60	4.00	0.53	0.08	6.70	13.10	4.20	1.60	2.00	14.00
19		19.00	31.60	4.00	0.51	0.06	8.08	16.00	5.10	1.00	1.40	10.00
20		25.40	31.60	4.00	0.53	0.08	6.70	15.40	6.00	0.80	1.20	12.00
21		31.80	31.60	4.00	0.43	0.10	4.22	13.00	5.50	0.80	1.30	10.70
22		25.40	54.60	4.00	0.53	0.08	6.70	18.00	6.00	1.06	1.63	11.00
23		25.40	28.20	1.00	0.53	0.08	6.70	13.40	4.00	1.40	2.15	11.60
24		25.40	28.20	2.00	0.53	0.08	6.70	12.65	4.60	1.70	2.10	11.55
25		25.40	28.20	6.00	0.53	0.08	6.70	13.15	5.00	1.50	2.00	11.10
26	[129]	16.00	36.00	1.56	–	–	10.00	19.30	–	1.52	–	–
27		16.00	36.00	1.56	–	–	10.00	18.90	–	1.45	–	–
28		16.00	36.00	1.56	–	–	10.00	18.60	–	1.56	–	–
29		16.00	36.00	1.56	–	–	10.00	20.70	–	0.85	–	–
30		16.00	36.00	1.56	–	–	10.00	21.10	–	0.89	–	–

31	[84]	36.00	34.50	11.50	0.53	0.07	7.58	15.20	_	3.00	–	19.10
32		36.00	34.50	11.50	0.53	0.07	7.58	12.40	_	3.00	–	19.10
33		36.00	34.50	11.50	0.53	0.07	7.58	13.80	_	3.00	–	19.10
34		36.00	34.50	11.50	0.53	0.07	7.58	14.50	_	3.00	–	19.10
35		36.00	34.50	11.50	0.53	0.07	7.58	11.70	_	3.00	–	19.10
36		36.00	34.50	11.50	0.53	0.07	7.58	12.40	_	3.00	–	19.10
37		43.00	34.50	9.47	0.58	0.07	8.52	19.30	_	2.80	–	24.90
38		43.00	34.50	9.47	0.58	0.07	8.52	15.20	_	2.80	–	24.90
39		43.00	34.50	9.47	0.58	0.07	8.52	15.20	_	2.80	–	24.90
40		43.00	34.50	9.47	0.58	0.07	8.52	16.50	_	2.80	–	24.90
41		43.00	34.50	9.47	0.58	0.07	8.52	15.20	_	2.80	–	24.90
42		43.00	34.50	9.47	0.58	0.07	8.52	15.20	_	2.80	–	24.90
43		57.00	34.50	6.90	0.43	0.10	4.51	17.20	_	3.00	–	24.40
44		57.00	34.50	6.90	0.43	0.10	4.51	13.10	_	3.00	–	24.40
45		57.00	34.50	6.90	0.43	0.10	4.51	13.80	_	3.00	–	24.40
46		57.00	34.50	6.90	0.43	0.10	4.51	17.90	_	3.00	–	24.40
47		57.00	34.50	6.90	0.43	0.10	4.51	14.50	_	3.00	–	24.40
48		57.00	34.50	6.90	0.43	0.10	4.51	15.20	_	3.00	–	24.40
49		43.00	55.00	9.47	0.58	0.07	8.52	24.10	_	3.00	–	24.90
50		43.00	55.00	9.47	0.58	0.07	8.52	22.80	_	3.00	–	24.90
51		43.00	55.00	9.47	0.58	0.07	8.52	19.30	_	3.00	–	24.90
52		43.00	55.00	9.47	0.58	0.07	8.52	20.00	_	3.00	–	24.90
53	[121]	5.00	37.00	4.00	0.50	0.06	8.33	31.80	_	0.50	0.74	3.29
54		5.00	37.00	4.00	–	–	8.33	33.60	_	–	–	–
55		5.00	37.00	4.00	–	–	8.33	31.00	_	–	–	–
56		12.00	37.00	4.00	0.50	0.06	8.33	26.80	_	1.49	1.66	7.37
57		12.00	37.00	4.00	–	–	8.33	24.90	_	–	–	–
58		12.00	37.00	4.00	–	–	8.33	30.00	_	–	–	–
59		18.00	37.00	4.00	0.50	0.06	8.33	24.50	_	1.54	1.89	7.63
60		18.00	37.00	4.00	–	–	8.33	24.90	_	–	–	–
61		18.00	37.00	4.00	–	–	8.33	25.20	_	–	–	–
62		26.00	37.00	4.00	0.50	0.06	8.33	23.20	_	1.49	1.73	7.37
63		26.00	37.00	4.00	_	_	8.33	24.80	_	–	–	–
64		26.00	37.00	4.00	_	_	8.33	23.40	_	–	–	–
65		5.00	41.00	4.00	_	_	8.33	27.50	_	–	–	–

66		5.00	41.00	4.00	_	_	8.33	25.80	_	–	–	–
67		5.00	41.00	4.00	_	_	8.33	26.40	_	–	–	–
68		12.00	41.00	4.00	_	_	8.33	30.00	_	–	–	–
69		18.00	41.00	4.00	_	_	8.33	24.60	_	–	–	–
70		18.00	41.00	4.00	_	_	8.33	23.30	_	–	–	–
71		18.00	41.00	4.00	_	_	8.33	24.00	_	–	–	–
72		26.00	41.00	4.00	_	_	8.33	22.10	_	–	–	–
73		26.00	41.00	4.00	_	_	8.33	21.70	_	–	–	–
74		26.00	41.00	4.00	_	_	8.33	22.80	_	–	–	–
75	[123]	16.00	30.00	3.00	0.61	0.06	10.10	16.30	5.78	1.06	1.44	9.09
76		19.10	32.00	3.00	0.66	0.06	10.41	15.56	5.78	0.91	1.52	9.09
77		22.18	30.00	3.00	0.60	0.06	10.00	14.44	5.48	0.91	2.35	9.70
78		25.40	30.00	3.00	0.40	0.06	6.71	13.33	4.74	0.99	1.74	10.46
79		32.30	32.00	3.00	0.64	0.07	9.63	12.59	5.78	0.83	1.29	9.70
80	[122]	25.40	27.58	4.00	0.40	0.04	10.00	30.54	–	2.93	2.93	11.60
81		25.40	27.58	4.00	0.80	0.04	20.00	26.10	–	2.93	2.93	16.85
82		25.40	27.58	4.00	1.20	0.04	30.00	26.60	–	3.91	3.91	24.79
83		25.40	27.58	4.00	_	_	2.98	26.38	–	–	–	–
84		25.40	27.58	4.00	_	_	4.79	26.76	–	–	–	–
85		25.40	27.58	4.00	_	_	5.25	27.49	–	–	–	–
86		25.40	27.58	4.00	_	_	6.30	27.67	–	–	–	–
87		25.40	27.58	4.00	_	_	11.27	22.68	–	–	–	–
88		25.40	27.58	4.00	_	_	12.42	22.96	–	–	–	–
89		25.40	27.58	4.00	_	_	16.14	19.58	–	–	–	–
90		25.40	27.58	4.00	_	_	16.86	20.62	–	–	–	–
91		25.40	27.58	4.00	_	_	24.31	19.83	–	–	–	–
92		25.40	27.58	4.00	_	_	24.98	19.84	–	–	–	–
93		25.40	27.58	4.00	_	_	25.91	16.96	–	–	–	–

Appendix D. MODELS FOR CORRODED BONDING PROPERTIES

This section presents the detailed information of the new probabilistic model for corroded bonding properties developed in this study. Several studies in the literature [144–148,152,153] defined corroded bonding properties (i.e., t_1^c, t_3^c, u_{b1}^c, u_{b2}^c, and u_{b3}^c) by modifying the uncorroded bonding properties based on the corrosion level. Table D-1 summarizes a number of existing models in the literature. Note that all of these models assumed that corrosion does not affect the ratio of u_{b2}/u_{b1}, thus u_{b2}^c can be determined based on the same ratio with u_{b1}^c.

Table D-1: Summary of existing modification models for corroded bonding properties

Model	**Model parameters for corroded bond-slip**			
	t_1^c/t_1	t_3^c/t_1^c	u_{b1}^c/u_{b1}	u_{b3}^c/u_{b3}
Cabrera [152]	$1.0-5.6(K/100)$	t_3/t_1^c	1	1
Auyeung et al. [153]	$\exp(-32.5K/100)$	t_3/t_1^c	1	1
Lee et al. [144]	$\exp(-5.6K/100)$	t_3/t_1^c	1	1
Chung et al. [146]	$0.116(K/100)^{-0.55}$	t_3/t_1^c	1	1
Bhargava et al. [145]	$\exp(-11.7(K-1.5)/100)$	t_3/t_1^c	1	1
Kivell et al. [147]	$1.2\exp(-0.076K)$	$0.26+0.13K \quad K<3$ $0.65 \quad 3\leq K<13$ $0.65-0.06(K-13) \quad 3\leq K<20$	1	$0.38\times$ $\exp(-0.3K)$ $+0.63$
Zhou et al. [148]	$0.28+(10.8/(K^{1.8}+13.9))$	t_3/t_1^c	$(0.123K+1)^{-1}$	1

These models were developed based on the highly scattered and limited experimental data with no quantification of uncertainties. In order to develop a new probabilistic model for corroded bonding properties, i.e., t_1^c, t_3^c, u_{b1}^c, u_{b2}^c, and u_{b3}^c, which quantifies the prevailing uncertainties, a database including 573 data points for t_1^c, 22 data points for t_3^c, 178 data points for u_{b1}^c, 17 data points for u_{b2}^c, and 22 data points for u_{b3}^c corresponding to different corrosion levels, is compiled in this study, as summarized in Table D-2. Note that corresponding to each of these tests, the uncorroded bonding properties are also collected in the database.

Table D-2: Source of experimental data for corroded bonding properties

Parameter	Number of data from each source									Total
	[159]	[155]	[154]	[145]	[156]	[157]	[147]	[158]	[148]	
t_1^c	10	4	260	120	20	77	48	17	17	573
t_3^c	–	–	10	–	–	–	5	–	7	22
u_{b1}^c	–	4	10	–	–	77	7	–	80	178
u_{b2}^c	–	–	–	–	–	12	5	–	–	17
u_{b3}^c	–	–	10	–	–	–	5	–	7	22

To estimate the maximum corroded bonding stress, i.e., t_1^c, the maximum uncorroded bonding stress, i.e., t_1, needs to be modified based on the corrosion level (i.e., percentage of mass loss K). When the corrosion level is low, the maximum bonding stress may increase due to the enhancement of friction caused by steel rust. However, this growth in maximum bonding stress can be neglected after the early stage of corrosion, as many of the models in the literature considered (e.g., [145] and [147]). By increasing the corrosion level, the mechanical interaction of bond-slip is damaged, and the maximum bonding stress would reduce significantly. To capture such effects, the proposed equation for the ratio of t_1^c to t_1 is a piecewise function depending on the corrosion level, as shown in Eq. (D-1), which is the best model form selected for t_1^c/t_1 among a group of candidate model forms examined with 573 observations from the experimental data.

Similar to t_1^c, the slip corresponding to maximum corroded bonding stress, i.e., u_{b1}^c, can be determined through modifying the corresponding uncorroded bonding property, i.e., u_{b1}, at each corrosion level. To this end, a group of candidate model forms for u_{b1}^c/u_{b1} is examined based on 178 experimental data points. The model selected for this ratio is shown in Eq. (D-2). Note that following the same assumption as t_1^c, the effect of minor corrosion (i.e., less than 3% mass loss) on u_{b1}^c is neglected. It is worth mentioning that in the existing models of u_{b1}^c, the effect of corrosion on this parameter is considered to be negligible, i.e., it is assumed that $u_{b1}^c/u_{b1} = 1$ [147].

According to the models of uncorroded bonding properties (e.g., [143]), the frictional residual bonding stress t_3 is linearly correlated with the maximum bonding stress t_1. A similar correlation can be applied to the corroded bonding properties, i.e., t_3^c has a linear relationship with t_1^c. Therefore, using 22 experimental observations from the compiled database, a piecewise function consisting of three linear equations is proposed for the ratio of t_3^c to t_1^c depending on the corrosion level, as shown in Eq. (D-3). Similarly, the slip at the end of plateau in corroded bond-slip model, i.e., u_{b2}^c, is linearly related to u_{b1}^c, following the existing models for uncorroded bonding. Therefore, a linear regression model for the ratio of u_{b2}^c to u_{b1}^c presented in Eq. (D-4) is developed using 17 experimental data points.

To estimate the slip corresponding to corroded residual frictional bonding stress, i.e., u_{b3}^c, it can be related to the corresponding uncorroded bonding property, i.e., u_{b3}, similar to t_1^c and u_{b1}^c. Thus, different models considering corrosion level are examined, and the model selected for u_{b3}^c/u_{b3} is shown in Eq. (D-5). Note that following the same assumption as t_1^c and u_{b1}^c, the effect of corrosion on u_{b3} is neglected for minor corrosion levels (i.e., less than 3% mass loss).

$$\frac{t_1^c}{t_1} = \begin{cases} 1.0 & K \le 3 \\ \exp(\theta_1 + \theta_2 K + e_1) K^{\theta_3} & K > 3 \end{cases} \tag{D-1}$$

$$\frac{u_{b1}^c}{u_{b1}} = \begin{cases} 1.0 & K \le 3 \\ \theta_9 + e_5 & K > 3 \end{cases} \tag{D-2}$$

$$\frac{t_3^c}{t_1^c} = \begin{cases} \theta_4 + \theta_5 K + e_2 & K \le 3 \\ \theta_6 + e_3 & 3 < K \le 12 \\ \theta_7 + \theta_8 K + e_4 & K > 12 \end{cases} \tag{D-3}$$

$$\frac{u_{b2}^c}{u_{b1}^c} = \theta_{10} + e_6 \tag{D-4}$$

$$\frac{u_{b3}^c}{u_{b3}} = \begin{cases} 1.0 & K \le 3 \\ K^{\theta_{11}} \exp(e_7) & K > 3 \end{cases} \tag{D-5}$$

In Eqs. (D-1) to (D-5), θ_i's with $i = 1, 2, \ldots, 11$ are model parameters, and e_i's with $i = 1, 2, \ldots, 7$ are model errors assumed as Gaussian with zero mean and standard deviation σ_i as a hyper-parameter. The first- and second-moment statistics of these parameters (i.e., mean, coefficient of variation (CoV), and correlation coefficients) are presented in Table D-3. In Bayesian statistics, the non-informative priors, i.e., locally uniform, are assumed for all parameters, which lead to the multivariate *t*-distribution for model parameters and the inverse chi-squared distribution for the hyper-parameter [130].

Table D-3: Regression parameters for the proposed probabilistic model

			Correlation coefficients		
Parameters for t_1^c/t_1	**Mean**	**CoV**	θ_1	θ_2	θ_3
θ_1	0.168	0.752	1.000	0.738	−0.947
θ_2	−0.019	0.351	0.738	1.000	−0.897
θ_3	−0.241	0.361	−0.947	−0.897	1.000
σ_1	0.541	0.470	–	–	–
Parameters for t_3^c/t_1^c	**Mean**	**CoV**	θ_4	θ_5	
θ_4	0.170	0.274	1.000	−0.711	
θ_5	0.160	0.307	−0.711	1.000	
σ_2	0.098	0.200	–	–	
			θ_6		
θ_6	0.650	0.043	1.000		
σ_3	0.093	0.288	–		
			θ_7	θ_8	
θ_7	1.069	0.191	1.000	−0.993	
θ_8	−0.035	0.276	−0.993	1.000	
σ_4	0.053	0.300	–	–	
Parameters for u_{b1}^c/u_{b1}	**Mean**	**CoV**	θ_9		
θ_9	0.750	0.062	1.000		
σ_5	0.514	0.066	–		
Parameters for u_{b2}^c/u_{b1}^c	**Mean**	**CoV**	θ_{10}		
θ_{10}	1.291	0.083	1.000		
σ_6	0.654	0.125	–		
Parameters for u_{b3}^c/u_{b3}	**Mean**	**CoV**	θ_{11}		
θ_{11}	−0.557	0.115	1.000		
σ_7	0.672	0.196	–		

To evaluate the assumptions of the proposed model, shown in Eqs. (D-1) to (D-5), diagnostic tests were performed, such as normality and homoscedasticity of model residuals; however, they are not shown here for brevity. Specifically, the normality plots show that the model residuals follow a Gaussian distribution, and residuals plots show no hint of heteroscedasticity.